NRL Report 6214
Copy No. 83 of 150 Copies

PROGRESS REPORT NO. 15

HYPERVELOCITY KILL MECHANISMS PROGRAM

[UNCLASSIFIED TITLE]

Sponsored by

Advanced Research Projects Agency
Ballistic Missile Defense Systems Branch
ARPA Order No. 149

Semiannual Technical Progress Report
for period ending 31 March 1964

October 1964

U. S. NAVAL RESEARCH LABORATORY
Washington, D.C.

CONTRIBUTORS

Aeronautical Research Associates of Princeton

General Electric Company – MSD

U.S. Naval Research Laboratory

U.S. Naval Ordnance Laboratory

CONTENTS

PROBLEM STATUS

This is the fifteenth progress report covering the work of the participants in the Hypervelocity Kill Mechanisms Program. Work on this problem is continuing.

Authorization
NRL Problem No. F04-11
ARPA Order No. 149-60 - Amendments 1 thru 7

SUMMARY

W. W. Atkins - M. A. Persechino
U. S. Naval Research Laboratory

INTRODUCTION

Progress Report No. 15 is a semiannual technical progress report covering the work of the participants in the Hypervelocity Kill Mechanisms Program for the period beginning 30 September 1963 to 31 March 1964. Reports covering the work completed during and prior to this reporting period are listed in Section Y.

The work of this program has involved comprehensive studies designed to evaluate the feasibility of defeating the mission of an intercontinental ballistic missile by fragment impact and/or by subsequent re-entry heating effects. These effects include: direct kill by impact, extent of aggravation or increase in damage caused by aerothermal effects on an R/V during re-entry, aerodynamic instability of nose cones caused by damage to the heat shield and structure, impact and thermal damage to internal components and warheads, and perturbations on the performance of ICBM booster vehicles. The HKM Program is divided into the following four phases of work:

1. Impact Damage. Initially BRL, NRL, AVCO and the Canadian Armament Research and Development Establishment were selected to study the effects of hypervelocity impacts on re-entry body materials and structures. Aerojet-General was selected to study the impact effects on propulsion systems. The work of Aerojet has been completed and the final report has been distributed. The impact work performed by AVCO has also been completed and a final report was included in Progress Report No. 13. The work completed by CARDE was reported in Progress Report No. 11. BRL is preparing a final report for their work on impacts into ablative structures. Only NRL is presently engaged in impact work for the HKM Program.

2. Aerothermal. In the early stages of the program, AVCO performed a multitude of experiments on cratered heat shield materials using rocket exhaust and plasma jet facilities in order to determine the thermodynamic effects on a damaged vehicle during re-entry. In the later stages of the program, punctured vehicles (vented and unvented) were analyzed. GE and AVCO performed analytical and experimental studies on

coupled and uncoupled flows, jet impingement, jet diffusion, and the determination of orifice coefficients for perforated re-entry vehicles. GE conducted an analytical study to determine the aerodynamic effects on a damaged vehicle during re-entry (the aeroballistic ranges and the wind tunnels of NOL and AEDC were utilized to provide experimental data). An effective kill mechanism did not evolve from these studies. During the latter part of the second year's effort ARAP was added to the participants in the aerothermal work and, at this time, a strong fundamental research effort on internal heating was established to determine a rationale for coupled and uncoupled flows, impinging jets, and wall jets. A flight test program employing a NASA propulsion and recovery system has been completed and the details of this program are described in Item 21 in the list of reports. These tests provided both external and internal heating data under actual and simulated environmental conditions.

3. Vehicle Vulnerability. The vulnerability work initially conducted to determine the vulnerability of re-entry body, warhead, and associated arming and fuzing components by BRL and Picatinny Arsenal have been terminated. A final report on the vulnerability of nuclear warheads to aero-thermal effects has been prepared by Picatinny Arsenal and distributed (See Item 22, Section Y).

Aerojet-General, under the technical management of the Weapons Laboratories, Detachment 4, ASD, Eglin AFB has completed the investigations to determine the vulnerability to fragment impact of both liquid and solid rocket propulsion systems. An analysis of the vulnerability of both the United States and other vehicles is included in the Aerojet final report (See Items 24, 25 and 26).

4. Intelligence. The intelligence phase of the work was designed to provide information and guide lines for the work performed in the other phases of the HKM Program. A report entitled "Soviet ICBM Re-Entry Body Study"has been prepared by Raytheon. This report provides a description of the Soviet ICBM based on early Soviet missile tests in the Pacific (See Item 1). Additional intelligence data are described in Section T of previous HKM Progress Reports.

PROGRESS

The work described below is a summary of the technical progress in the remaining phases of the HKM program for the period ending 31 March 1964.

1. Impact Damage Phase

The investigation by the Ballistic Research Laboratories of impact damage to composite targets utilizing aluminum jet pellets fired from an inhibited jet charge is under completion and a final report describing this work is expected by the end of the next reporting period. No report for this reporting period has been received and consequently is omitted from the text of this report.

The impact work conducted by NRL is reported in Section B and includes studies of: the effect of projectile density and angle of impact on ablative hole size, the minimum energy required for the perforation of flat-plate and conical structures, and impact damage to foam-filled enclosures (See Section B9). The projectiles used in these studies were nylon, aluminum, steel and uranium spheres.

Damage effectiveness of dense projectiles fired at low impact angles (10°) appear to be much superior to the lighter projectiles, as indicated by the penetration results obtained with uranium projectiles. The maximum penetration capability of residual spall material was determined by measuring the maximum depth of penetration into aluminum witness plates and was plotted as a function of velocity. These results indicate that, for aluminum and steel spheres, the maximum depth of the spall particle penetrations decrease as the velocity increases, for velocities greater than 5 km/sec.

Of the metallic projectiles, the more dense projectiles produced the deepest spall penetrations and the smallest hole sizes in the ablatives.

Hypervelocity impacts into ablative targets backed by enclosures filled with polyurethane foam gave a measure of the effectiveness of these materials for preventing residual or spall damage. The effectiveness for preventing spall damage increased as the foam density was increased.

Comparison with normal angle impacts of the hole sizes in the ablatives made with firings at impact angles between 45° and 70° indicate very strongly that larger perforation diameters are obtained with the angle shots.

More data are to be obtained for thin ablative composite targets with ablative thickness to projectile diameter ratios (t/d values) between 0.5 and 1.0. These data

will be compared with existing hole-size correlations for t/d values between 1 and 4. An experimental-theoretical study is planned for determining a physical basis for scaling projectile and target parameters and for estimating the spall energy resulting from hypervelocity impact into composite structures.

2. Aerothermal Phase

In the early phases of the HKM Program, a series of wind tunnel tests were performed in the Naval Ordnance Laboratory Hypersonic Wind Tunnel No. 4 to investigate aerodynamic stability on a damaged re-entry vehicle. Static stability coefficients of pitch, yaw, and roll were obtained at a Mach number of ten on .04783 scale models of a Mark 3 R/V. The impact damage on the models were simulated by removing portions of the nose and flare sections of the model, causing configurational assymetry. Performance data obtained with these models are included in the section of the body of this report designated as NOLTR 61-84. These results were used to supplement the previously reported analytical program conducted by the General Electric Company to determine the effect on the R/V trajectory of small hypervelocity fragment impact.

During this reporting period, Aeronautical Research Associates of Princeton and GE have continued internal heating and structural studies needed to develop the technology for assessing the potential of thermal kill of a perforated re-entry body. Because of contract renewal difficulties the work by AVCO was temporarily delayed and no report was available for this period. Previous phases of the AVCO studies have dealt with the flow and heat transfer of an expanding jet on the walls of an enclosure. In the next reporting period the concentration will be on the details of the jet mixing process. This investigation will extend the theoretical and experimental investigations of turbulent compressible jets which had been previously conducted within a limited range of Mach numbers and initial jet stagnation temperature to ambient temperature ratios. The AVCO investigation will include higher temperature ratios. With these results the ability of this analysis to predict jet mixing processes in the high temperature region will be determined. An important consequence of the test results of the ARAP and GE work conducted during this period was the increased effort directed toward understanding the mechanisms of coupled flow phenomena. It has been shown experimentally and analytically

that the heat flux entering the interior of a punctured vehicle under coupled conditions ($A/V^{2/3} > 0.05$) can be many times greater than that for uncoupled conditions ($A/V^{2/3} < 0.01$) where A is the area of the hole and V is the internal volume of the perforated vehicle. A flow mechanism, which can be shown to account for heat fluxes of the magnitudes observed in the experimental test facilities has been developed and verified experimentally by means of heat flux mapping and flow visualization techniques. Details of this mechanism which involves a combination of free shear layer and jet impingement effects are discussed in Section L.

In Section H, tests conducted in AEDC Tunnel C at Mach 10 and in the Malta Rocket Exhaust Facility at Mach 3 are reported. The internal heating from these two series of tests conducted in widely different environments correlated well with turbulent shear layer theory.

During the past six months the problem of possible countermeasure against thermal kill was investigated and is also reported in Section H. Lightweight urethane foam was used to fill the internal volume of the model R/V, and the "effective heat of ablation" was used to determine the performance of the foam. Additional studies are planned in order to develop a better understanding of the heat protection characteristics of lightweight foams in vehicles perforated by damage from hypervelocity impact. Various types of foam-filled models will be tested in the GE-RSD 5-megawatt Air Arc and the Malta Rocket Exhaust Facilities.

A correlation of AEDC and Malta Internal Heating Data for single perforations and no venting was applied to the C-1 target vehicle (a slender shaped-cone vehicle with a ballistic coefficient of 3000 lb/ft). Generalized results were obtained for the value of $A/V^{2/3}$ required to cause thermal kill of representative types of vehicle structures having the above geometry and a re-entry velocity of 25,000 ft/sec.

Use of the correlation of hole-size and fragment mass from impact data reported by NRL demonstrated the extreme sensitivity of lethal fragment mass to the size of the vehicle under attack (see pages H-37 thru H-39).

Comparisons of characteristics of the flow through machined orifices and those produced by hypervelocity impact into ablative structures were made in a test program performed

in AEDC Tunnel D. The mass flow rates were predictable by a viscous modification to inviscide expansion theory. Pressure surveys of the supersonic internal jets formed from tangential approach flow revealed the two-dimensional decay characteristic of the jets. The existence of two general types of internal jets, depending on the orifice pressure ratio, were disclosed by oil film photographs. See pages H-40 to H-58 for orifice flow tests and results.

The present investigation on structural type damage by GE is primarily concerned with the effects of openings caused by impact or local melting subsequent to impact. The effects of large openings on the load capability of cylinders subjected to axial and bending loads are being studies in support of an analytical technique for predicting these effects. Computational techniques will be applied to hardened and unhardened ICBM re-entry vehicle designs, and formulation of thermal analysis techniques and structural failure criteria will begin.

HYPERVELOCITY KILL MECHANISMS PROGRAM
ARPA ORDER NO. 149-60

Semiannual Progress Report for Period
Ending 31 March 1964

Ballistic Research Laboratories
Aberdeen, Maryland

(not available for this printing)

A

NRL Memorandum Report 1562

HYPERVELOCITY KILL MECHANISMS PROGRAM
ARPA ORDER NO. 149-60

Impact Damage Phase

Semiannual Progress Report for Period
Ending 31 March 1964

J. J. Condon

This research was supported by the Advanced Research Projects Agency, Ballistic Missile Defense System Branch.

NOTE: This report is for inclusion in the overall HKM Report. The page designation for this Section of the report is the letter "B"

U.S. NAVAL RESEARCH LABORATORY
WASHINGTON, D.C.

CONTENTS

PROBLEM STATUS

This is a Semiannual Technical Progress Report,
work on this project is continuing.

AUTHORIZATION

NRL Problem 62F04-11B
ARPA Order No. 149-60
Amendments 1 - 7

SUMMARY

During this period the effect of projectile density on ablative hole size and minimum perforation requirements was examined. The projectiles were uranium (with 8.5 % Mo.), steel, aluminum and nylon. The projectile masses ranged from 1 to 10-gm. The angle of impact was varied from 90° to 10°. All projectiles were saboted and the velocities varied from 2.5 to 7.8 km/sec with the major portion of data in the 6 to 7 km/sec range. The ablative targets were composite made from 1/2-inch and 1-inch thick astrolite and phenolic nylon flat plates, nose cone models, and flat-plate ablative structures in direct contact with polyurethane foam.

Experiments were designed to determine the effect of projectile density by impacting similar targets with different density spheres of the same mass and velocity. The depths of the rear spall penetration into aluminum witness blocks behind the targets showed that the spall penetration is greater for the impacts associated with higher density projectiles. The results also show the greater penetration and perforation capability of dense projectiles, such as uranium, particularly when impacting at low angles e.g. 10°.

INTRODUCTION

The object of this work is to determine the impact results on ablative materials and re-entry vehicle structures from hypervelocity impact with compact projectiles of various densities. Analytical means are used to explain the experimental results and to correlate significant parameters so that accurate and reliable impact predictions can be made. Empirical relationships have been established for penetration, minimum perforation and complete perforation of various composite materials used in missile structures. The majority of the impact experiments are accomplished using targets which closely approximate the outer structure of actual vehicles. A limited number of impacts are made into actual vehicle sections.

PROGRESS

Composite targets with ablative thicknesses of 0.5 to 1 inch were impacted with uranium, steel, aluminum and nylon spheres with masses of 1 to 10 grams and velocities ranging from 2.5 to 7.8 km/sec with the major portion of firings in the 6 to 7 km/sec range. The target materials were astrolite and phenolic nylon bonded to steel, aluminum and magnesium in configurations of flat plates, nose cone models, and flat-plate ablative structures in direct contact with foam blocks. The saboted projectiles impacted the targets at angles ranging from 10° to 90°.

The experiments were designed to determine the effect of projectile density on ablative hole size and minimum perforation. Similar targets were impacted with two-gram uranium, steel, aluminum and nylon spheres at two different velocities of about 5.2 and 7 km/sec. Minimum perforation was examined down to a 10° angle of obliquity using both uranium and steel spheres. Nose cone model impact results were compared to flat plate target results for similar impact conditions. Polyurethane foam with densities of 3.1 and 7 lb/ft^3 was examined for determining its effectiveness in stopping the rear spall resulting from aluminum sphere impacts.

The effective hole diameters in the ablative materials were calculated from areas measured with a polar planimeter. The data for all the firings are summarized in Table A and photographs of the targets are shown in Appendix A. The bond between the ablative and metal back-up was approximately 1/16-inch of rubber unless otherwise noted. The ablative thicknesses

are accurate to ± 1/32-inch. The uranium projectiles were made from 91.5% of depleted uranium and 8.5% of molybdenum for mechanical strength, giving an overall density of 17.4 gm/cc.

EFFECT OF PROJECTILE SIZE AND DENSITY

In order to determine the effects of projectile density and size on the ablative perforation diameter D_A and rear spall energy, four different density and size projectiles of the same mass, were impacted normally (90°) into the same type of target at velocities of 5 and 7 km/sec. The targets consisted of 0.5-inch laminated phenolic-refrasil bonded to 0.125-inch aluminum (2024-T3) with ~ 0.062-inch rubber bond and epoxy adhesive. The two-gram spherical projectiles consisted of uranium (with 8.5% Mo.), steel, aluminum and nylon and impacted the targets with trajectories normal (90°) to the ablative surface at energy E equal to approximately 25 and 50 kj. The uranium projectile was fired only at the lower velocity, ≈ 5 km/sec. The ratios of the ablative thickness t to projectile diameter d were 2.16, 1.6, 1.14, 0.84 for the uranium, steel, aluminum and nylon spheres respectively. The rear spall was captured by an 8" x 8" x 4" 1100F aluminum witness block with the face of the block aligned parallel to the rear of the aluminum back-up and spaced four inches away. Pertinent information is summarized below in Table I and a more complete description is given in Table A and the photographs of Appendix A.

TABLE I
Impact Characteristics in Ablative Structures

Round No.	Projectile Material	t/d	D_A (cm)	D_A/d	E (kj)	P (cm)*	Velocity (km/sec)
Projectile Velocity ≈ 5 km/sec							
4-940	Uranium	2.16	4.6	7.81	24.75	1.28	5.13
4-939	Steel	1.60	4.9	6.13	27.10	0.96	5.20
4-947	Aluminum	1.14	5.3	4.77	23.90	0.62	4.90
4-959	Nylon	0.84	5.1	3.38	25.90	0.29	5.00
Projectile Velocity ≈ 7 km/sec							
1-1-98	Steel	1.60	5.10	6.40	56.80	0.90	7.5
1-1-99	Aluminum	1.14	6.00	5.41	58.40	0.37	7.7
4-954	Nylon	0.84	6.50	4.30	47.00	0.47	6.8
4-960	Nylon	0.84	6.25	4.14	46.34	0.61	6.7
4-956	Nylon	0.84	6.60	4.37	42.68	0.49	6.5
4-957	Nylon	0.84	6.10	4.04	40.36	0.43	6.3

* P(cm) depth of penetration of the residual fragments striking the witness plate.

A plot of ablative hole size D_A vs impact velocity V is shown in Figure 1. For similar projectiles the results in all cases show an increase in hole size with higher velocity. In all cases the largest projectiles (lowest density and t/d values) produced a larger perforation with only one exception, the nylon sphere falls between the steel and aluminum at 5 km/sec. The slope of the curve for D_A vs V decreases as the projectile density increases. It should be noted that the strength characteristics of these projectiles increase as the density increases. A possible explanation of this decrease in slope is that the weaker material (nylon) may be breaking up earlier during perforation than the stronger material (e.g. steel) for the same impact velocity. As a result of disintegrating sooner, the projectile particles spread laterally at an earlier time and increase the perforation size at a faster rate than the stronger material. A plot of ablative perforation diameter D_A / projectile diameter d vs impact velocity in Figure 2 shows that the D_A/d values increase as the density increases.

To determine the relative penetration capability of the rear spall produced by these impacts, the maximum penetration of the spall into an 1100F aluminum block was measured and is plotted in Figure 3 as P vs impact velocity. At the lower velocity ($\approx$ 5 km/sec) the depth of maximum penetration increases as the projectile density increases. The spall penetration decreases at the higher velocity for the steel and aluminum projectiles and increases for the nylon sphere impacts .

The spall penetration for the aluminum spheres decreases at a faster rate than for the steel. The situation for nylon is peculiar in that the spall penetration actually increases at the higher velocity. Examination of the photographs for these firings in Appendix A also shows that the amount of spall impacting the aluminum block increases with the higher velocity nylon projectile. This is also true for the aluminum projectile impacts. For the steel projectile, the spall pattern seems to be more concentrated at the lower velocity. The spall pattern associated with the uranium projectile impact is more concentrated than any of the other three projectiles.

An estimate of the size of the hole in the aluminum back-up can be made by averaging the major and minor measured diameters. This estimated average diameter is 12.2 cm, 10.3 cm, 9.5 cm, and 7.6 cm respectively for the nylon, aluminum, steel and uranium projectile impacts at 5 km/sec.

MINIMUM PERFORATION FOR LOW ANGLE IMPACTS

A series of oblique impacts were made into phenolic refrasil bonded to steel and aluminum back-ups using steel and uranium (with 8-1/2% Mo.) spheres. The purpose was to determine the accuracy of the required minimum perforation energy as determined from the data reported in Reference 1 and to examine the effect of projectile density. The data reported in Reference 1 were obtained for steel projectiles impacting into phenolic refrasil bonded to aluminum and steel back-ups. Two aluminum projectile impacts into phenolic nylon bonded to steel back-ups are also included in the discussion.

One of the phenolic nylon targets was a model nose cone (Round No. 4-935) and the other a flat plate specimen simulating the model was placed directly in contact with a block of foam (4-944), (see photographs in Appendix A). The pertinent conditions and results are listed in Table II. A more complete description of the data can be found in Table A.

TABLE II

Round No.	Target Material	T_t (cm)	Proj. Mass (gm)	Proj. Matl.	Impact Angle	Impact Vel. (km/sec)	E_n (kj)	E^*_{min} (Ref.1)	Cond. of Target
1-1-107	Ast/Al	1.75	5.096	Uranium	10°	5.24	2.11	--	Perf.
1-1-110	Ast/Al	1.75	4.992	Steel	10°	5.97	2.68	1.48	N.P.
1-1-106	Ast/St.	1.75	1.045	Steel	25°	7.40	5.10	4.30	M.P.
1-1-94	Ast/St.	3.81	4.991	Steel	40°	7.03	51.00	56.00	N.P.
4-952	Ast/St.	1.91	1.046	Steel	30°	3.12	1.28	5.70	N.P.
4-944	Ph.Ny/St.	1.75	2.650	Aluminum	45°	4.59	13.93	--	N.P.
4-935	Ph.Ny/St.	1.75	2.800	Aluminum	45°	3.78	10.10	--	N.P.

N.P. Not Perforated
M.P. Minimum Perforation Condition

* E_{min} is defined as the energy required, based on the normal component of velocity, to just crack the metal back-up.

The superior penetration capability of dense projectiles, particularly at small impact angles, is clearly shown by the results obtained with the steel and uranium projectile impacts at angles of 10°. The targets for these two impacts were the same type and the projectile masses were approximately equal. Although the impact velocity for the uranium projectile was lower than the steel projectile, the target (Round No. 1-1-107) was completely perforated while the target for Round Number 1-1-110

impacted by the steel projectile was not perforated (the rubber bond material in this target was nearly intact). The impact energy (using the normal component of velocity to the target surface) necessary to just crack the back-up is $\approx$ 1.48 kilojoules based on the steel projectile impact data reported in Reference 1. This amount was exceeded in both cases, 2.68 kilojoules for the steel and 2.11 kilojoules for the uranium projectile impact. There are two other aspects of these impacts which can be seen by an examination of the photographs in Appendix A. In the case of the uranium projectile (Round No. 1-1-107) impact, no residual fragments came through the perforation to hit the witness plate spaced 10 inches from and parallel to the rear of the target. However, the witness plates that were 90° to the target surface and positioned to capture the front spall were penetrated 0.38 cm by fragments from the uranium while the fragments from the steel projectile perforated a total thickness of 2.54 cm. It appears that a greater amount of projectile particles traveling at higher velocities ricochet off the target surface with the steel or the lighter projectiles at this impact angle. The type of petal formation in the back-up resulting from the uranium striking the target has several interesting characteristics. The petals that were formed at 90° to the trajectory (top and bottom petals in the photograph shown in Appendix A) were broken off and recovered. The petals formed parallel to the trajectory and nearest the gun muzzle were bent straight-up, whereas the petals furthest from the gun muzzle were bent over in the direction of the projectile flight.

In Round Number 1-1-106 the back-up was cracked open and represents a condition very close to minimum perforation. The impact energy based on the 25° component of impact velocity was 5.10 kilojoules which is somewhat greater than 4.3 kilojoules, the amount needed for minimum perforation based on the previous data of Reference 1.

The back-ups for the 30° and 40° impacts were not perforated by the steel projectile impacts. The 30° result (4-952) is in agreement with the estimated energy needed, since the impact energy is much less than the minimum perforation value. The impact energy from the 40° impact (1-1-94) is about 9% less than the estimated amount required for minimum perforation and again perforation did not occur.

The two impacts listed at the bottom of Table II were obtained using aluminum projectiles and are included to show the effects of lower density projectiles. As previously mentioned, one of these targets was a model nose cone (4-935) and the other was placed directly in contact with a block of foam (4-944). Although the impact energy at 45° was much higher than the estimated amount needed for minimum perforation by steel projectiles, neither target was perforated. The ablative was perforated and the back-ups were bulged.

Based on these results, it appears that the determination of the minimum perforation requirement, particularly for dense projectiles at low angles, is not established.

It is also necessary that additional data be acquired to determine the minimum perforation energy for different density projectile materials. An analytical approach incorporating both projectile energy and density and using values of pressure measured on the rear of the target will be of considerable value in establishing the minimum perforation requirement.

ALUMINUM PROJECTILE IMPACTS

A number of different target configurations were impacted with aluminum spheres over a wide range of velocities with impact angles ranging from 90° to 45°. Different correlations were examined in order to have a common basis for comparing hole sizes in the ablative materials. In Figure 4, a correlation for steel impacts into ablative structures is used, that has previously been reported in Reference 1. As can be seen in this Figure, the hole sizes for the 90° impacts are very close to the E/T correlation, except for Round Number 1-1-82. Round Number 1-1-82 did not have a rubbery type bond between the ablative and steel back-up and this may have been the cause of the larger perforation. In this plot the hole sizes for the non-normal impacts, with the exception of Round Number 4-948, are grouped above the 90° impacts. It was found that the difference between the 90° and less than 90° perforations could be reduced by dividing the major diameter of the projection on the front target surface d_p into the ablative perforation diameter D_A. This is designated as D_A/d_p and is plotted in Figure 5 for the same data shown in Figure 4. Although non-dimensional hole sizes do not completely remove the effects from oblique impacts, there is a considerable reduction in scatter. Larger perforation diameters with oblique impacts did not show up as strongly in earlier firings with steel projectiles primarily because higher t/d values were used. In these data t/d values are approximately 1.

Nose Cone Models

Three model nose cones (similar to those used in the Malta rocket exhaust experiments in the Aerothermal Phase of the HKM Program) were impacted to produce a perforation in one side of the cone. The rocket exhaust results obtained with impacted models were compared with results obtained by machining a hole of the same size in a similar model and subjecting it to the same heat flux environment. Before impacting the models, the approximate impact conditions for producing the required hole size were established by impacting flat plates made of the same materials and thickness as the nose cone model. The two plates simulating the two sides of the cone were oriented at the same angle to each other, as the nose cone angle, with the steel back-ups of the plates facing each other at the same distance apart. Aluminum projectiles were selected to minimize residual damage to the opposite wall (it was necessary to produce a perforation in only one side of the cone and have very little or no damage to the other side of the cone). An abbreviated tabulation of the results is listed in Table III. More complete data are given in Table A and the photographs in Appendix A.

TABLE III

Model Nose Cones

Round No.	Impact Angle	Proj. Mass (gm)	Complete Perf.	Ablative Perf. D_A (cm)	Target	Impact Velocity (km/sec)
4-937	70°	2.83	yes	7.70	1/2"Ph.Ny. + 1/8"St.	3.77
4-938	70°	2.83	yes	≈ 8.25	"	3.94
4-935	45°	2.83	no	8.30	"	3.78
			Simulated Model Nose Cone			
4-930	90°	3.01	yes	7.2	1/2"Ph.Ny. + 1/8"St.	5.62
4-931	45°	3.01	yes	11.2	"	5.13
4-934	45°	2.83	yes	8.4	"	4.50

In figure 5, the correlation of D_A/d vs E/T, the comparison between the two configurations is shown. The hole sizes in the nose cone models were slightly larger than those in the flat plates primarily because of the small radius of curvature in the nose cone models. In the nose cone model impacts, the ablative cone always broke loose from the steel liner. This particular effect of the shock and vibration due to impact cannot be simulated by a flat plate specimen.

Penetration of Foam Material by Rear Spall Fragments

Impacts were made with aluminum spheres at 45° and 60° into flat plate ablative targets which were held in tight contact with a foam block. The targets were the same type as those used in the simulated nose cone model impacts and the projectile velocities were slightly higher than the previous impacts. The foam block was a 1-foot cube and was held in an aluminum box with 0.125-inch walls. Two different density polyurethane foams were used to show the effect of foam density on rear spall penetration. One shot was fired without foam in the foam box (see photos for Round No. 4-948), and two additional witness plates were placed at the rear of the empty box. In Round Number 4-955 a steel sphere of similar mass was used to compare the effects of projectile density on rear spall penetration, but was at a lower velocity than the aluminum projectiles. The effect of projectile impact angle is shown by the results of Round Numbers 4-944 and 4-945. Table IV is a brief summary of the results, further details can be found in the Table and Appendix at the end of the report.

The ablative hole size in 4-948 where no foam was used behind the target is smaller than those where foam was used. These ablative hole sizes are compared with other aluminum projectile data in Figure 4.

Comparison of an Aluminum Sphere with an Aluminum Jet Pellet Impact

The results obtained in Round Number 1-1-108 by impacting an aluminum sphere into a fiberglas laminate target is compared to the results reported in Reference 2 for an aluminum jet pellet impact into a similar target. This 1-inch thick glass-cloth material bonded with permatex to a 1/4-inch 4130 steel back-up plate was obtained from Firestone (No. 20-16-09-01). The same type of target was impacted with an aluminum jet pellet by Firestone in shot number 600-72. The mass of the two projectiles was approximately the same (3.2 and 3.4 gm) but the velocity of the aluminum jet was about 1.4 km/sec higher

TABLE IV

Round Number	4-944*	4-945	4-946@	4-948+	4-955
Proj. Matl.	Al	Al	Al	Al	Steel
Mass (g)	2.65	2.65	2.65	2.65	2.71
Proj.Vel(km/sec)	4.59	5.42	5.68	5.84	3.80
Impact Angle	45°	60°	60°	60°	60°
Foam Density (lb/ft^3)	7.00	7.00	3.10	None	3.10
Max.Pene. of Foam (cm)	4(1)	Perf.	Perf.	N.A.	Perf.
Crater Mouth of Foam (cm)	13.5x11.5	9.30	≈Same as Abl.Perf.	N.A.	11.50
No. Perf. in Foam	0	3	14	N.A.	2
No. Perf. in Box (Rear)	0	0	1	17	0
No. Perf. in Box (Side)	0	0	1	2	0
Wall Thickness of 61S Al Box	1/8-inch	1/8-inch	1/8-inch	1/8-inch	1/8-inch
Condition of Box	Not distorted	(2)	(2)	Not distorted	Not distorted
Abl.Perf. Dia. (cm)	9.50	10.00	10.50	7.20	4.30

* B-U not perforated

(1) Caused by bulge in B-U

(2) Rear of box bulged and welded seams partially broken

\+ Round No. 4-948 -
- No. perforations of 1st witness plate = 14
- No. perforations of 2nd witness plate = 1
- No. steel fragments inside box = 10
- No. aluminum fragments inside box = 20
- No. steel fragments outside box = 5
- No. aluminum fragments outside box = 65
- Total mass steel fragments inside box = 1.9g
- Total mass Al fragments inside box = 0.2g
- Total mass steel fragments outside box = 1.0g
- Total mass Al fragments outside box = 1.5g

@ Round No. 4-946 -
- Total mass of fragments thru the foam = 4g
- No. fragments >1/2g thru the foam = 2

than the sphere. The 9.2 km/sec jet pellet produced a hole of 3-1/4 x 3 inches (7.94 cm. av.) and the 7.8 km/sec sphere made a hole of 6.9 cm diameter in the glass cloth. Comparing the glass cloth hole size results on an E/T basis shows good agreement. Both hole sizes are only slightly lower than determined by the E/T expression of Reference 1, which gives hole diameters of 8.35 cm and 7.5 cm for the aluminum jet and the aluminum sphere respectively. The hole size in the steel back-up with the jet was 3.2 x 3.8 cm as compared to 7.8 x 4.4 for the spherical projectile indicating that a much stronger shock passes through the material for the spherical case.

Uranium Sphere Impacts

Two and five-gram uranium spheres were used to determine the effects of high density projectiles on the impact results into ablative composite targets. The velocity varied between 5 and 5.5 km/sec. All impact angles were 90° except for the 10° impact (Round No. 1-1-107) previously discussed. Three impacts were made into the same thickness target with three different back-up materials. For approximately the same energy, a perforation of 10.9 cm diameter was made in the ablative material with the steel back-up as compared to 4.9 and 5.0 cm for the aluminum and Mg back-ups respectively. It appears that the steel back-up produces a higher intensity shock reflection than with the less dense back-up material. More data are required in order to determine whether this is a significant effect.

In order to compare the uranium sphere impacts with previous data for less dense projectiles, the ablative hole diameters were plotted in Figure 6 along with the E/T expression obtained in Reference 1 for steel projectiles. Except for Round Number 1-1-103 with the steel back-up, the hole sizes for impacts with uranium spheres are smaller than those produced by the less dense projectiles.

CONCLUSIONS AND FUTURE PLANS

Minimum perforation requirements will be studied in more detail for projectile density effect, particularly at low impact angles. Correlations will be established for minimum perforations using aluminum, steel and uranium projectiles against composite ablative targets with aluminum and steel back-ups.

Impact data will be obtained for thin ablative composite targets with t/d values between 0.5 and 1.0. These data and

existing information for higher t/d values between 1 and 4 will be examined and compared with existing hole size correlations.

Experiments will be designed to provide information for theoretical composite structure impact models in order to determine the validity and accuracy of these models. Current techniques will be utilized for studying wave propagation and interaction with the cratering processes in ablative materials. This experimental-theoretical study will provide a firm physical basis for scaling projectile and target parameters and estimating the spall energy resulting from impact.

REFERENCES

(1) Persechino, M.A., "Hypervelocity Impacts Into Ablative Materials" - 6th Hypervelocity Impact Symposium, Vol.IV, page 235, May 1963. (S)

(2) Glass, C.M., Kronman, S., Ballistic Research Laboratories, "Hypervelocity Kill Mechanisms Program" - Semiannual Progress Report No. 13, February 1964. (S)

APPENDIX A

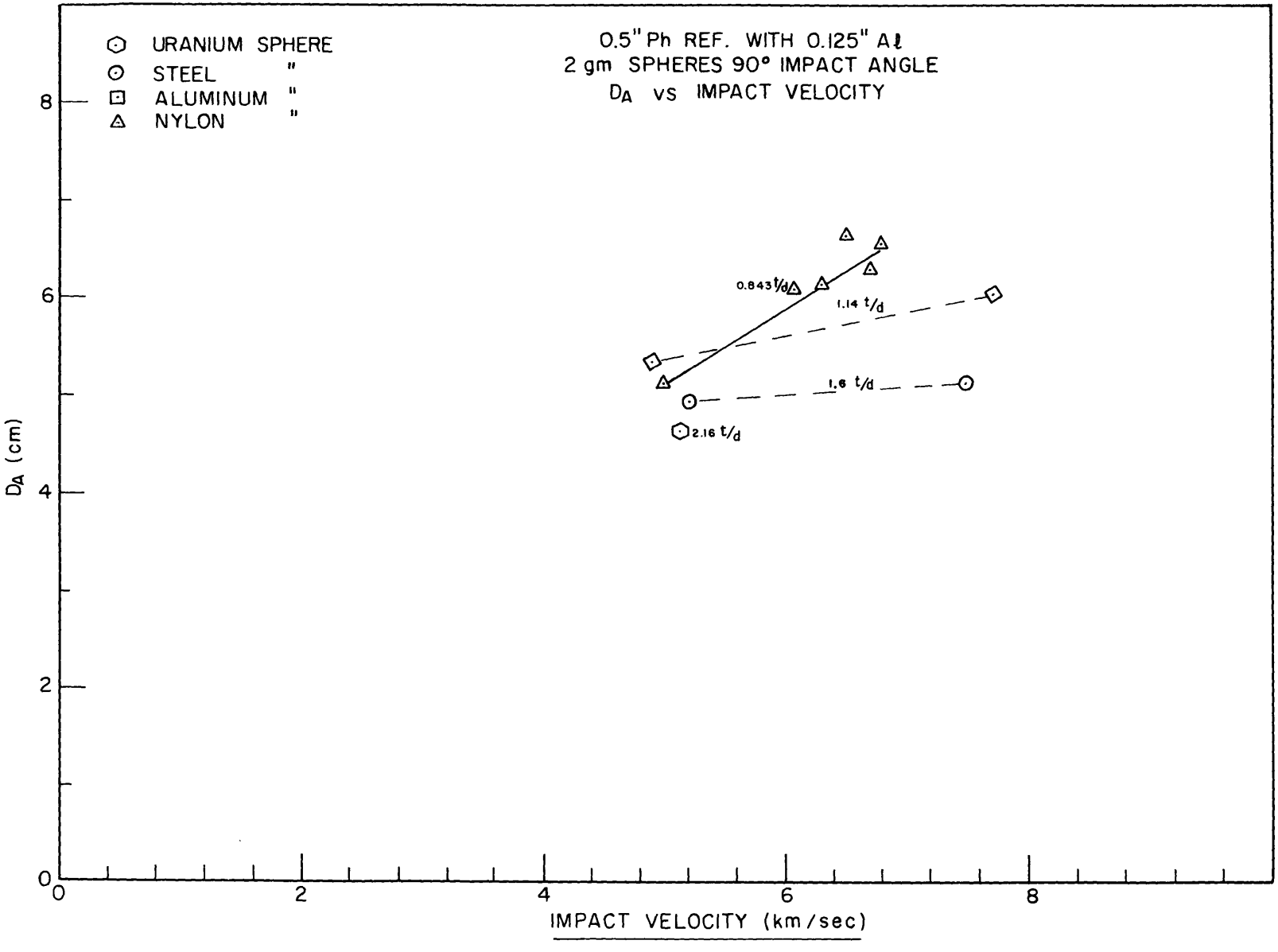

Figure 1 - Hole size vs impact velocity

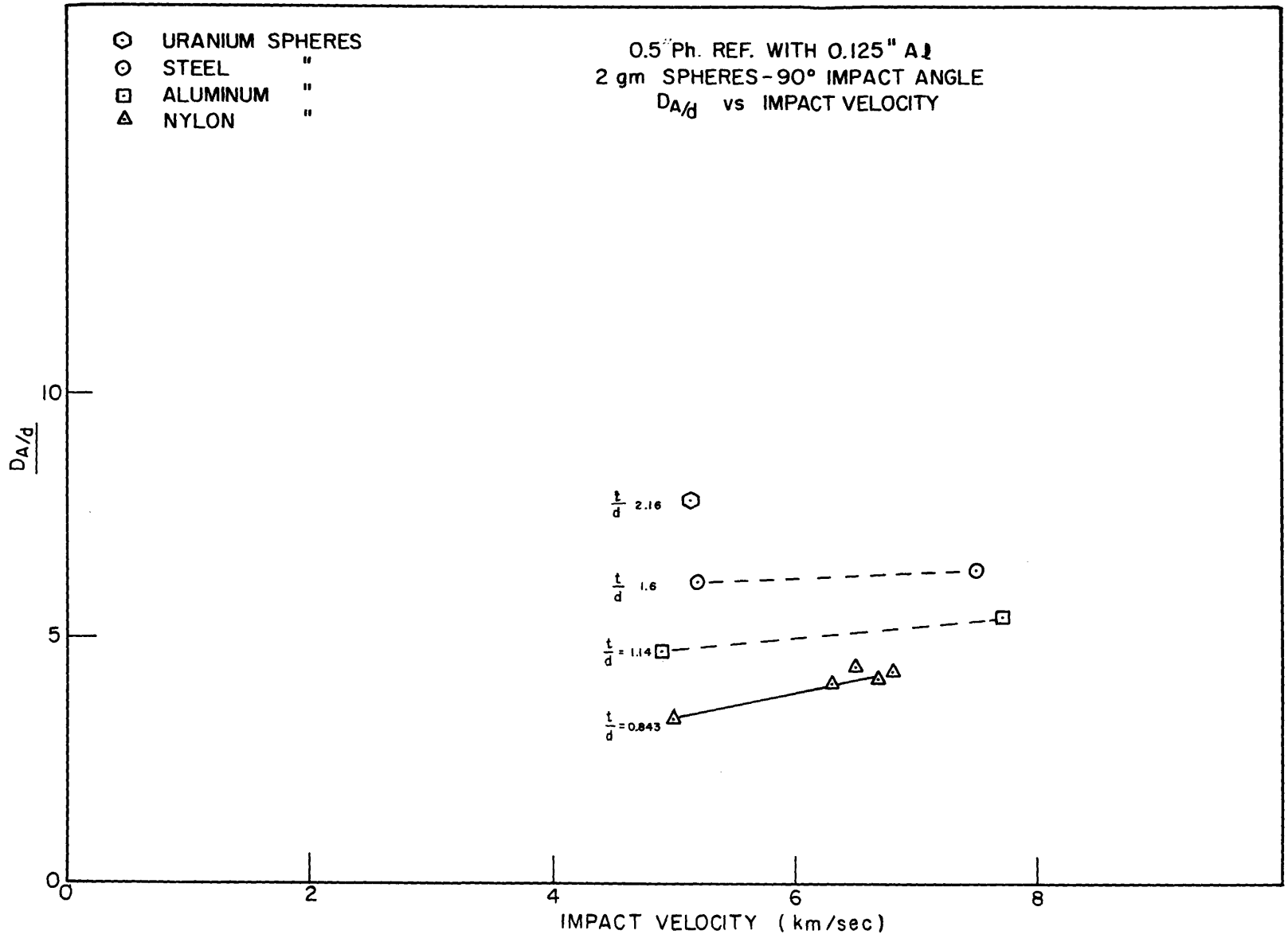

Figure 2 - Hole size/projectile dia. vs impact velocity

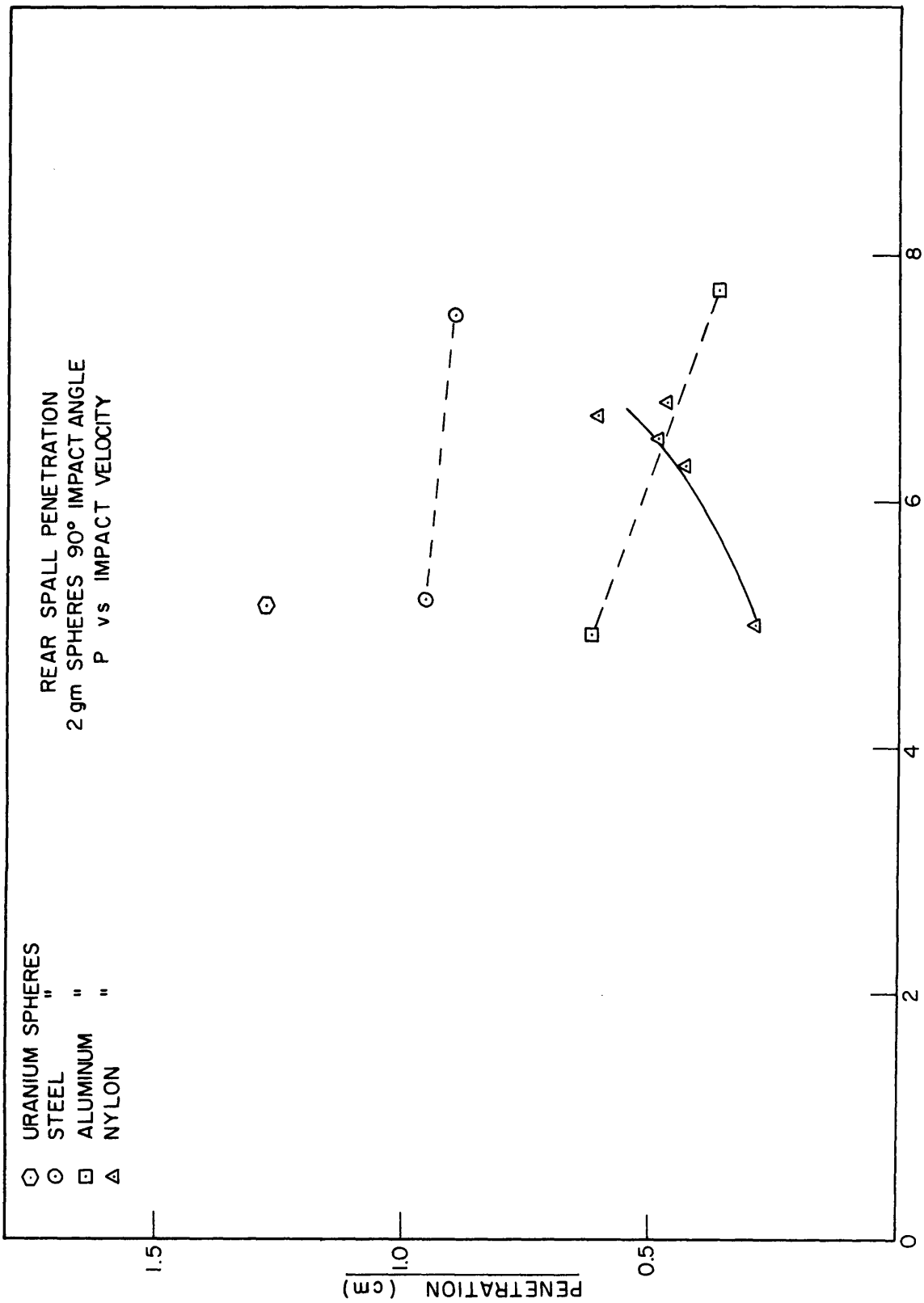

Figure 3 - Rear spall penetration into 1100F aluminum vs projectile impact velocity

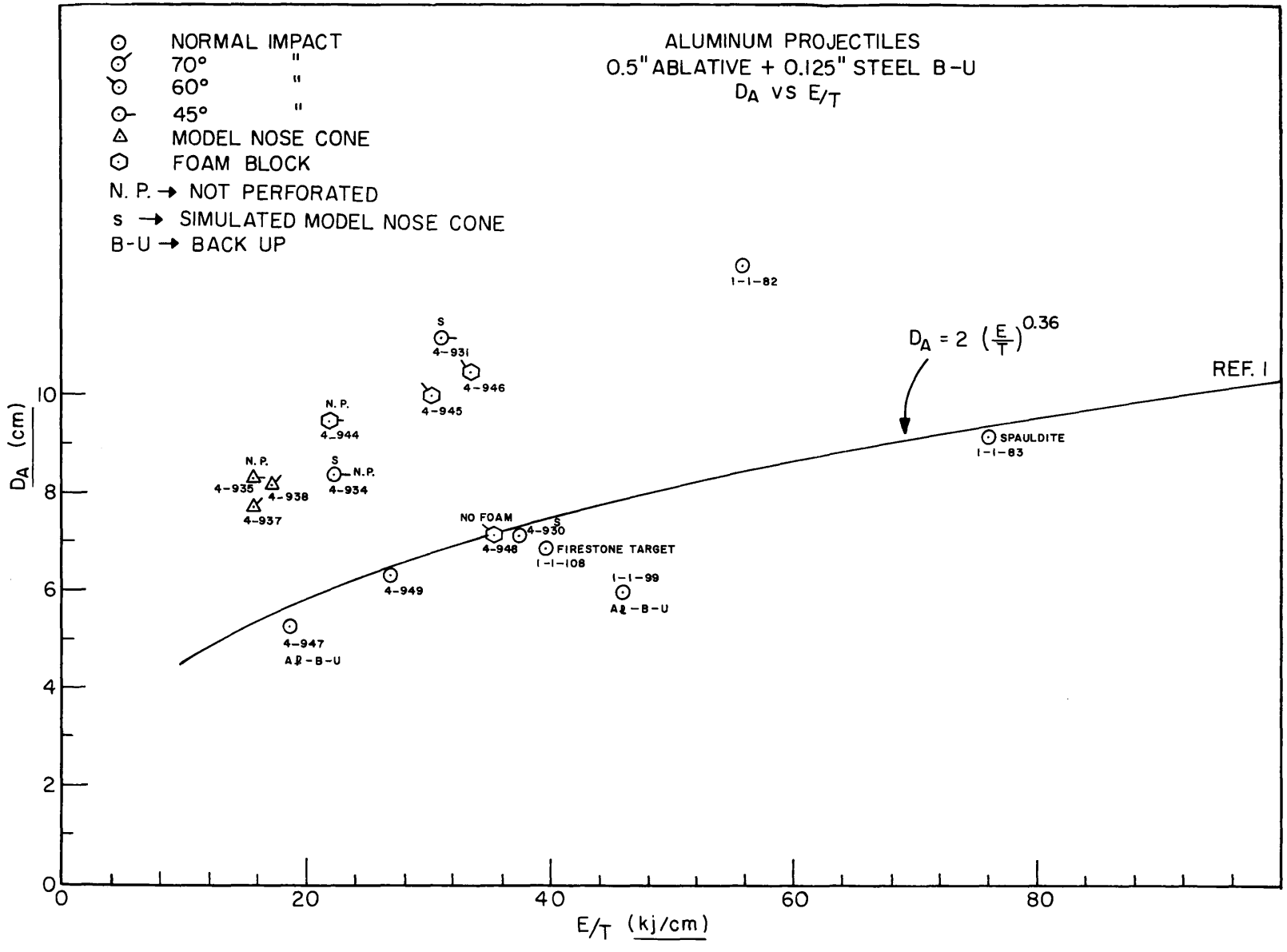

Figure 4 - Ablative hole size vs impact energy/ablative thickness

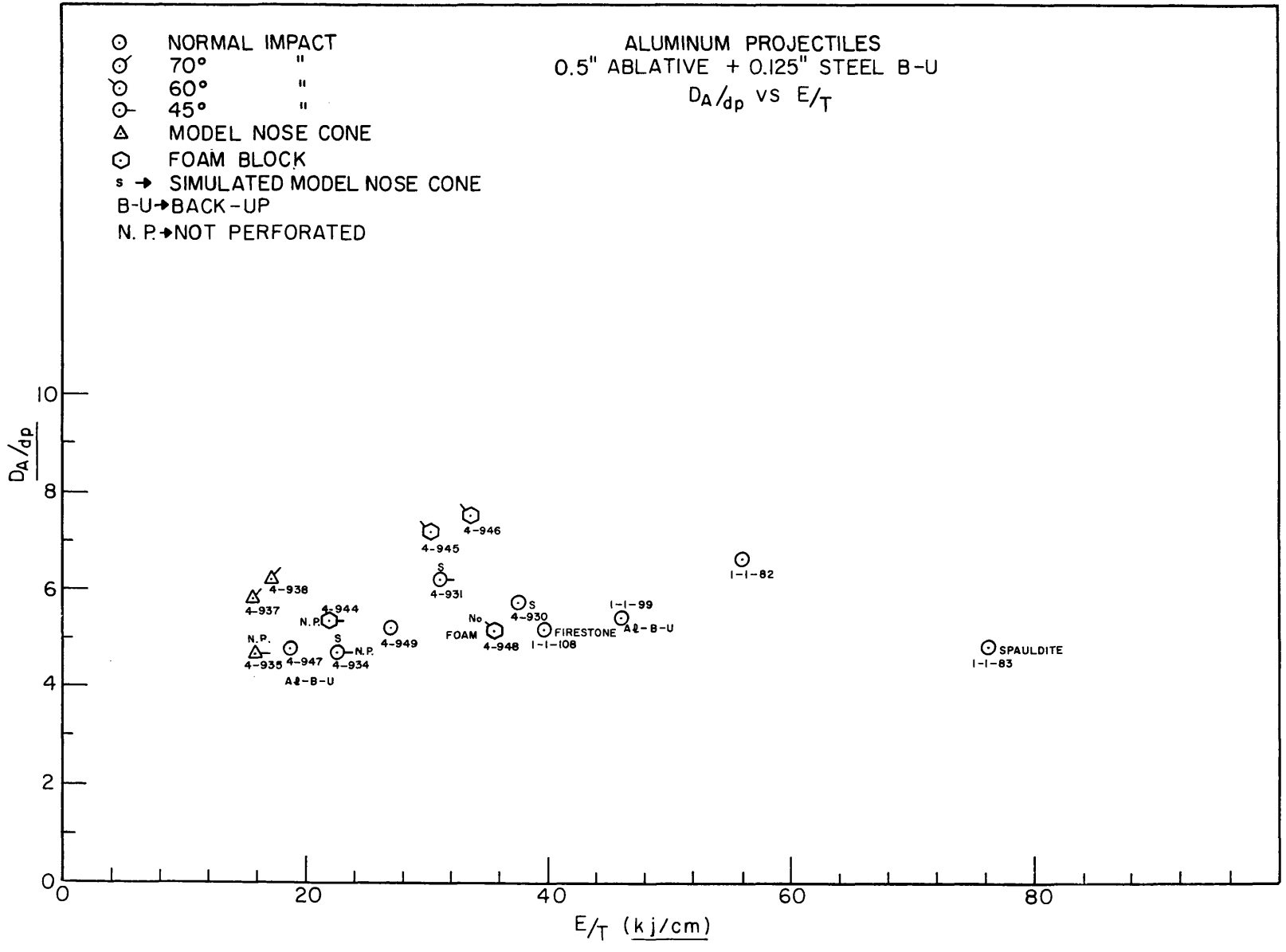

Figure 5 - Normalized ablative hole size vs impact energy/ablative thickness

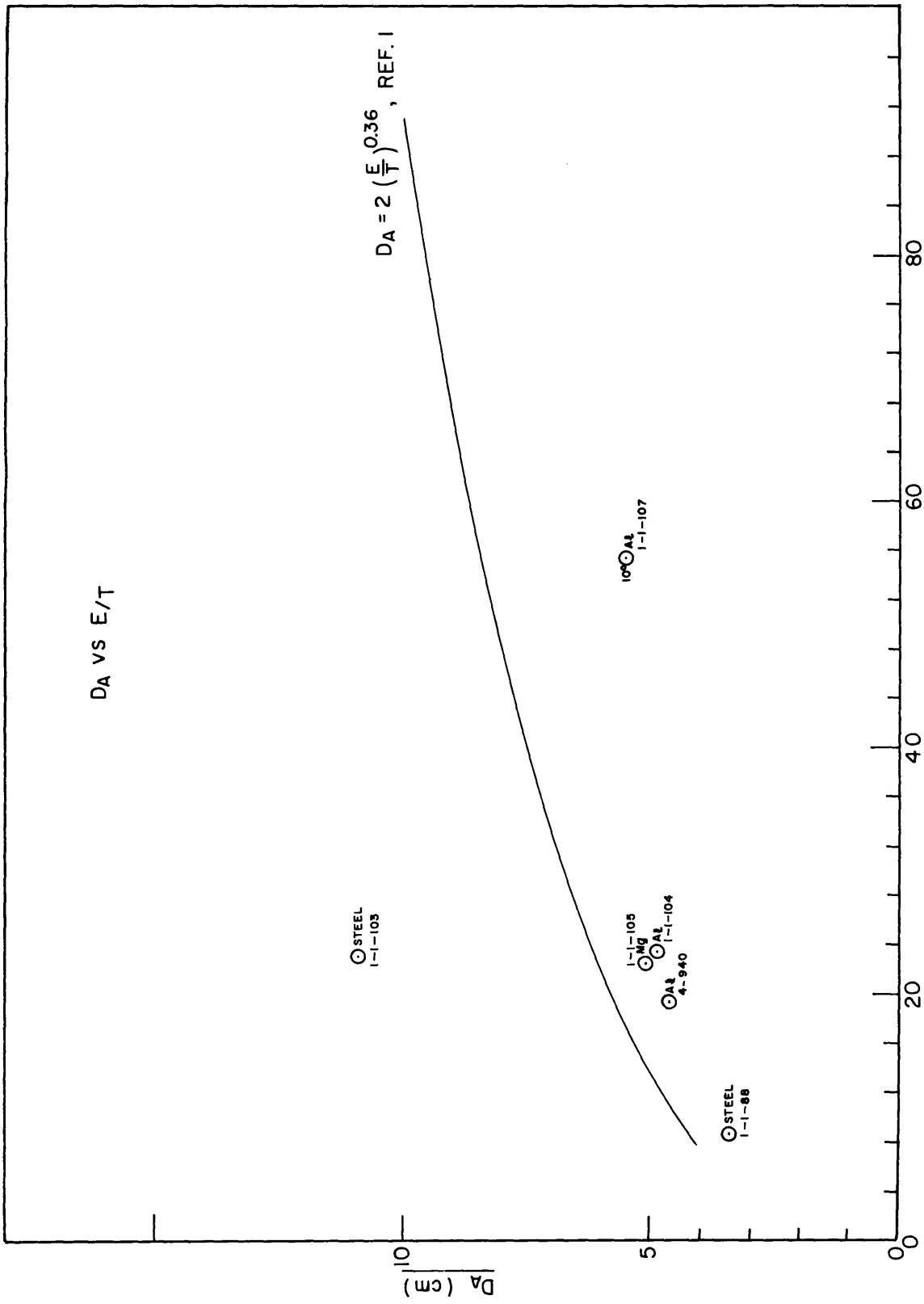

Figure 6 - Ablative hole size vs impact energy/ablative thickness for uranium spheres

ROUND NO. 4-939

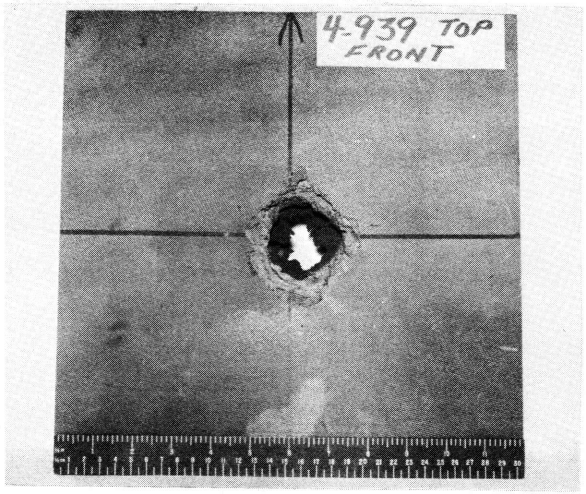

FRONT TARGET

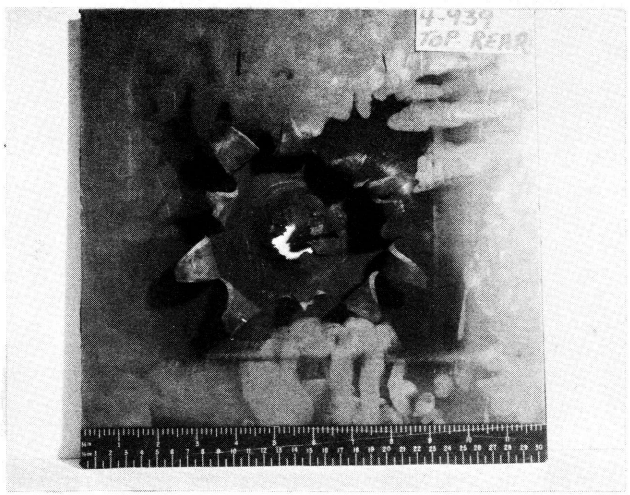

REAR TARGET

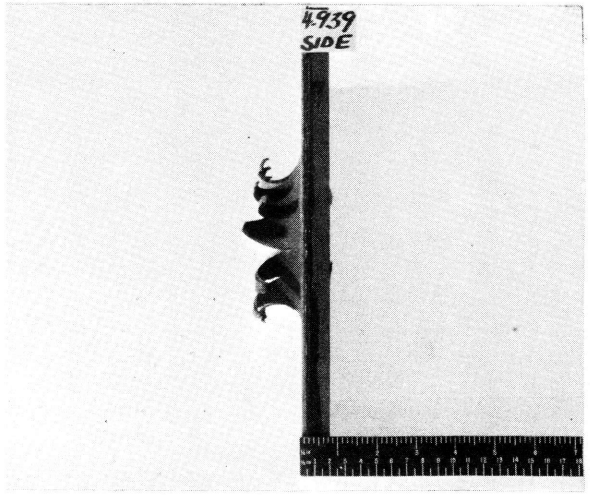

EDGE TARGET

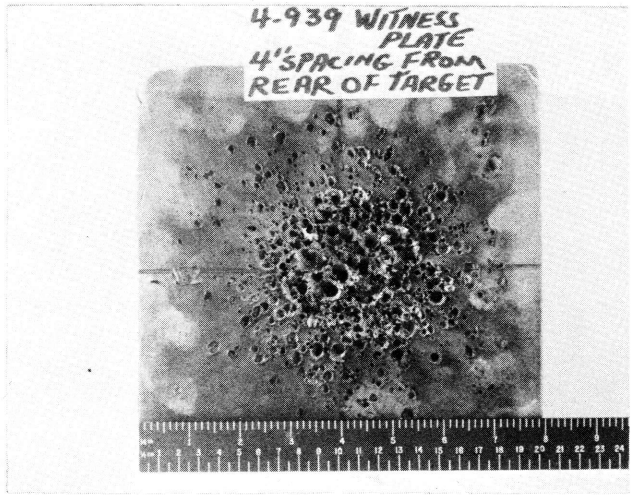

W. P. 1-5" BLOCK
S = 4" FROM POINT OF IMPACT
Pm = 0.96 cm

ROUND NO 1-1-98

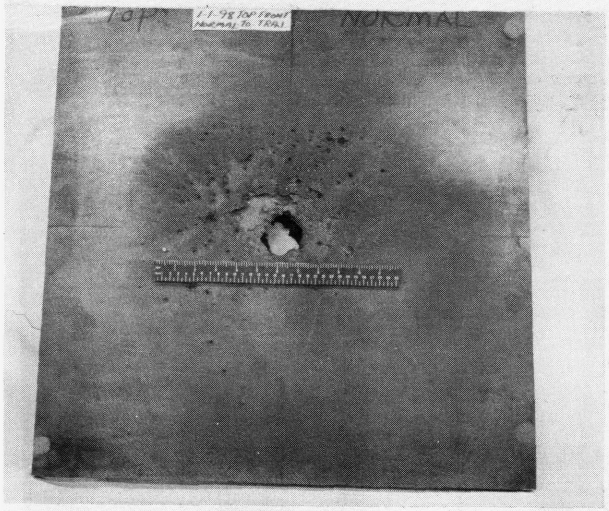

FRONT TARGET

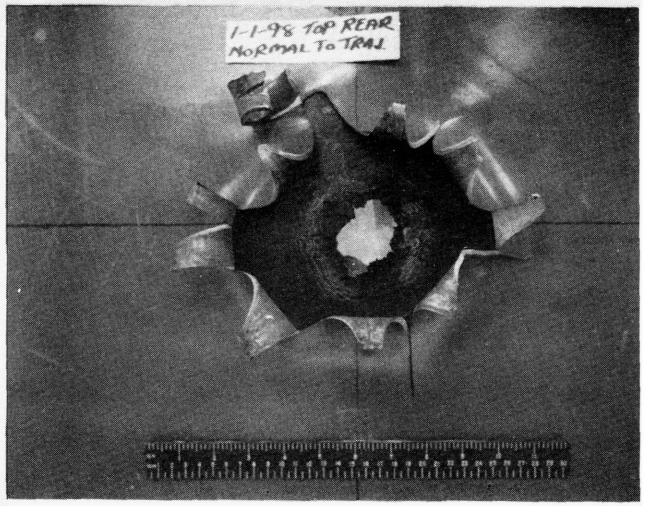

REAR TARGET

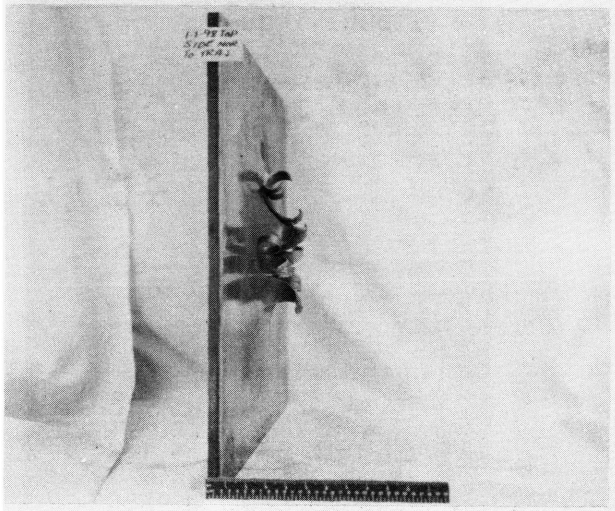

EDGE TARGET

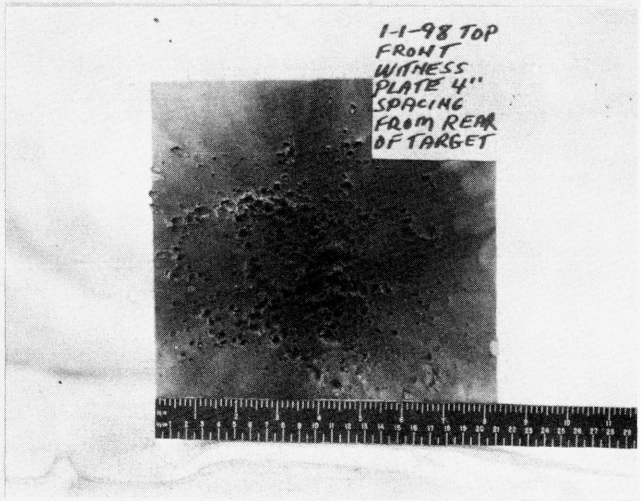

W. P. 1-4" BLOCK. s = 4"
Pm = 0.9 cm

ROUND NO. 4-940

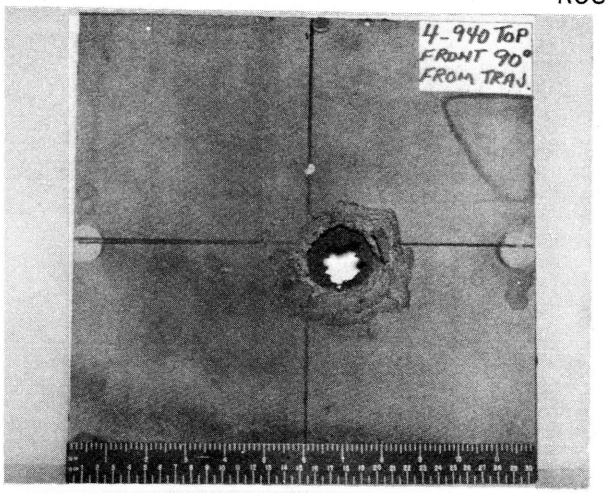

FRONT TARGET

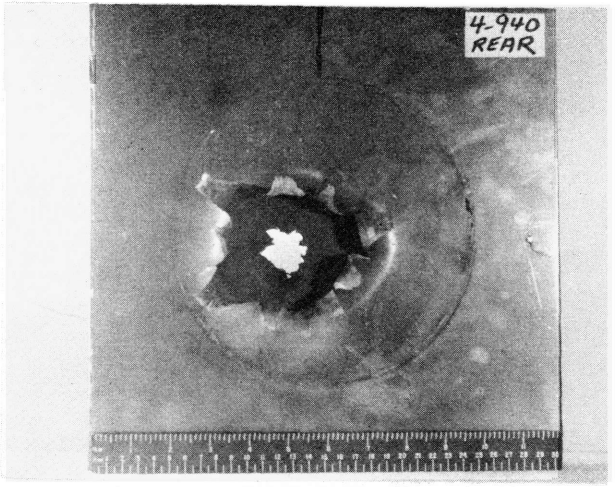

REAR TARGET

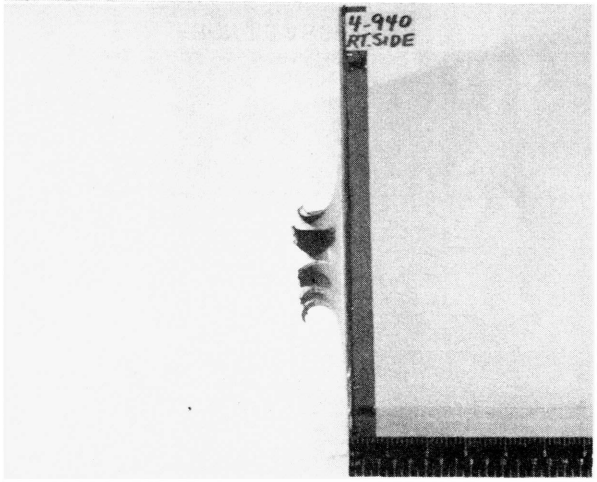

EDGE TARGET

W. P. 1-4" THICK BLOCK s = 4"
Pm = 1.28 cm

ROUND NO. 4-947

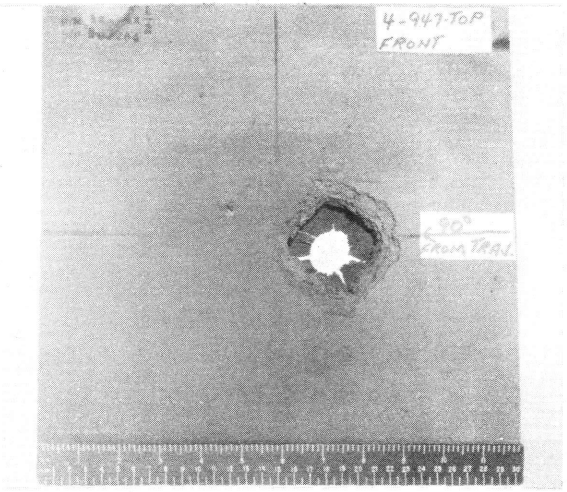

FRONT TARGET

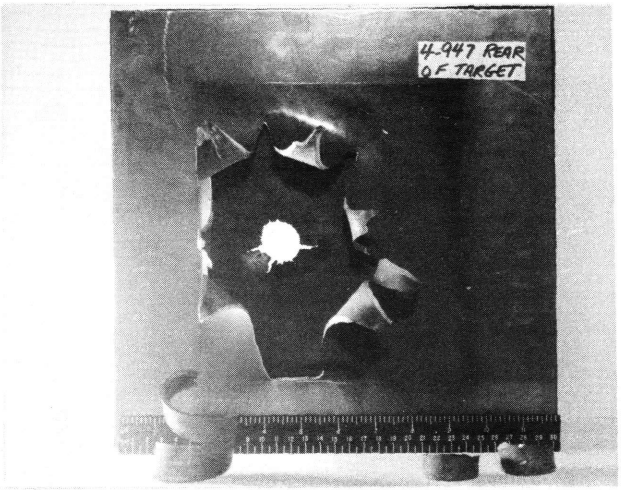

REAR TARGET

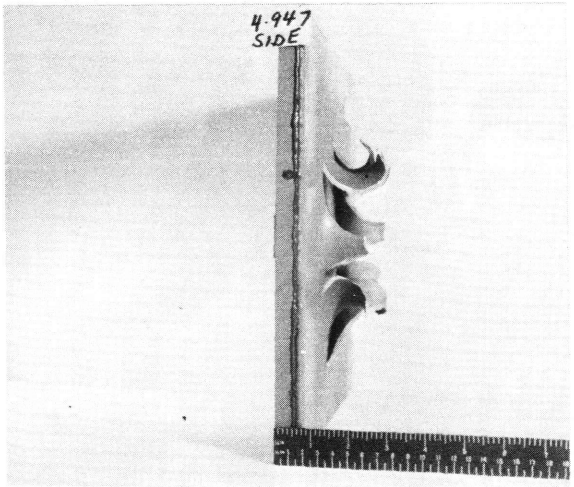

EDGE TARGET

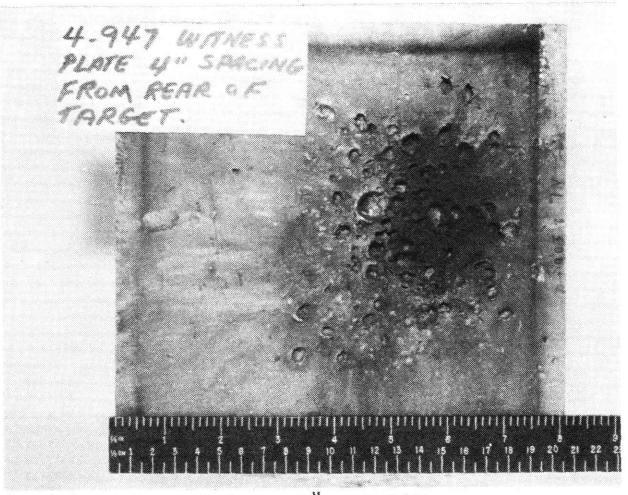

W. P. 1-5" BLOCK
s = 4" FROM POINT OF IMPACT
Pm = 0.62 cm

ROUND NO. 1-1-99

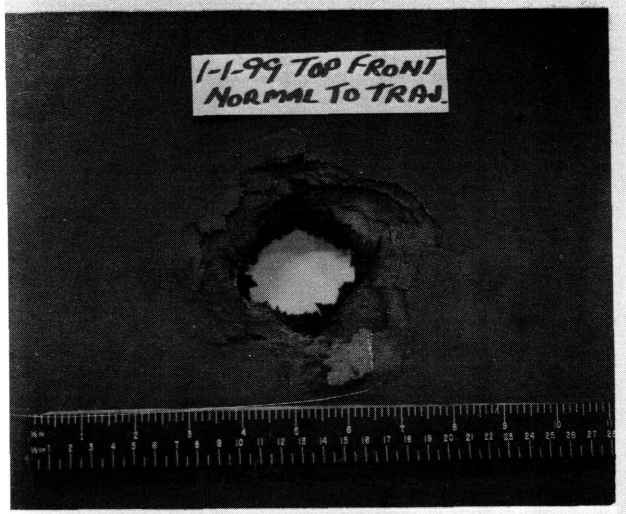

FRONT TARGET

REAR TARGET

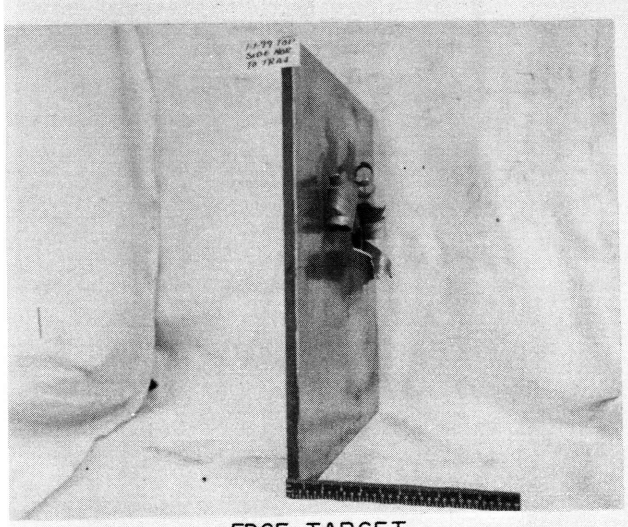

EDGE TARGET

W. P. 1-4" BLOCK s = 4"
Pm = 0.37cm

ROUND NO. 4-959

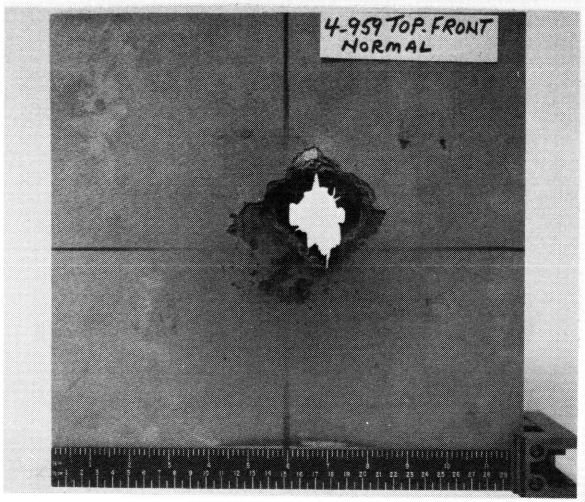

FRONT TARGET

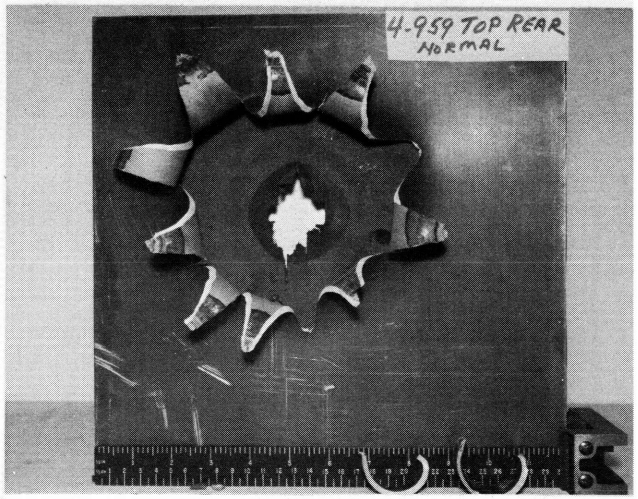

REAR TARGET

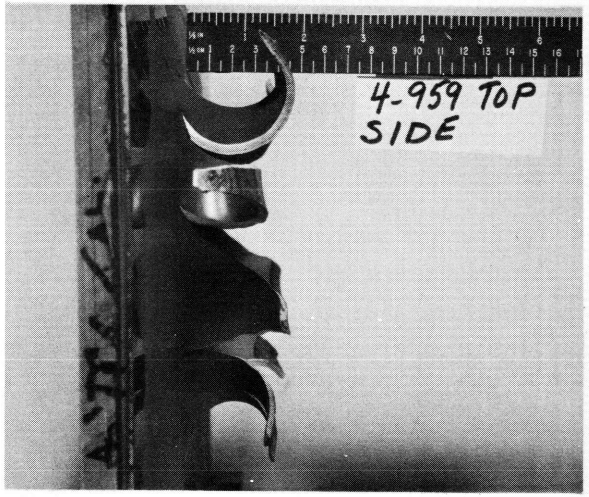

EDGE TARGET

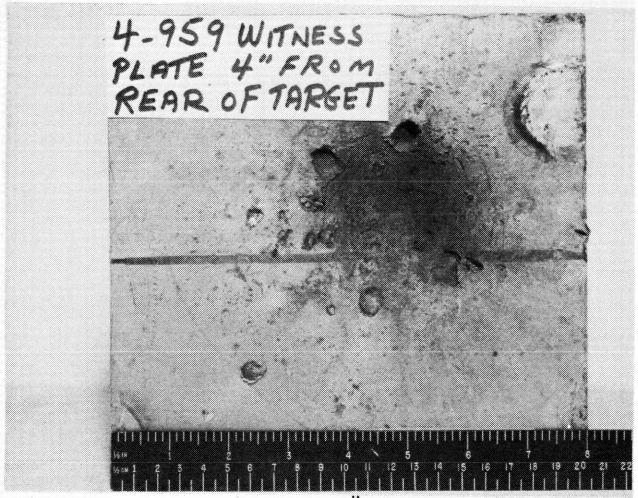

W. P. 1-5" BLOCK
s = 4" FROM POINT OF IMPACT
Pm = 0.29cm

ROUND NO. 4-954

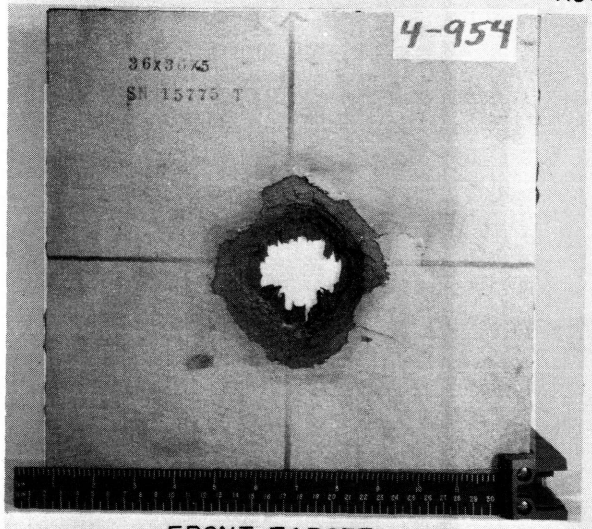

FRONT TARGET

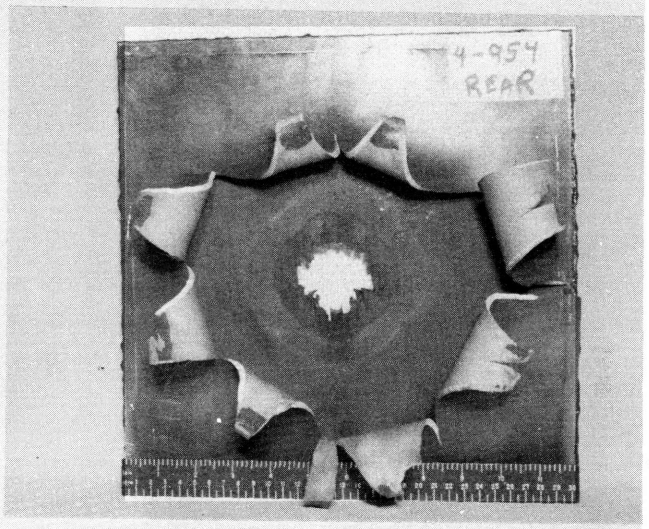

REAR TARGET

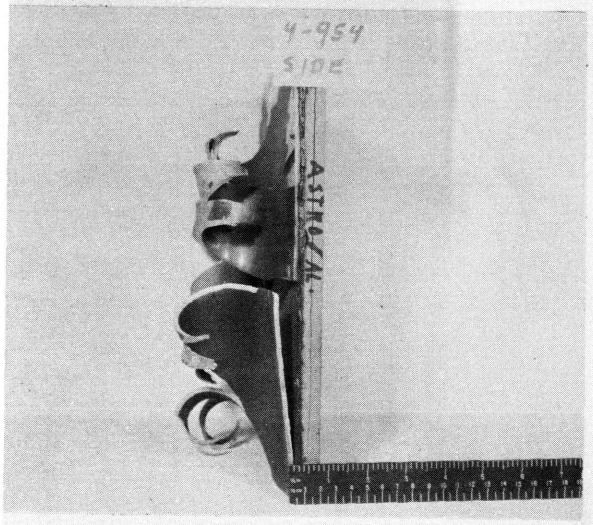

EDGE TARGET

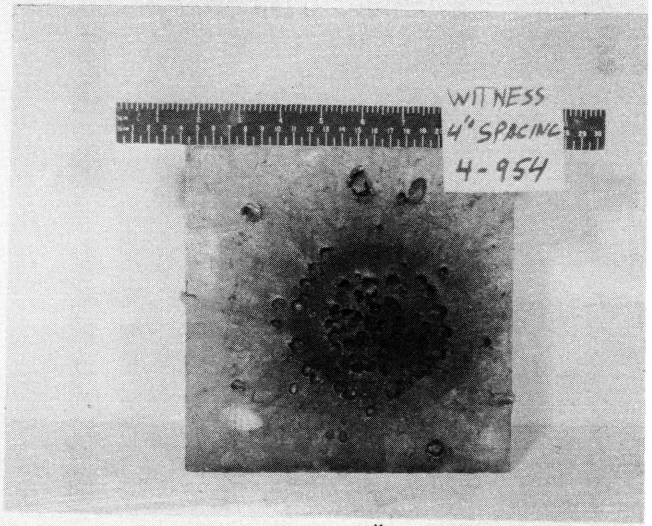

W. P. 1-5" BLOCK
s = 4" FROM POINT OF IMPACT
Pm = 0.47cm

ROUND NO. 4-960

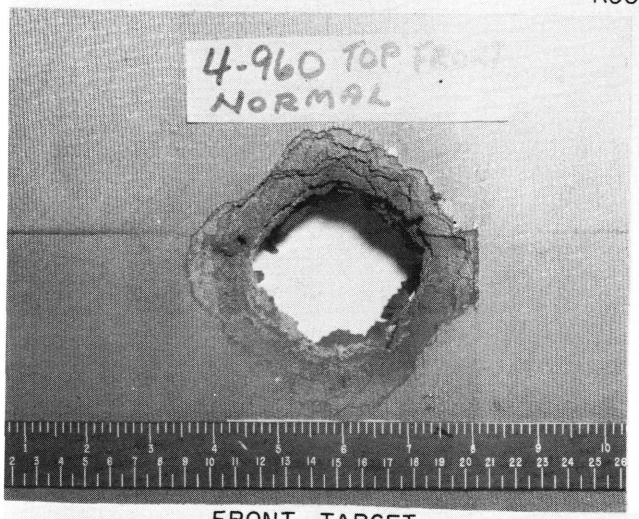

FRONT TARGET

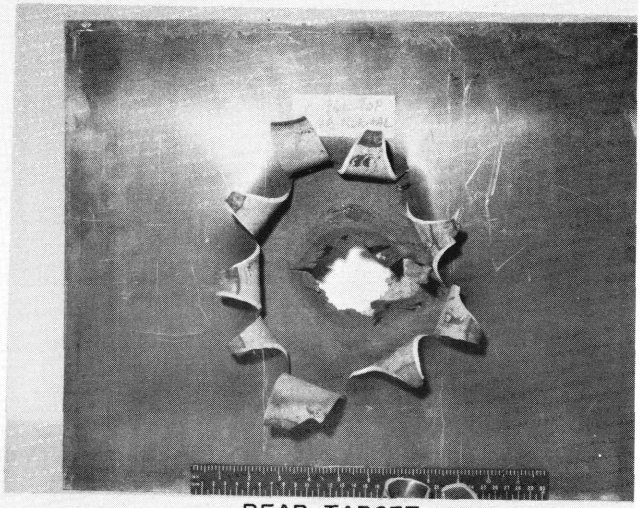

REAR TARGET

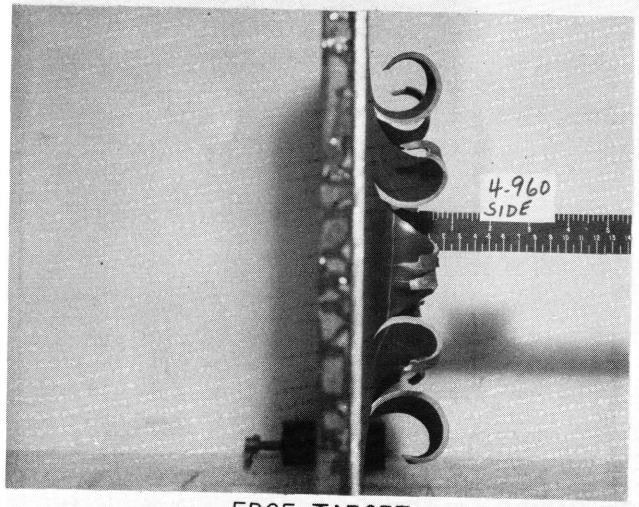

EDGE TARGET

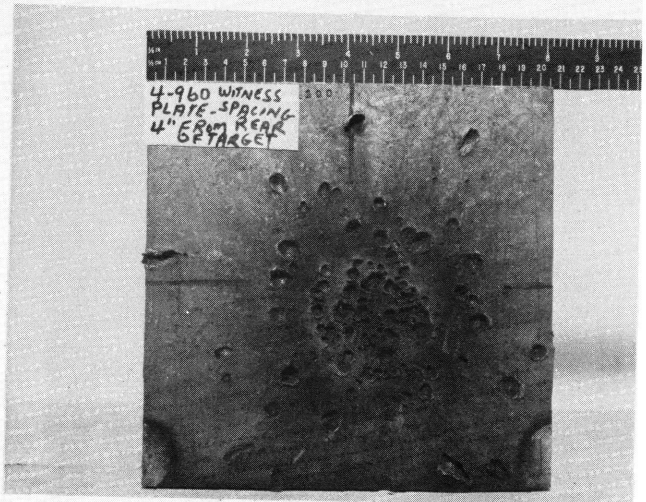

W. P. 1 - 5" BLOCK
s = 4" FROM POINT OF IMPACT
Pm = 0.61cm

ROUND NO. 4-956

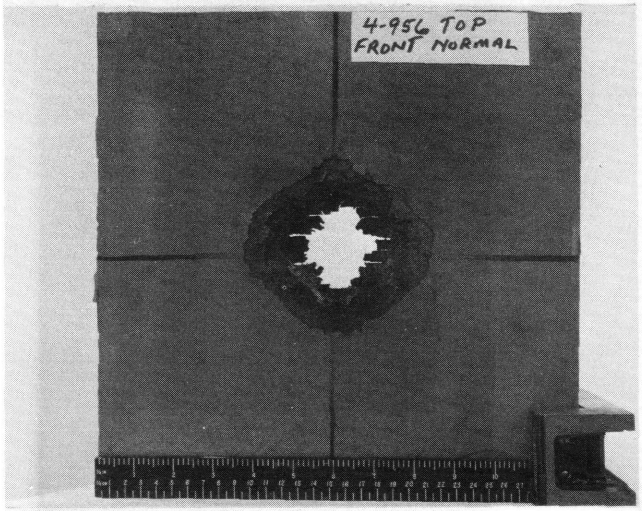

FRONT TARGET

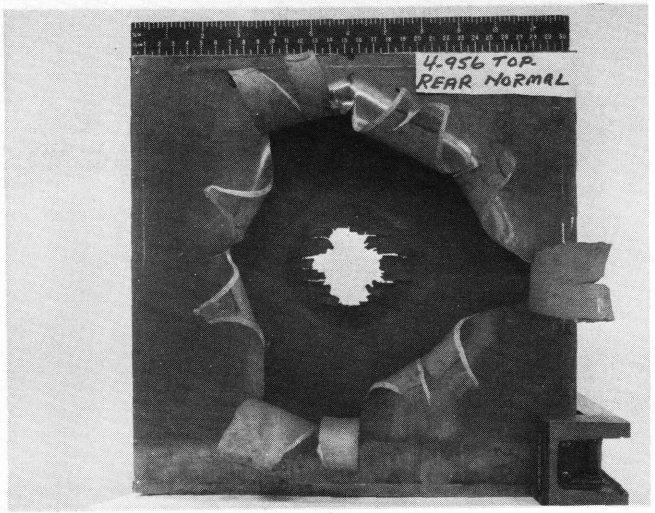

REAR TARGET

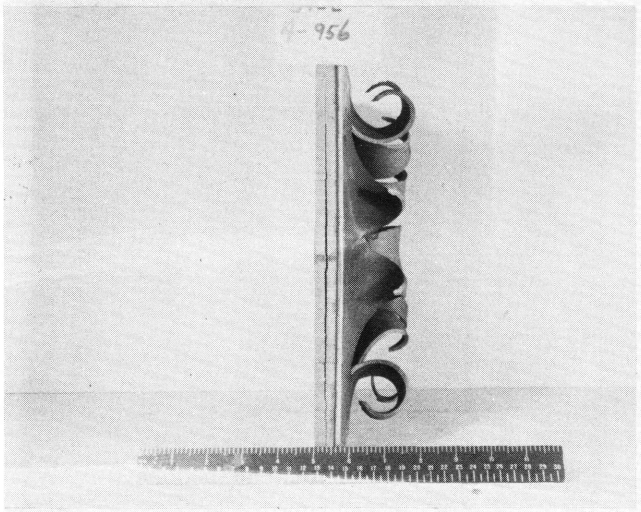

EDGE TARGET

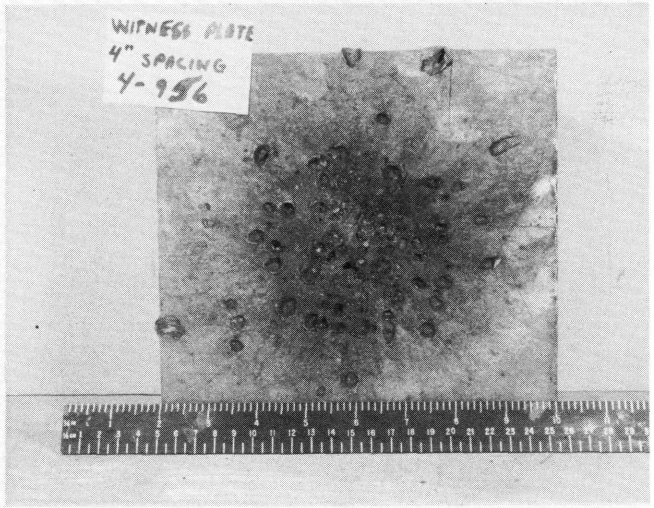

W. P. 1-5" BLOCK
s = 4" FROM POINT OF IMPACT
Pm = 0.49 cm

ROUND NO. 4-957

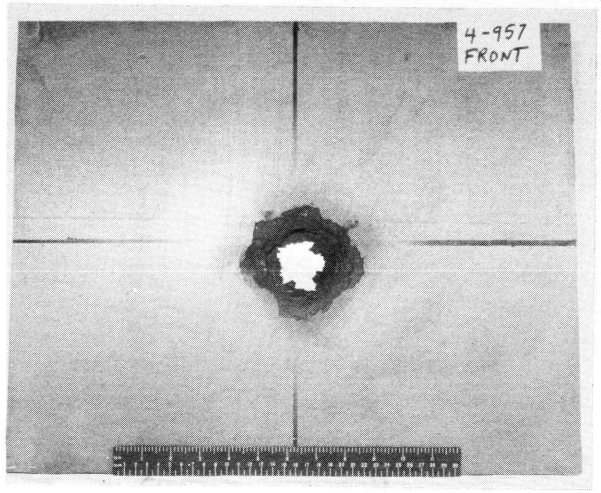

FRONT TARGET

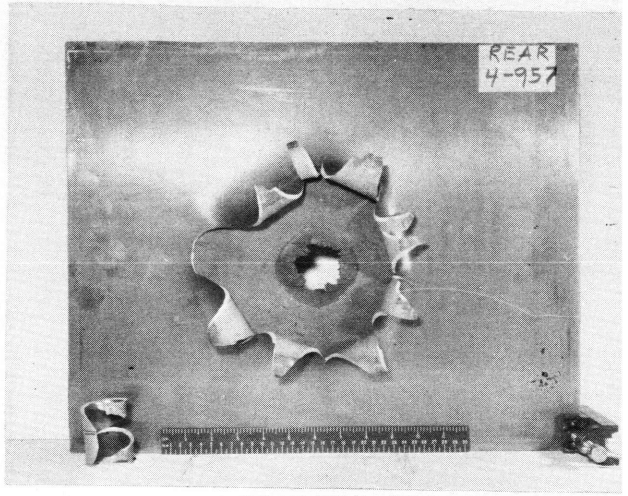

REAR TARGET

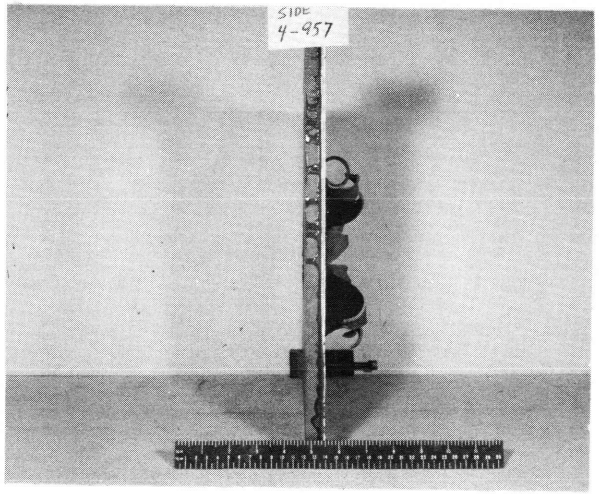

EDGE TARGET

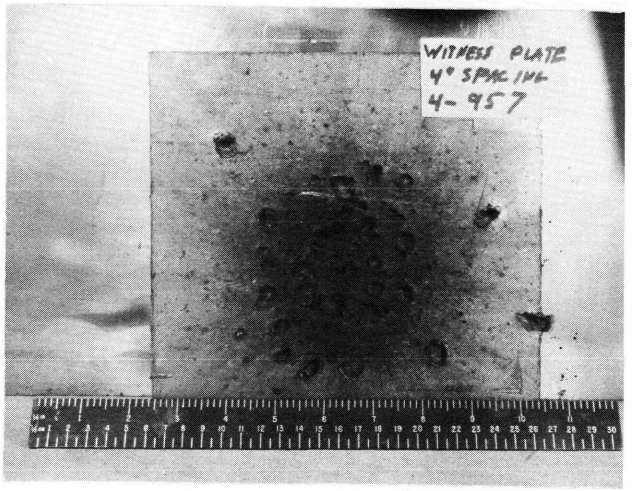

W. P. = 1-5" BLOCK
s = 4" FROM POINT OF IMPACT
Pm = 0.43cm

ROUND NO. 1-1-108

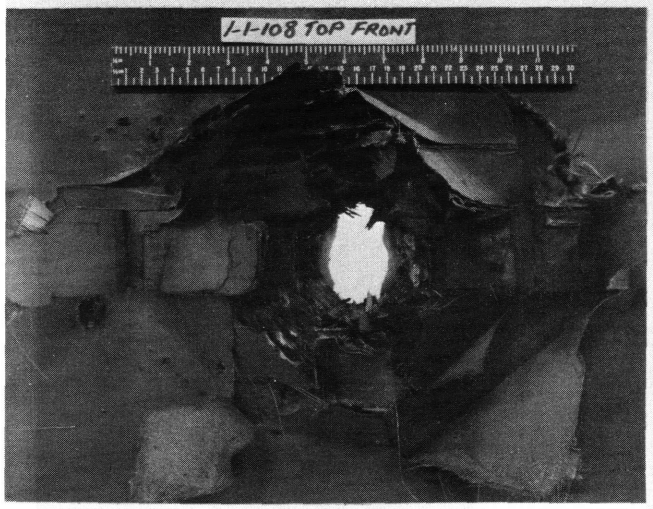

FRONT TARGET

REAR TARGET

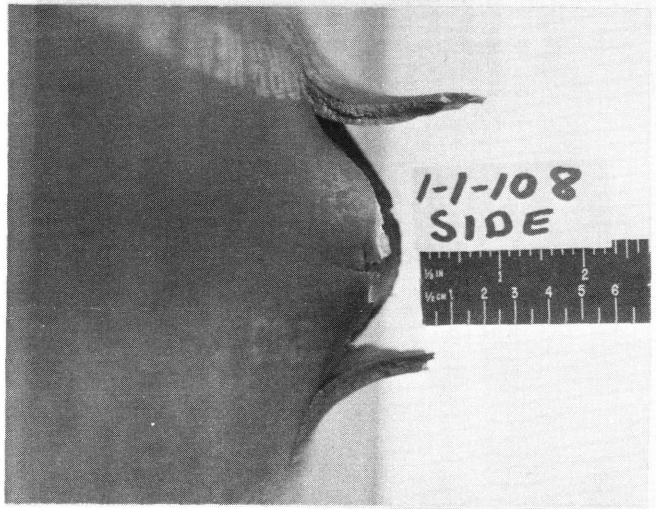

EDGE TARGET

W.P. 1-1/2" PLATE. s = 10" FRAGMENT MASS 16.710g
Pm = 0.76 cm

ROUND NO. CBA-6

FRONT TARGET

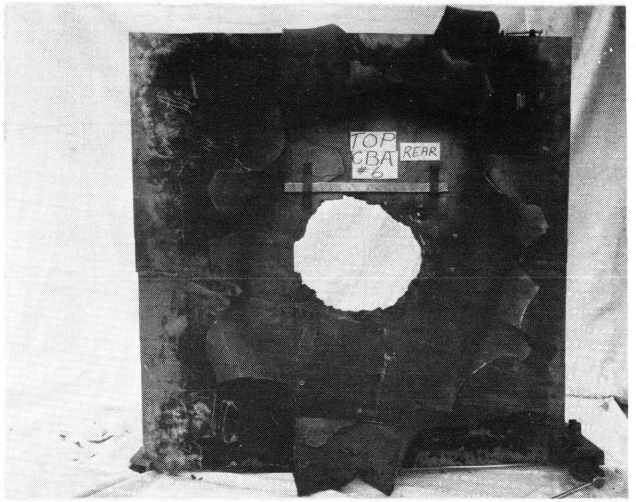

REAR TARGET

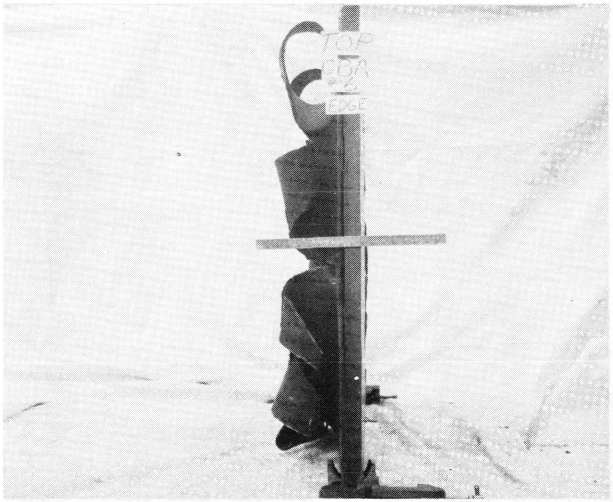

EDGE TARGET

W. P. 1-3/4" STEEL
s = 20" FROM IMPACT POINT
Pm = PERFORATION

ROUND NO. 1-1-82

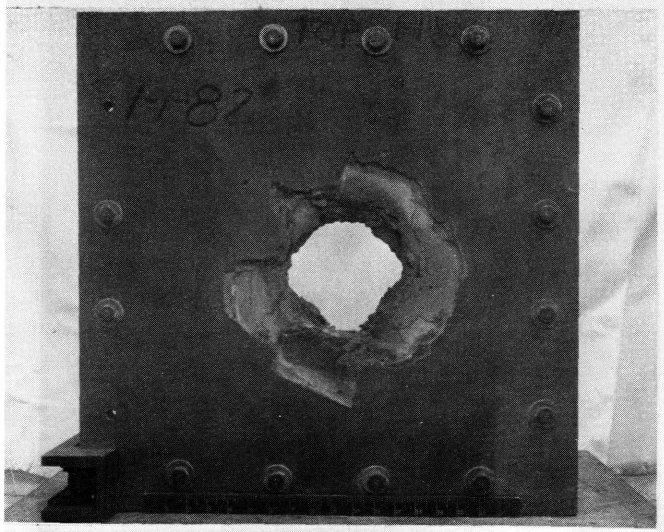

FRONT TARGET

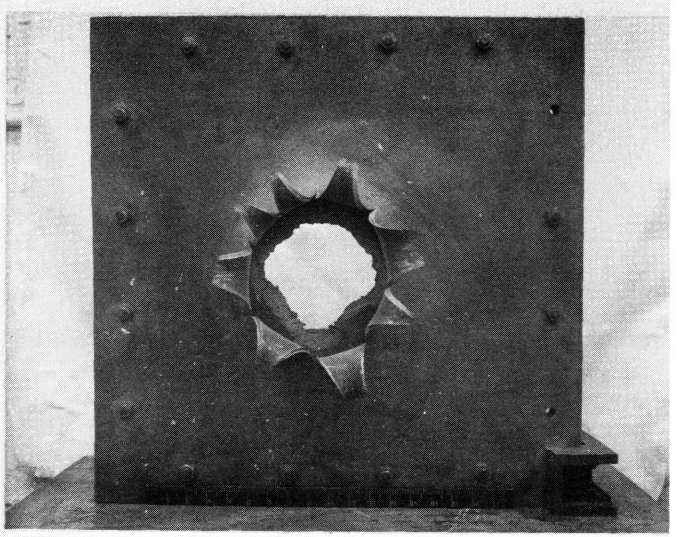

REAR TARGET

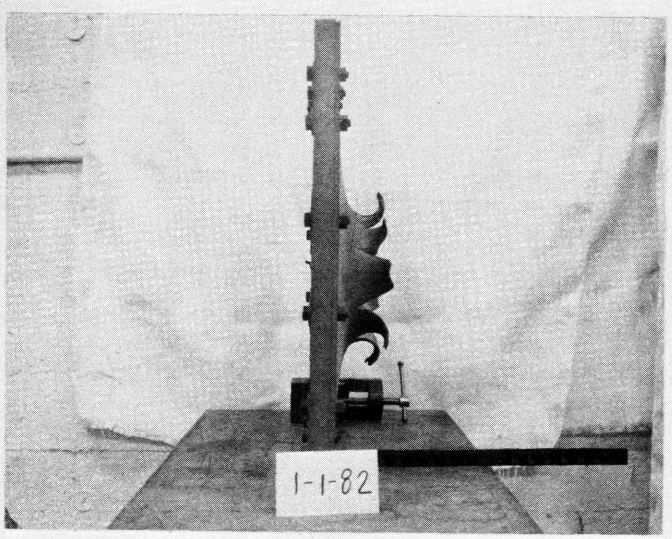

EDGE TARGET

ROUND NO. 1-1-83

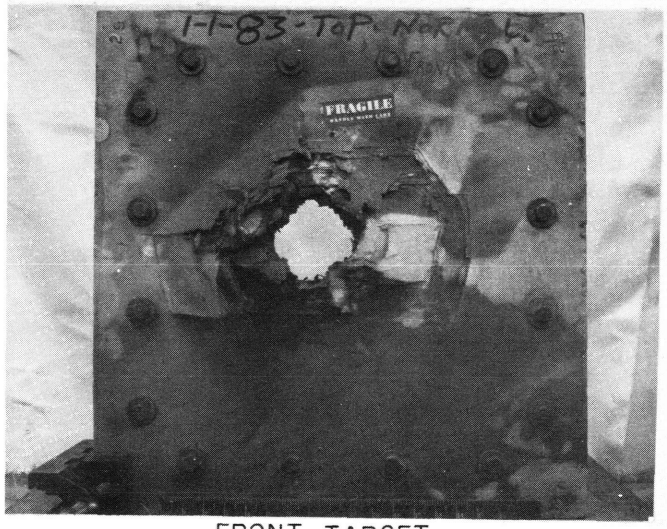

FRONT TARGET

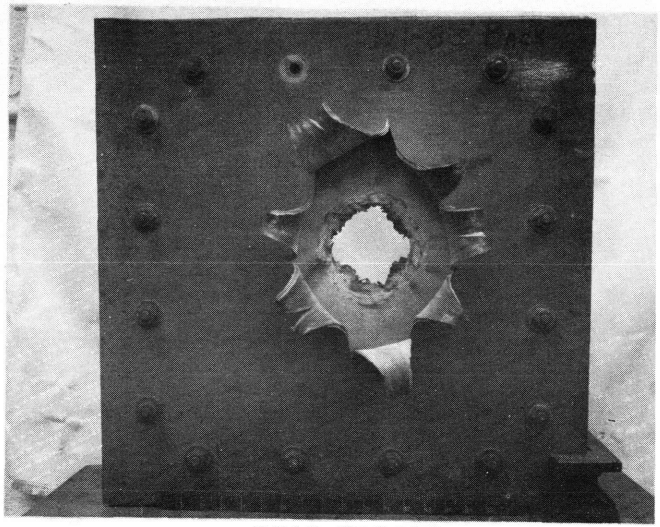

REAR TARGET

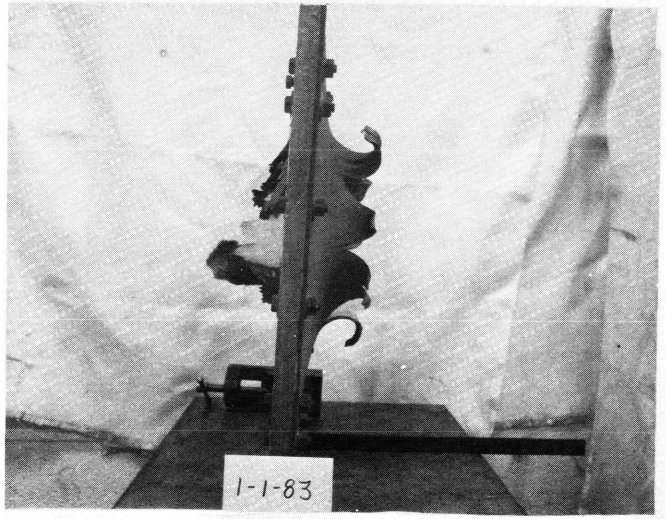

EDGE TARGET

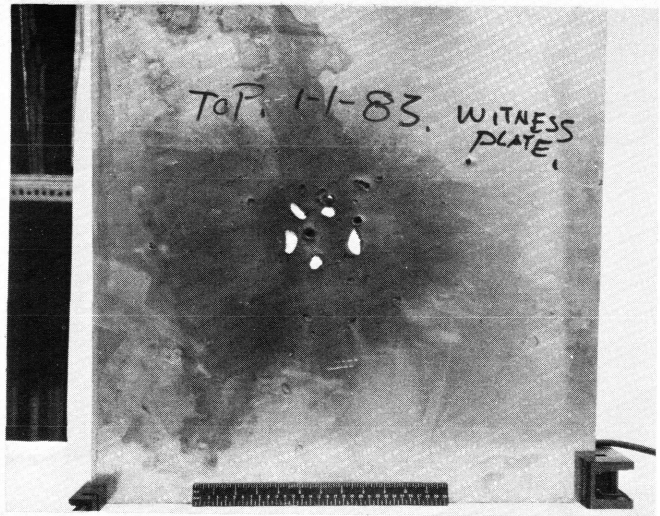

W.P. 1-1/2" PLATE. s = 11.5"

ROUND NO. 1-1-97

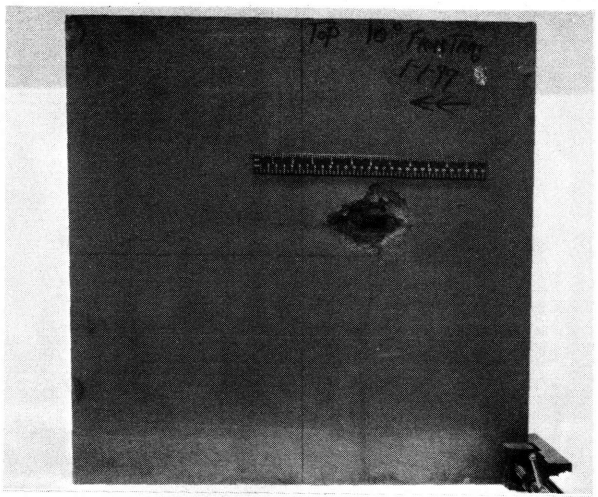

FRONT TARGET

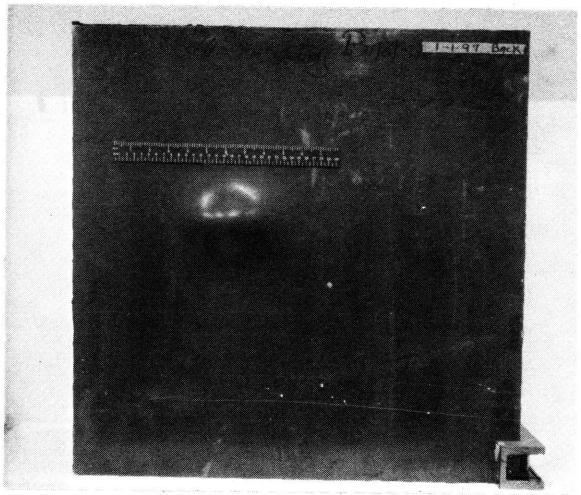

REAR TARGET

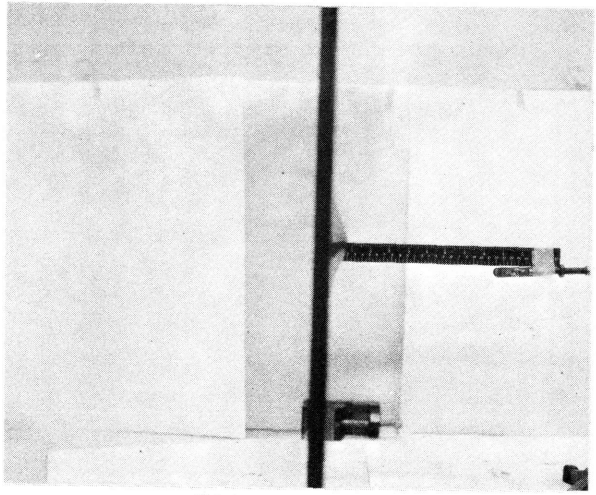

EDGE TARGET

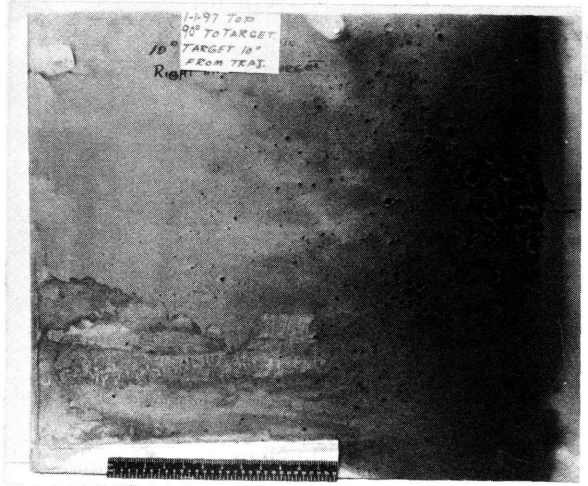

W. P. 2-1/2" PLATES
s = 10"
90° TO TARGET FACE
Pm = 1.61 cm

ROUND NO. 1-1-86

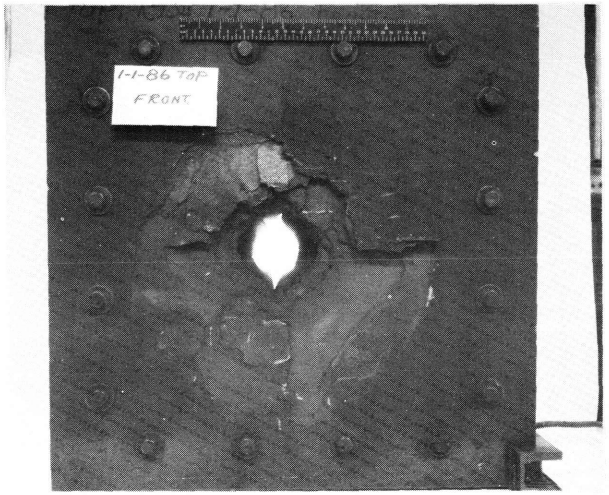

FRONT TARGET

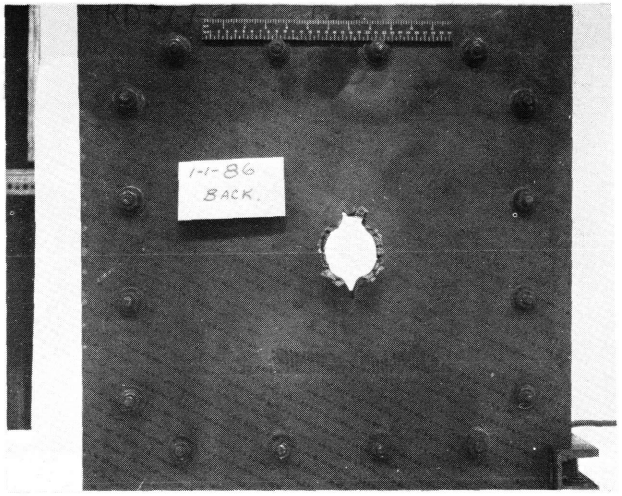

REAR TARGET

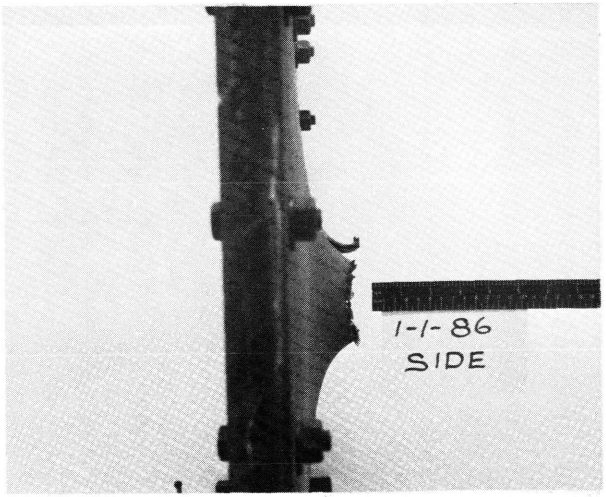

EDGE TARGET

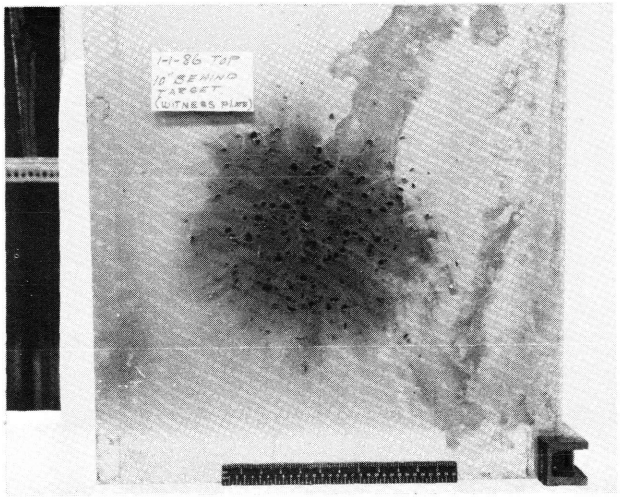

W. P. 1-1/2" PLATE
s = 10"
Pm = 1.21 cm

ROUND NO. 1-1-87

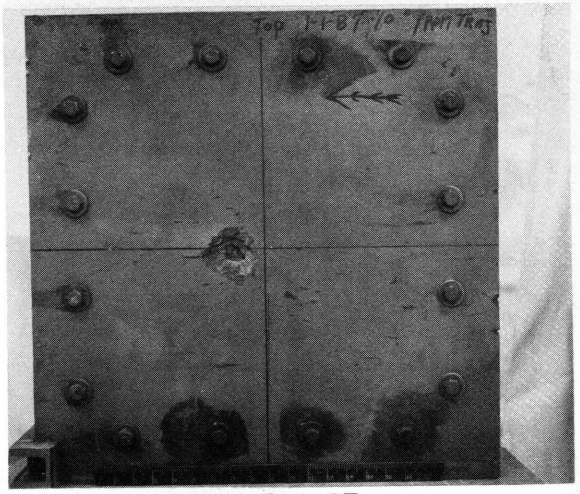

FRONT TARGET

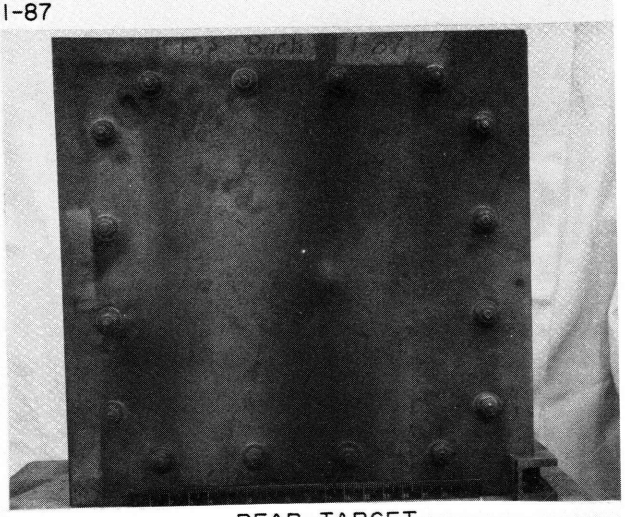

REAR TARGET

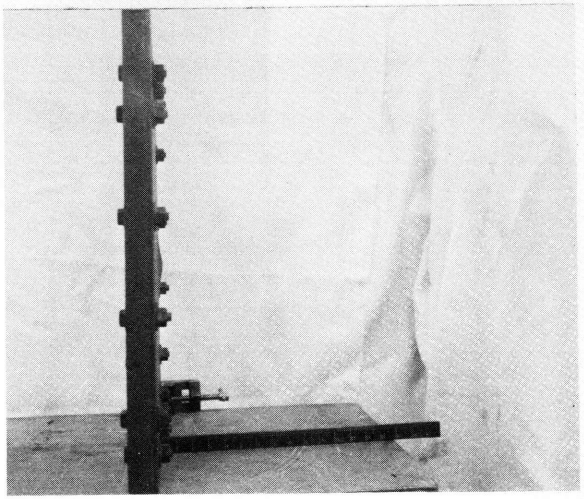

EDGE TARGET

W. P. 4-1/2" PLATES.
s = 13 1/2" FROM POINT OF IMPACT
Pm = 3.12 cm

ROUND NO. 1-1-93

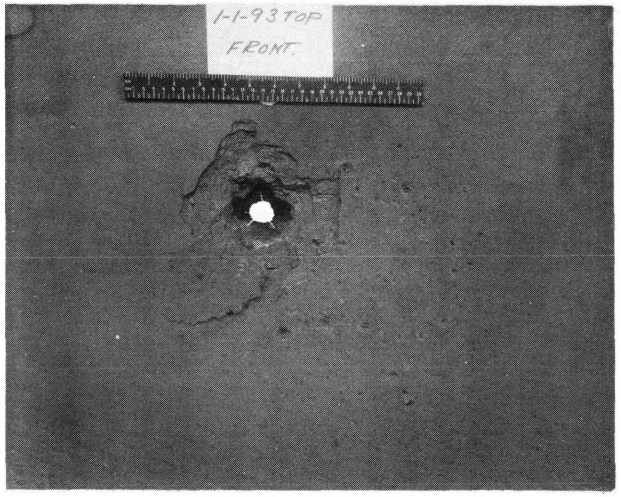

FRONT TARGET

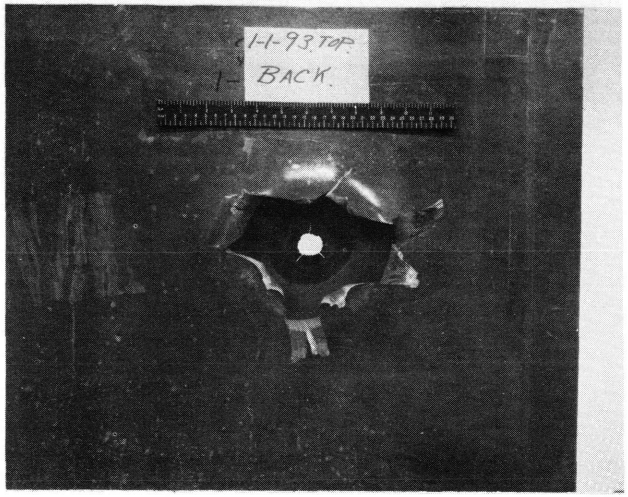

REAR TARGET

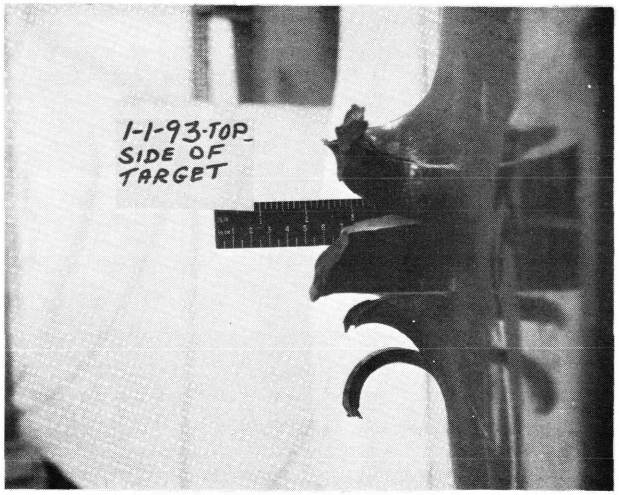

EDGE TARGET

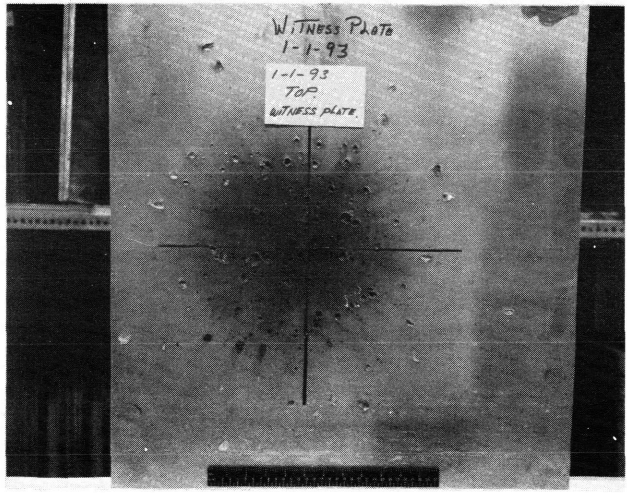

W. P. 1-1/2" PLATE
s = 10"
Pm = 1.0 cm

ROUND NO. 1-1-94

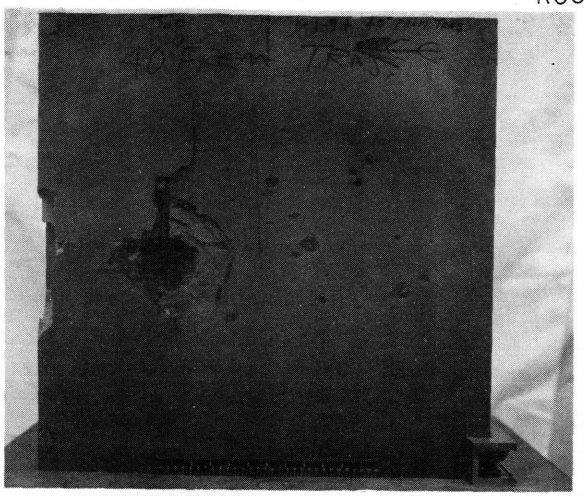

FRONT TARGET

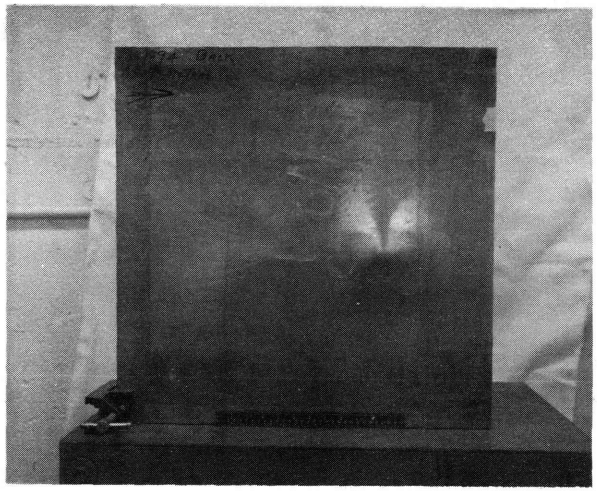

REAR TARGET

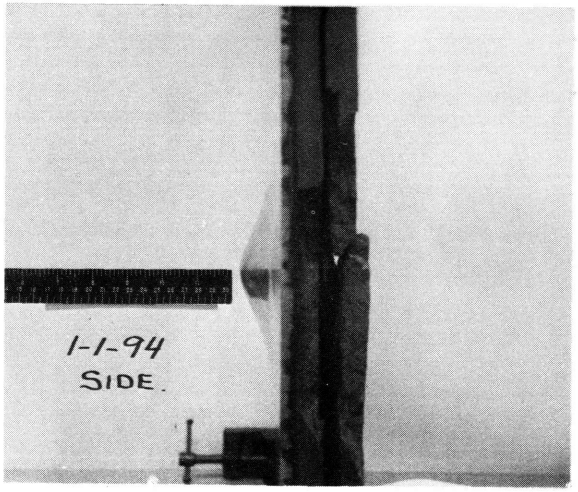

EDGE TARGET

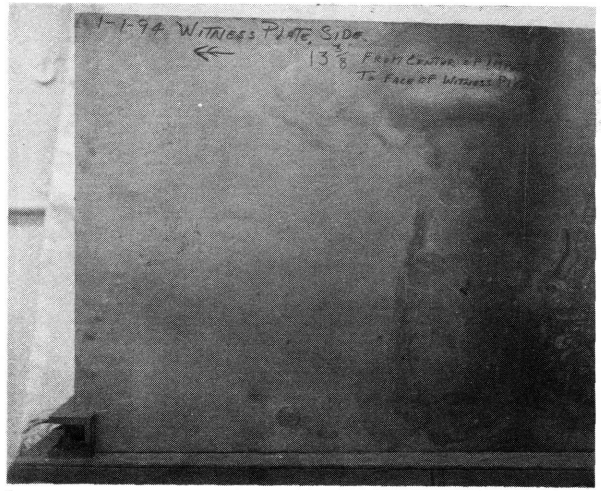

W. P. 1-1/2" PLATE
s = 13 3/8" FROM POINT OF IMPACT
90° TO TARGET FACE
Pm = 0.11 cm

ROUND NO. I-I-95

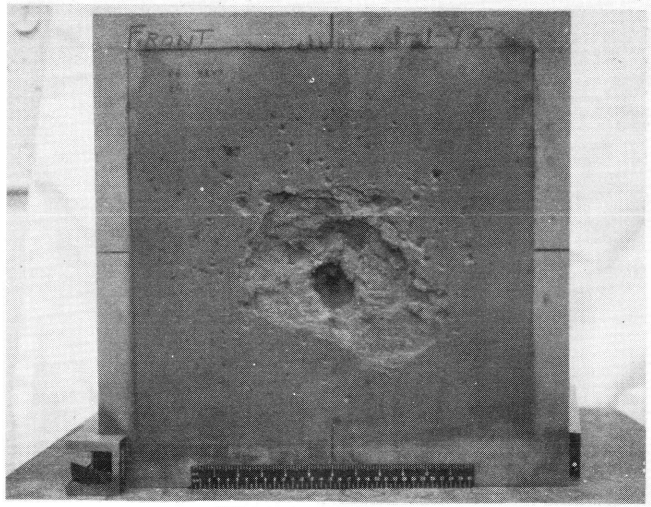

FRONT TARGET

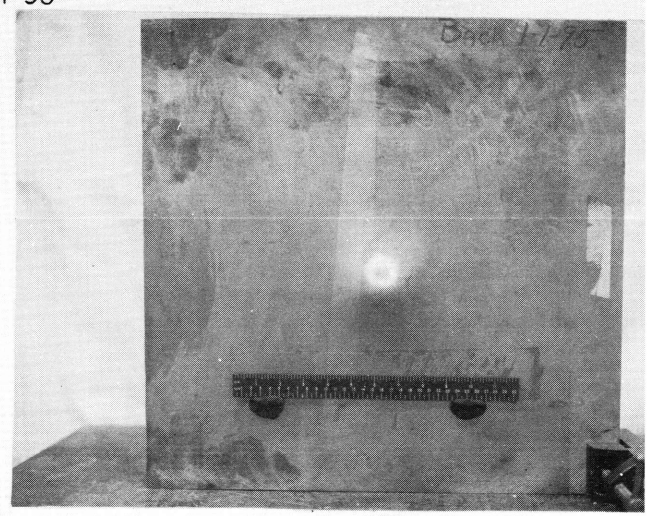

REAR TARGET

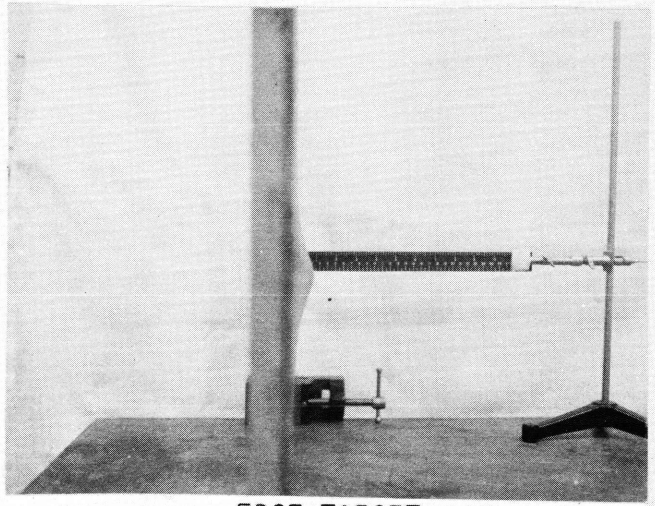

EDGE TARGET

ROUND NO. 1-1-88

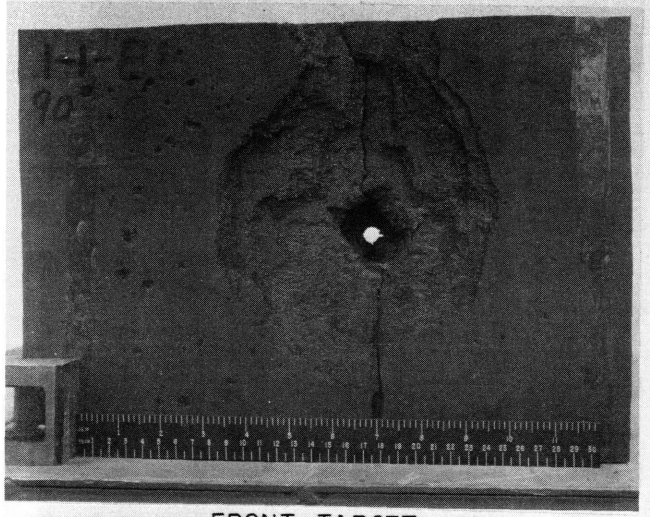

FRONT TARGET

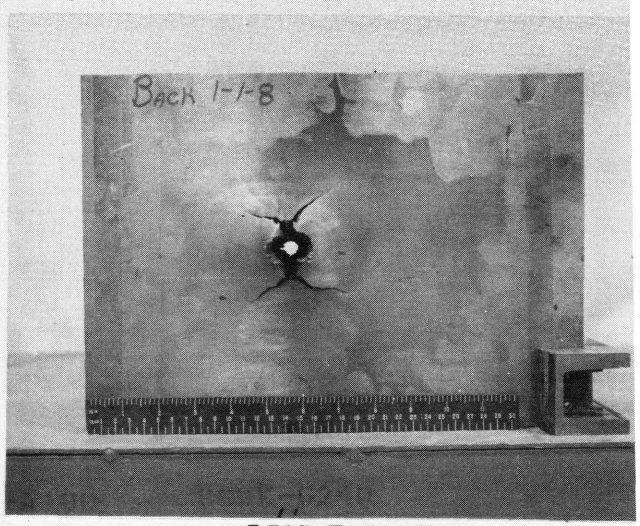

REAR TARGET

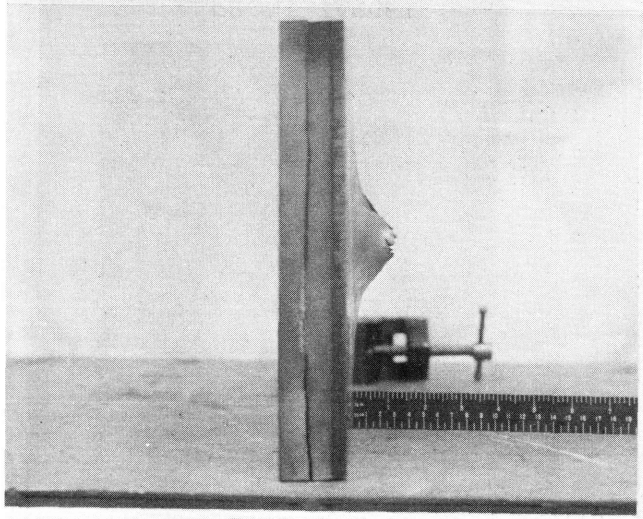

EDGE TARGET

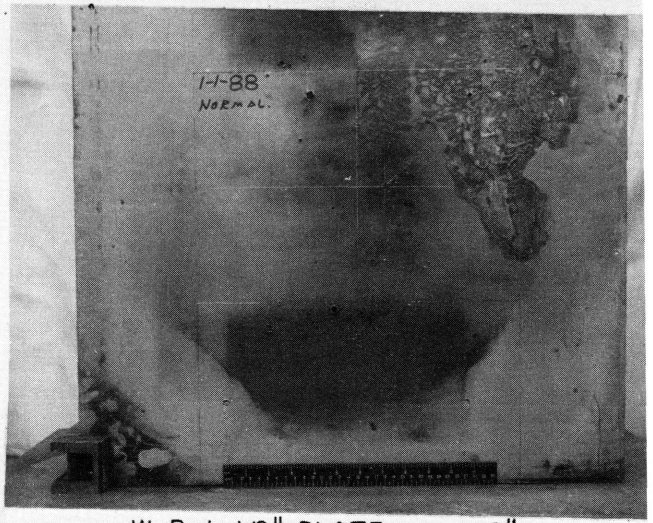

W. P. 1-1/2" PLATE. s = 10"
Pm = 0.34 cm

ROUND NO. 1-1-103

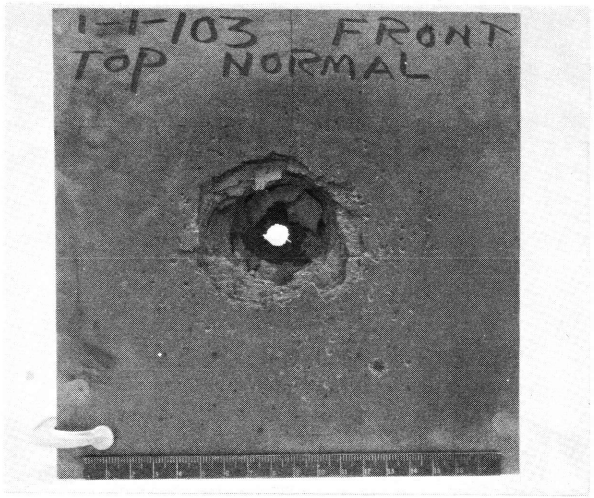

FRONT TARGET

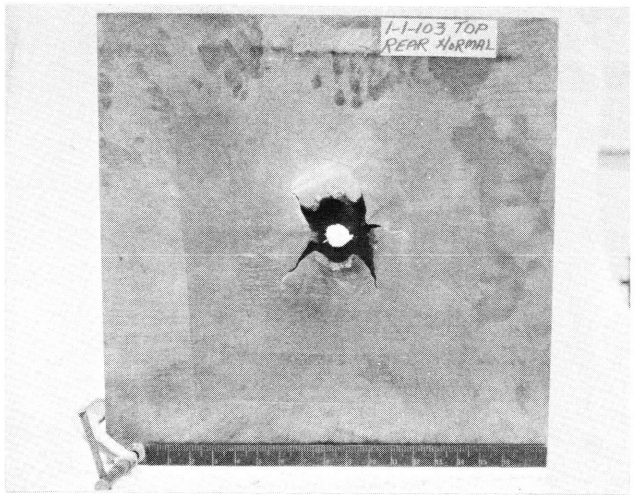

REAR TARGET

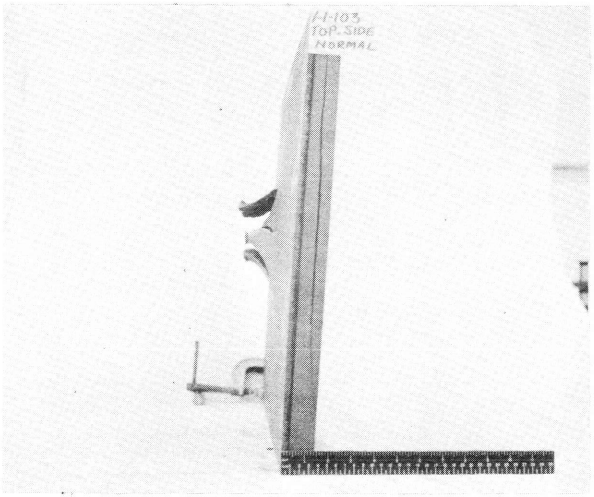

EDGE TARGET

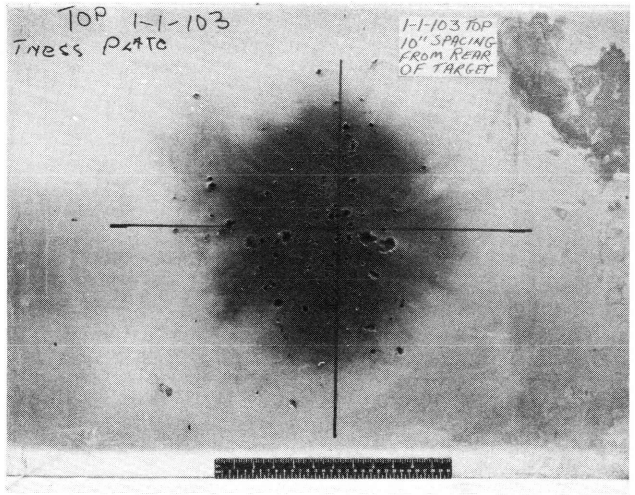

W. P. 1-1/2" PLATE
s = 10"
Pm = 1.24 cm

ROUND NO. 1-1-104

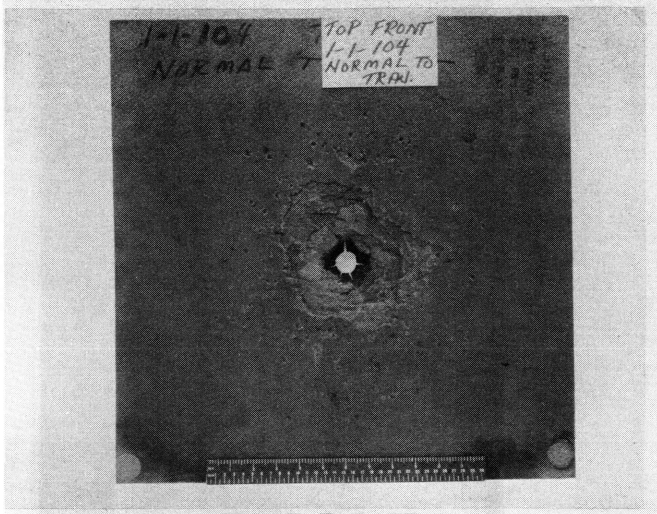

FRONT TARGET

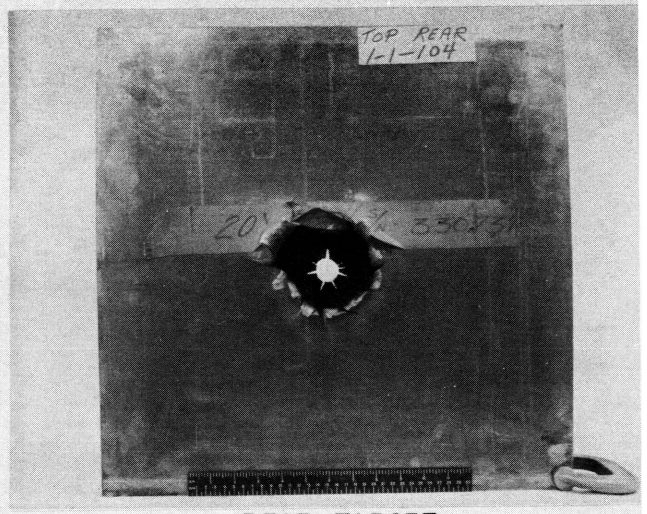

REAR TARGET

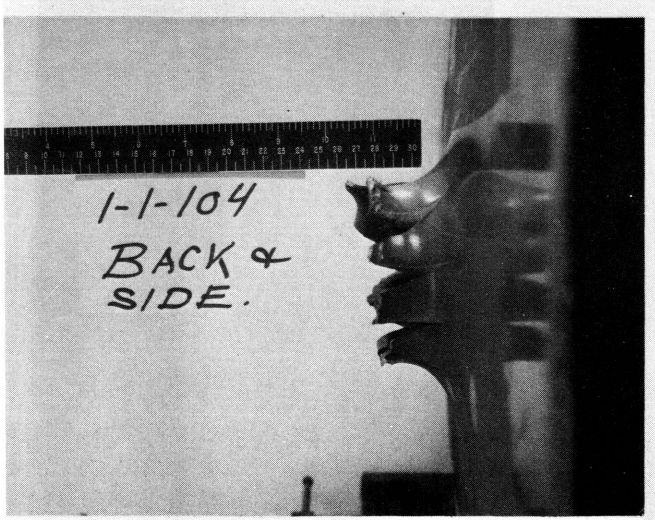

EDGE TARGET

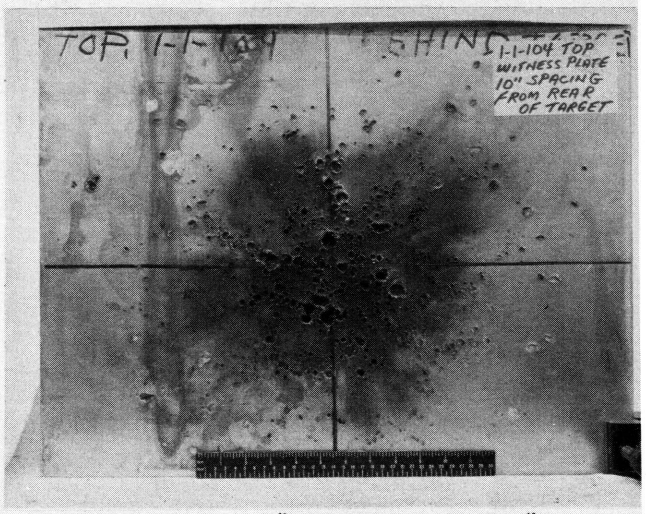

W. P. 2-1/2" PLATES. s = 10"
Pm = 2.02 cm

ROUND NO. 1-1-105

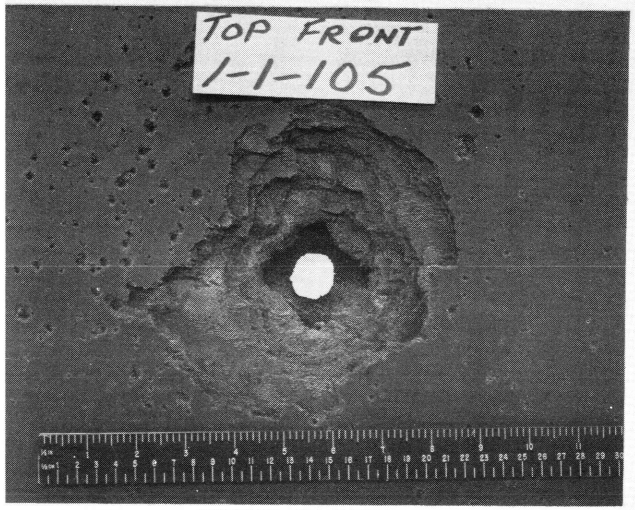

FRONT TARGET

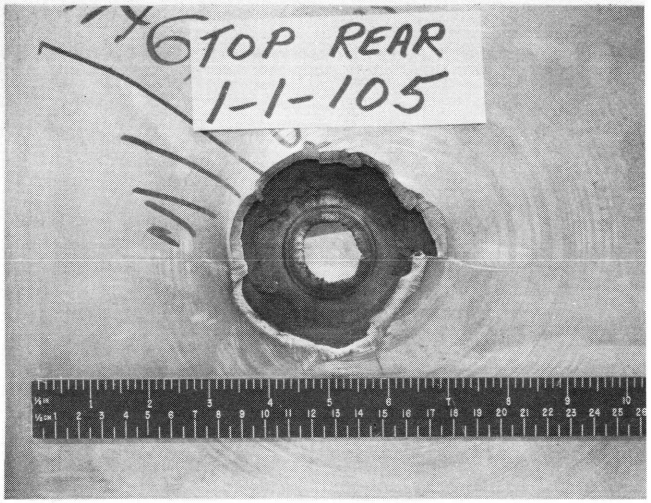

REAR TARGET

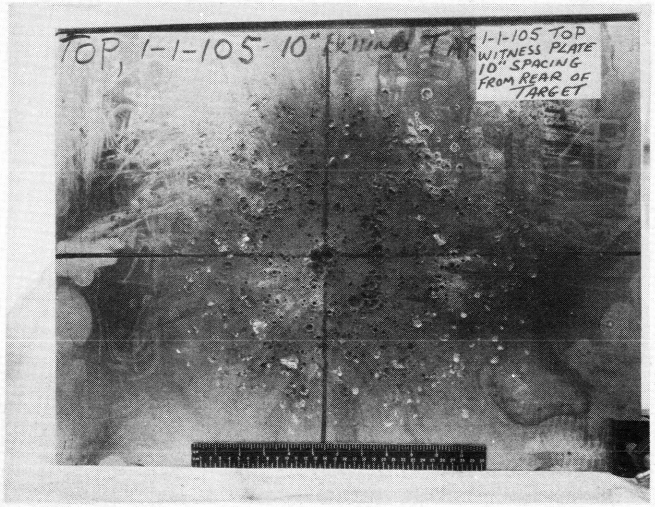

W. P. 2-1/2" PLATES. s = 10"
Pm = 1.76 cm

ROUND NO. 1-1-106

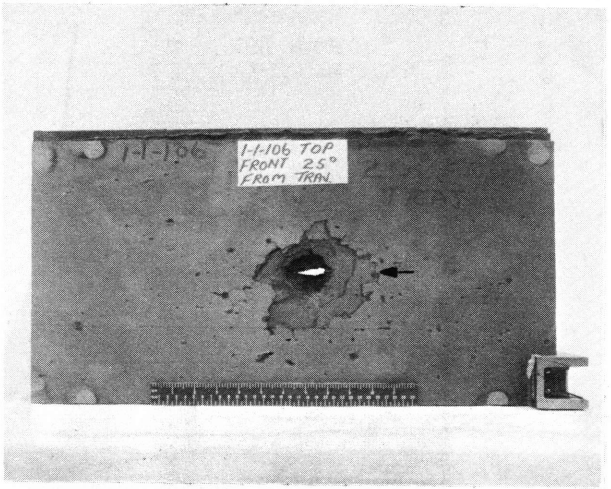

FRONT TARGET

REAR TARGET

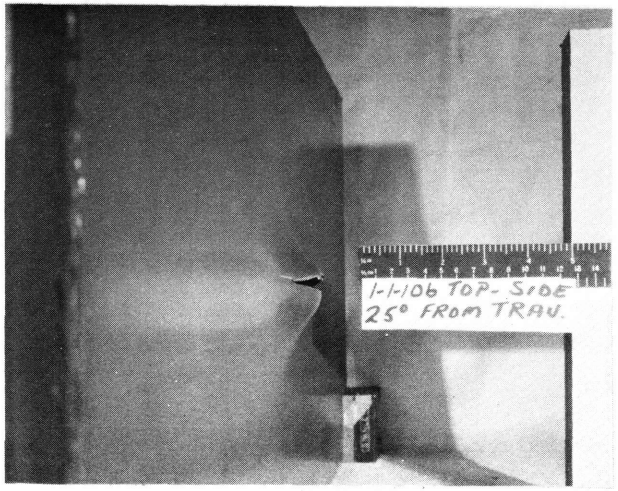

EDGE TARGET

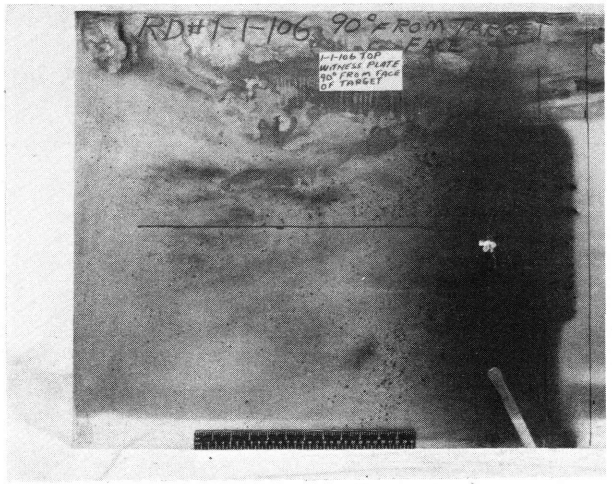

W. P. 1-1/2" PLATE
16 3/4" FROM TARGET IMPACT POINT
90° FROM TARGET FACE
Pm = 0.22 cm

ROUND NO. 1-1-107

FRONT TARGET

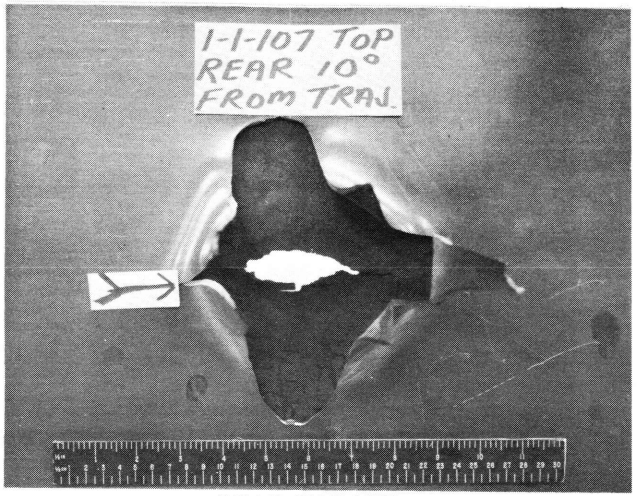

REAR TARGET

EDGE TARGET

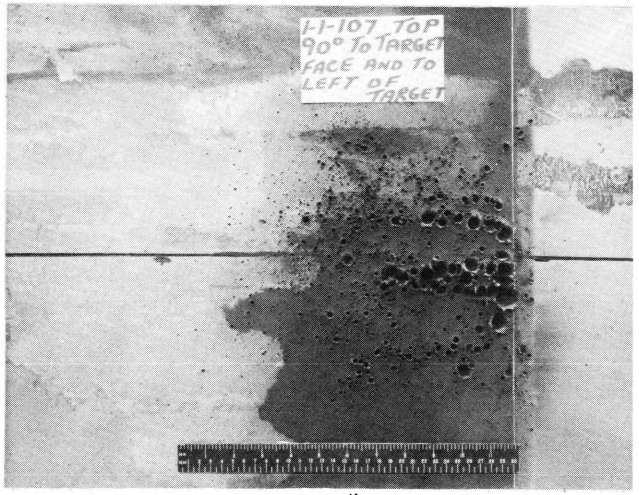

W. P. 2-1/2" PLATES
15 3/4" FROM TARGET IMPACT POINT
90° FROM TARGET FACE
Pm = 0.38 cm

ROUND NO. 1-1-110

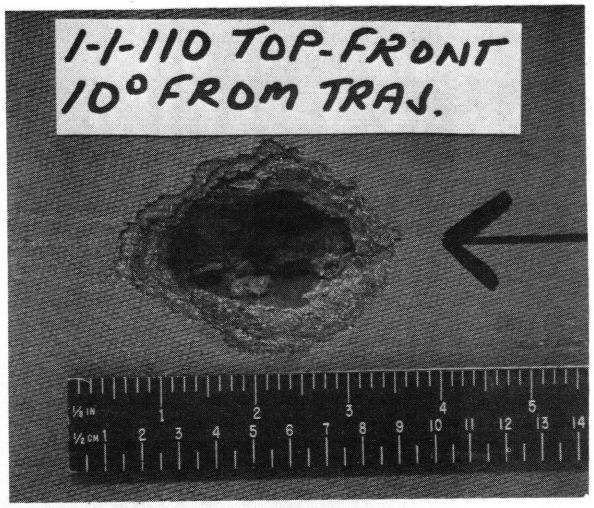

FRONT TARGET

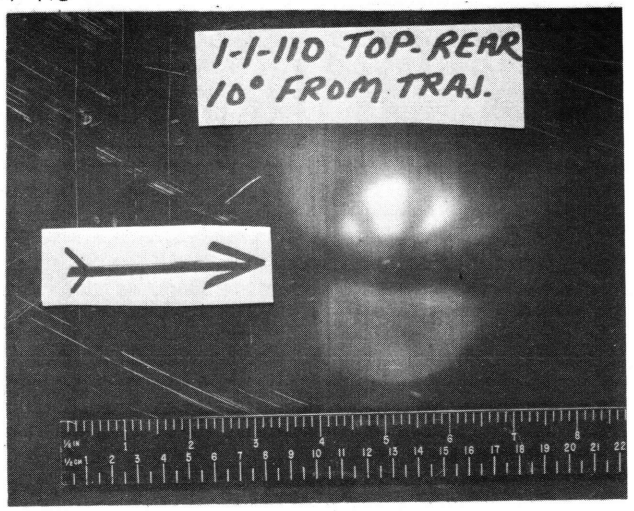

REAR TARGET

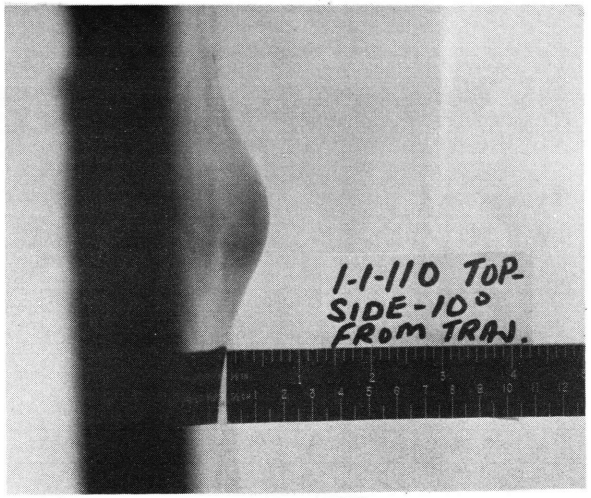

EDGE TARGET

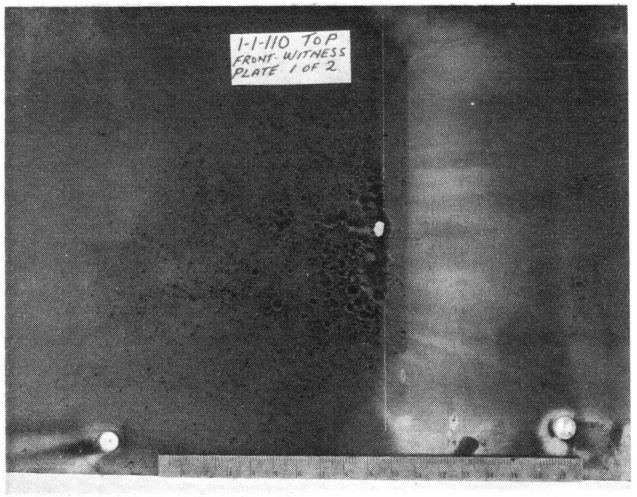

W. P. 2-1/2" PLATES
19 3/4" FROM TARGET IMPACT POINT
90° FROM TARGET FACE

ROUND NO. 4-961

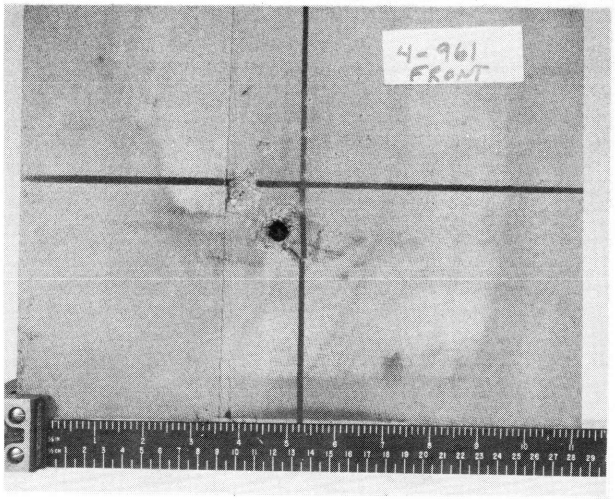

FRONT TARGET

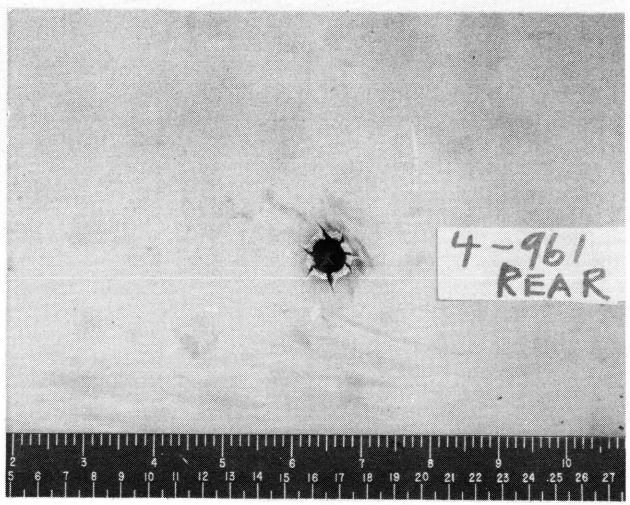

REAR TARGET

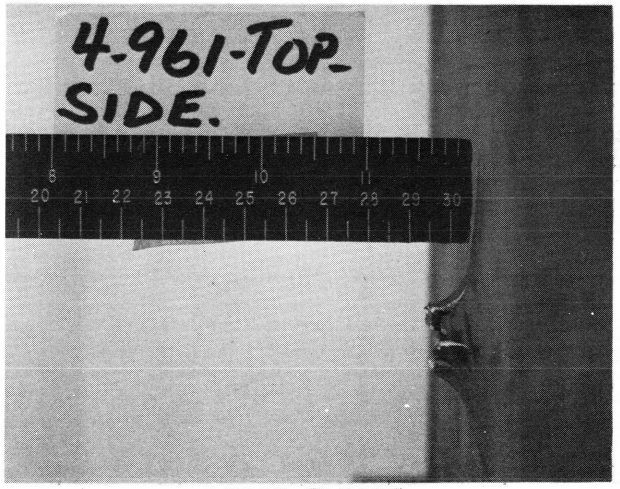

EDGE TARGET

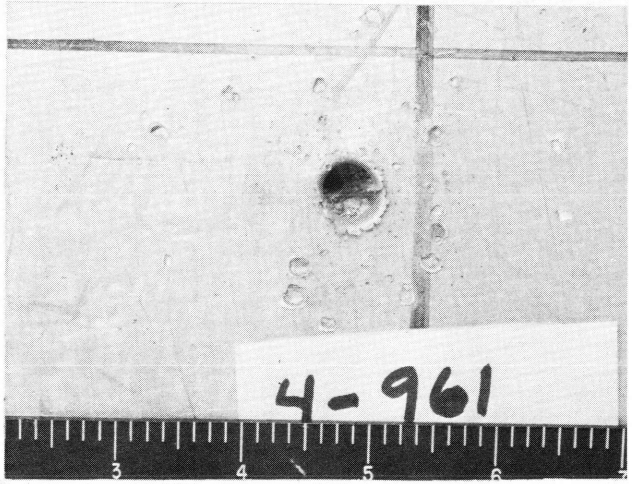

W. P. 1-5" BLOCK
s = 4" FROM POINT OF IMPACT
Pm = 1.37 cm

ROUND NO. 4-958

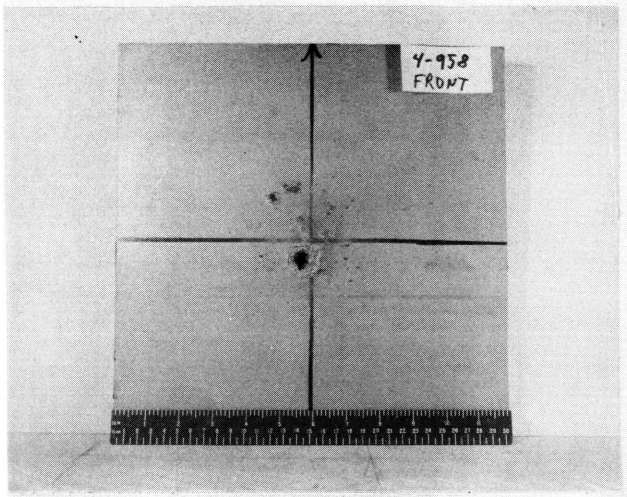

FRONT TARGET

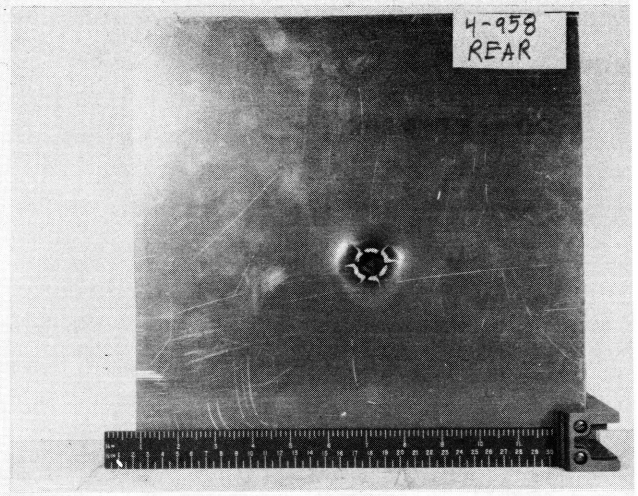

REAR TARGET

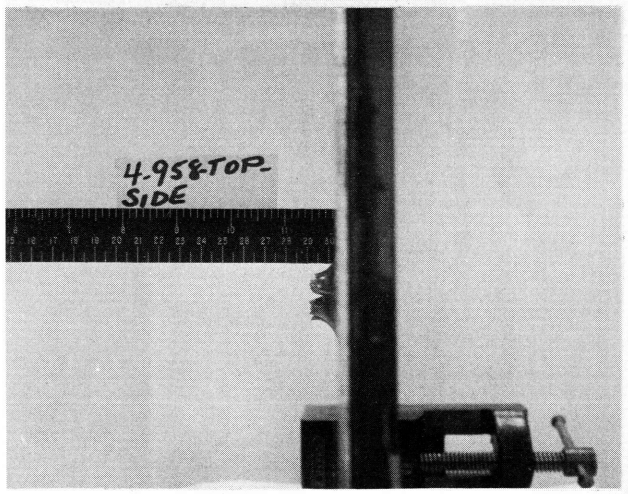

EDGE TARGET

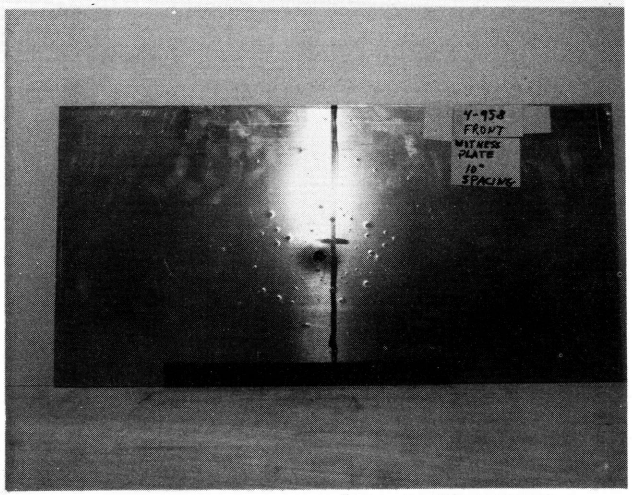

W. P. 1-1/2" PLATE
s = 10" FROM POINT OF IMPACT
P m = PERFORATED

ROUND NO. 4-930 SIMULATED MODEL NOSE CONE TARGET

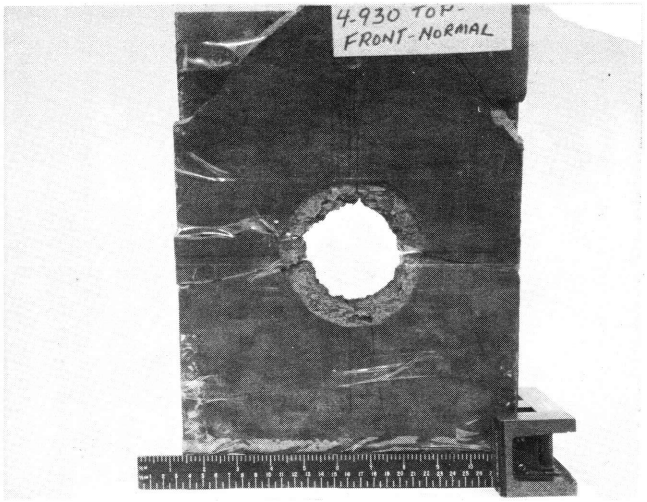

FRONT TARGET NO.1 NORMAL TO TRAJECTORY

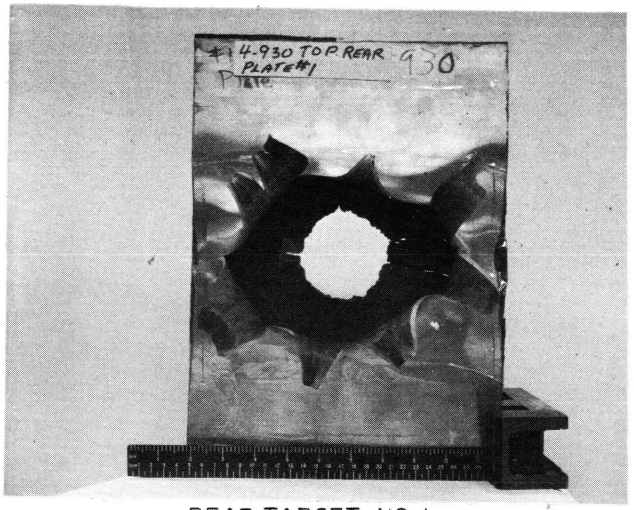

REAR TARGET NO. 1

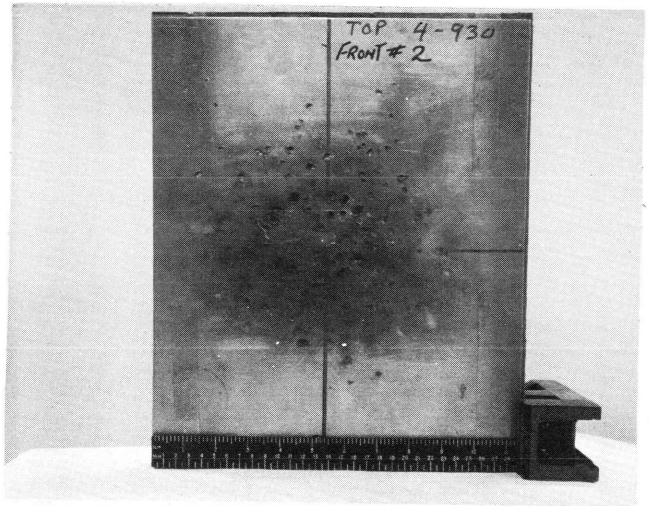

FRONT TARGET NO. 2, 70° FROM TRAJECTORY
6 1/2" BACK OF TARGET NO.1 IMPACT POINT

BACK TARGET NO. 2

ROUND NO. 4-931 SIMULATED MODEL NOSE CONE TARGET

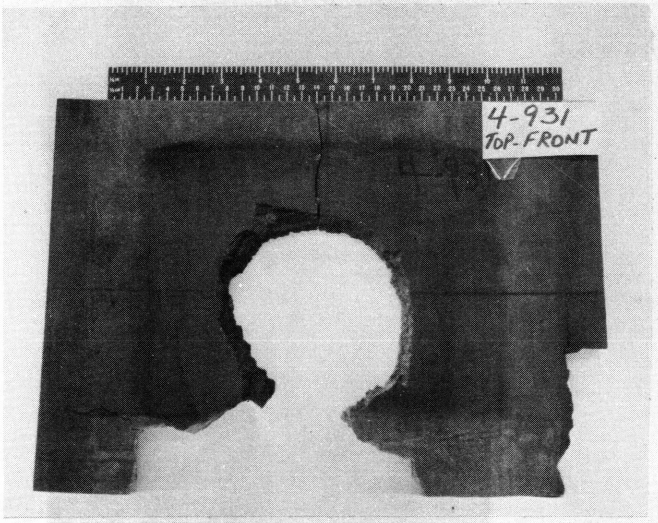

FRONT TARGET NO.1 45° FROM TRAJECTORY

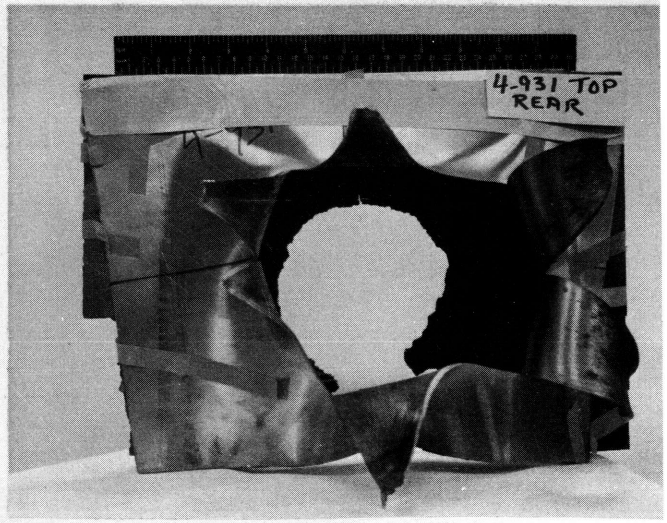

REAR TARGET NO. 1

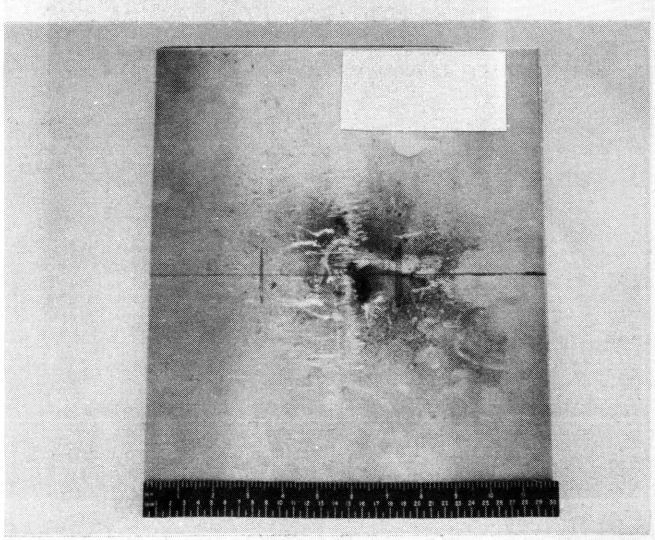

FRONT OF TARGET NO. 2. 25° FROM TRAJECTORY
6 1/2" BACK OF TARGET NO.1 IMPACT POINT.

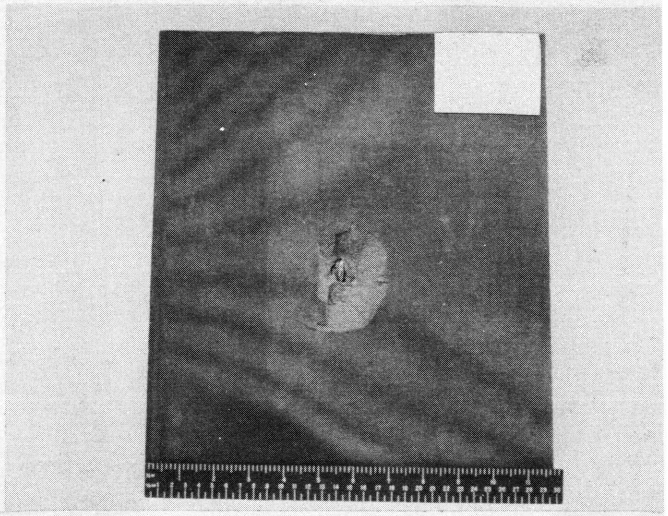

REAR TARGET NO. 2.

ROUND NO. 4-934 SIMULATED MODEL NOSE CONE TARGET

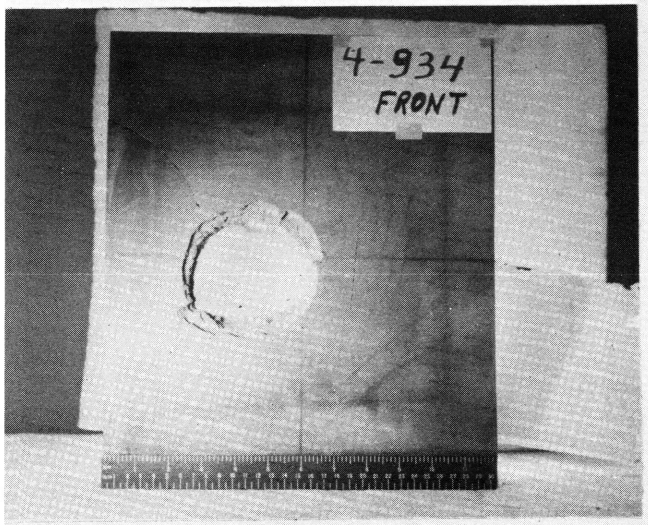

FRONT TARGET NO. I 45° FROM TRAJECTORY

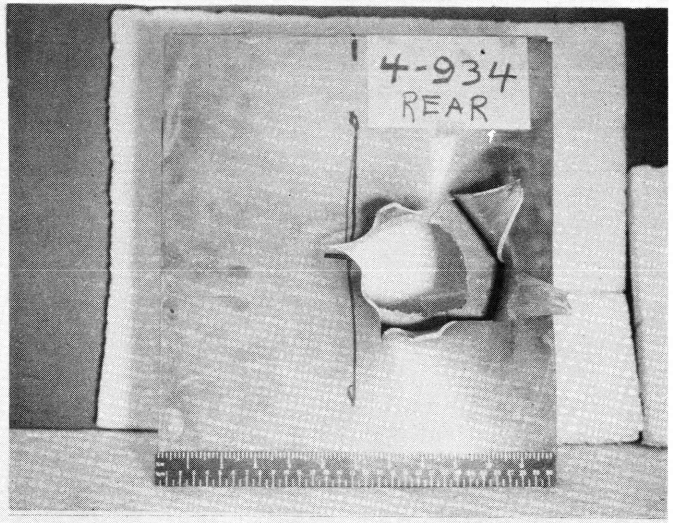

REAR TARGET NO. I

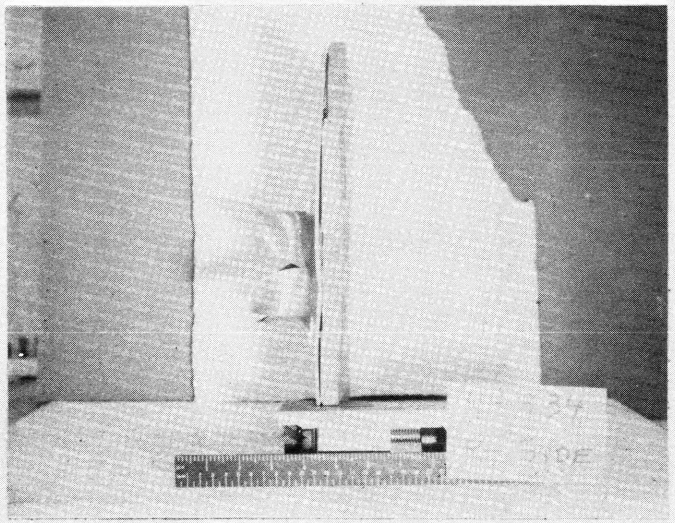

EDGE TARGET NO. I

ROUND NO. 4-935

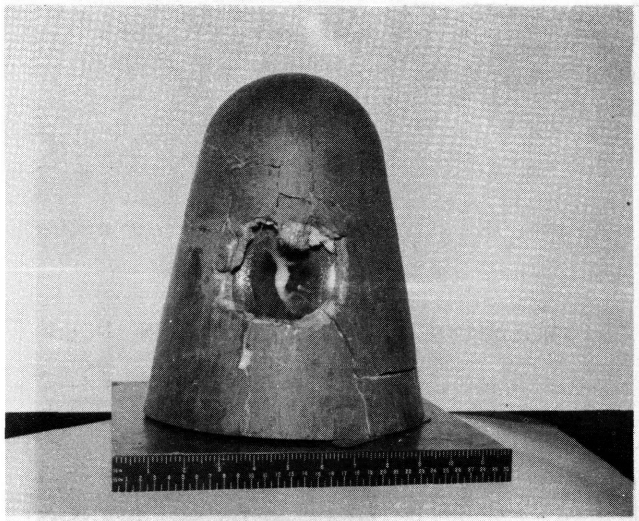

FRONT NOSE CONE, 45° FROM TRAJECTORY

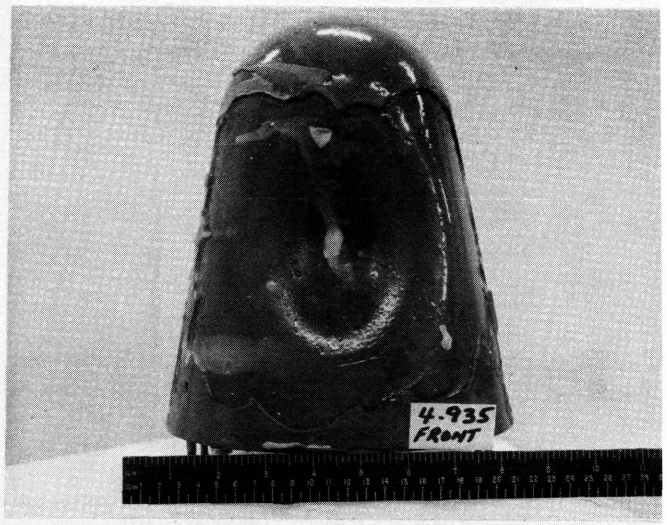

FRONT NOSE CONE LINER

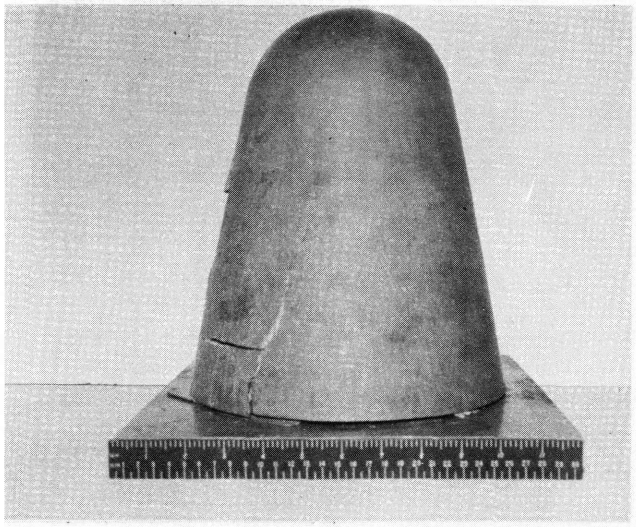

SIDE NOSE CONE

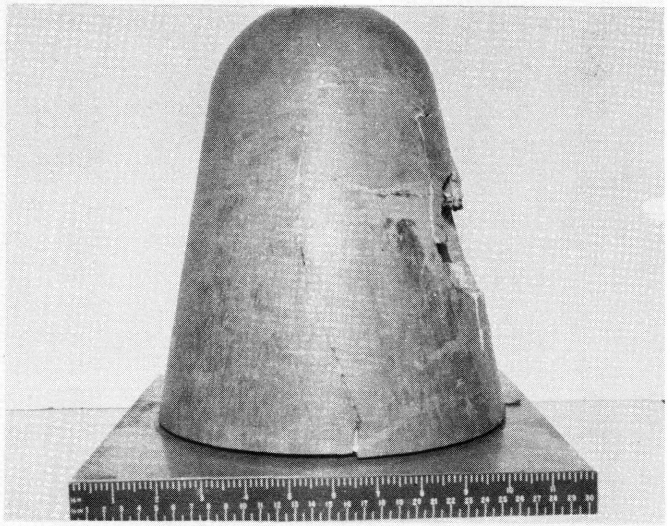

SIDE NOSE CONE

ROUND NO. 4-937

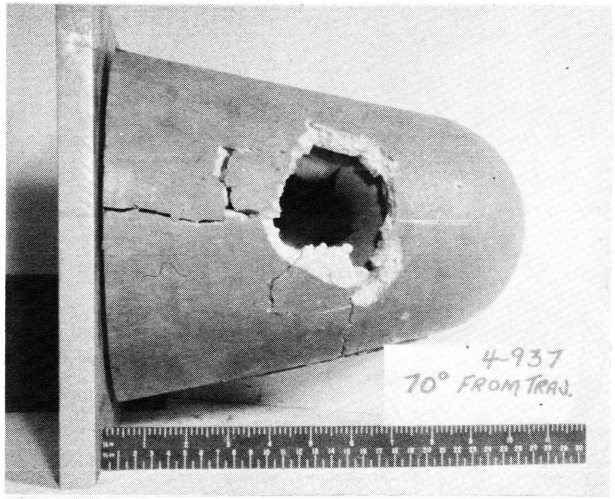

FRONT NOSE CONE, 70° FROM TRAJECTORY

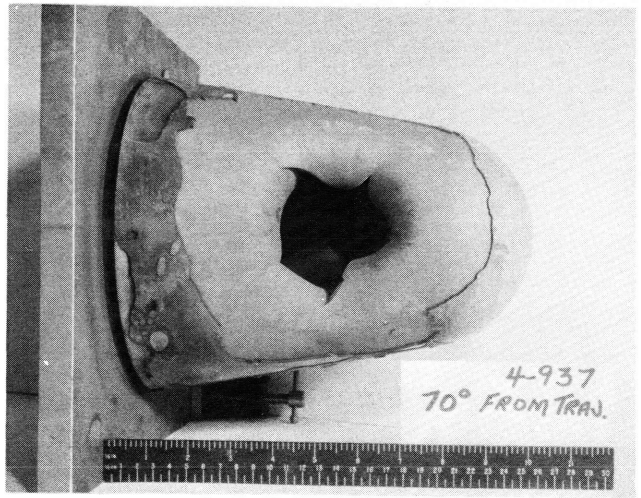

FRONT NOSE CONE LINER

ROUND NO. 4-938

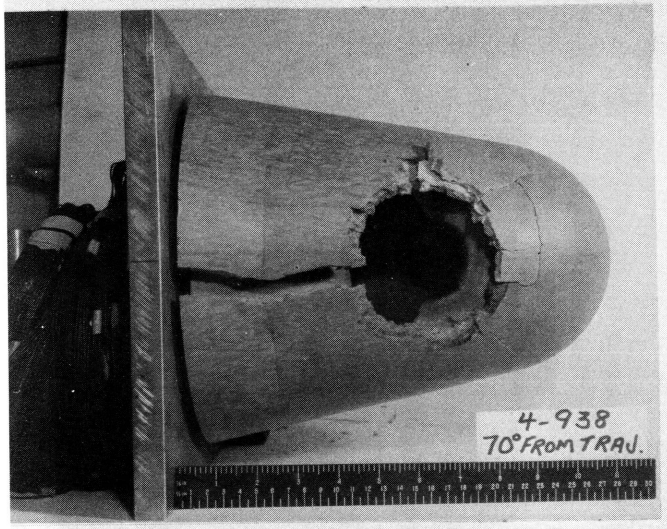

FRONT NOSE CONE, 70° FROM TRAJECTORY

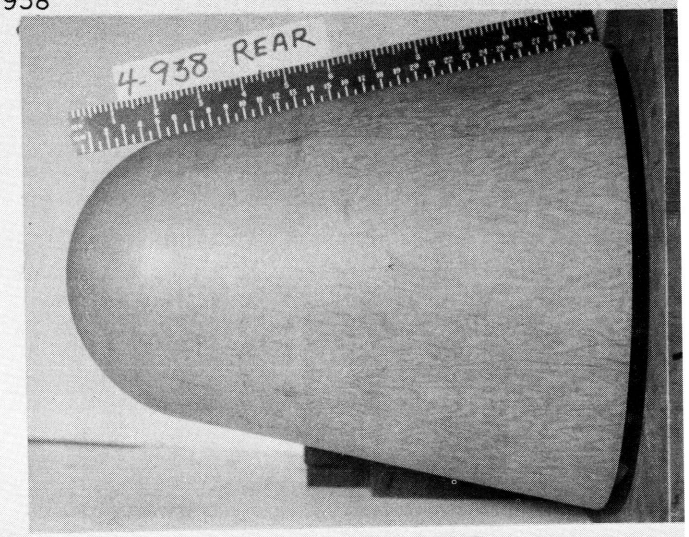

REAR NOSE CONE

SIDE NOSE CONE

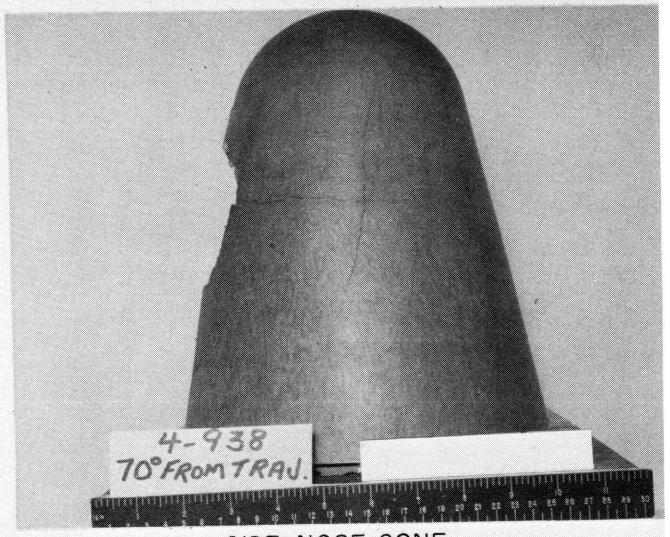

SIDE NOSE CONE

ROUND NO. 4-944

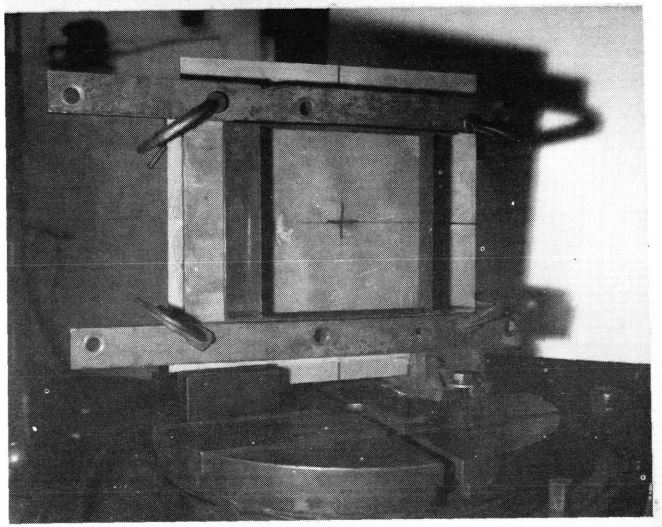

FRONT TARGET BEFORE FIRING

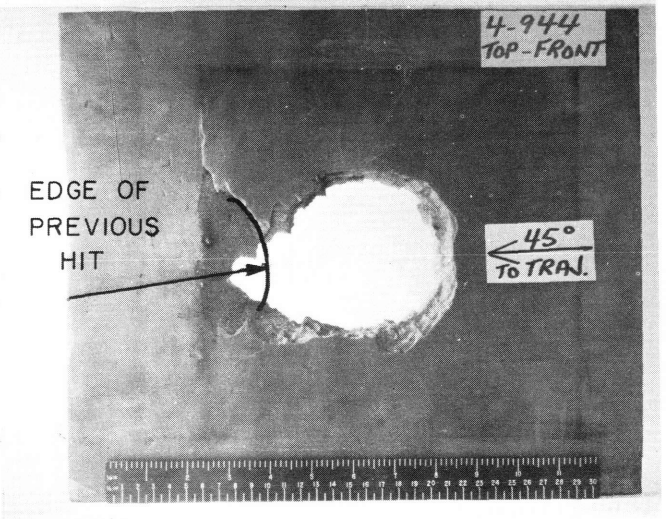

FRONT TARGET AFTER FIRING

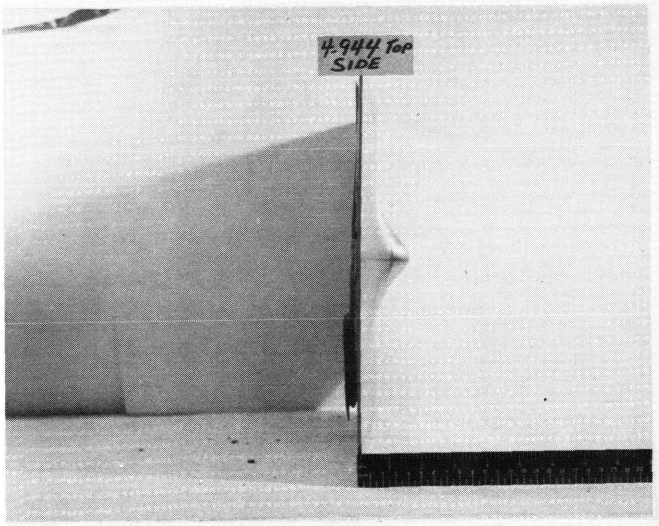

EDGE TARGET

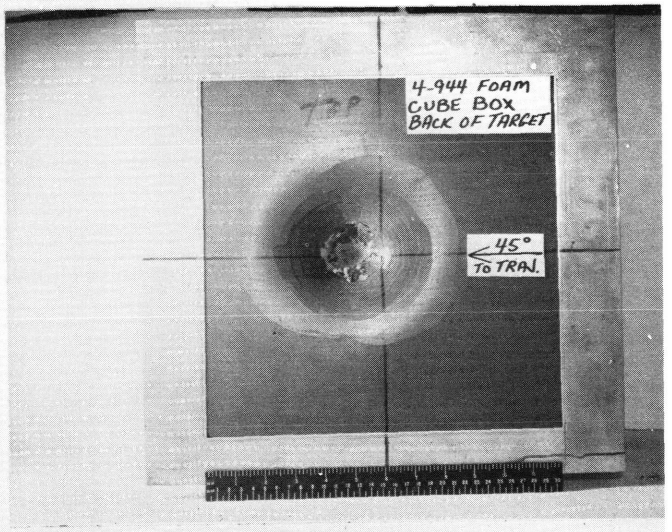

FRONT FOAM

ROUND NO. 4-945

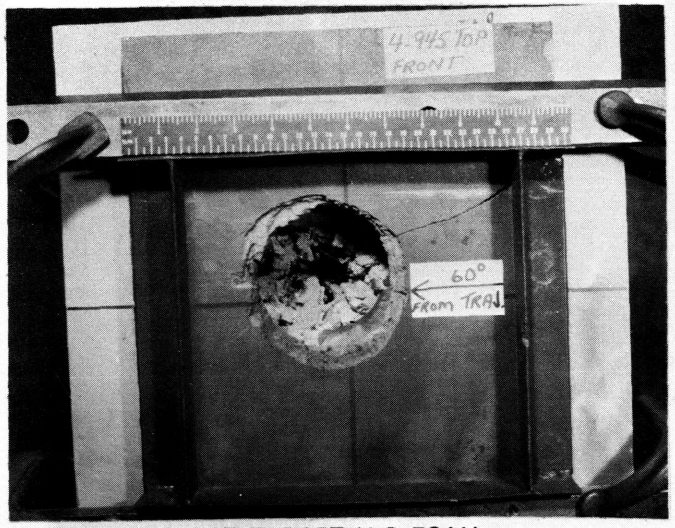

FRONT TARGET AND FOAM

FRONT BACKUP AND FOAM

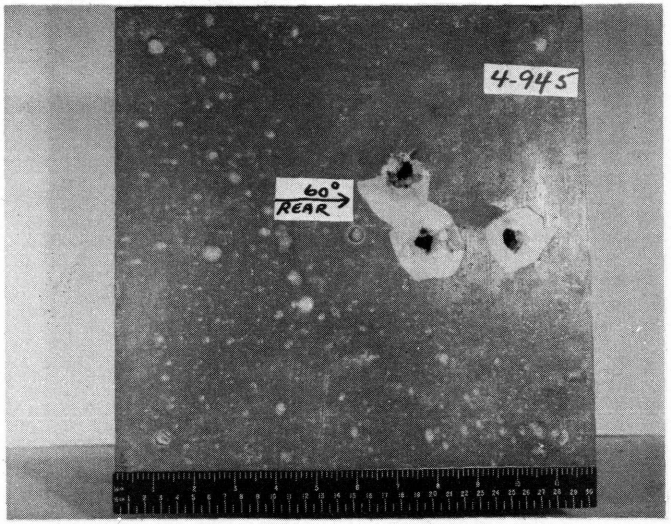

REAR FOAM

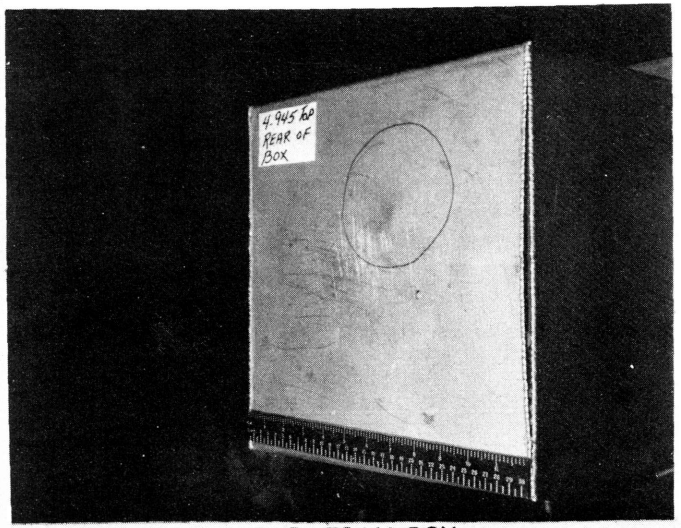

REAR FOAM BOX

ROUND NO. 4-946

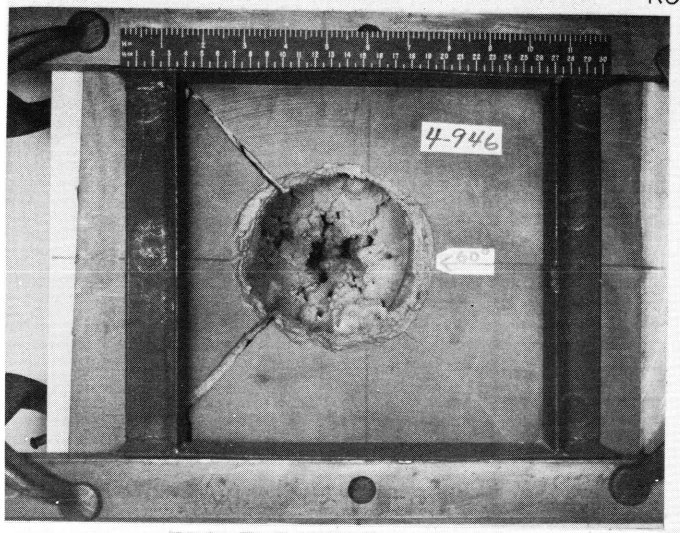

FRONT TARGET AND FOAM

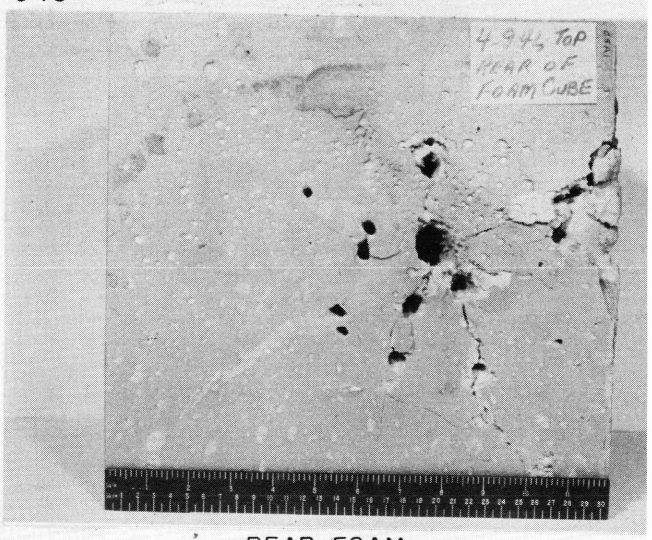

REAR FOAM

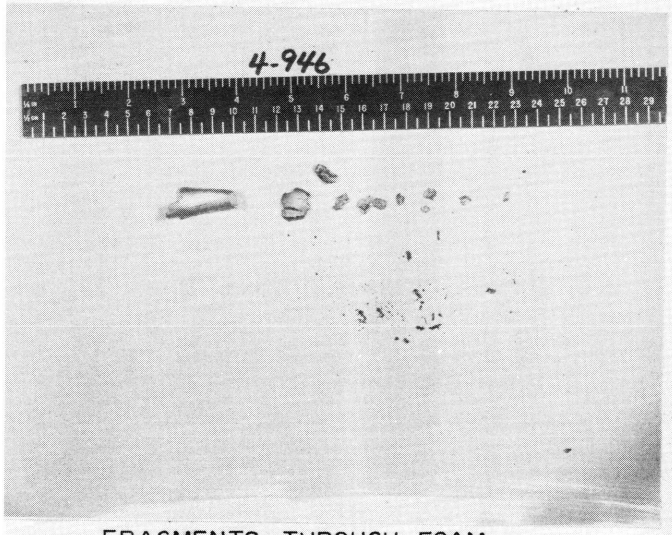

FRAGMENTS THROUGH FOAM

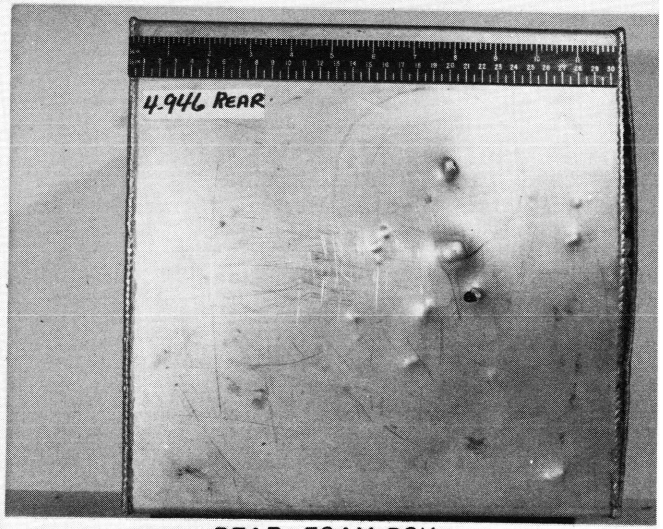

REAR FOAM BOX

ROUND NO. 4-948

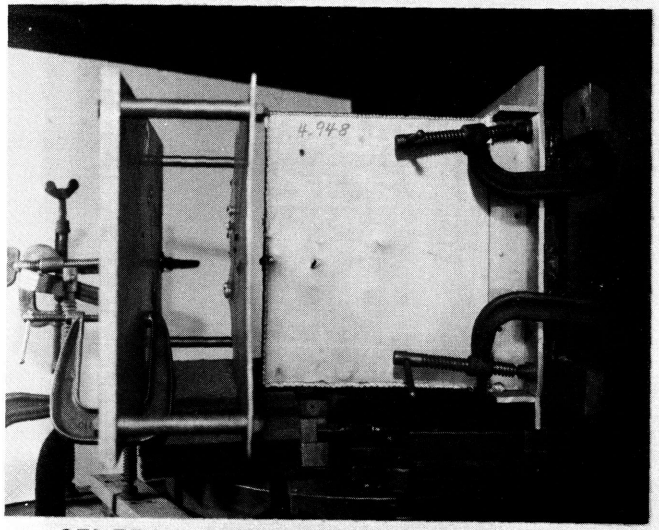

GENERAL ARRANGEMENT-AFTER FIRING

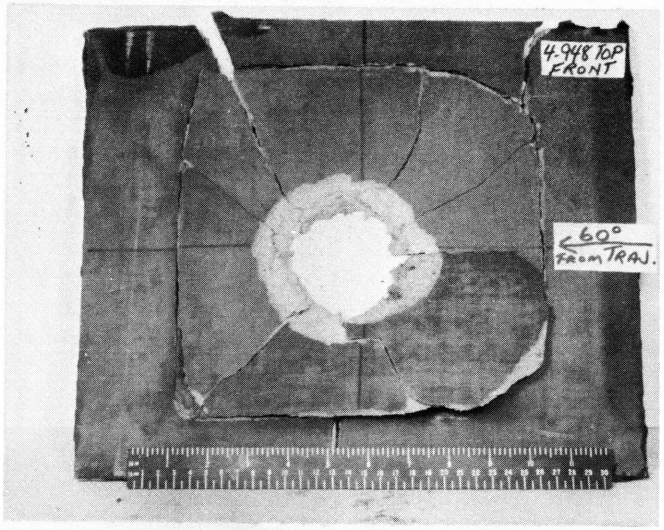

FRONT TARGET

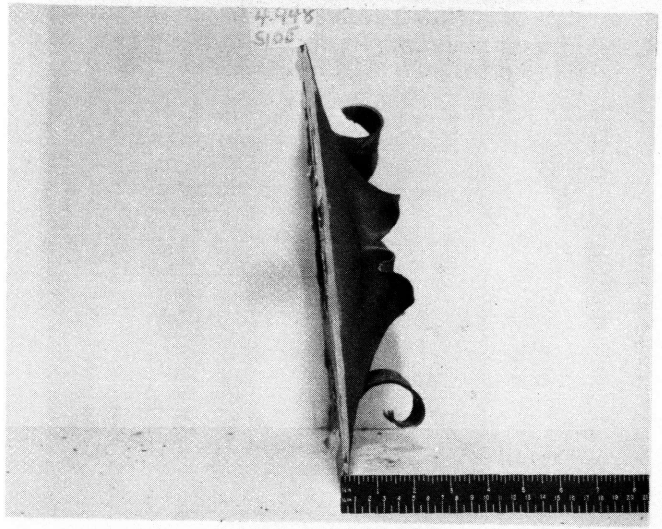

EDGE TARGET

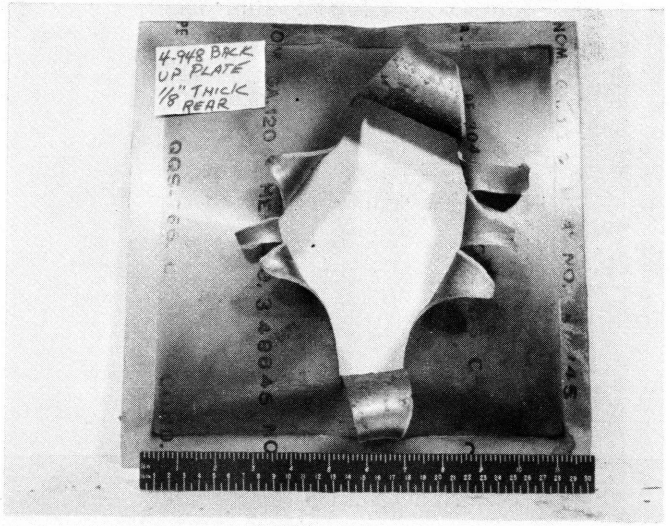

REAR TARGET

ROUND NO. 4-948 CONTINUED

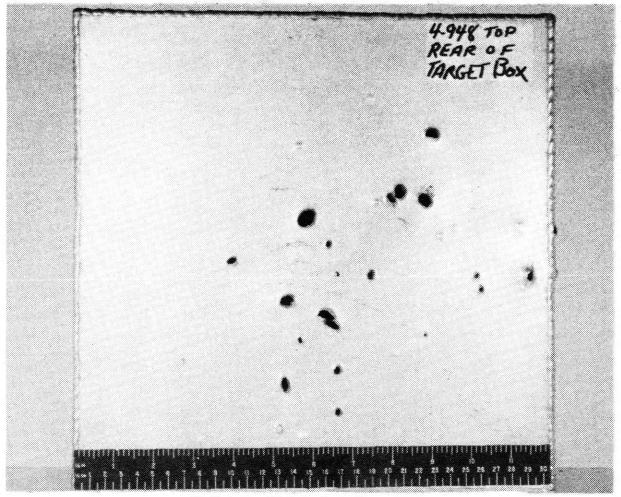

REAR TARGET BOX

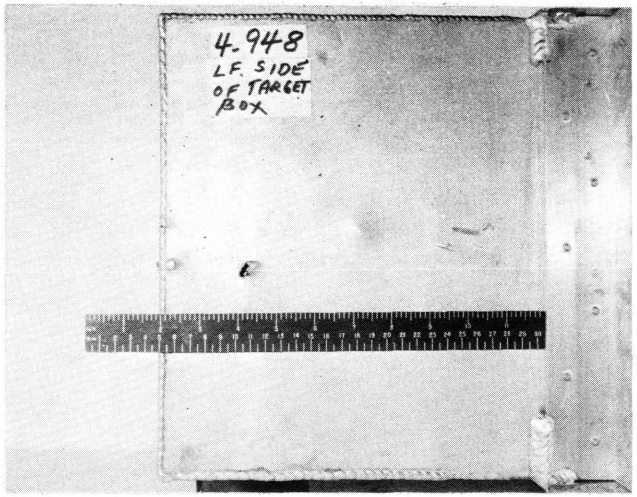

LEFT SIDE TARGET BOX

W. P. NO.1 1-1/8" PLATE
s = 2 1/8" FROM REAR OF TARGET BOX
Pm = PERFORATED

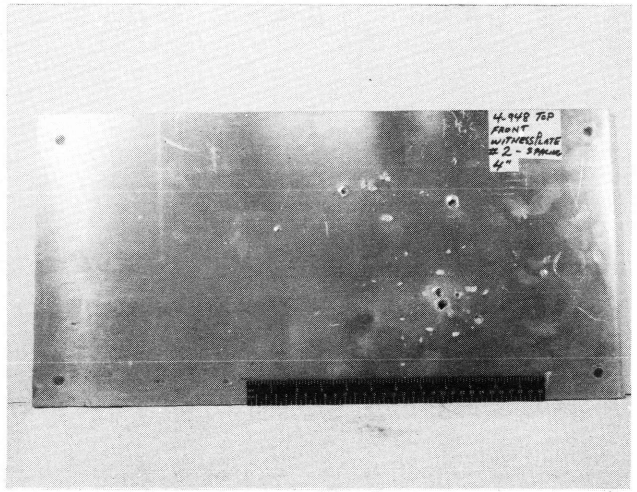

W. P. NO. 2 1-1/2" PLATE
s = 4" FROM W.P. NO.1
Pm = PERORATED

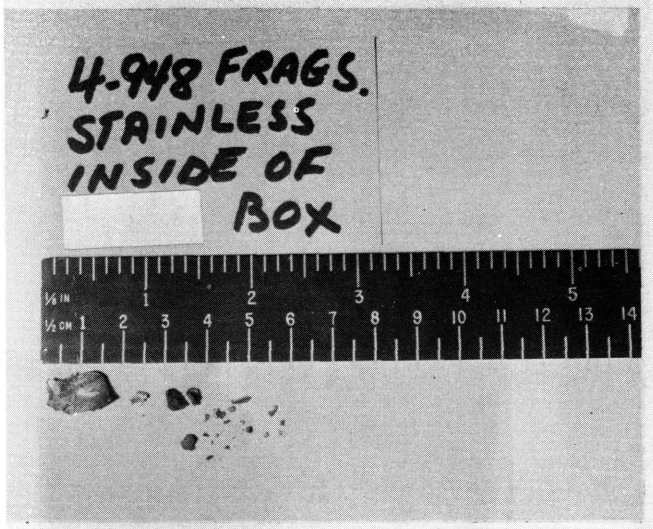

S. S. FRAGMENTS INSIDE BOX

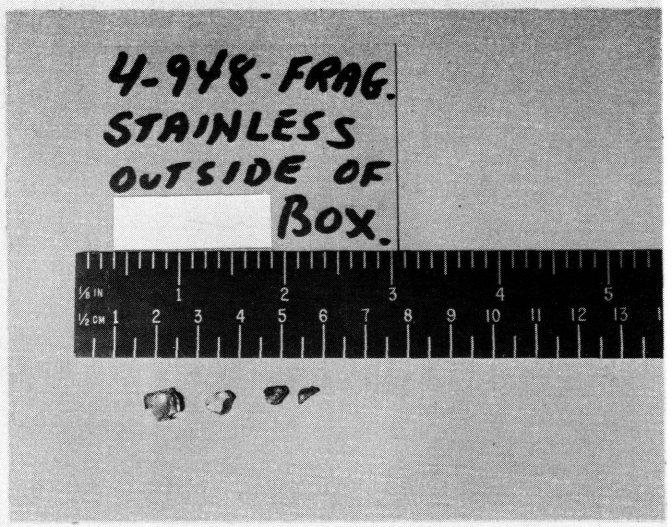

S. S. FRAGMENTS OUTSIDE BOX

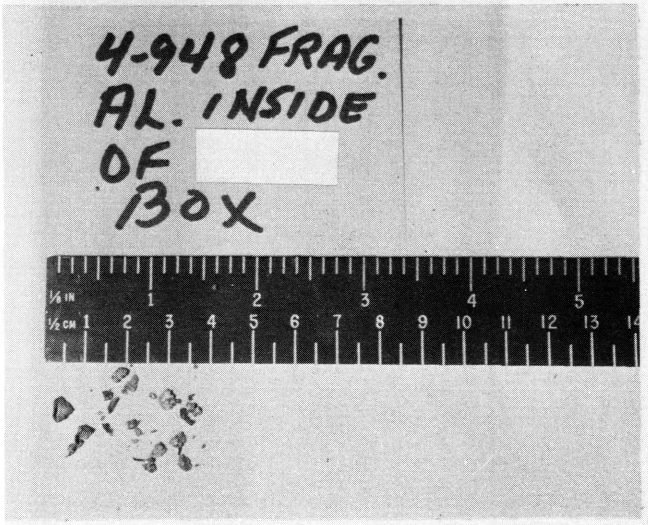

Al FRAGMENTS INSIDE OF BOX

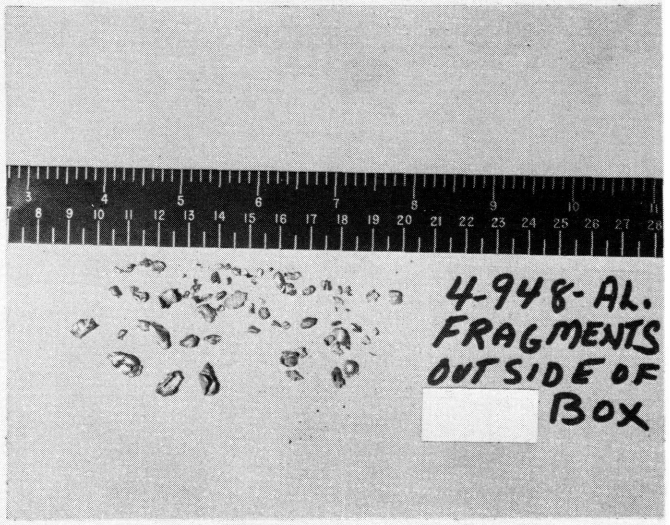

Al FRAGMENTS OUTSIDE OF BOX

ROUND NO. 4-955

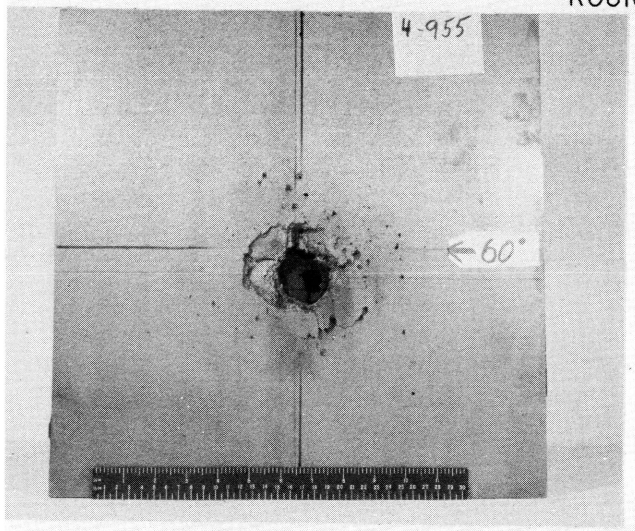

FRONT TARGET

REAR TARGET

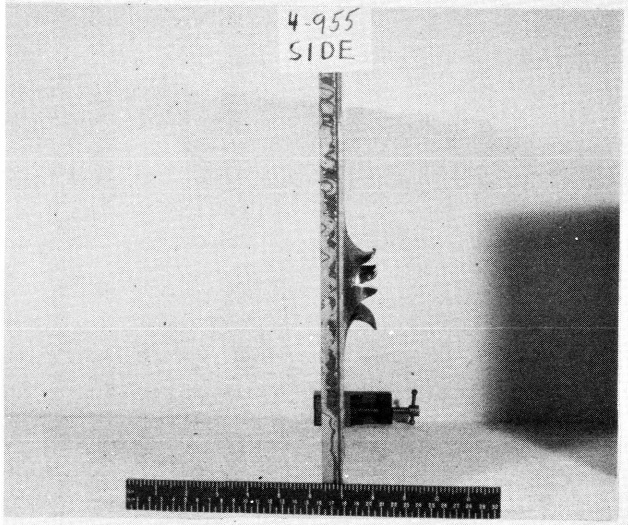

EDGE TARGET

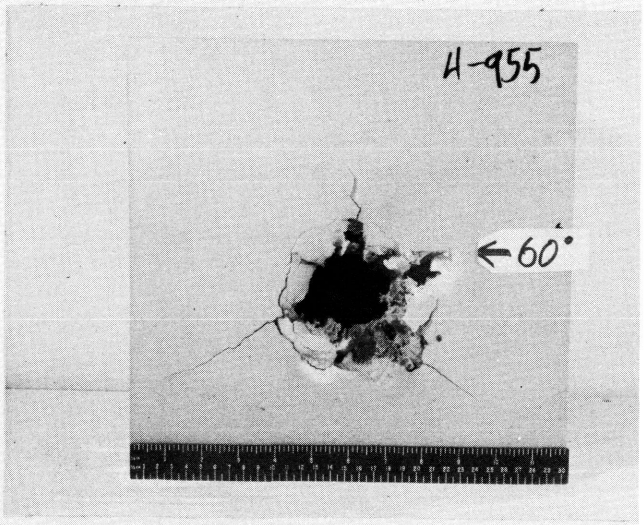

FRONT FOAM

ROUND NO. 4-949

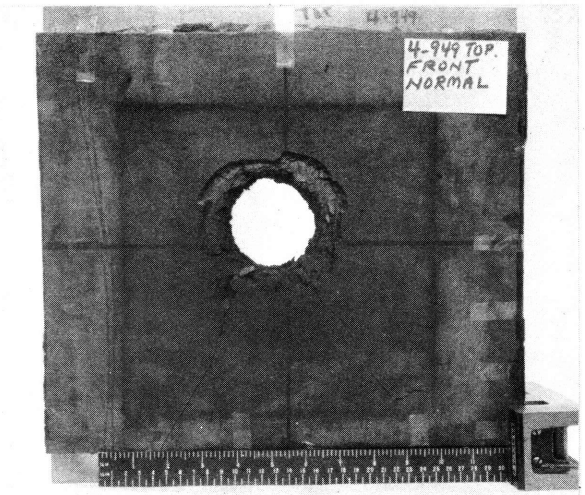

FRONT TARGET

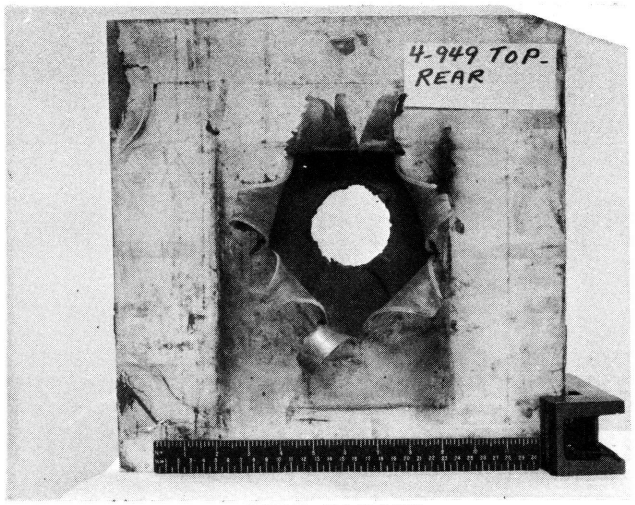

REAR TARGET

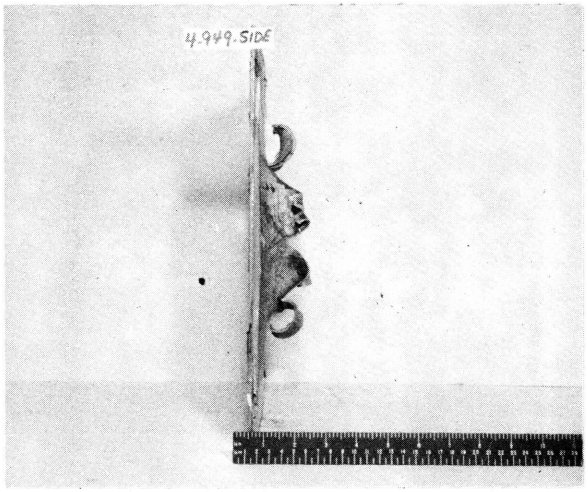

EDGE TARGET

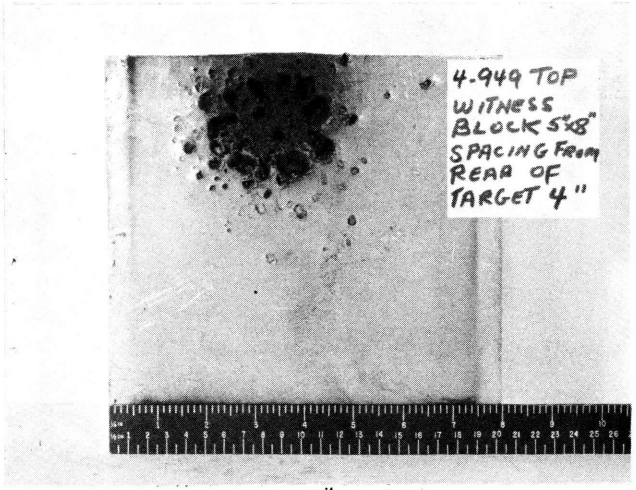

W. P. 1-5" BLOCK
s = 4" BEHIND POINT OF IMPACT
Pm = 1.37 cm

ROUND NO. 4-952

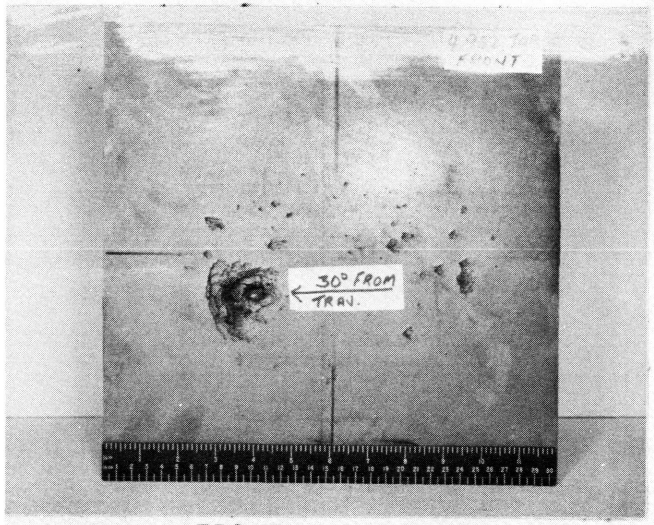

FRONT TARGET

REAR TARGET

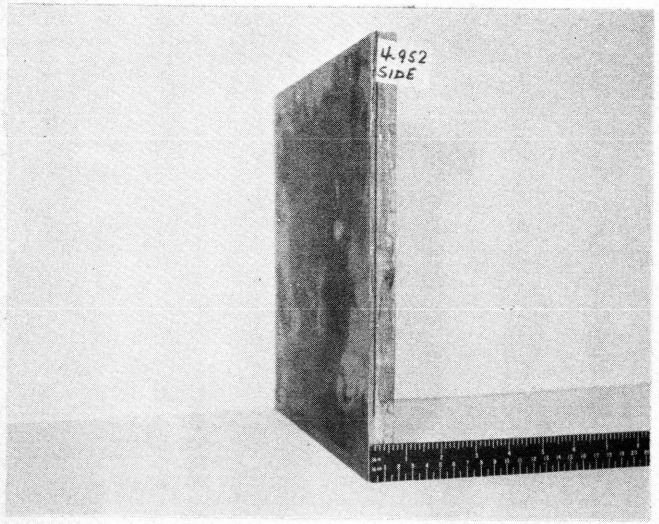

EDGE TARGET

TABLE A

IMPACT CHARACTERISTICS IN ABLATIVE STRUCTURES

Round No	Page No (Appendix A)	TARGET			PROJECTILE						ABLATIVE MATERIAL										BACK-UP		REMARKS
		Ablative Material Size (in)	Back-up Thickness (in)	Angle De-grees	Size (in)	Material	Mass (gms)	Impact Velocity (km/sec)	Normal Com-ponent of Vel (km/sec)	Impact Energy & Energy Using Normal Velocity (kj)	Penetration (cm)	Hole Dimensions (cm)		Minimum Dia (cm)	Area (cm^2)	Diameter (cm)	Front Spall Dimensions (cm)		Rear Spall Dimensions (cm)		Hole Dimensions (cm)		
												Major	Minor				Major	Minor	Major	Minor	Major	Minor	
4-939	B-15	12 x 12 x 9/16 Ph Ref L	0 125 Al 2024-T3	90	Sphere 0 312 Dia	Steel R C 65	2 04	5 151	-	27 063	Complete Perf	5 2	5 1	4 7	18 52	4 9	7 5	7 5	-	-	10 1	8 9	
1-1-98	B-16	24 x 24 x 1/2 Ph Ref L	0 125 Al 2024-T3	90	Sphere 0 312 Dia	Steel R C 65	2 031	7 477	-	56 800	Complete Perf	5 5	5 3	4 6	20 07	5 1	13 4	11 5	7 9	7 6	18 0	12 3	
4-940	B-17	12 x 12 x 9/16 Ph Ref L	0 125 Al. 2024-T3	90	Sphere 0 232 Dia	Uranium 8-1/2% Mo	1 882	5 128	-	24 745	Complete Perf	4 9	4 5	4 3	16 65	4 6	9 3	8 1	-	-	8 2	6 9	8" Dia Al tube used as spacer between target and W P
4-947	B-18	12 x 12 x 9/16 Ph Ref L	0 125 Al 2024-T3	90	Sphere 0 437 Dia	Al 2017-T4	2 001	4 885	-	23 875	Complete Perf	5 9	5 9	5 0	22 19	5 3	9 1	8 0	-	-	11 0	9 6	Spacer prevented complete petaling
1-1-99	B-19	24 x 24 x 1/2 Ph Ref L	0 125 Al 2024-T3	90	Sphere 0 437 Dia	Al 2017-T4	1 981	7 678	-	58 392	Complete Perf	6 8	6 4	5 1	28 13	6 0	12 3	11 1	-	-	24 1	15 5	
4-959	B-20	12 x 12 x 17/32 Ph Ref L	0 125 Al 2024-T3	90	Sphere 0 593 Dia	Nylon	2 041	5 041	-	25 933	Complete Perf	6 3	5 5	4 3	20 52	5 1	8 0	7 7	8 0	6 7	12 2	12 2	Ablative partially delaminated
4-954	B-21	12 x 12 x 1/2 Ph Ref L	0 125 Steel 4130	90	Sphere 0 593 Dia	Nylon	2 044	6 782	-	47 007	Complete Perf	7 1	7 1	5 9	33 03	6 5	12 0	10 5	9 2	7 9	19 0	15 6	Back-up partially separated from ablative and cracked to edge
4-960	B-22	16 x 20 x 1/2 Ph Ref L	0 125 Al 2024-T3	90	Sphere 0 593 Dia	Nylon	2 039	6 742	-	46 341	Complete Perf	6 9	6 8	6 1	33 36	6 5	11 6	10 7	-	-	18 5	16 0	
4-956	B-23	12 x 12 x 9/16 Ph Ref L	0 125 Al 2024-T3	90	Sphere 0 593 Dia	Nylon	2.052	6 450	-	42 684	Complete Perf	7 3	7 0	5 7	34 45	6 6	11 7	11 2	9 4	8 0	19 0	17 5	Ablative partially delaminated
4-957	B-24	20 x 16 x 1/2 Ph Ref L	0 125 Al 2024-T3	90	Sphere 0 593 Dia	Nylon	2 033	6 301	-	40 358	Complete Perf	6 4	6 4	5 8	29 16	6 1	11 1	10 3	8 3	7 6	15 7	14 6	Ablative partially delaminated
1-1-108	B-25	24 x 24 x 1 Glass Cloth L/	0 25 Steel 4130	90	Sphere 0 520 Dia	Al 2024-T3	3 356	7 760	-	101 045	Complete Perf	8 2	8 2	-	37 29	6 9	27 0	22 7	-	-	7 8	4 4	Target obtained from Firestone Tire & Rubber Co
CBA-6	B-26	48 x 48 x 1-9/16 Ph Ref L	0 25 Steel 4130	45	Sphere 2 45 Dia	Al 2024-T3	358 7	4 580	3 239	3762 117 1881 582	Complete Perf	37 0	33 0	32 0	927 73	34 4	80 33	54 2	-	-	91 44	73 66	Ablative and Back-up separated
1-1-82	B-27	24 x 24 x 1 Ph Ref L	0 25 Steel 1016	90	Sphere 0.75 Dia	Al 2017-T4	10 10	5 302	-	141 962	Complete Perf	14 2	13 4	11 6	126 46	12 7	30 0	-	18 4	17 4	17 5	16 4	No fragments hit witness plate
1-1-83	B-28	24 x 24 x 1 Spauldite	0 25 Steel 1016	90	Sphere 0 76 Dia	Al 2017-T4	10 15	6 124	-	190 330	Complete Perf	10 5	9 9	7 8	66 39	9 19	34 7	20 8	14 1	13 8	23 4	17 8	No bonding between abl & B-U 6 fragments perforated 1/2" 1100F Al witness plate 10" from target
1-1-97	B-29	24 x 24 x 1/2 Ph Ref L	0 125 Steel 4130	10	Sphere 0 530 Dia	Steel R C 65	9 993	4 018	0 698	80 665 2 434	Complete Perf	3 54	8 2	5 7	-	29 81	6 16	11 0	9 5	-	-	Bulged*	1 77 cm
1-1-86	B-30	24 x 24 x 1 Ph Ref L	0 25 Steel 1016	90	Sphere 0 421 Dia	Steel R C 65	4 993	7 033(a)	-	123 485 3 722	Complete Perf	10 3	10 0	8 7	68 90	9 36	39 0	38 0	-	-	7 0	6 0	(a) Velocity taken from 1-1-87 with same gun conditions
1-1-87	B-31	24 x 24 x 1-1/32 Ph. Ref L	0 25 Steel 1016	10	Sphere 0 421 Dia	Steel R C 65	4 993	7 033(a)	1 221	123 485	Complete Perf	2 8	2 5	2 1	-	3 94	2 2	7 1	6 7	-	-	Bulged*	0 74 cm
1-1-93	B-32	28 x 28 x 1-3/32 Ph Ref L	0 25 Al 2024-T3	90	Sphere 0 421 Dia	Steel R C 65	4 991	5 582	-	77 757	Complete Perf	6 5	6 1	4 3	25 74	5 7	17 4	16 6	-	-	15 0	11 6	
1-1-94	B-33	24 x 24 x 1-3/32 Ph Ref L	0 25 Steel 4130	40	Sphere 0 421 Dia	Steel R C 65	4 991	7 033a	4 52	123 435 51 007	6 28	8 9	7 4	5 5	37 03	6 9	21 0	16 7	-	-	Bulged*	2 37 cm	Partially delaminated & broke out to the edge (a) Velocity taken from RD 1-1-87
1-1-95	B-34	20 x 20 x 1-3/32 Ph Ref L	0 25 Steel 4130	90	Sphere 0 312 Dia	Steel R C 65	2 027	7 001	-	49 676	5 36	5 5	3 7	-	18 52	4 9	22 0	16 1	-	-	Bulged*	1 32 cm	
1-1-88	B-35	10 x 14 x 1-3/32 Ph Ref L	0 25 Steel 4130	90	Sphere 0 232 Dia	Uranium 8-1/2% Mo	1 888	5 396	-	27 486	Complete Perf	4 0	3 6	2 6	8 90	3 37	21 4	16 3	-	-	2 5	1 7	Ablative split vertically & delaminated
1-1-103	B-36	20 x 20 x 1-3/32 Ph Ref L	0 25 Steel 4130	90	Sphere 0 324 Dia	Uranium 8-1/2% Mo	5 08	5 315	-	71 753	Complete Perf	11 4	10 7	-	93 10	10 9	18 0	16 9	-	-	6 8	5 5	Target delaminated & split vertically from center to top
1-1-104	B-37	20 x 20 x 1-3/32 Ph Ref L	0 25 Al 2024-T3	90	Sphere 0 324 Dia	Uranium 8-1/2% Mo	5 058	5 359	-	72 774	Complete Perf	5 7	5 1	3 8	18 78	4 9	17 5	14 9	-	-	9 9	8 0	Back-up separated from ablative
1-1-105	B-38	20 x 20 x 1-3/32 Ph. Ref L.	0 25 Magnesium	90	Sphere 0 324 Dia	Uranium 8-1/2% Mo	5 068	5 265	-	70 243	Complete Perf	5 9	5 7	4 2	19 81	5 0	17 0	11 2	-	-	8 4	8 1	
1-1-107	B-39	24 x 24 x 1/2 Ph Ref L	0.125 Al 2024-T3	10	Sphere 0 324 Dia	Uranium 8-1/2% Mo	5 096	5 240	0 91	69 962 2 11	Complete Perf	7 0	4 6	-	23 68	5 5	9 5	8 5	-	-	18 6	12 6	Nothing hit witness plate from back of target
1-1-110	B-40	20 x 20 x 1/2 Ph Ref L	0 125 Al 2024-T3	10	Sphere 0 421 Dia	Steel R C 65	4.992	5 970	1 036	88 960 2 679	3 62	5 2	3 4	-	13 03	4 1	7 5	5 8	-	-	Bulged*	1 8 cm	
1-1-106	B-41	12 x 24 x 1/2 Ph Ref L	0 125 Steel 4130	25	Sphere 0 250 Dia	Steel R C 65	1 045	7 393	3 124	28 558 5 099	Cracked Back-up	5 3	5 3	4 9	18 65	4 9	14 6	12 2	-	-	Bulged*	1 6 cm	Back-up cracked open—no fragment came through back of target
4-961	B-42	12 x 24 x 1/2 Ph Ref L	0 125 Steel 4130	90	Sphere 0 250 Dia	Steel R C 65	1 045	1 973	-	2 034	Complete Perf	1 08	1 08	-	1 13	1 2	2 75	2 2	-	-	1 3	1 07	
4-958	B-43	12 x 12 x 17/32 Ph Ref L.	0 125 Steel 4130	90	Sphere 0 250 Dia	Steel R C 65	1 045	2 191	-	2 508	Complete Perf	1 2	1 1	-	1 42	1 3	2 8	2 5	-	-	1 8	1 6	
4-930	B-44	14 x 10 x 1/2 Ph Nyl L	0 125 304 S S	90	Sphere 0 500 Dia	Al 2017-T4	3 01	5 624	-	47 602	Complete Perf	7 4	7 2	-	40 39	7 2	11 3	10 9	-	-	16 9	13 0	Simulated nose cone Ablative separated from back-up & broke into 5 pieces
4-931	B-45	14 x 10 x 1/2 Ph Nyl L	0 125 304 S S	45	Sphere 0 500 Dia	Al 2017-T4	3 01	5 128	3 626	39 576 19 788	Complete Perf	10 9	10 9	-	98 84	11 2	12 6	12 6	-	-	17 0	13 0	Simulated nose cone (part. of sabot hit abl)
4-934	B-46	14 x 12 x 1/2 Ph Nyl L	0 125 304 S S	45	Sphere 0 490 Dia	Al 2024-T3	2 828	4 500	3 182	28 634 14 317	Complete Perf	9 9	7 3	-	55 75	8 4	12 5	10 3	-	-	11 1	8 7	Simulated nose cone ablative cracked out to edge
4-935	B-47	Ph Nylon L Nose Cone	0 125 304 S S	45	Sphere 0 490 Dia	Al 2024-T3	2 824	3 782	2 674	20 197 10 096	Did not perf back-up	8 9	8 6	5 7	54 71	8 3	11 0	8 3	-	-	-	-	Nylon cone came loose from liner Extensive cracking of ablative
4-937	B-48	Ph Nylon L Nose Cone	0 125 304 S S	70	Sphere 0 490 Dia	Al 2024-T3	2 828	3 787	3 540	20 065 17 720	Complete Perf	7 4	7 0	-	47 04	7 7	10 1	8 0	-	-	7 1	6 7	Ph nylon cracked down to base and came loose from liner
4-938	B-49	Ph Nylon L Nose Cone	0 125 304 S S	70	Sphere 0 490 Dia	Al 2024-T3	2 819	3 944	3 706	21 925 19 359	Complete Perf	8 3	7 5	6 0	-	-	9 5	8 8	-	-	-	-	Ablative on opposite side of cone cracked from impact Vertical crack to base from impact
4-944	B-50	12 x 14 x 1/2 Ph Nyl L	0 125 304 S S	45	Sphere 0 480 Dia	Al 2024-T3	2 649	4 587	3 243	27 868 13 93	Did not perf back-up	9 2	8 8	-	71 17	9 5	10 4	10 1	-	-	Bulged*	3 9 cm	7 lbs /cu ft 12" cube urethane foam behind target
4-945	B-51	12 x 14 x 1/2 Ph Nyl L	0 125 304 S S	60	Sphere 0 480 Dia	Al 2024-T3	2 649	5 415	4 689	38 837 29 121	Complete Perf	10 1	9 7	-	79 23	10 0	12 4	12 0	-	-	10 7	8 2	7 lbs /cu ft 12" cube urethane foam behind target
4-946	B-52	12 x 14 x 1/2 Ph Nyl L	0 125 304 S S	60	Sphere 0 480 Dia	Al 2024-T3	2 648	5 678	4 917	42 685 32 010	Complete Perf	10 5	10 0	-	86 65	10 5	12 9	12 1	-	-	15 5	11 4	3 1 lbs /cu ft 12" cube urethane foam behind target
4-948	B-53	12 x 14 x 1/2 Ph Nyl L	0 125 304 S S	60	Sphere 0 480 Dia	Al 2024-T3	2 65	5 839	5 057	45 174 33 885	Complete Perf	7 6	7 0	-	40 33	7 2	12 9	11 7	-	-	20 2	13 5	No foam in box behind target, extensive cracking of ablative
4-955	B-54	16 x 16 x 1/2 Ph Ref L	0 125 Al 2024-T3	60	Sphere 0 343 Dia	Steel R C 65	2 705	3 795	3 286	19 479 14 604	Complete Perf	4 7	4 4	4 0	14 65	4 3	8 4	7 6	6 9	5 9	7 3	6 1	3 1 lbs /cu ft urethane foam behind target
4-949	B-55	12 x 14 x 1/2 Ph Nyl L	0 125 304 S S	90	Sphere 0 480 Dia	Al 2024-T3	2 64	5 101	-	34 347	Complete Perf	6 4	6 4	6 1	30 84	6 3	11 3	11 3	-	-	14 1	11 6	Ablative separated from back-up
4-952	B-56	12 x 12 x 9/16 Ph Ref L	0 125 Steel 4130	30	Sphere 0 250 Dia	Steel R C 65	1 046	3 123	1 562	5 101 1 276	2 35	3 1	2 5	-	5 03	2 5	5 3	4 7	-	-	Bulged*	65 cm	

*Maximum height of back-up bulge measured from rear surface of back-up

DOCUMENT NO. 64SD629

This document contains 86 pages
Copy number 108 of 198 copies.

HYPERVELOCITY KILL MECHANISMS PROGRAM (U)

Aerothermal Phase

Semi-Annual Progress Report
For Period Ending

31 March 1964

SPONSORED BY

Advanced Research Projects Agency
Ballistic Missile Defense Systems Branch
ARPA Order No. 149-60
Program Code No. 3730

This research was supported by the Advanced Research Projects Agency, Ballistic Missile Defense Systems Branch, and was monitored by the U. S. Naval Research Laboratory (Code 6240) under Contract No. Nonr 3295-(00)(X).

CONTRACTOR, GENERAL ELECTRIC COMPANY
RE-ENTRY SYSTEMS DEPARTMENT

D. E. Nestler, Technical Director
E. Richardson, Program Manager

GENERAL ELECTRIC

RE-ENTRY SYSTEMS DEPARTMENT
A Department Of The Missile and Space Division
3198 Chestnut Street, Philadelphia 4, Penna.

LAN: 5610-16-1

CONTENTS

ILLUSTRATIONS

ILLUSTRATIONS (Cont'd)

TABLES

SUMMARY

Under the aerothermal phase of the program, GE-RSD has continued thermal and structural studies intended to develop the technology required to assess re-entry induced thermostructural kill of a re-entry vehicle which has been perforated by hypervelocity impact.

During the past six months, emphasis has been placed on the understanding of the "coupled flow" internal heating mechanism associated with single perforations in unvented compartments. Tests of instrumented axisymmetric models containing machined perforations were conducted at Mach 10 in AEDC Tunnel C, and in the Malta Rocket Exhaust Facility at Mach 3. The internal heating from these two series of tests in widely different environments correlated well with turbulent shear layer theory for the entire range of perforation sizes which were tested ($A/V^{2/3}$ from .01 to 0.27). The Malta series of tests included an actual impact perforation for comparison with the machined perforations. A convenient correlation equation was derived from the analysis of these tests, to replace the time-consuming evaluation of the formal theory.

The protective effect of a lightweight urethane foam filler within a model having a simulated impact perforation was determined in a Malta rocket exhaust test. The "effective heat of ablation" concept was used to characterize the performance of the foam.

The internal heating correlation derived from the AEDC and Malta tests was applied to a slender sharp-cone advanced target vehicle having a ballistic coefficient of 3000 lb/ft^2. Generalized results were obtained for the value of $A/V^{2/3}$ required to cause thermal kill of several representative vehicle structure designs, for any size vehicle having the stated geometry and re-entry conditions. The use of the currently accepted impact perforation correlation demonstrated an extreme sensitivity of lethal fragment mass to the size of the vehicle being attacked.

The flow characteristics of machined and impact perforation orifices having supersonic tangential approach flow were determined in a test program performed in AEDC Tunnel D. The measured flow rates were predicted reasonably well by a viscous modification to inviscid expansion theory. Pressure surveys of the supersonic internal jets formed from tangential approach flow revealed the two-dimensional jet decoy characteristic of such jets. This characteristic had been hypothesized previously as an explanation for low impingement heat fluxes obtained in ground and flight tests of perforated models. Oil film photographs disclosed the existence of two general types of internal jet development, depending on the orifice pressure ratio.

Structural studies concentrated on the effects of relatively large openings on the load capability of cylinders subjected to axial and bending loads. A modest test program was conducted in support of an analytical method devised to predict the effects of such openings. Mylar cylinders having various sizes and shapes of cutouts were subjected to axial and bending loads to determine buckling limits. Correlation of test results indicated that modifications to the prediction method are required.

No data were obtained from the ICBM piggyback flight experiment conducted on the WAC program because of booster malfunction.

I. AEDC TUNNEL C INTERNAL HEATING TESTS

A. Facility and Model Description

A series of seven tests were performed in AEDC Tunnel C to determine the internal heating to models having simulated impact perforations. Tunnel C is a 50-inch diameter, continuous, closed-circuit wind tunnel with an axisymmetric, contoured Mach 10 nozzle. Nominal operating conditions for the tests were as follows:

Reservoir pressure P_o	1800 psia
Reservoir temperature T_o	1900°R
Free-stream Mach no. M_∞	10
Free-stream Reynolds no. Re_∞	2.2×10^6 per ft.
Test medium	Air
Stagnation enthalpy h_s	475 btu/lb

The test model (Figures 1 and 2) was a 10 degree semi-vertex angle sharp cone with a 15-inch base diameter. The model was the same model used previously for tests in the Cornell Aeronautical Laboratory wave superheater tests described in Reference 1, but with a sharp nose tip and with base plate modifications required for tunnel mounting. The model contained a double shell construction, with an inner stainless steel shell of .030 inch wall thickness forming the test cavity and serving as a heat flux calorimeter, and an outer stainless steel shell of 0.150 inch wall thickness forming the external configuration and structural support. The shells were separated by a 0.3125 inch insulating air space, which also provided space for routing instrumentation leads. Inserts which fit in the cone wall provided a variety of simulated perforation sizes at two diametrically opposite locations. The vertical surfaces of the perforations were cylindrical, rather than locally perpendicular to cone meridians. A vent orifice was also provided in the base plate and could be either open or closed.

Instrumentation consisted of 34 thermocouples and 8 pressure taps in the inner shell, and 9 thermocouples and 3 pressure taps in the outer shell. A copper slug calorimeter was installed in the downstream side of each insert, as shown in Figure 1. A total pressure probe rake was mounted to the base of the model to measure boundary layer profiles at the aft end of the model downstream of the perforations. Thermocouples were recorded for 40 seconds after start of run, at a sampling rate of 20 per second. Pressure readings were obtained over a 3 minute interval required for obtaining equilibrium in the 16 ft. length of tubing involved.

B. Test Procedure

The tests which were performed are listed in Table 1. Tests 1 through 5 provided a systematic variation in perforation diameter for a single perforation, with no base plate venting. These tests varied the coupled flow parameter $A/V^{2/3}$ from .009 to .188. Run 6 provided two perforations of equal diameter located opposite each other, with no base plate venting. Run 7 provided a base plate vent for a single perforation on the cone.

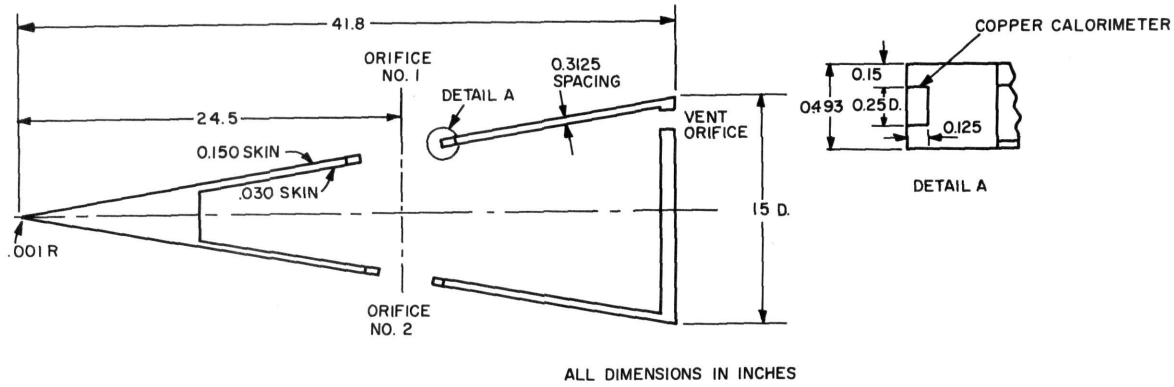

Figure 1. AEDC Tunnel C Internal Heating Model

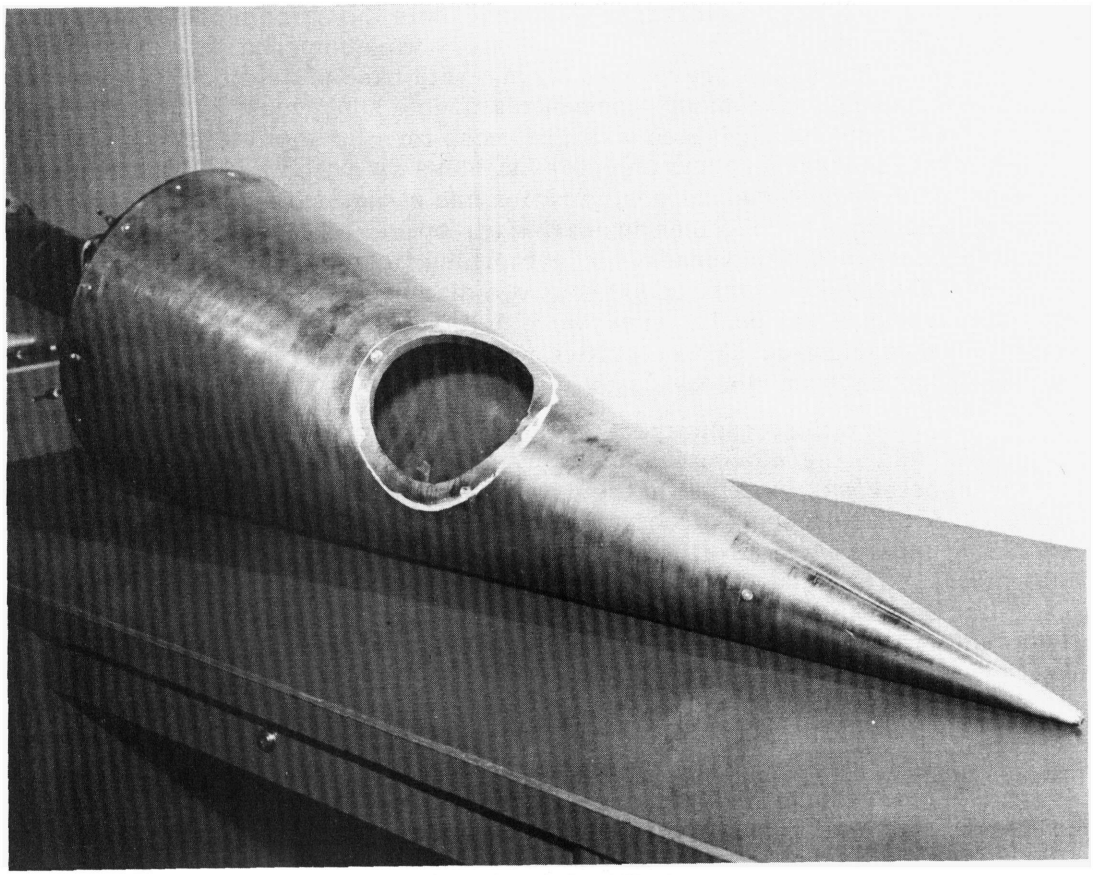

Figure 2. AEDC Tunnel C Internal Heating Model with 6.269" Diameter Perforation (prior to nose tip modification)

TABLE 1. AEDC TUNNEL C INTERNAL HEATING TEST AGENDA

Test Number	$A/V^{2/3}$	Perforation Diameters (inches)		Base Plate Vent Diameter (inches)
		No. 1	No. 2	
1	.009	1.402	-	-
2	.019	1.982	-	-
3	.047	3.144	-	-
4	.094	4.443	-	-
5	.188	6.269	-	-
6	-	3.144	3.144	-
7	-	3.144	-	1.402

A = perforation cross-section area
V = internal volume

Temperature records were used to determine heat fluxes at a time of about 3 seconds from start of test. The thin-wall one-dimensional heat flux technique was used, with evaluation being accomplished by an AEDC computer program employing a 21-point least squares fit to the data.

C. Results

Internal heat flux maps are presented for all seven runs in Figures 3 through 9. In all cases of single perforations, the maximum heat flux appears to occur on the 180 degree meridian opposite the perforation. A local maximum appears to exist at about one-quarter of the base diameter, measured from the 180 degree meridian. The heat flux patterns strongly suggest the type of flow pattern (see sketch below) inferred previously from the heat flux maps for vented models of the Wallops Island program (References 1, 2, and 3) for perforation locations away from the stagnation point.

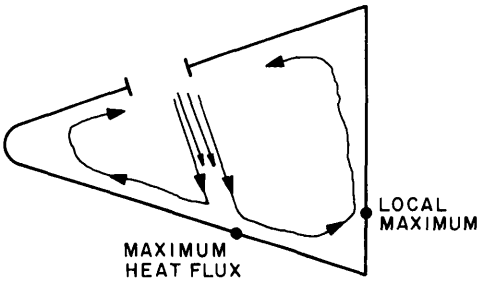

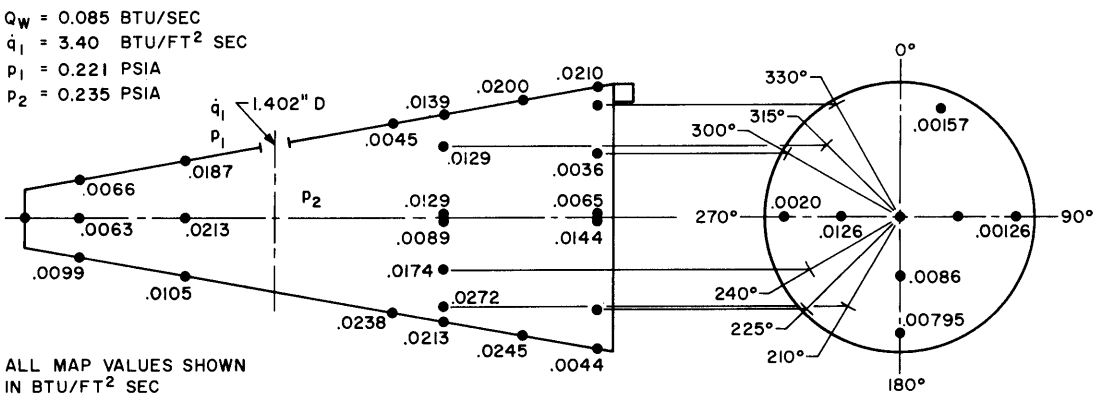

Figure 3. AEDC Test No. 1 - Heat Flux Map

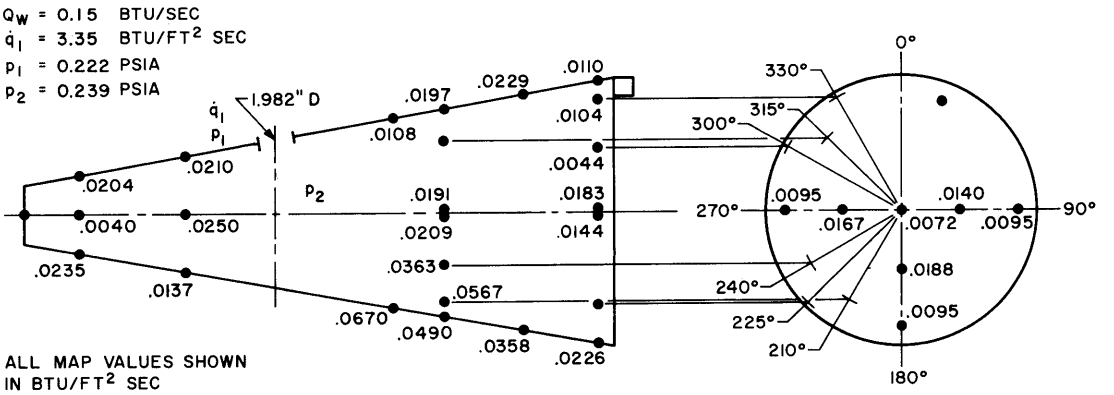

Figure 4. AEDC Test No. 2 - Heat Flux Map

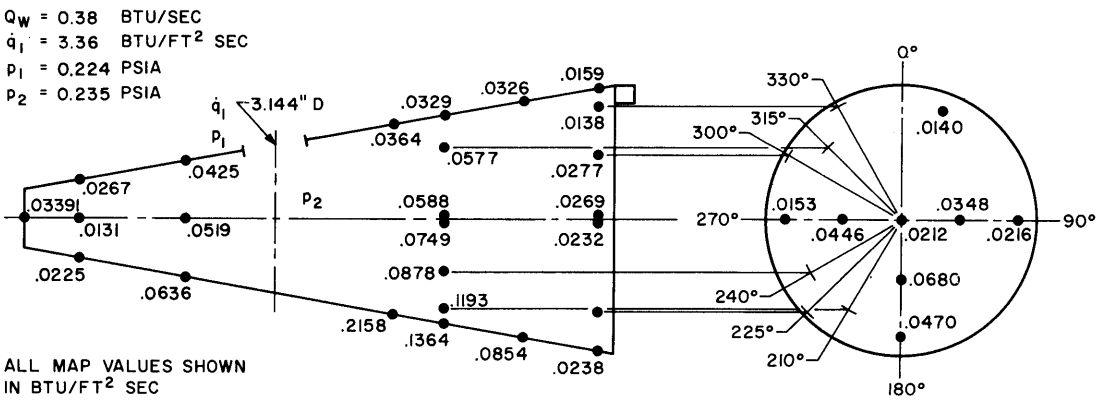

Figure 5. AEDC Test No. 3 - Heat Flux Map

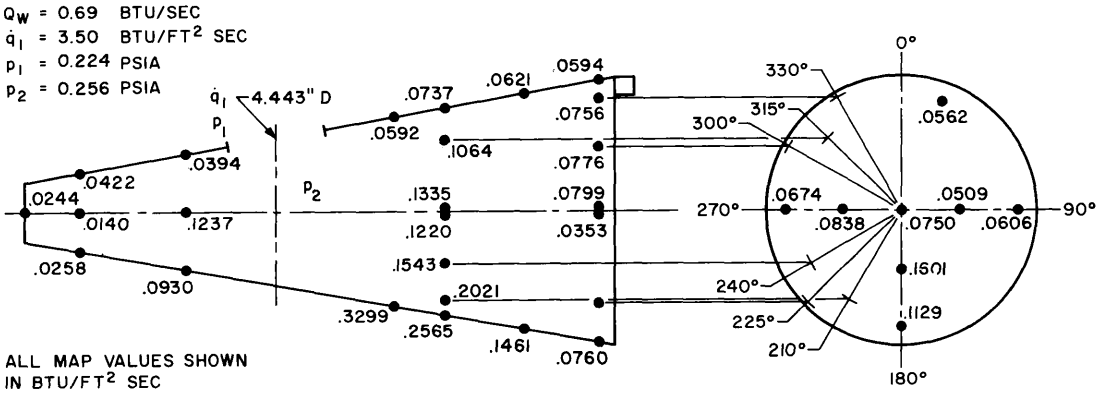

Figure 6. AEDC Test No. 4 - Heat Flux Map

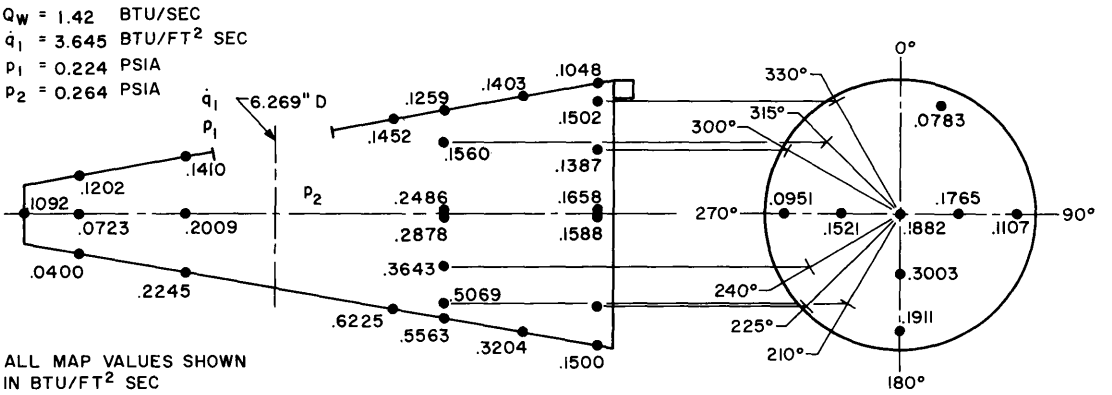

Figure 7. AEDC Test No. 5 - Heat Flux Map

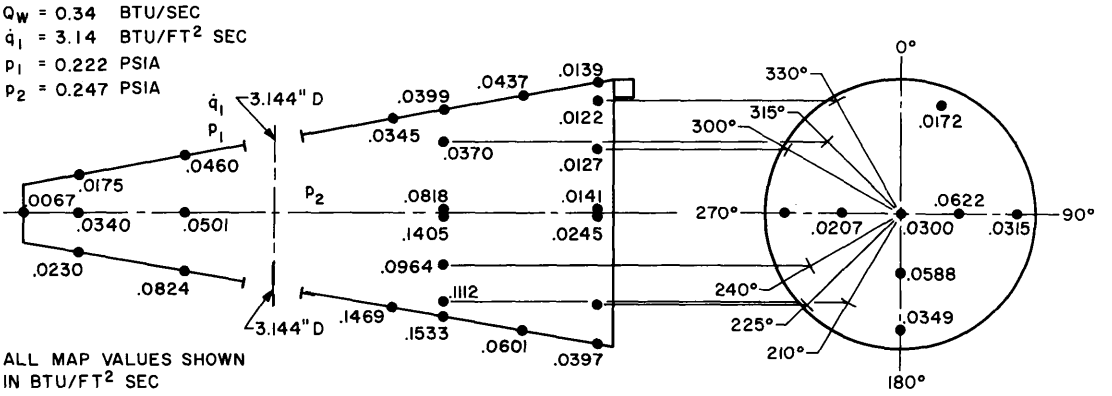

Figure 8. AEDC Test No. 6 - Heat Flux Map

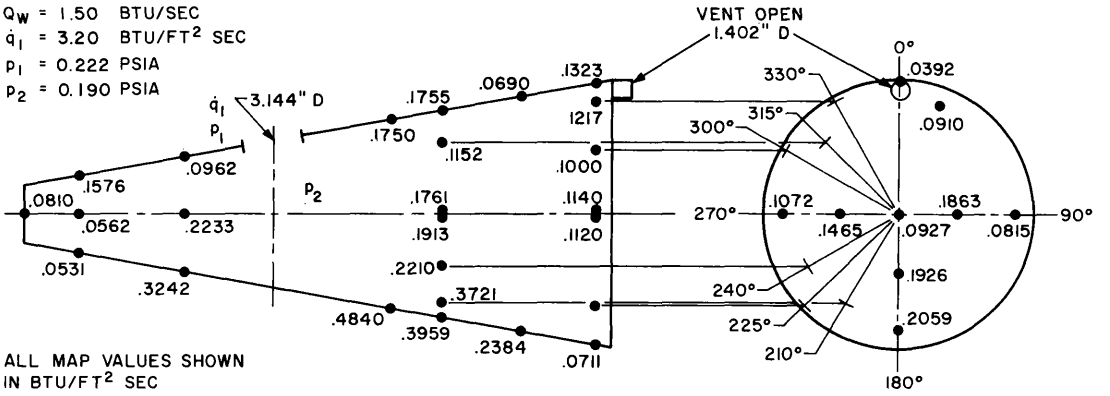

Figure 9. AEDC Test No. 7 - Heat Flux Map

In no case did high heat fluxes develop directly downstream of the perforation, such as occurred in the rocket exhaust tests conducted by the Ballistic Research Laboratory (Reference 4). Further discussion of the internal heating mechanism for single perforations is given in Appendix A.

The heat flux distributions of Figures 3 through 9 were integrated graphically over the internal surface area to obtain the total rate of heat absorption Q_W by the walls of the perforated volume. The resulting values of Q_W are listed on the respective flux maps. For Tests 1 through 5, the values of Q_W are plotted vs perforation cross-section area A in Figure 10. A remarkably consistent correlation is seen to result, considering that the values of Q_W are subject to at least ±10 percent error. Also shown in Figure 10 is the prediction of the Donaldson relation for "coupled flow" energy influx for these test conditions. The Donaldson relation is: (from Reference 5 or 6)

$$E_{in} = \frac{dE}{d\theta} = .0316 \frac{\gamma}{\gamma - 1} \, pUA \qquad (1)$$

in which:

$E_{in} = dE/d\theta$ = rate of energy addition to internal volume
γ = isentropic exponent = 1.40
p = local surface pressure = 0.22 psia
U = local surface flow velocity = 4600 ft/sec
A = perforation cross-section area

} for tests under discussion

Since Equation (1) was derived for large Mach numbers and for temperatures in the stagnant region which are small compared to the stagnation temperature in the undisturbed flow, it represents an upper limit to the expected energy influx due to steady flow turbulent mixing energy exchange. A more refined theoretical prediction can be derived from the compressible turbulent mixing analysis of Chow and Korst (Reference 7), whose results can be written as: (See Appendix A)

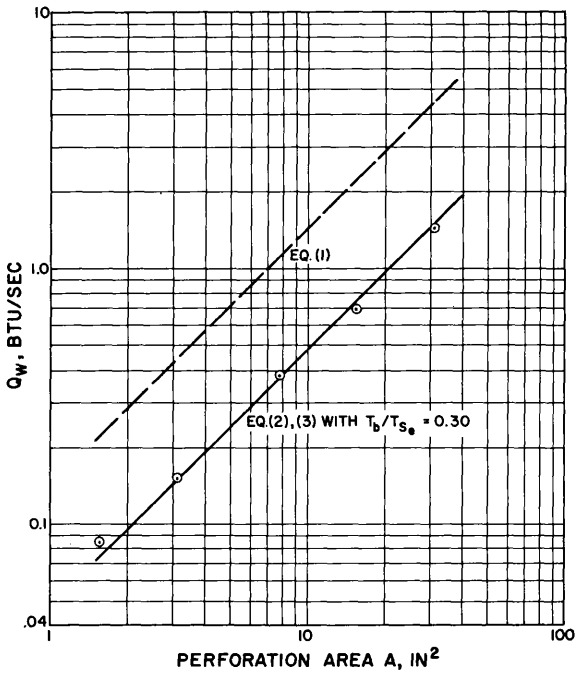

Figure 10. Results of AEDC Tunnel C Internal Heating Tests for Single Perforations and No Venting

$$E_{in} = \frac{dE}{d\theta} = \frac{\gamma}{\gamma - 1}\ pUA \left(1 - \frac{T_b}{T_{S_e}}\right) \frac{I_2(\eta_j)}{\sigma} \tag{2}$$

in which:

T_b/T_{S_e} = ratio of cavity internal air temperature to stagnation temperature of external flow

$I_2(\eta_j)$ = value of auxiliary shear layer integral below the dividing streamline

σ = similarity parameter for co-ordinate system (jet spread parameter)

Equation (2) is observed to be a more general form of Equation (1). Unfortunately, quantitative predictions using Equation (2) require a knowledge of the temperature ratio T_b/T_{S_e}. In the present series of experiments, this quantity can only be determined empirically by matching the experimental results with Equation (2). This is readily done by assuming:

$$Q_W \approx E_{in} \tag{3}$$

which is equivalent to assuming that a quasi-steady state condition exists within the model internal volume after an initial transient filling process (i.e., internal pressure and temperature are approximately constant, and all of the entering energy must be absorbed by the walls). The validity of this assumption is checked in Appendix A. By combining Equations (2) and (3), a mean value of $T_b/T_{S_e} = 0.30$ was computed by iteration for the values of Q_W shown in Figure 10. The following values were used in the calculation:

$\gamma = 1.4$
$p = 0.22$ psia
$U = 4600$ ft/sec
$\sigma = 35$ (for local Mach number of 7.1 - see Figure A-3, Appendix A)

The value of $I_2(r_j)$ is a function of T_b/T_{S_e}, and is determined as shown in Appendix A.

As shown in Figure 10, the Chow-Korst analysis (Equation 2) with $T_b/T_{S_e} = 0.30$ gives a reasonable match to the measured values of Q_W. The deviation of the data from a slope of unity, when plotted as Q_W vs A, indicates that T_b/T_{S_e} is increasing slightly as A increases. This trend can be rationalized theoretically by considering that if A is increased, the energy influx rate E_{in} attempts to increase in direct proportion to A, per Equation (2); but the wall heat absorption rate Q_W cannot increase as rapidly as A, due to the 0.8 exponent on decayed jet velocity which arises in the jet impingement turbulent heat flux relation. Hence, the internal air will equilibrate at a relatively higher temperature T_b for larger values of A.

It is noteworthy that the value of Q_W for two diametrically opposite perforations is not twice the value of Q_W for a single perforation of the same diameter. As shown in Figures 5 and 8, two diametrically opposite perforations resulted in a slightly smaller value of Q_W than that for a single perforation. Apparently the jet-like circulation induced by the external flow past each perforation causes a collision of jet flows in the middle of the internal volume, with more thorough mixing and heating of the air prior to impingement on the walls.

Also of interest is the large increase in internal heating caused by the opening of the base plate vent. A comparison of Figures 5 and 9 shows that for the same size perforation on the cone, a vent having a diameter of one-half the perforation diameter caused an increase in Q_W to four times its value for no venting. An analysis of this test was performed, using the measured pressures and heat rate to the wall in the quasi-steady venting analysis developed in References 1 and 2. Assuming choked outflow through the vent with an orifice coefficient of 0.8, the following quantities result from simultaneous solution of the continuity and energy balance equations:

T_2	Mean internal temperature	$620^{\circ}R$
m_1	Inlet flow rate (m_1 = exit flow rate m_2)	.005 lb/sec
$m_1 h_s$	Rate of energy influx	2.25 btu/sec
f_W	Fraction of energy influx absorbed by internal walls $f_W = \frac{Q_W}{m_1 h_s}$	0.67

This value of f_W compares well with the values of 0.65 and 0.75 obtained for the ground and flight tests of the Wallops Island program for an inlet orifice 60 degrees from the stagnation point, with venting on the cone (References 1, 2, and 3). The inlet flow rate is about 45 percent of the value predicted by the inviscid Prandtl-Meyer expansion theory, probably due to approach flow viscous effects. (See Section V).

Average internal and external static pressures are also shown in the heat flux maps of Figures 3 through 9. In all runs, the internal pressure was very uniform, with approximately ±1 percent variation existing among the 6 internal pressure readings. It should be noted that the internal pressure exceeds the external pressure for tests with no vent open in the base plate. The ratio of internal to external static pressure increases with perforation diameter from about 1.05 for the smaller perforations to 1.18 for the largest perforation. This increase in internal pressure is caused by the addition of energy to a closed volume, as discussed in Appendix A.

The temperature responses of the calorimeter slugs on the downstream surface of the perforations (Figure 2) were used to determine initial heat fluxes near the beginning of the test runs. These heat fluxes were converted to heat transfer coefficients, which are plotted vs perforation diameter in Figure 11 for runs with no venting. Also shown in Figure 11 are laminar and turbulent theoretical predictions based on an approximate method. In brief, the method employs flat plate heat flux relations to the boundary layer which develops along the downstream surface, as shown in the following sketch.

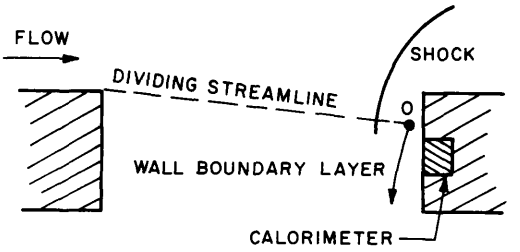

Local properties were determined by isentropic expansion to internal pressure from stagnation conditions corresponding to the dividing streamline of the separated turbulent shear layer. The location of this streamline was determined by the method of Chow and Korst (Reference 7), as discussed in Appendix A. Since the local Reynolds number Re_s based on distance measured from O in the sketch is on the order of 1000, a laminar wall boundary layer should exist. The agreement of laminar theory with experiment is excellent for the three smaller perforations. For the two larger perforations, the lower experimental values suggest transition to a turbulent boundary layer, possibly due to increased turbulence levels associated with longer separated flow paths before re-attachment. However, the data for these two runs is in question because of the calorimeter slugs popping out during the run, due to expansion of the RTV bond used to install the slugs. (Air gaps existed around the slugs for the three smaller perforations.)

The analysis of this group of tests is complete, with the exception of a comparison of maximum internal heat fluxes with a theoretical prediction employing jet diffusion and jet impingement heat flux relations.

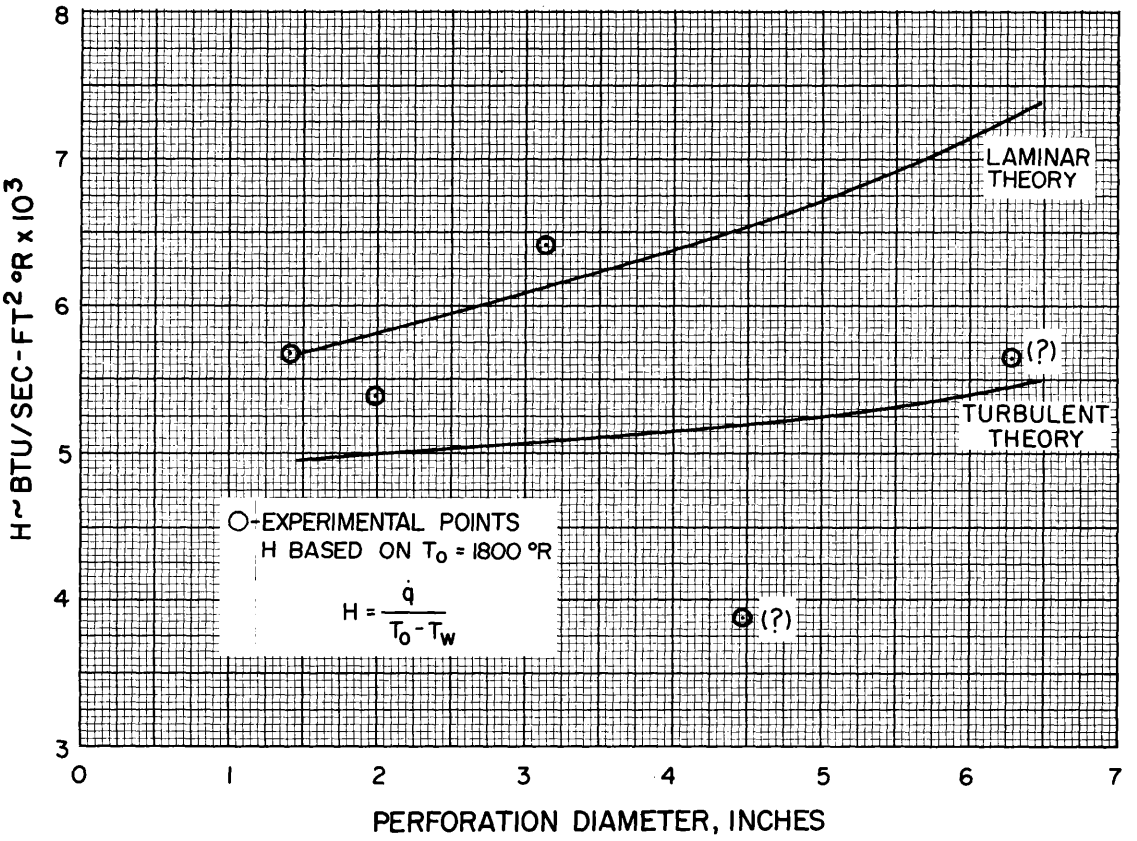

Figure 11. Heat Transfer to Downstream Perforation Surface-AEDC Tunnel C Data

II. MALTA ROCKET EXHAUST INTERNAL HEATING TESTS

A. Facility and Model Description

A series of seven tests are being conducted in Pit Four of the Malta Rocket Exhaust Facility to determine the internal heating to open and foam-filled models having simulated and actual impact perforations. The Malta Pit Four Facility utilizes a 15 inch exit diameter contoured shockless nozzle on a liquid propellant rocket motor body. The fuel is ethyl alcohol with liquid oxygen as an oxidizer. Nominal operating conditions for the tests are as follows:

Chamber pressure	600 psia
Chamber temperature	6000°R
Chamber enthalpy	3250 btu/lb
Free-stream Mach number	3.0
O/F ratio	2.1
Test medium	Exhaust gases ($\gamma = 1.20$, mol. wt. = 25)
Model stagnation pressure	.170 psia

The test models are all of a common design, being blunt cones of 10^{o} 45' semi-vertex angle and 9.8 inch base diameter. The heat shields are laminated phenolic nylon, bonded by Epon 6 to Inconel 600 structures which form the test cavities and serve as heat flux calorimeters. The heat shield thickness provides sufficient insulation to prevent any structure temperature rise due to external heating for run times up to 15 seconds. A section drawing of the model is shown in Figure 12, which gives dimensions of interest. A photograph of a model on the test stand is shown in Figure 13.

B. Test Procedure

The test agenda being followed is shown in Table 2. In all cases, a single perforation exists on the conical portion of the model, located as shown in Figure 12. Tests 1 through 4 consider the internal heating to open internal volumes, while Tests 5 through 7 investigate the response of internal foam fillers containing simulated impact cavities. Instrumentation for Tests 1 through 5 consists of 28 to 30 chromel-alumel thermocouples on the backface of the Inconel structure, with leads routed in the bond space between the heat shield and structure, and 4 pressure taps in the backplate of the model. In addition, Tests 1 and 2 included 2 stainless steel slug calorimeters installed in stainless steel ring inserts, as shown in Figure 12.

TABLE 2. MALTA ROCKET EXHAUST INTERNAL HEATING TEST AGENDA

Test Number	$A/V^{2/3}$	Perforation Diameter (inches)	Type of Perforation	Internal Foam	Run Time (sec.)
1	.11	2.5	Machined	None	5
2	.27	4.0	Machined	None	5
3	.18	3.25*	Impact	None	5
4	.07	2.0	Machined**	None	5
5	-	4.0	Machined	Urethane, ρ = 7.8 lb/ft^3	10
6	-	4.0	Machined	Urethane, ρ = 3.0 lb/ft^3	15
7	-	4.0	Machined	Urethane, ρ = 3.0 lb/ft^3	15

A = initial perforation cross-section throat area
V = initial free internal volume
*Effective diameter of equivalent area circle
**The machined perforation for Test Number 3 contained a bevelled approach contour (see Figures 12 and 23). All other machined perforations were cylindrical orifices.

C. Results

To date, Tests 1 through 5 have been completed, with Tests 6 and 7 scheduled for April 1964. Pre-test and post-test photographs of test models for Tests 1 through 5 are shown as Figures 14 through 26. The white deposits seen in Figures 15 and 17 are combustion residue of the RTV gap filler material which ignited upon shutdown. Among the more significant post-test visual observations which can be made are the following:

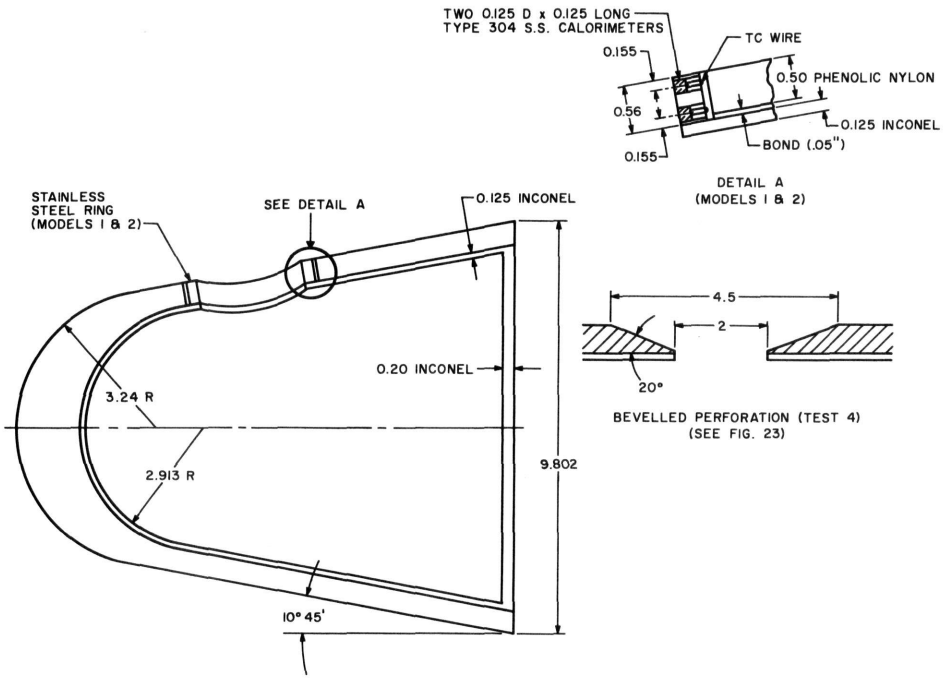

Figure 12. Malta Rocket Exhaust Internal Heating Model

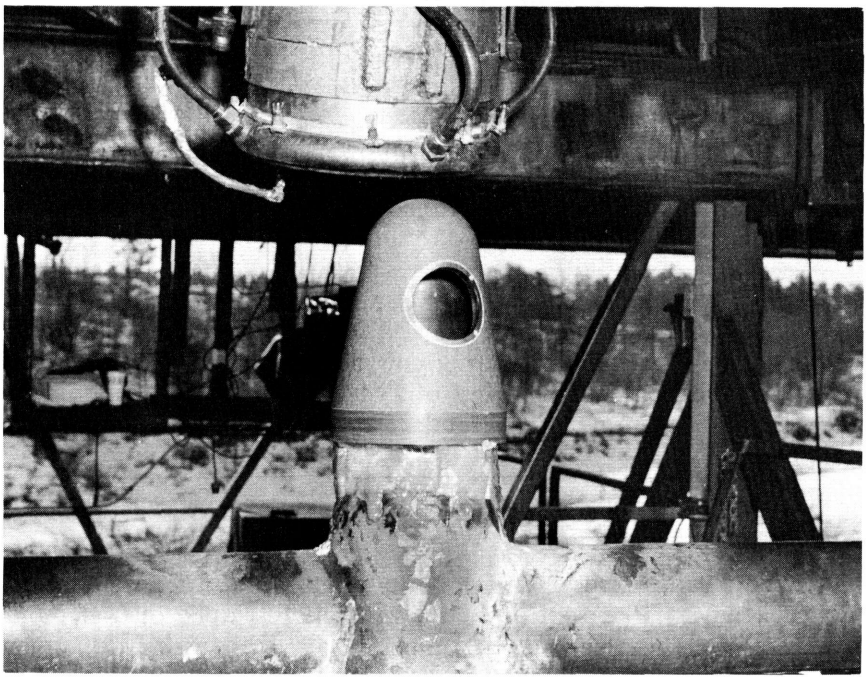

Figure 13. Malta Test Model Number Two on Test Stand

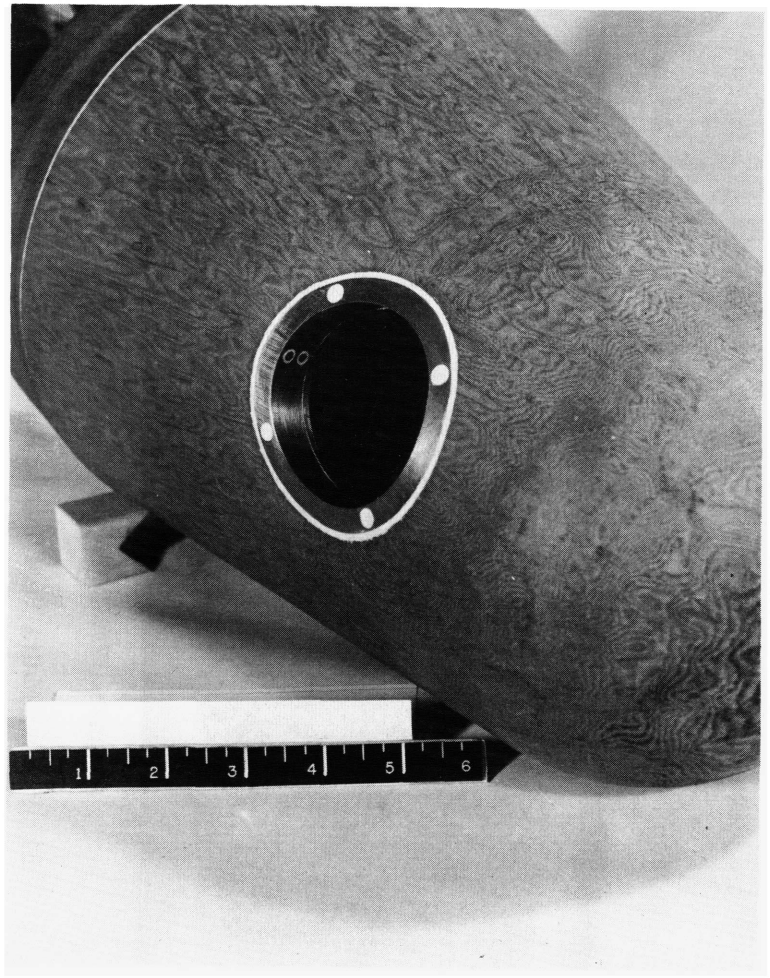

Figure 14. Malta Test One - Pre-test View

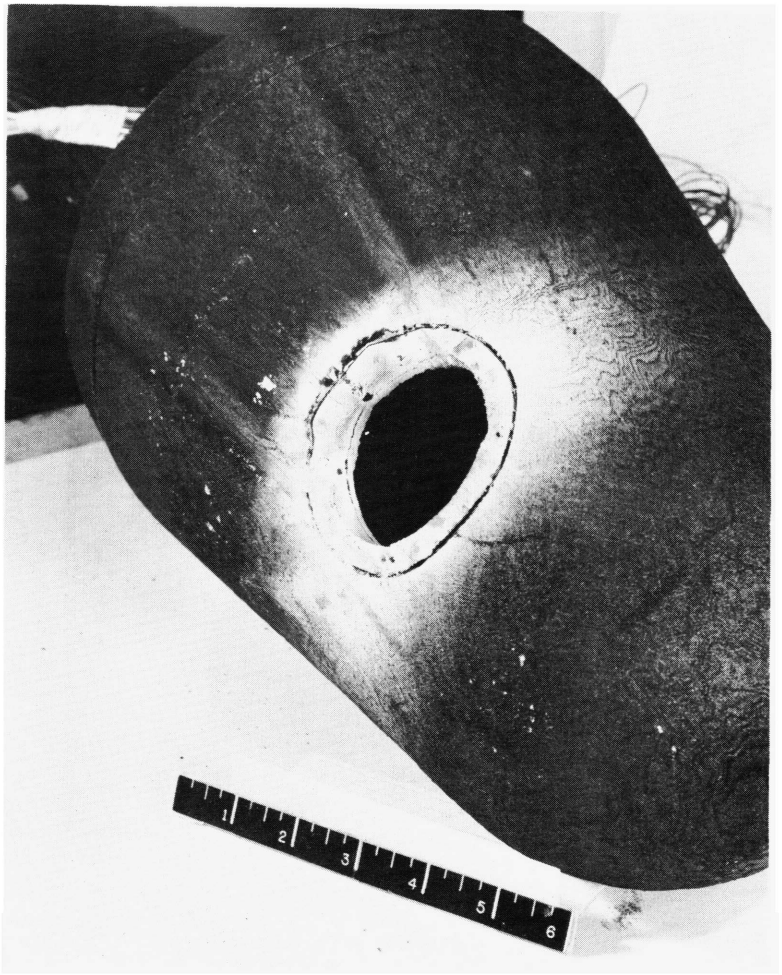

Figure 15. Malta Test One - Post-test View

Figure 16. Malta Test Two - Pre-test View

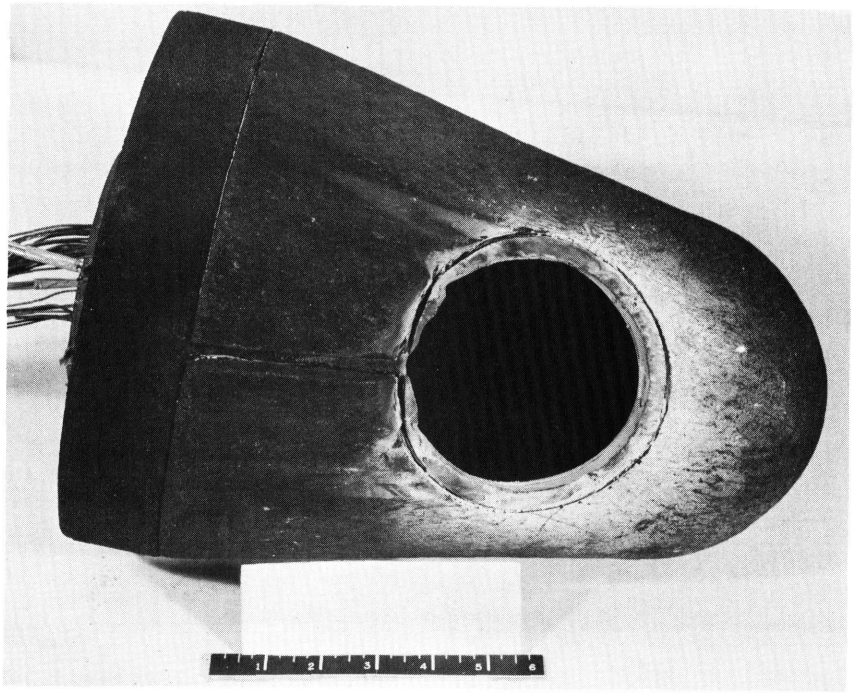

Figure 17. Malta Test Two - Post-test View

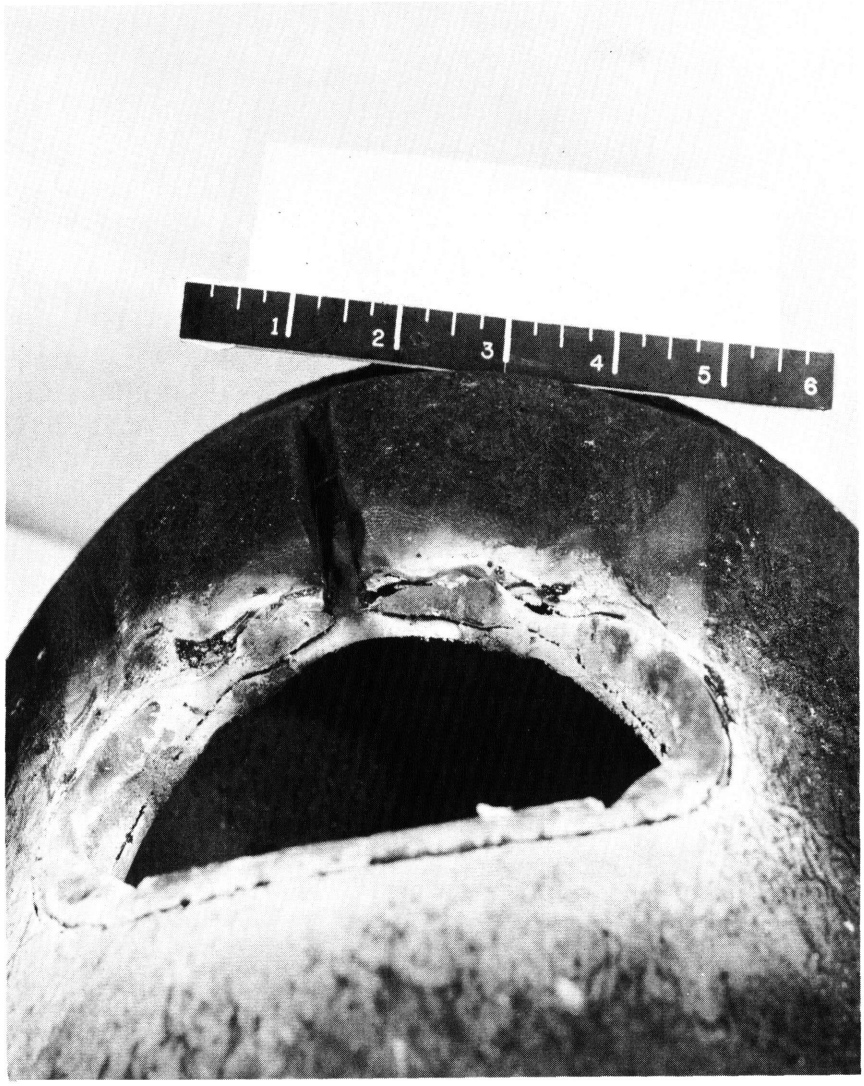

Figure 18. Malta Test Two - Close-up of Crack

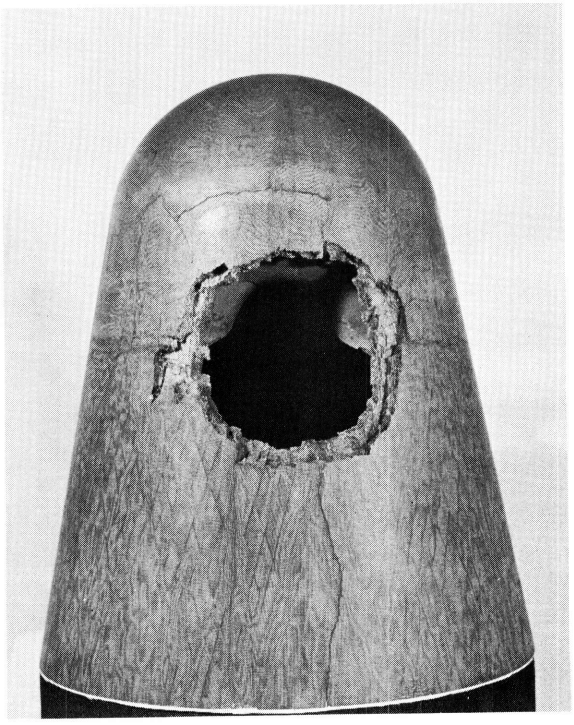

Figure 19. Malta Test Three - Pre-test View

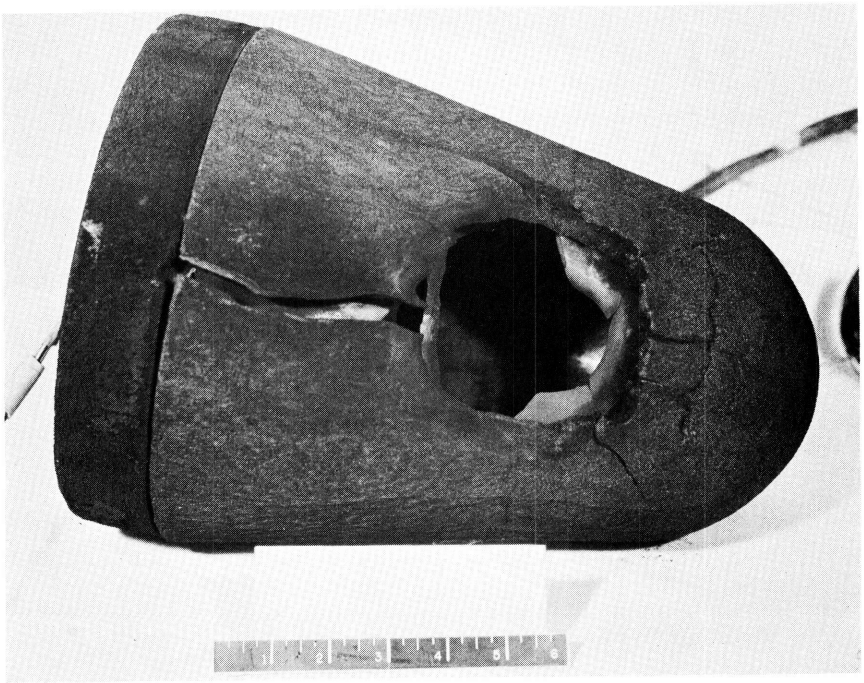

Figure 20. Malta Test Three - Post-test View

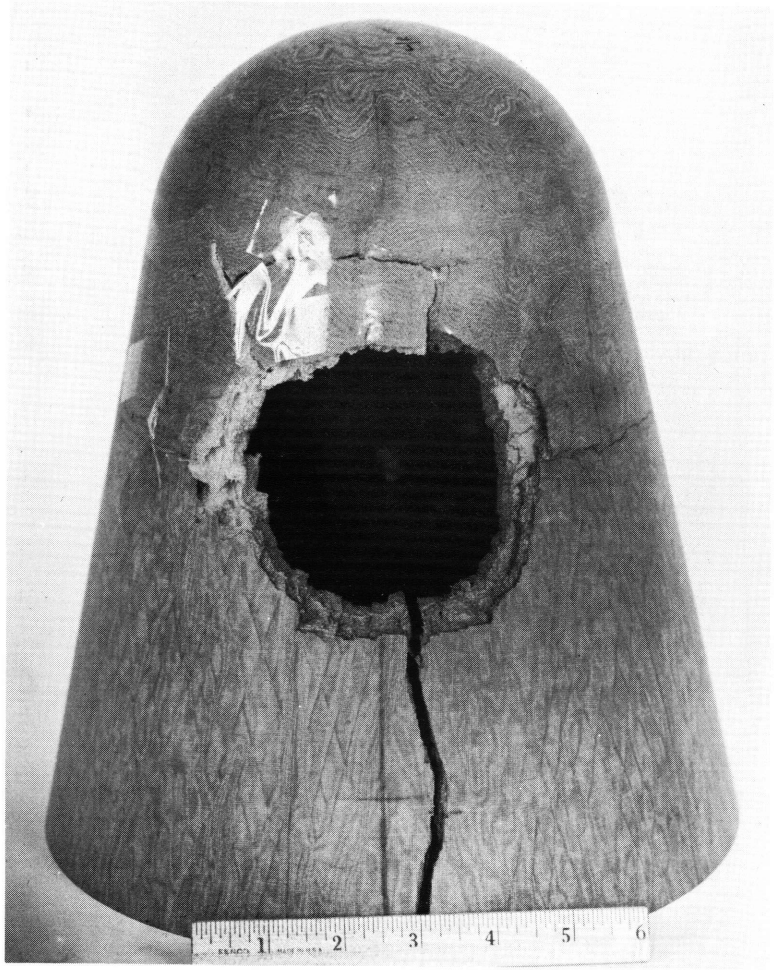

Figure 21. Malta Test Three - Heat Shield After Impact

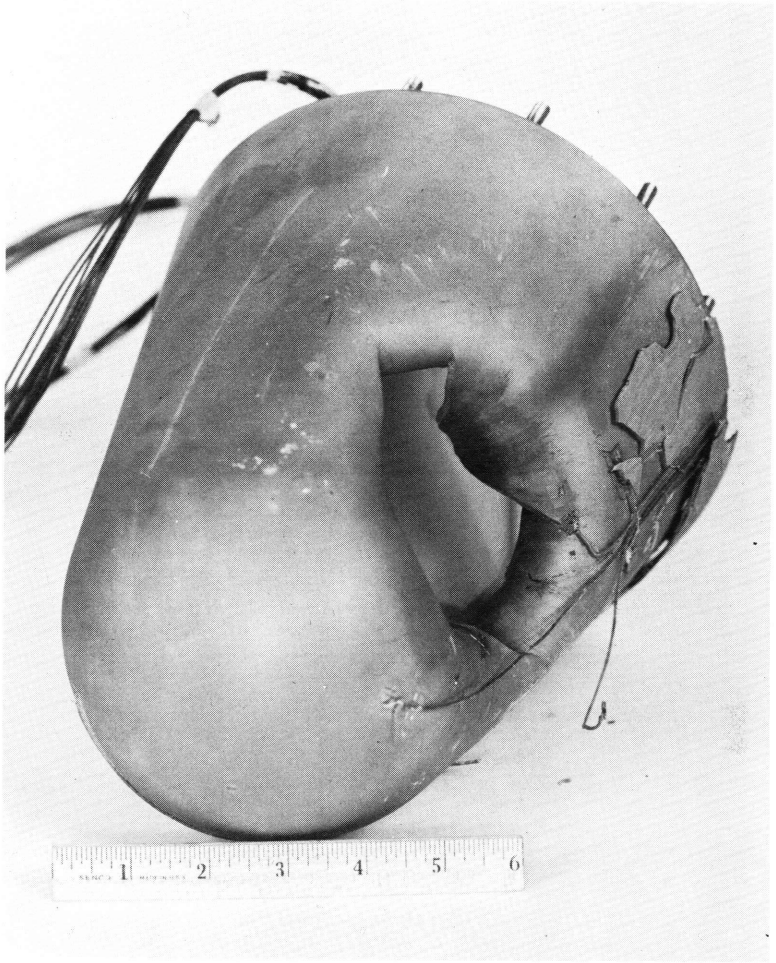

Figure 22. Malta Test Three - Structure After Impact

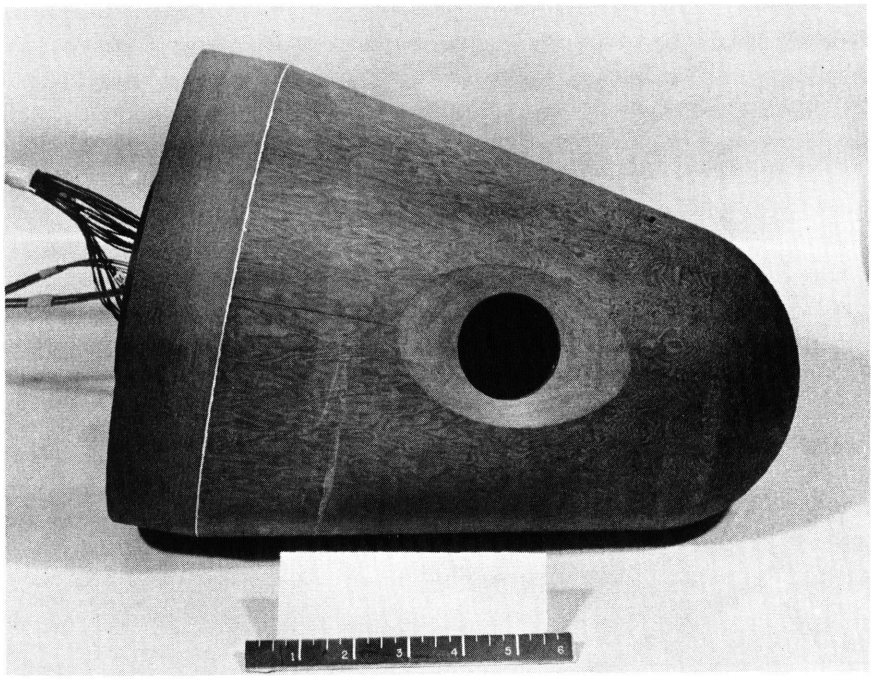

Figure 23. Malta Test Four - Pre-test View

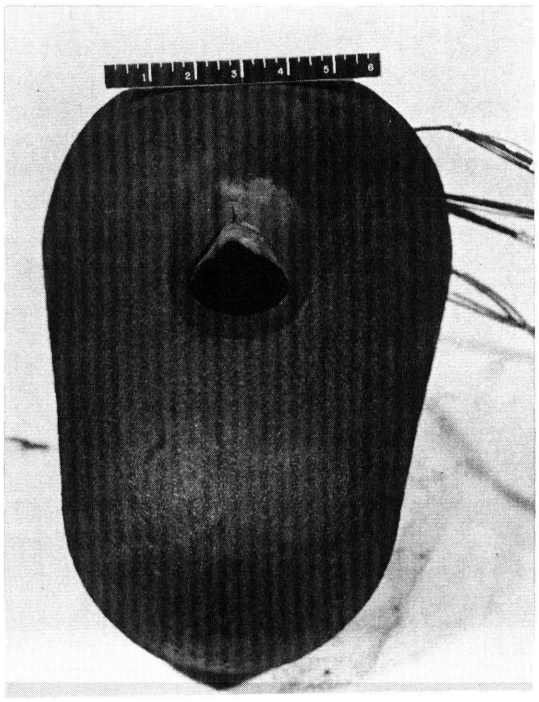

Figure 24. Malta Test Four - Post-Test View

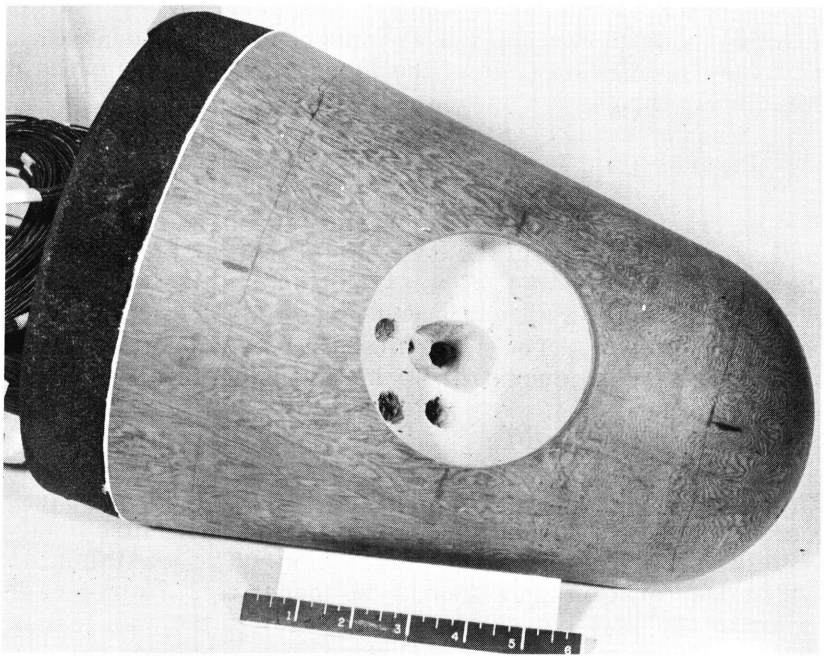

Figure 25. Malta Test Five - Pre-test View

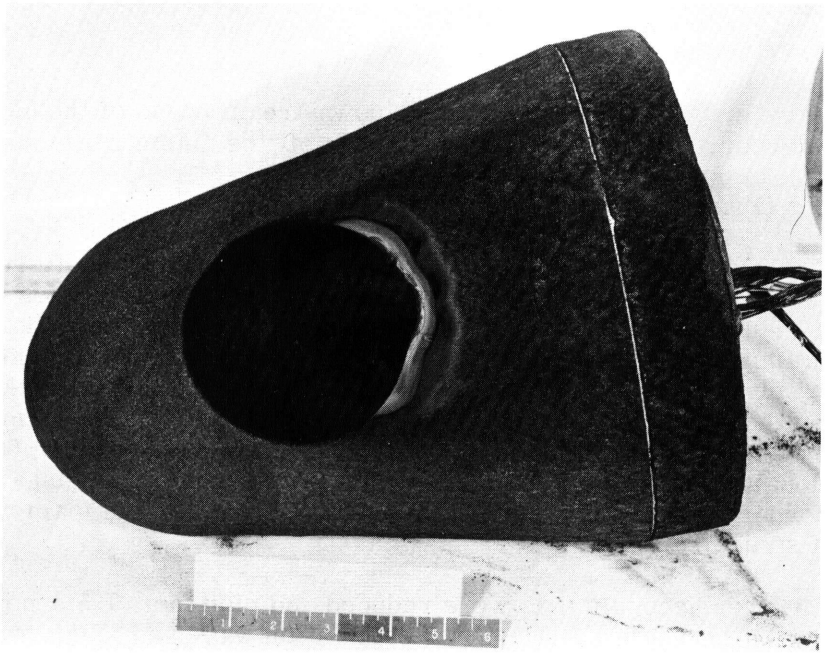

Figure 26. Malta Test Five - Post-test View

Test No. 1 (Figures 14 and 15)

The two calorimeter slugs in the insert ring had burned out. Erosion had occurred at the downstream edge of the insert ring; however, the ring had not melted completely through.

Test No. 2 (Figures 16, 17, and 18)

The insert ring had melted completely through at the downstream edge. A longitudinal crack developed in the heat shield from the downstream edge of the insert to the aft end of the model. Fastax motion pictures showed that this crack occurred at about 1 second after start of test, and progressively opened up during the remainder of the test. The crack may have been due to thermal shock, aggravated by the stress concentration due to the perforation.

Test No. 3 (Figures 19 and 20)

The major longitudinal crack, which was caused by impact, opened up during the test. A hole was burned through an Inconel structure petal caused by impact, on the downstream side of the perforation. The maximum longitudinal dimension of the perforation grew from 3.25 inches to 3.75 inches during the test. The condition of the model after impact but prior to thermal test is shown in Figures 21 and 22. In preparing for thermal test, the heat shield was pulled together to permit bonding of the longitudinal impact crack. Several loose pieces near the perforation periphery were also bonded in. The perforation for this test was caused by a 2.5 gram aluminum sphere at 12,900 ft/sec, striking 70 degrees from the surface longitudinal meridian, and was impacted in the Naval Research Laboratory's Light Gas Gun Facility.

Test No. 4 (Figures 23 and 24)

Some erosion and melting of the downstream edges of the heat shield and structure occurred, being maximum slightly off the diametral meridian.

Test No. 5 (Figures 25 and 26)

The urethane foam ablated in a typical cavity-heating pattern. A char layer developed on the foam surface. The initial and final cavities in the foam are shown in Figures 27 and 28. The initial cavity was a somewhat idealized simulation of an impact cavity obtained in a 12-inch cube of the same foam, placed behind a flat plate phenolic nylon - steel composite target having thicknesses corresponding to those of the test model. The target perforation and foam cavity were caused by a 2.5 gram aluminum sphere at 17,800 ft/sec, striking 60^{o} from the surface longitudinal meridian, fired by NRL in their Light Gas Gun Facility. The deep secondary penetrations below the primary crater in the foam were caused by pieces of structure.

The thermocouple data were reduced and plotted at 0.5 second intervals. A one-dimensional thin wall heat flux calculation was used to convert the slopes of the temperature-time curves to heat flux at 2 seconds after start of test. Heat flux maps are plotted for Tests 1 through 4 in Figures 29 through 32, which also show average internal and external static pressures at 2 seconds. The error associated with each local heat flux is estimated to be at least ± 10 percent. The heat flux distributions are seen to be quite similar to those obtained in the AEDC

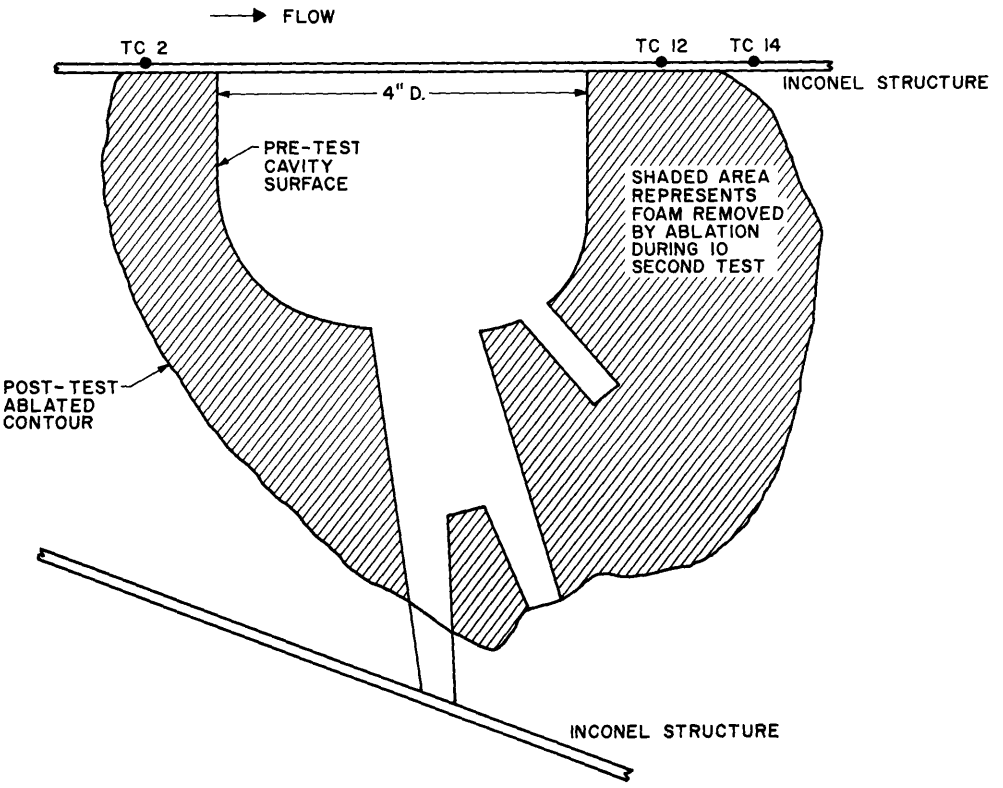

Figure 27. Malta Test Five - Foam Ablation
(Longitudinal Section through 0 Degree Meridian)

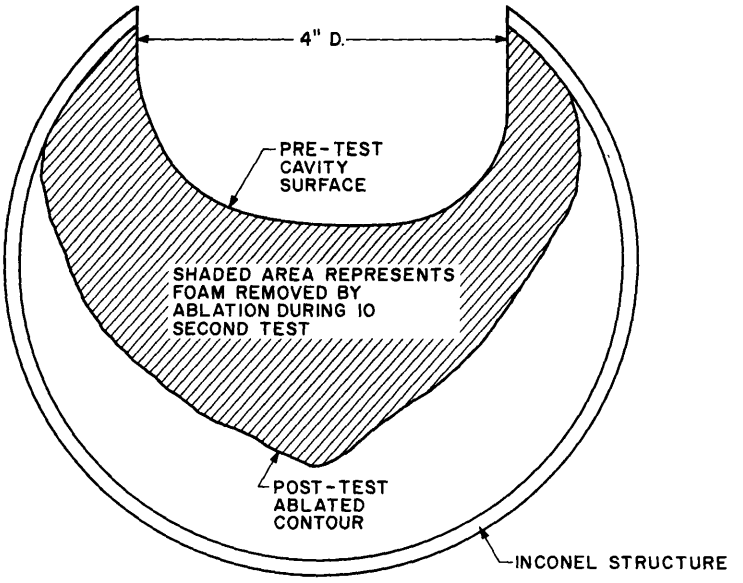

Figure 28. Malta Test Five - Foam Ablation
(Transverse Section Perpendicular to 0 Degree Meridian)

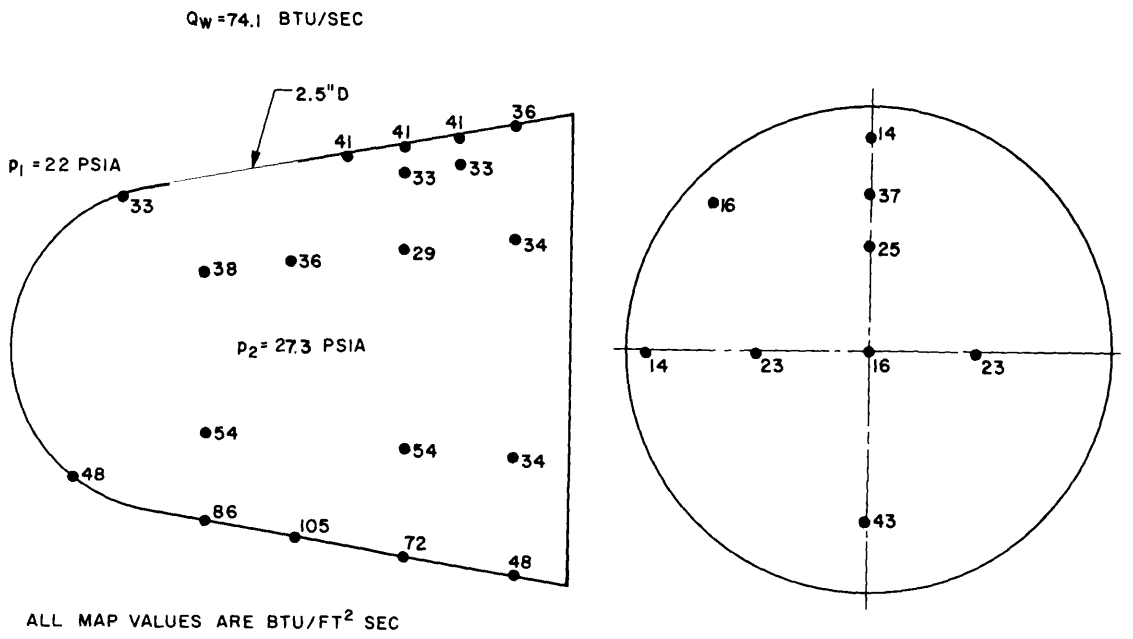

Figure 29. Malta Test One - Heat Flux Map

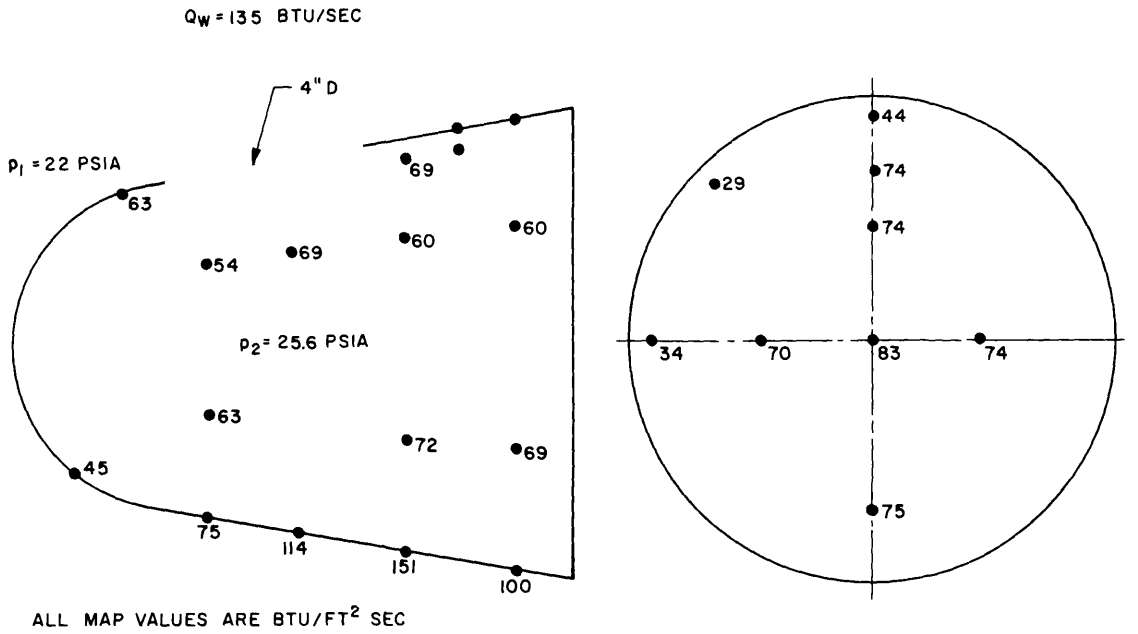

Figure 30. Malta Test Two - Heat Flux Map

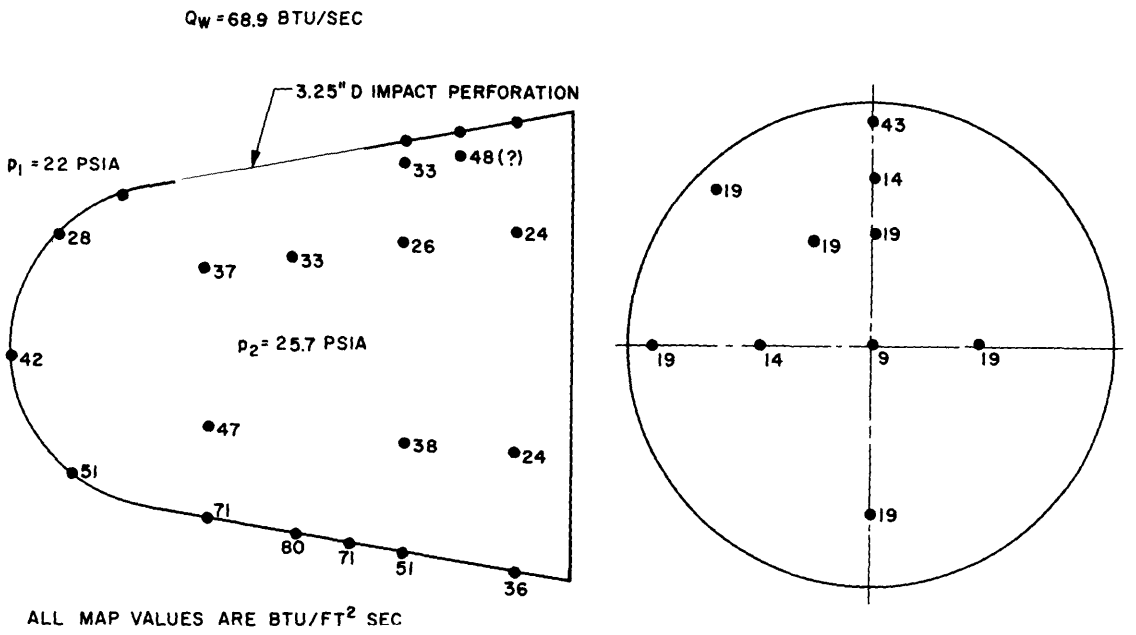

Figure 31. Malta Test Three - Heat Flux Map

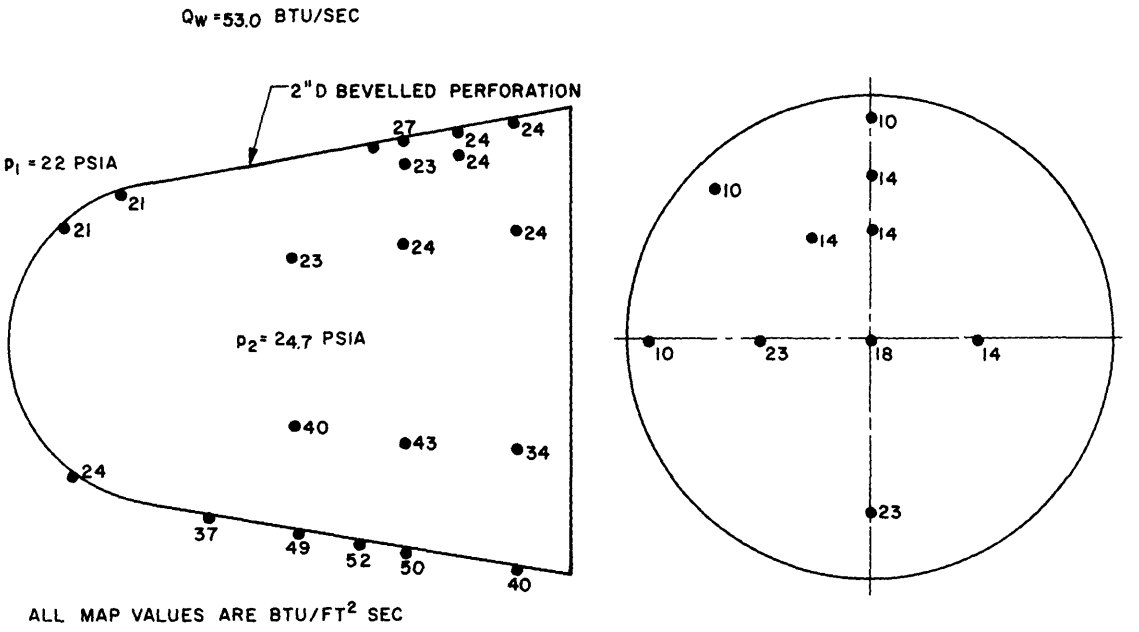

Figure 32. Malta Test Four - Heat Flux Map

tests described earlier, with maximums occurring on the meridian 180 degrees from the perforation. Even for Tests 3 and 4, in which thinner downstream edges are provided by impact and bevelling, respectively, the wall thickness of the model downstream of the perforation was apparently sufficient to turn the induced internal flow approximately 90 degrees.

The heat flux distributions of Figures 29 through 32 were integrated graphically over the internal surface area to obtain the total rate of heat absorption Q_W by the walls of the perforated volume. The resulting values of Q_W are listed on the respective flux maps. These values of Q_W are plotted vs initial perforation cross-section area A in Figure 33. Also shown in Figure 33 is the prediction of the Donaldson relation (Equation 1) for "coupled flow" energy influx for these test conditions (γ = 1.20, p = 22 psia, U = 6000 ft/sec). As discussed previously, Equation (1) represents an upper limit to the energy influx due to turbulent exchange across a steady shear layer flow. The Chow-Korst relation (Equation 2) with σ = 15 for Malta conditions is seen to bracket the measured values for a range of T_b/T_{S_e} of 0.1 to 0.5 The model containing an actual impact perforation gave a relatively low value of Q_W apparently due to the more thorough mixing of the induced jet flow caused by deflection off the structure petals (see Figure 22). This increased mixing prior to jet impingement causes a greater internal gas temperature (larger T_b/T_{S_e}), which reduces the value of Q_W. The machined perforation results again show a trend toward an increase in T_b/T_{S_e} as A increases, as was the case for the AEDC results.

The internal heat flux distributions for Tests 1 through 4 are plotted in Figure 34 as a normalized heat flux ratio $\dot{q}/\dot{q}_{max}$ vs S, the surface distance from the estimated jet impingement point. Also shown is the average locus of the results for Malta Pit Four Test M2A of the Wallops Island program (References 1 and 3), in which a 0.375 inch diameter inlet orifice was located on the nose 60 degrees from the stagnation point, with two exit vents on the cone. Although large data scatter exists, it appears that the dashed curve represents a reasonable first approximation to a universal internal heat flux distribution, provided that:

- the perforation downstream wall thickness is sufficient to turn the induced shear layer flow 90 degrees; and,
- the internal jet flow is fully developed upon impingement on the opposite wall.

For application to vehicles whose size differs from that of the Malta test models, the abscissa of Figure 34 should strictly be a dimensionless length ratio such as S/D, where D is the maximum diameter of the perforated compartment. An equivalent method is indicated on Figure 34, as an adjusted distance co-ordinate S which is scaled to the Malta model size.

In the preceding discussions, no heat flux maps or distributions have been shown for Test 5. For this test, the urethane foam provided enough insulation such that negligible temperature rises occurred at all locations which were still protected by foam at the end of the test. The highest temperature reached was 580°F, at a location 0.8 inches downstream of the perforation (T.C.#12, Figure 27). For this location, a maximum heat flux of about 60 btu/ft^2 sec occurred at 3.5 seconds during the run.

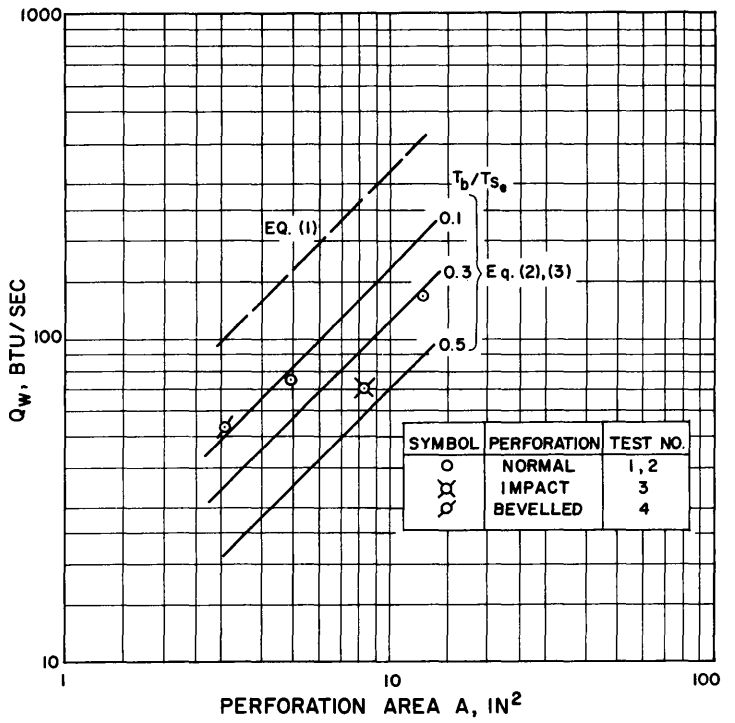

Figure 33. Results of Malta Rocket Exhaust Internal Heating Tests for Single Perforations and No Venting

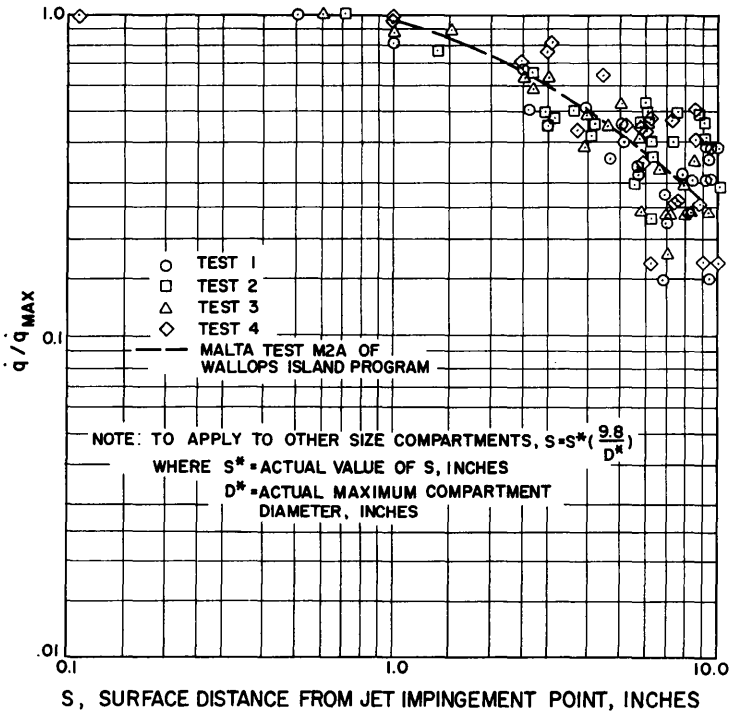

Figure 34. Heat Flux Distributions for Malta Tests

Some idea of the relative protection afforded by the foam can be obtained by comparing structure temperature rises for corresponding locations for Tests 2 and 5, as shown in Figure 35. Care must be taken in interpreting these results, since a longer test time obviously would have caused more structure to be exposed, with subsequent significant temperature rises. Thus, the foam serves as an energy absorber to provide a time delay in the heating of the structure. The thermal performance of this particular foam (Hetrofoam 368) in the Malta Pit Four environment can be characterized by an average heat of ablation Q*, defined in the usual manner:

$$Q^* = \frac{\dot{q}}{\dot{m}} \qquad (4)$$

in which $\dot{q}$ = heat flux to foam surface

$\dot{m}$ = rate of mass loss per unit surface area
($\dot{m} = \rho \dot{y}$, where $\dot{y}$ = foam ablation rate)

The value of Q* was computed in two ways:

- The total volume of foam ablated was estimated from Figure 35 to be approximately 0.13 ft^3, or a weight of about 1.0 lb. The rate of energy input to the foam was assumed to be the same as the value of Q_W for Test 2, giving a total of 1350 btu added during the 10 second run. Thus, the value of Q* is simply 1350 btu/lb on this basis.

- The local heat flux at the deepest portion of the foam cavity was assumed to be 60 percent of the external heat flux, based on cavity heating correlations. For this assumption, $\dot{q} \approx 200$ btu/ft^2sec at a point where $\dot{y} \approx 2.5$ inches/5 seconds ≈ 0.5 in/sec. Equation (3) yields Q* = 1230 btu/lb for this approach. Since either method of estimating Q* involves rather gross assumptions, a reasonable estimate of Q* for the foam of this particular test appears to be 1300 btu/lb ± 20 percent.

The temperature responses of the calorimeter slugs on the downstream surface of the perforations for Tests 1 and 2 (Figure 12) were used to determine initial heat fluxes near the beginning of the test runs ($\theta \sim 0.5$ seconds). Laminar and turbulent theoretical predictions were also made, using the approximate method described earlier in Section I. The results are tabulated below:

Test number	1		2	
Perforation diameter, inches	2.5		4.0	
Calorimeter (see Figure 12)	A	B	A	B
Measured heatflux, btu/ft^2 sec	650	550	650	550
Theoretical heat flux, btu/ft^2 sec				
Laminar	285	170	300	180
Turbulent	455	370	470	380

The magnitude and distribution of measured heat flux suggests that the turbulent theory gives a better prediction than laminar theory, despite the low value of Re_x (on the order of 1.5×10^4). The measured values exceed the turbulent theory by about 40 percent, perhaps due to the high degree of turbulence and fluctuations in the rocket exhaust environment.

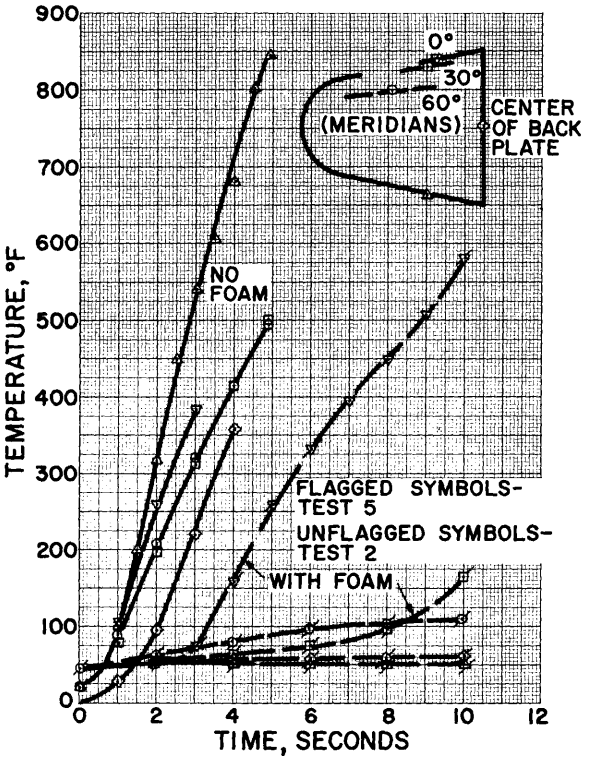

Figure 35. Effect of Internal Foam on Structure Temperature Rises for Typical Thermocouple Locations

The internal pressure histories of Tests 1 through 4 show an interesting trend (see Figure 36). In all cases, the internal pressure rose to a maximum during the first 0.5 seconds of exposure, and decreased gradually thereafter during the remainder of the test. The maximum internal pressure exceeded the external cone pressure by as much as 30 percent. This effect is due to the addition of energy to a closed volume, as discussed in Appendix A. There is a trend in the early portion of the test for the internal pressure to increase with increasing perforation area; however, Test 1 does not follow this pattern. By the end of the run, the ratio of internal to external pressure had decreased to approximately 1.1, in agreement with the AEDC test values.

The internal pressure history for Test 5 is also shown in Figure 36. Little rise in pressure was observed on three of the pressure taps, due to the presence of the foam. However, one pressure tap gradually rose during the test, indicating that a slow leakage path existed through the foam at this location. Post-test inspection of the model revealed that this pressure tap had become exposed by the end of the test.

The final two tests of the current program are scheduled for early April. Test 6 will contain the same simulated impact cavity as shown in Figure 27, but in a 3 lb/ft^3 urethane foam. Test 7 will contain a deeper cavity in the same 3 lb/ft^3 urethane foam used for Test 6. Instrumentation will consist of 20 thermocouples on the Inconel structure and 10 thermocouples located within the foam. These latter thermocouples will be supported by rods threaded into the structure and should indicate approximate foam ablation rates during the tests.

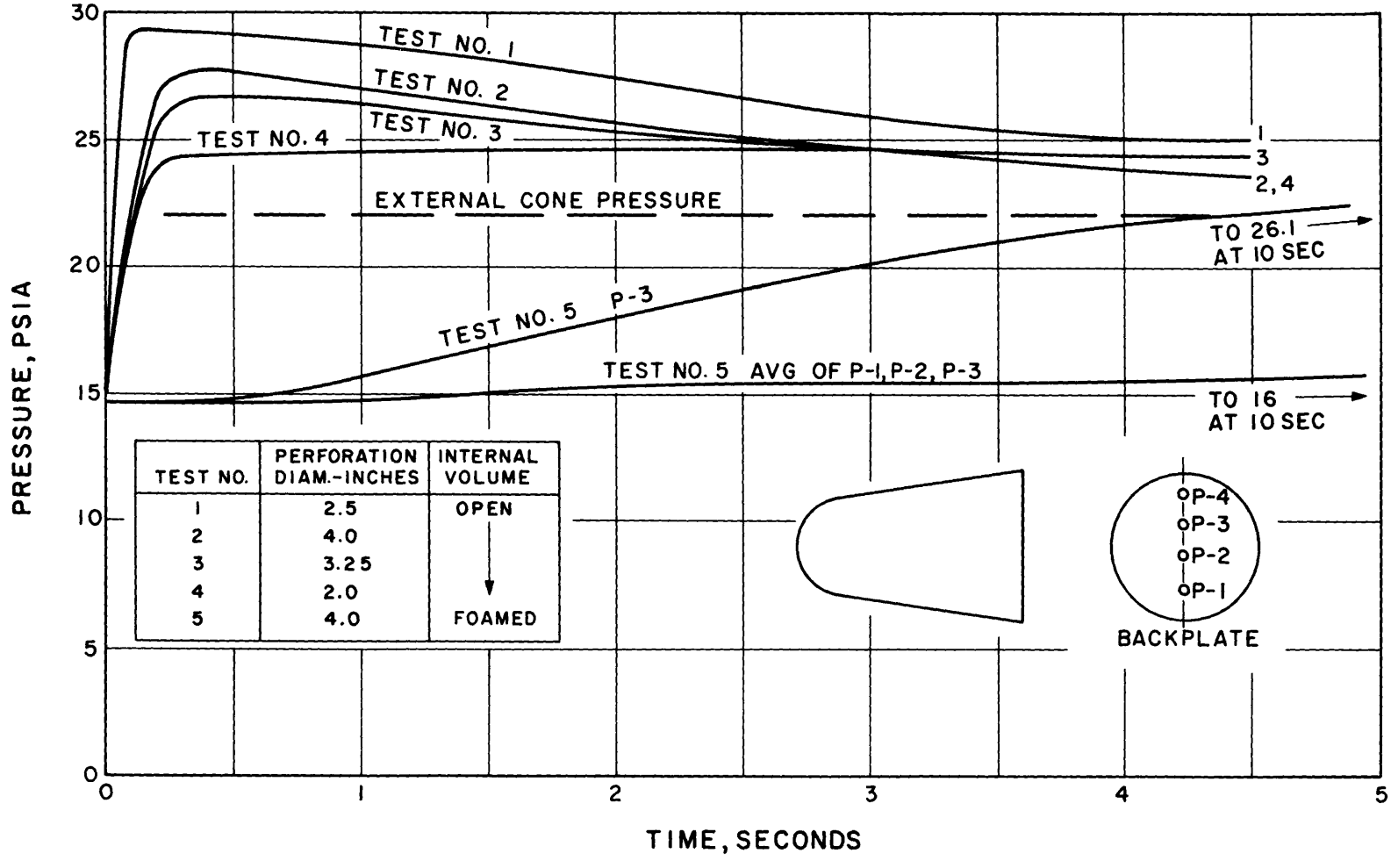

Figure 36. Average Internal Pressure Histories for Malta Tests

III. CORRELATION OF AEDC AND MALTA INTERNAL HEATING TEST DATA FOR SINGLE PERFORATIONS

The review of the AEDC and Malta internal heating test results given above has shown that the internal heating due to single perforations can be predicted reasonably well by the Chow-Korst turbulent shear layer theory, provided that a reasonable estimate is made of the temperature ratio T_b/T_{S_e}. In Figure 10, the AEDC results were seen to give excellent agreement with theory for $T_b/T_{S_e} = 0.3$. In Figure 33, the Malta results were seen to agree reasonably well with theory for $T_b/T_{S_e} \approx 0.3$, but with considerable scatter, due primarily to perforation shape effects. Based on these observations, it is apparent that Equations (2) and (3) can be used to deduce the following dimensionless correlating parameter Ψ for rate of internal energy absorption by the walls of a singly perforated compartment:

$$\Psi = \frac{Q_W}{\left(\frac{\gamma}{\gamma - 1}\right)\left(\frac{p\,UA\,I_2(\eta_j)}{\sigma J}\right)} \tag{5}$$

in which the term containing T_b/T_{S_e} has been dropped by assuming it to be approximately constant. The value of $I_2(\eta_j)$ requires a considerable amount of calculation for each test condition; therefore it is more convenient to eliminate $I_2(\eta_j)$ by the approximation $I_2(\eta_j) \sim C^{1.25}$ which was derived empirically from evaluation of $I_2(\eta_j)$ for $T_b/T_{S_e} = 0.3$ in the manner explained in Appendix A. With this substitution, Equation (5) becomes:

$$\Psi = \frac{Q_W}{\left(\frac{\gamma}{\gamma - 1}\right)\left(\frac{p\,UA\,C^{1.25}}{\sigma J}\right)} \tag{6}$$

The test results of Figures 10 and 33 are presented in terms of Ψ according to Equation (6) plotted vs perforation area A in Figure 37. It is seen that the choice of Ψ achieves a reasonable correlation of data for two widely different environments having values of Q_W which differ by more than an order of magnitude. It is not surprising that the Malta tests with a bevelled simulated perforation and an actual impact perforation deviate somewhat from the mean correlation line. Other scatter must be attributed to experimental error and the effects of variable T_b/T_{S_e}.

The mean correlation line shown in Figure 37 yields the following equation:

$$Q_W = 0.4\left(\frac{\gamma}{\gamma - 1}\right)\left(\frac{pUA}{\sigma J}\,C^{1.25}\right) \tag{7}$$

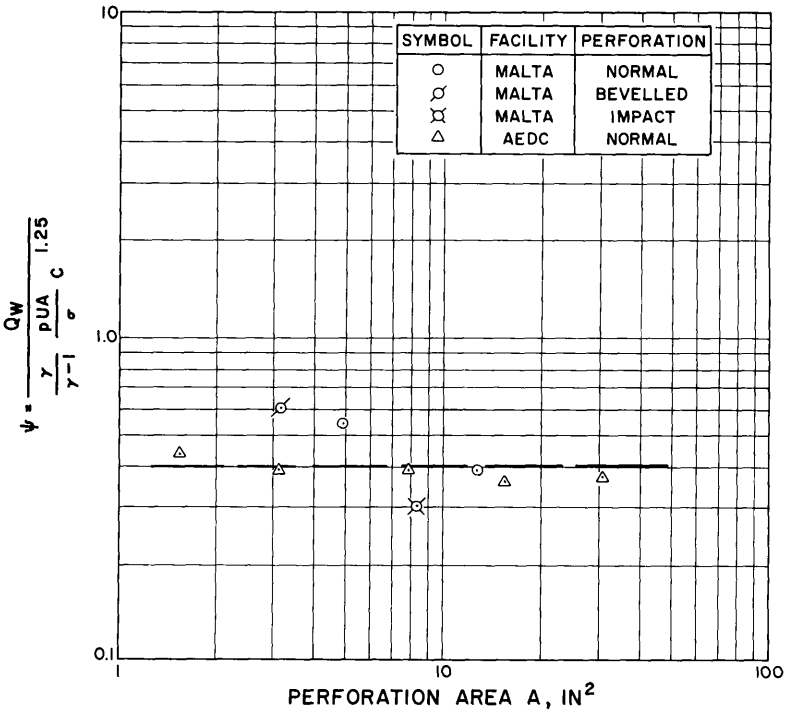

Figure 37. Correlation of AEDC and Malta Internal Heating Data for Single Perforations and No Venting

in which:

Q_W = rate of heat absorption by internal structure, btu/sec

γ = isentropic exponent of the test medium

p = local external static pressure at perforation location, psia

U = local external velocity at edge of boundary layer, at perforation location, ft/sec

A = perforation cross-section area, in^2

C = Crocco number = $U/\sqrt{2gJ\,h_s}$

h_s = stagnation enthalpy, btu/lb

σ = jet mixing similarity parameter

J = mechanical equivalent of heat = 778 ft. lb/btu

The values of the variables used in evaluating Ψ from Equation (6) are listed below for each test environment:

	AEDC Tunnel C Model of Fig. 1	Malta Pit Four Model of Fig. 12
γ	1.4	1.2
p psia	0.22	22
U ft/sec	4600	6000
C	0.955	0.50
σ	35	15.5

An alternate method of correlating internal heating data due to a single perforation was proposed in Reference 6. This method was based on the fluctuating shear layer concept of Charwat et al (Reference 8), which led to the relation:

$$dE/d\theta \approx Q_W \sim \rho U h_s A \tag{8}$$

By use of perfect gas assumptions, Equation (8) can be written:

$$Q_W \sim \frac{\gamma}{\gamma - 1} \; pUA \left(1 + \frac{\gamma - 1}{2} M_1^2\right) \tag{9}$$

In Equation (9), M_1 is the local external Mach number; other symbols were defined in Section I. Equation (9) suggests that the proper correlating parameter would be:

$$\Psi' = \frac{Q_W}{\left(\frac{\gamma}{\gamma - 1}\right) pUA \left(1 + \frac{\gamma - 1}{2} M_1^2\right)} \tag{10}$$

rather than Ψ of Equation (6). When Equation (10) was applied to the test results of Figures 10 and 33, the Malta tests were found to yield values of Ψ' which were an order of magnitude higher than the values of Ψ' for the AEDC tests. Therefore it is concluded that shear layer fluctuation effects are secondary to the basic shear layer energy exchange mechanism which was the basis for Equation (7).

IV. THERMAL KILL OF RE-ENTRY VEHICLES DUE TO SINGLE PERFORATIONS

A. Introduction

The thermal kill of re-entry vehicles due to single perforations can now be investigated by means of Equation (7) developed above. The following assumptions are made:

- The re-entry vehicle compartment which is perforated is a sealed, unvented compartment whose walls can withstand any pressure differential caused by the perforation.

- Thermal kill occurs when the average structure temperature reaches the structure melting point.

- The effect of perforation enlargement due to re-entry heating is neglected.

Before proceeding with the analysis, some discussion of these assumptions is warranted. The first assumption is made from the standpoint of the defense system designer who lacks detailed intelligence information concerning internal bulkhead and aft cover thicknesses and materials. If first-hand knowledge of such information is available, as in the vulnerability evaluation of a U. S. design, this assumption can be relaxed in favor of a stress analysis to determine pressure stresses. It is quite conceivable, for example, that the vehicle aft cover would be vented to wake pressure to permit a lighter aft cover design. In this case, a perforation of the aft compartment would result in greater internal heating than predicted by Equation (7), due to the effects of venting. Further, the internal pressure buildup may be sufficient to blow out the aft cover, whether or not venting exists. The resulting large mass flow through the aft end of the vehicle could then lead to serious thermal and aerodynamic effects.

The second assumption is made for the purpose of simplifying the analysis. Previous structural studies reported in Reference 1 showed that thermostructural failure will actually occur at a structure temperature somewhat below the melting point; however, the rate of temperature rise is so great at this time that the melting temperature would be reached very shortly thereafter. Hence the melting temperature is used as a matter of convenience. Another aspect of this assumption is the neglect of local hot spot areas such as the region directly opposite the perforation. The heat flux maps of Figures 3 through 7 and Figures 29 through 32 indicate that a large section of the structure opposite the perforation will probably have melted before the average temperature rise reaches melting. More refined thermostructural kill calculations considering this effect will require additional structural studies of the type described in Section VI.

The third assumption is made both as a matter of convenience and lack of knowledge. Insufficient data exist at present to define the rate of enlargement of single perforations under realistic re-entry heating conditions. The only results obtained for single perforations are Malta rocket exhaust tests of Reference 4 and the present Malta Test Three. These results indicate widely different enlargement rates, with the condition of the downstream surface of the perforation apparently being of prime importance. Neglect of the perforation growth is, of course, conservative from the defense system designer's viewpoint, since consideration of this effect would promote earlier failure.

B. Analysis

The rate of average temperature rise of the structure of a perforated compartment is well-approximated by the thin-wall heat flux relation:

$$\frac{d\bar{T}}{d\theta} = \frac{\dot{\bar{q}}}{\rho C_p t} \tag{11}$$

in which:

$\bar{T}$ = average structure temperature

θ = time

$\bar{\dot{q}}$ = average heat flux to structure

ρ = density of structure

C_p = specific heat of structure

t = thickness of structure

The average heat flux $\bar{\dot{q}}$ is defined as:

$$\bar{\dot{q}} = \frac{Q_W}{A_s} \tag{12}$$

in which:

Q_W = total rate of energy absorption by structure

A_s = total surface area of structure

Integrating Equation (11) from time θ_1 to time θ_2, and substituting Equation (12) for $\bar{\dot{q}}$ and Equation (7) for Q_W yields an expression for the average structure temperature rise $\overline{\Delta T}$, assuming perforation at time θ_1:

$$\overline{\Delta T} = \frac{0.4}{A_s t \bar{J}} \int_{\theta_1}^{\theta_2} \frac{\frac{\nu}{\nu - 1} \; pUA C^{1.25} \, d\theta}{\rho C_p \sigma} \tag{13}$$

Assuming all quantities except p and U under the integral sign to be constant at their average values between θ_1 and θ_2, Equation (13) can be rewritten:

$$\overline{\Delta T} = \frac{0.4 \, K}{\bar{\rho} \bar{C}_p t \bar{\sigma} \bar{J}} \quad \frac{\bar{\nu}}{\bar{\nu} - 1} \quad \bar{C}^{1.25} \quad \frac{A}{V^{2/3}} \quad \int_{\theta_1}^{\theta_2} pU \, d\theta \tag{14}$$

in which the ratio $A/V^{2/3}$ has been introduced by the substitution:

$$K = \frac{V^{2/3}}{A_s} \tag{15}$$

with V being the internal volume of the perforated compartment.

For a given vehicle flying a given trajectory, Equation (14) gives the value of the average structure temperature rise at the time θ_2 due to a perforation at the time θ_1. For a thermostructural kill, ΔT must equal ΔT_m, the temperature rise to melting. Therefore Equation (14) yields the following expression for the critical value $(A/V^{2/3})_{crit}$ required for thermal kill at time θ_2 due to perforation at time θ_1:

$$\left(\frac{A}{V^{2/3}}\right)_{crit} = \frac{\gamma}{\gamma - 1} \frac{(\overline{\rho C}_p t \, \Delta T_m) \, \bar{\sigma} J}{0.4 \, K \bar{C}^{1.25} \int_{\theta_1}^{\theta_2} pU \, d\theta} \tag{16}$$

C. Results

Equation (16) was evaluated for a high ballistic coefficient vehicle such as the C-1 target vehicle (Reference 1) having $W/C_DA = 3000$ lb/ft^2 and a semi-vertex cone angle of 11 degrees. The following values of $\bar{\gamma}$, $\bar{\sigma}$, $\bar{K}$, and $\bar{C}$ are appropriate:

$\bar{\gamma} = 1.3$ $\qquad$ $K = 0.16$

$\bar{\sigma} = 37$ $\qquad$ $\bar{C} = 0.95$

The C-1 trajectory of Reference 11 was used to compute the time variation of cone pressure p and velocity u needed to evaluate the integral in Equation (16). The results are represented in generalized form in Figure 38, which is applicable to any size vehicle and structure design having the given cone angle θ_V, ballistic coefficient β, and re-entry conditions of the C-1 vehicle. Similar curves could be plotted for any combination of θ_V, β, and re-entry conditions V_E, γ_E.

Results such as those of Figure 38 can be used to generate curves of lethal perforation diameters for thermal kill as a function of intercept altitude, kill altitude, type of structure, structure material, structure thickness, and vehicle length. Examples of such calculations for the C-1 type of vehicle are shown in Figures 39 and 40 for an intercept altitude of 60,000 feet and thermal kill by an altitude of 30,000 feet. Monocoque and honeycomb sandwich structures are considered, with steel or aluminum as the material. The structure thickness requirement was assumed to vary in direct proportion to the vehicle length, with the design thicknesses for the C-1 vehicle length of 23.5 feet being obtained from Reference 1.

Figure 39 shows results for a perforation of the forecone region, while Figure 40 shows results for a perforation of the aftcone region. Equation (16) yields the scaling relation:

$$D \sim A^{1/2} \sim L^{3/2} \tag{17}$$

where L is the vehicle length, for the assumption that $t \sim L$. Therefore the lethal perforation diameter for thermal kill is seen to be relatively sensitive to the size of the vehicle. A vehicle the size of the C-1 design is seen to require relatively large perforation diameters to accomplish thermal kill, while vehicles of smaller size can be killed thermally by more modest perforation diameters.

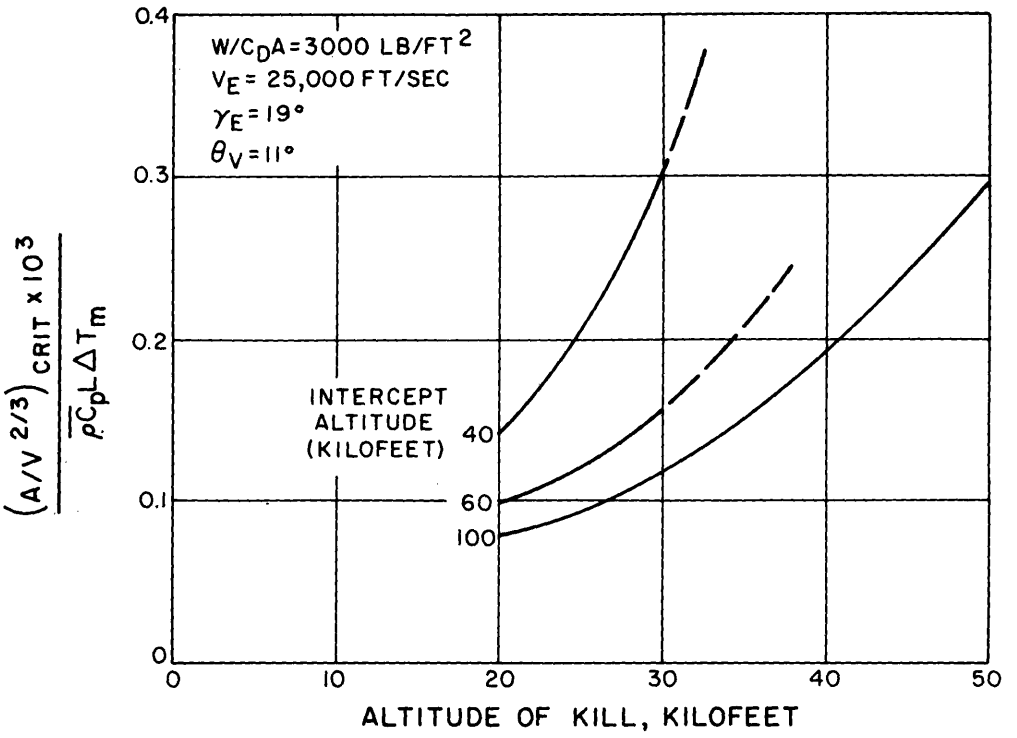

Figure 38. Critical Perforation Area Required for Thermal Kill

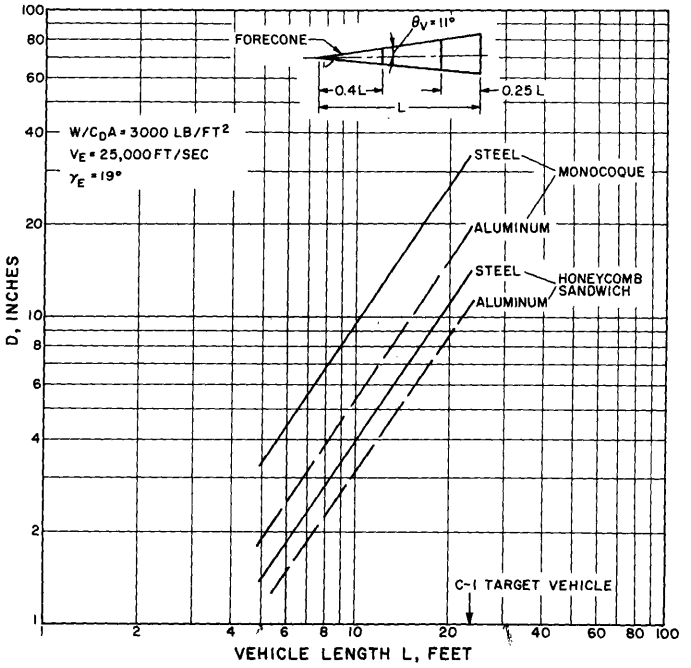

Figure 39. Perforation Diameter Required to Cause Thermal Kill by 30,000 Foot Altitude for Intercept at 60,000 Foot Altitude - Perforation in Forecone

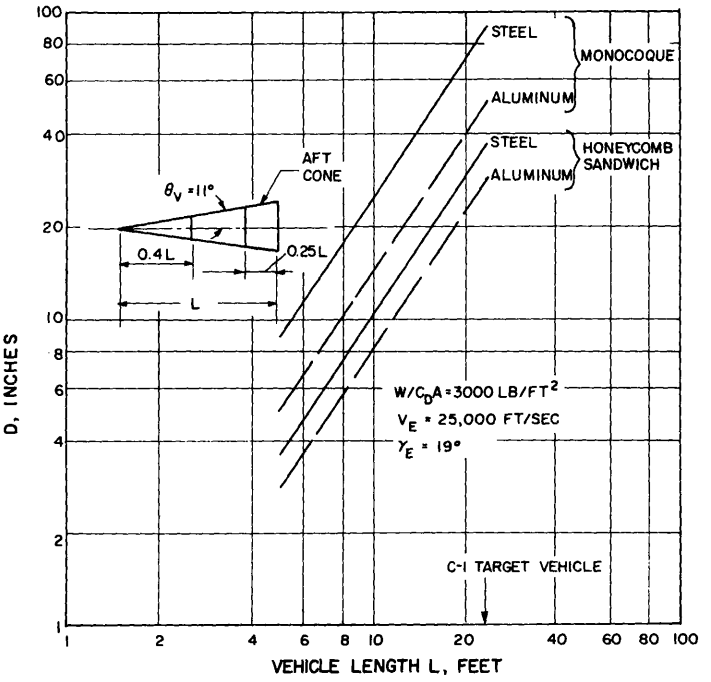

Figure 40. Perforation Diameter Required to Cause Thermal Kill by 30,000 Foot Altitude for Intercept at 60,000 Foot Altitude - Perforation in Aftcone

The effect of intercept altitude on lethal perforation diameter for a given kill altitude is shown in Figure 41, for a perforation in the forecone region of a 10 foot long vehicle. It is seen that little is gained by intercepting above 60,000 feet altitude, due to the relatively low pressure and heat flux at this altitude. However, lethal perforation size begins to increase sharply for intercept altitude below 60,000 feet.

Since the correlation of Persechino (Reference 9) for hypervelocity impact perforations of re-entry vehicles structures indicates that:

$$D \sim m^{0.36} \tag{18}$$

where m is the mass of the attacking fragment, it follows from Equation (17) that:

$$m \sim L^{4.17} \tag{19}$$

In other words, the lethal fragment mass required for thermal kill increases by a factor of $(2)^{4.17} = 18$ for a doubling of the vehicle length. For example, the application of Persechino's correlation to the C-1 type of vehicle gives the following results for aluminum honeycomb sandwich structure and an assumed heat shield thickness of 1.0 inch:

Vehicle Length (ft)	Location of Perforation	Lethal Mass (grams) for Thermal Kill by 30,000 ft.*
10	Forecone	4
20	Forecone	70
10	Aftcone	50
20	Aftcone	900

*for intercept at 60,000 ft, at 25,000 ft/sec relative intercept velocity.

These results dramatically illustrate the importance of accurate intelligence information regarding the size of the hostile vehicle, when sizing the fragments in a particle impact defense system.

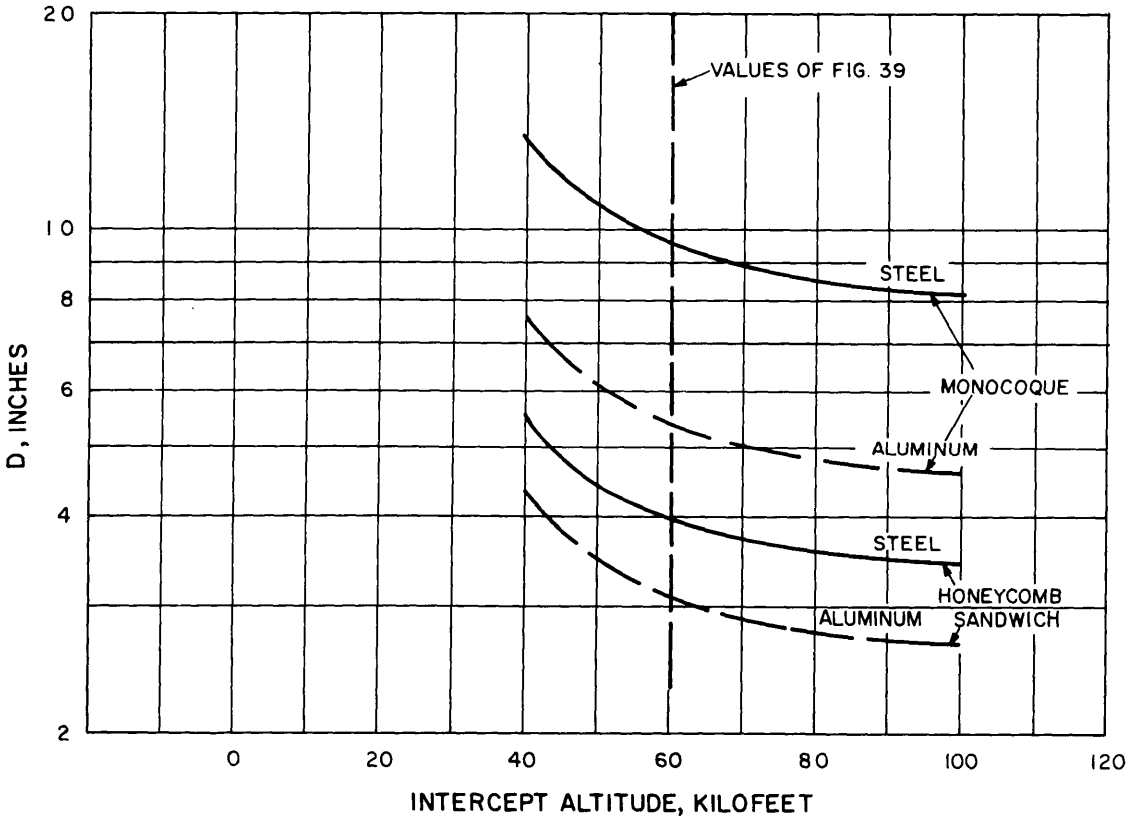

Figure 41. Effect of Intercept Altitude on Perforation Diameter Required for Thermal Kill by 30,000 Foot Altitude - Perforation in Forecone; L=10 Feet

V. AEDC TUNNEL D ORIFICE FLOW TESTS

A. Introduction

The theoretical solution for the internal pressure response of a perforated compartment requires knowledge of the effective flow resistance of the perforation. Since the external flow approaches the orifice roughly perpendicular to its axis, turning losses exist which must be considered when applying orifice flow relations. Further, the external flow is supersonic over most of the vehicle surface, leading to shock losses upon impingement on the downstream lip of the perforation.

In previous work (e.g., Reference 10), inviscid Prandtl-Meyer expansion theory was proposed to provide a first approximation to the orifice flow rate for supersonic tangential approach flow. Since no experimental data were available in the open literature to verify this technique, a series of wind tunnel tests were conducted at the Naval Ordnance Laboratory to determine flow coefficients for various orifice geometries and pressure ratios. These results (reported in Reference 11) showed measured values which fell well below the inviscid theory for small expansion angles ($p_2/p_1 > 0.6$), presumably due to viscous effects. However, inconsistencies in the effects of orifice diameter were apparent, and data were obtained only for one supersonic Mach number ($M_1 = 1.5$). Therefore a more extensive program was undertaken in AEDC Tunnel D to corroborate and extend the NOL results. The objectives of the program were to obtain:

- Extension of flow coefficient measurements to Mach 5, including actual impact perforations in addition to drilled orifices.
- Probing of jets developed from supersonic tangential approach flow expanding through orifices, to determine jet shape and velocity profiles.
- Photographs of expanding jet flow directions.

B. Test Procedure

The tests were performed by mounting a pressure-tight box having a volume of approximately 2 cubic feet to the tunnel side wall and placing various orifice inserts in the side of the box which formed part of the tunnel wall. Schematic drawings showing top and front views of the set-up are given in Figures 42 and 43, respectively. Steady state flow rates were established by evacuating the box to the desired pressure ratio. The flow rates were measured by a calibrated flow nozzle in the vacuum line. The static pressure upstream of the box was measured by a pressure tap located 5.81 inches upstream of the test orifice centerline. Static pressure within the box was determined by the average of 6 pressure taps. The major portion of the data showed variations of less than ± 2 percent among these 6 readings for a given setting.

Pitot pressure surveys of the expanding jet within the box were obtained at several locations downstream of selected orifices by means of an adjustable survey rake containing 17 probes (Figures 44 and 45). The rake head could be rotated about two axes (ϑ, ϕ in Figure 44) and could be moved anywhere in the box. The probe tubing was stainless steel with an inside diameter of .050 inches.

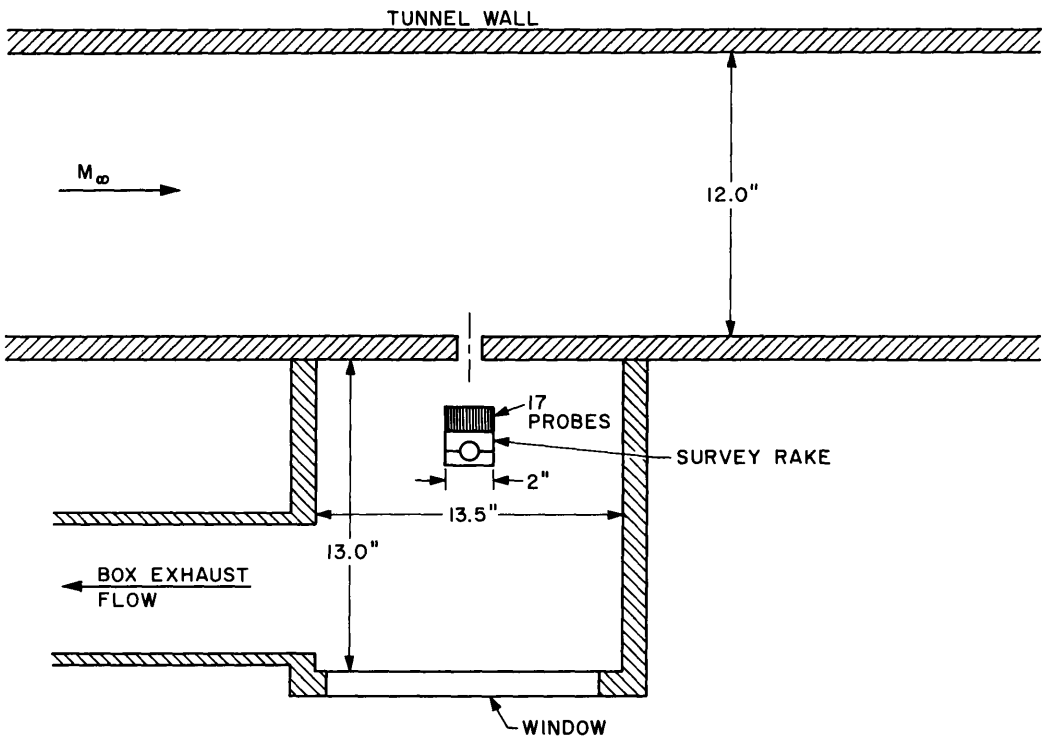

Figure 42. AEDC Orifice Test Set-up (Top View)

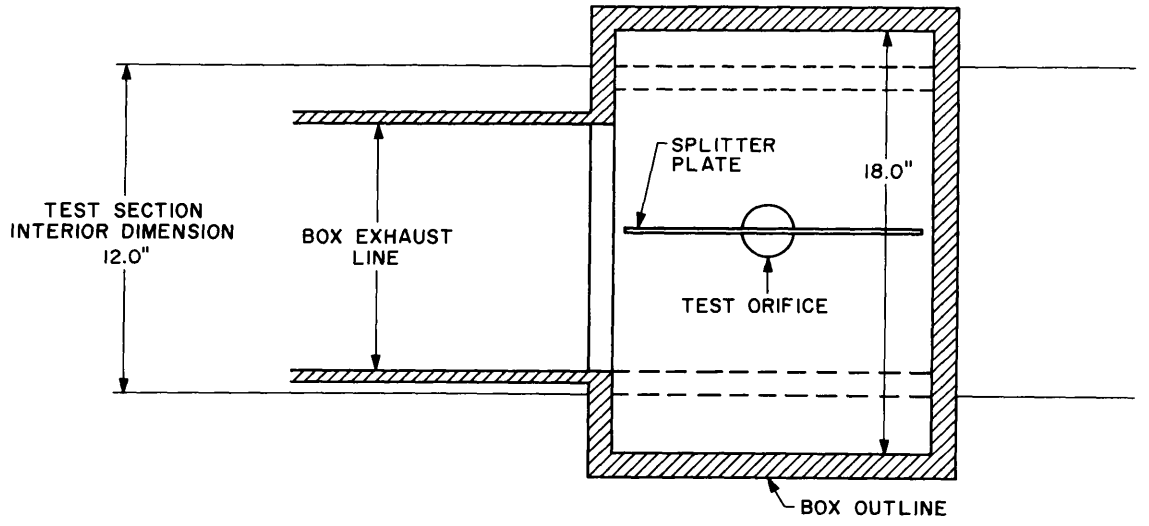

Figure 43. AEDC Orifice Test Set-up (Front View)

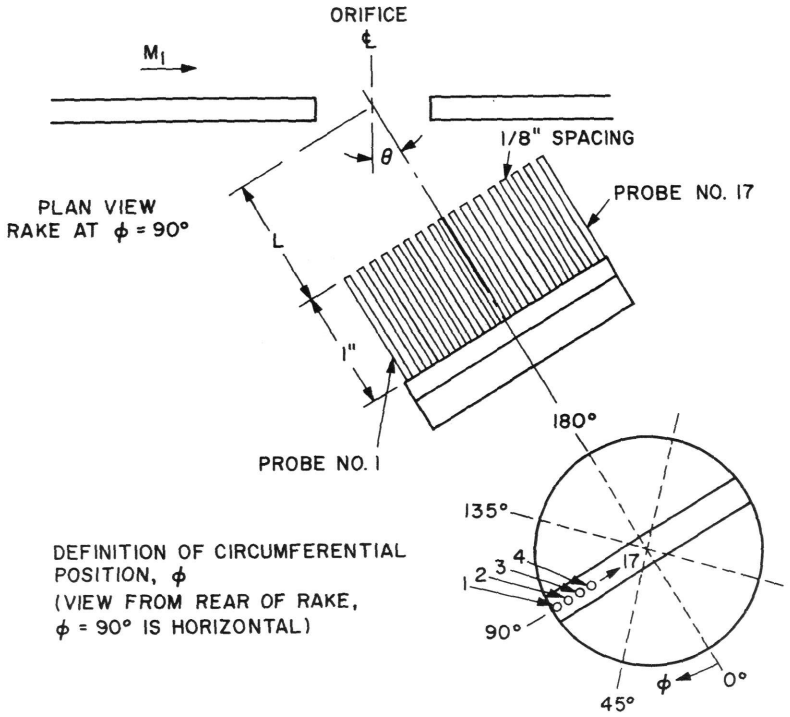

Figure 44. Survey Rake Detail

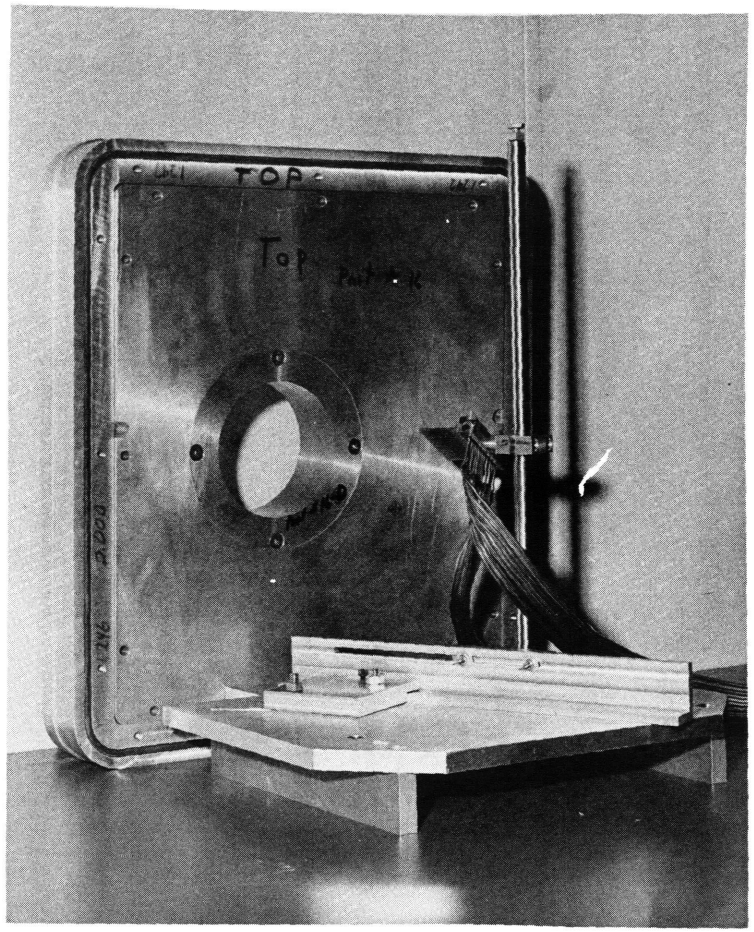

Figure 45. Survey Rake with Configuration 3B

A survey rake was also located inside the tunnel test section on the tunnel wall 8.13 inches downstream of the test orifice centerline to measure tunnel boundary layer profiles.

Flow vizualization by means of Schlieren photography was attempted; however, the densities were too low for the flow to be seen. As an alternate measure, a horizontal splitter plate sharpened to a knife edge was placed perpendicular to the orifice and on the horizontal diameter (Figure 43). Phosphorescent oil was sprayed on the plate before each test. The jet produced during the test caused the oil to run in streaks. After the test, the plate was removed and photographed in ultra violet light.

The test matrix which was followed is shown in Table 3. A typical orifice insert is shown in Figure 45 prior to installation in the tunnel. Views of the inserts containing actual impact perforations are given in Figures 46 through 49. The nominal test conditions for each Mach number were as follows:

	M_1	1.47	3.00	5.01
Tunnel Reservoir Conditions	p_o psia	60.7	43.7	14.16
	T_o ^oR	540	540	540

TABLE 3. ORIFICE FLOW TEST MATRIX

Configuration Number	Orifice Dia. D (inches)	Orifice Plate Thickness t (inches)	t/D	θ Degrees	Mach Number M_1 1.47	3.00	5.01
1A	1.0	0.2	0.2	90	XP	XP	X
1B	1.0	0.5	0.5			XP	
1C	1.0	2.0	2.0		X	XP	X
2A	2.0	0.2	0.1			X	
2B	2.0	1.0	0.5			X	
2C	2.0	2.0	1.0			X	
3A	4.0	0.5	0.125		X	X	X
3B	4.0	2.0	0.5		X	X	X
4A	1.4*	1.25	0.89	Note 1	X	XP	X
4B	2.4*	1.25	0.52	Note 2	X	X	X
5A	2.0	0.2	0.1	60		X	
5B	2.0	2.0	1.0	60		X	

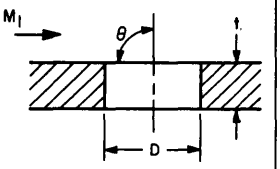

X - Mass flow rates were measured for this condition

P - Jet survey was taken for this condition

* Effective diameter for equivalent circular area

Note 1. Impact perforation (Figures 46 and 47) caused by 1/4" D. steel sphere at normal incidence at 17,360 ft/sec in 1.0 inch molded phenolic nylon bonded to 0.25 inch Mg backup structure.

Note 2. Impact perforation (Figures 48 and 49) caused by 5/16" D. steel sphere at normal incidence at 15,865 ft/sec in 1.0 inch molded phenolic nylon bonded to 0.25 inch Al backup structure.

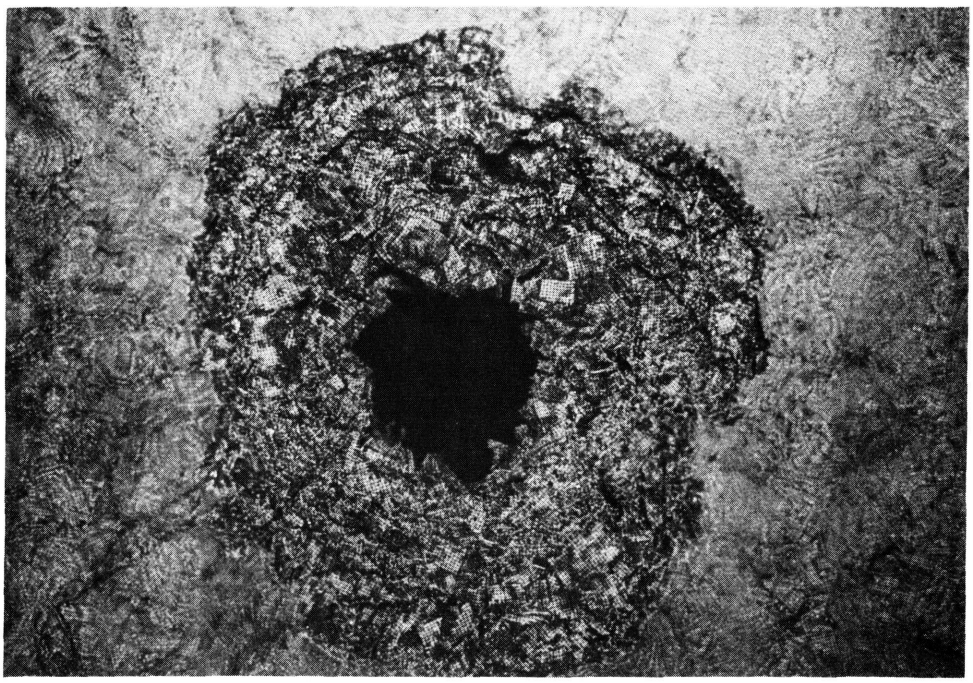

Figure 46. Configuration 4A - Front View (From Tunnel)

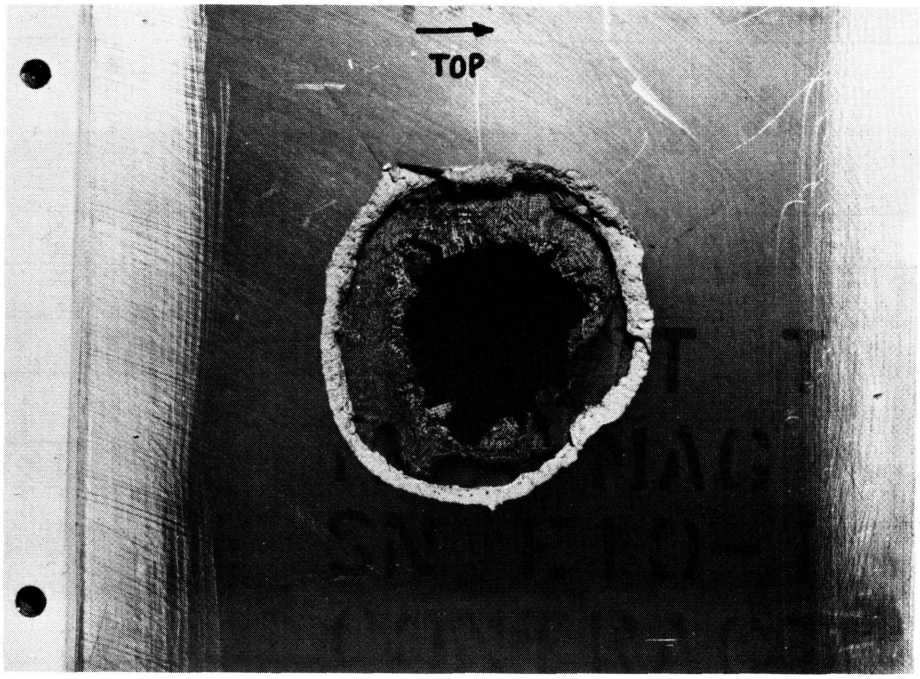

Figure 47. Configuration 4A - Back View (From Box)

Figure 48. Configuration 4B - Front View (From Tunnel)

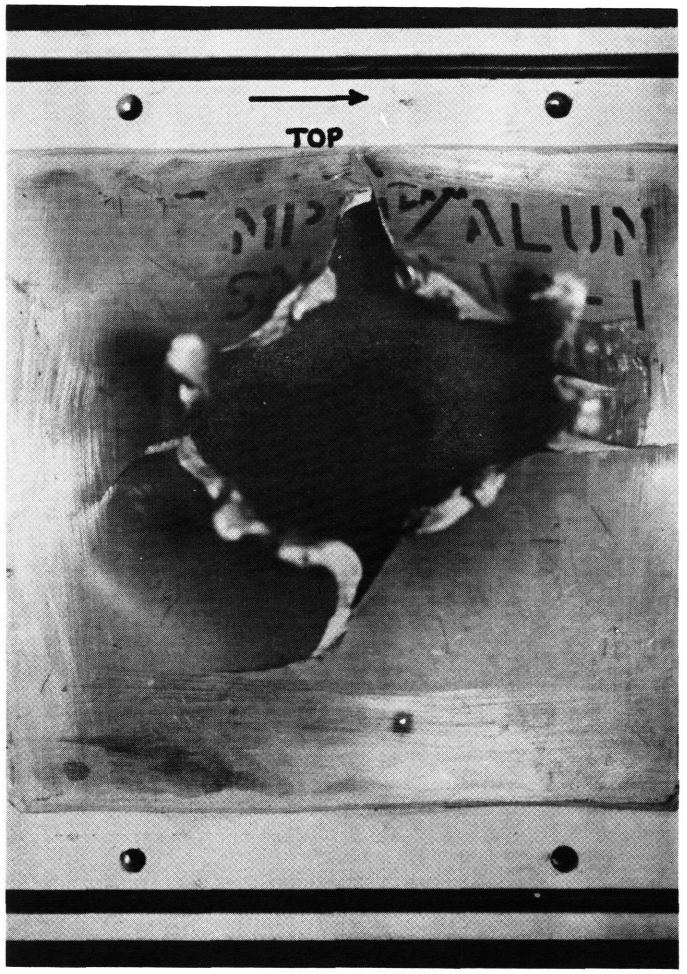

Figure 49. Configuration 4B - Back View (From Box)

C. Flow Rates

Graphs of measured flow rate vs static pressure ratio across the orifice are given in Figures 50 through 55. The basic flow rate data for orifice diameters of 1.0, 2.0, and 4.0 inches are given in Figures 50, 51 and 52, respectively. The data at $M_1 = 5$ for D = 1.0 inches were omitted from Figure 50 because of obvious inaccuracies due to the low magnitude of the flow rates being measured. It is seen that variations in orifice wall thickness t had relatively little effect on the flow rate.

The effect of orifice obliquity is shown in Figure 53. The effect of tilting the orifice axis 30 degrees in a downstream direction as shown in Figure 53 (θ = 60 degrees) is to increase the flow rate from 20 to 50 percent over the values for θ = 90 degrees. This increase is probably due to the reduced shock losses associated with a smaller flow turning angle.

The flow rates for the two impact perforations are given in Figures 54 and 55. A comparison of these two figures shows that the flow rate for the larger perforation was comparable to that for the smaller perforation, despite a difference of a factor of 3 in their flow areas. This result appears to be attributable to the added flow resistance of the "orange peel" condition of the aluminum structure of the larger perforation, caused by impact. The magnesium structure of the smaller perforation does not exhibit this orange peel effect, but shears in a straight plug fashion.

In Figures 50 through 55 the reduction in flow rate as Mach number M_1 increases is not a true Mach number effect, but is caused by the lower static pressure upstream of the orifice associated with expansion from reservoir conditions.

Initial comparison of measured flow rates with theory consisted of a calculation of the flow rate based on isentropic expansion theory for the given test conditions. This method yielded the solid curves labelled "Inviscid Theory" in Figures 50 through 55. These curves were computed using from the continuity equation:

$$m = \rho_2 U_2 A \sin\Delta\nu \qquad (20)$$

in which:

m = mass flow rate through orifice

ρ_2 = density after expansion to p_2

U_2 = velocity after expansion to p_2

A = orifice cross-section area

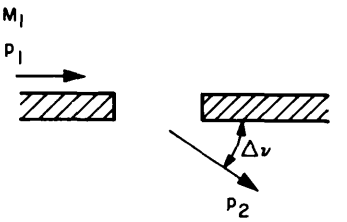

$\Delta\nu$ = turning angle of flow in expanding from p_1 to p_2

The quantities ρ_2, U_2, and $\Delta\nu$ were determined from the isentropic tables of Reference 12 for γ = 1.4, for a flow expanding from M_1. It is seen that for the basic data for D = 1.0, 2.0, and 4.0 inches (Figures 50, 51 and 52), the measured flow rates fall far below the inviscid theory. This circumstance

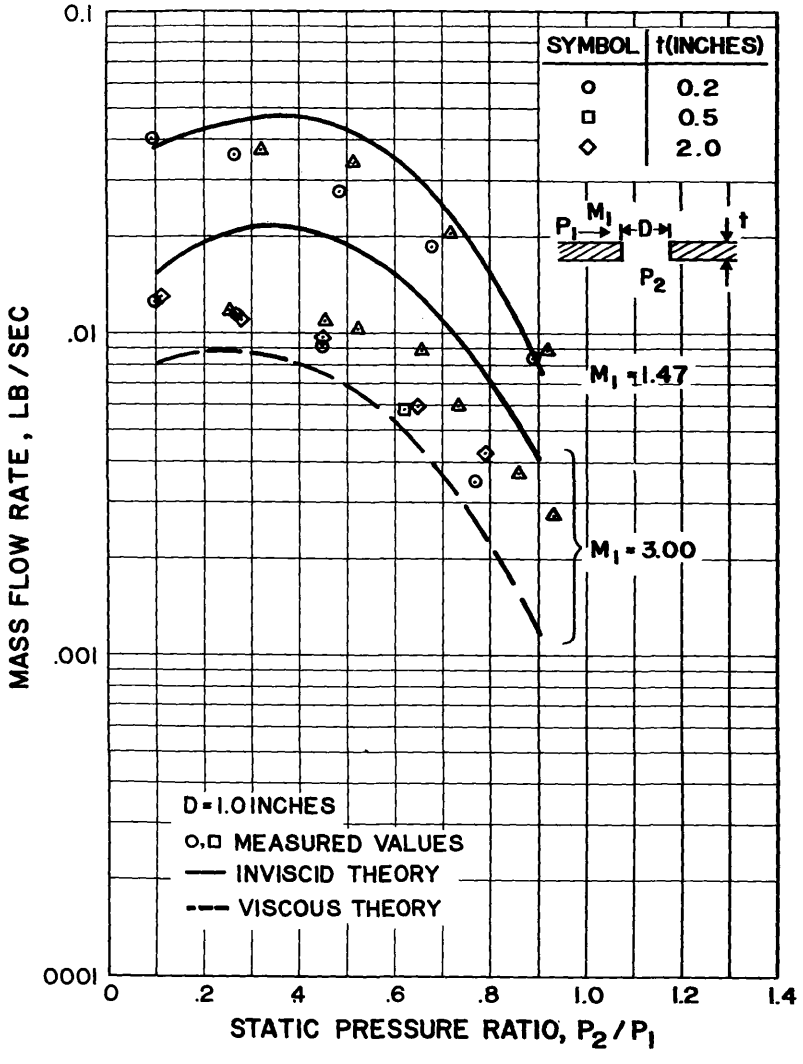

Figure 50. AEDC Orifice Flow Rates - D = 1.0 Inches

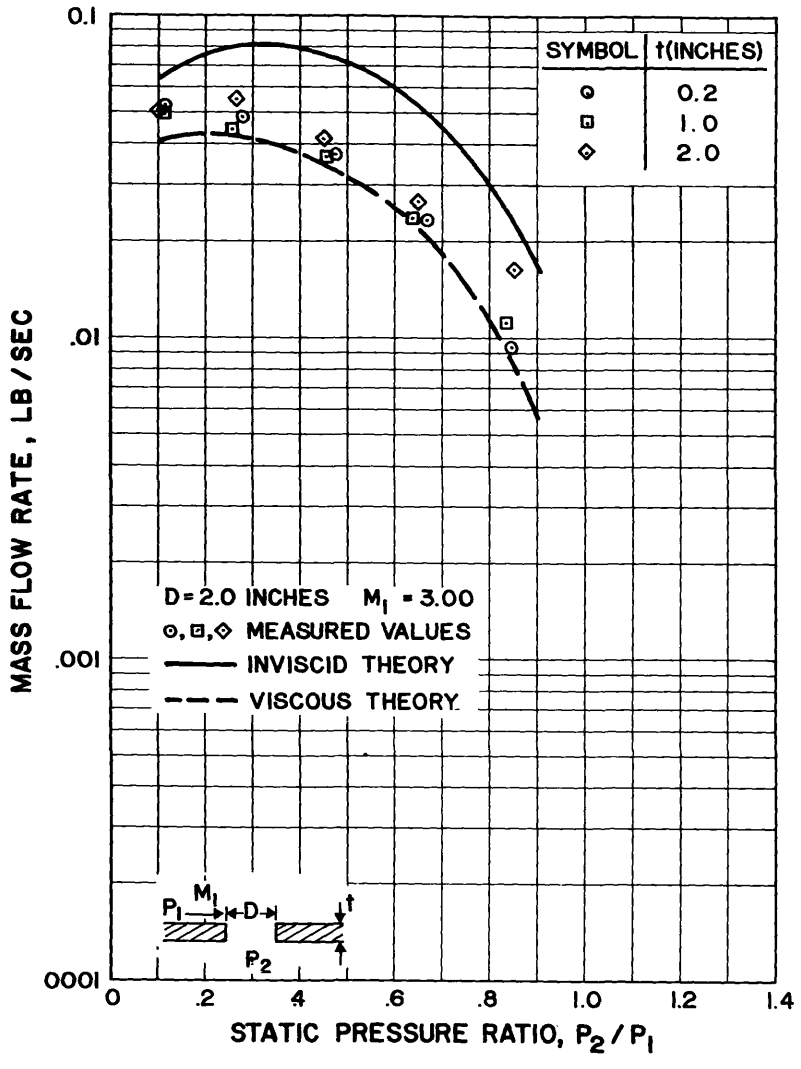

Figure 51. AEDC Orifice Flow Rates - D = 2.0 Inches

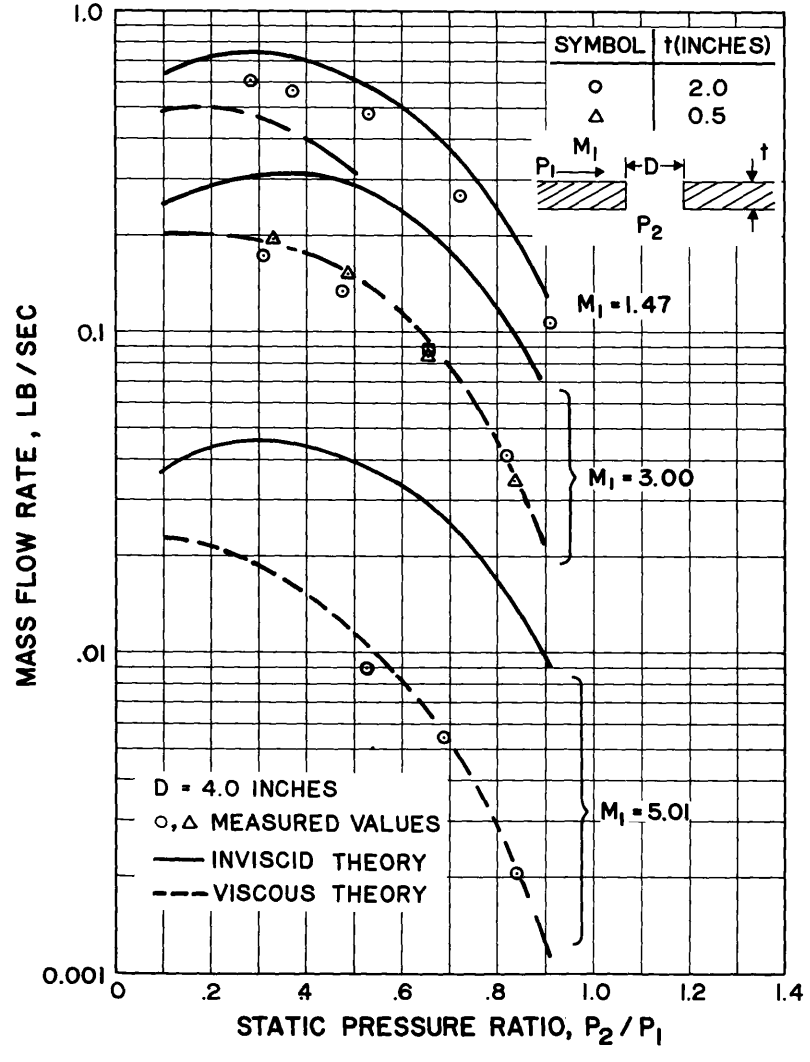

Figure 52. AEDC Orifice Flow Rates - D = 4.0 Inches

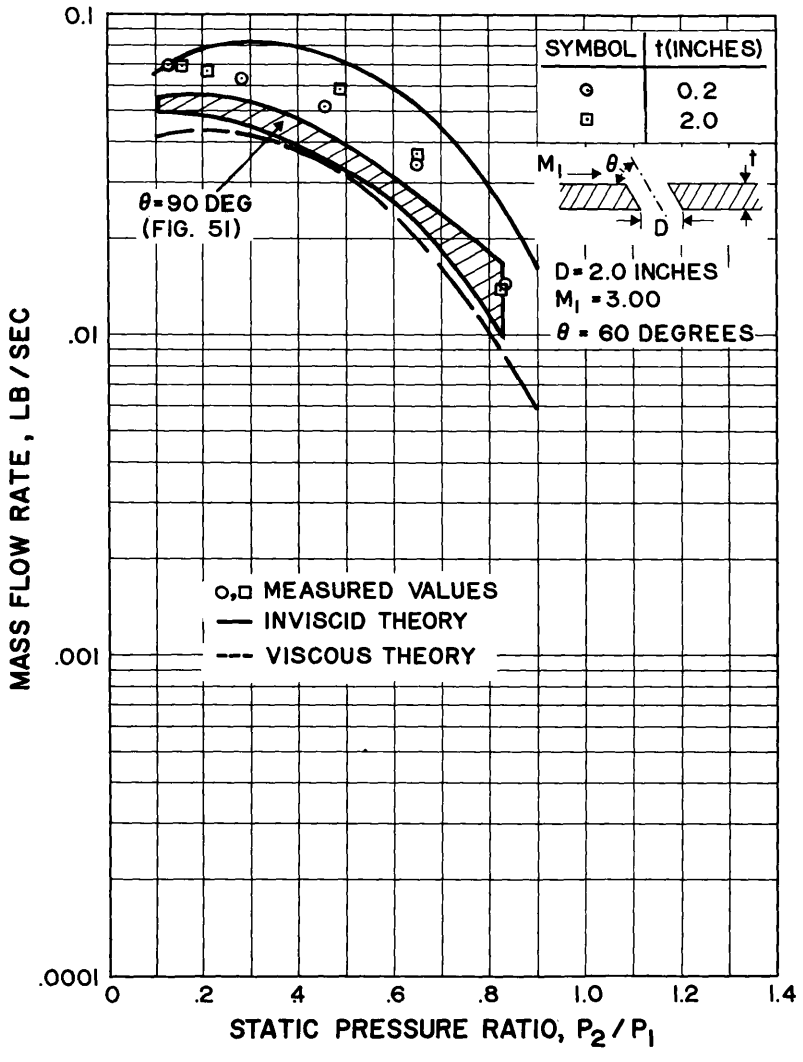

Figure 53. Effect of Orifice Obliquity on Flow Rates

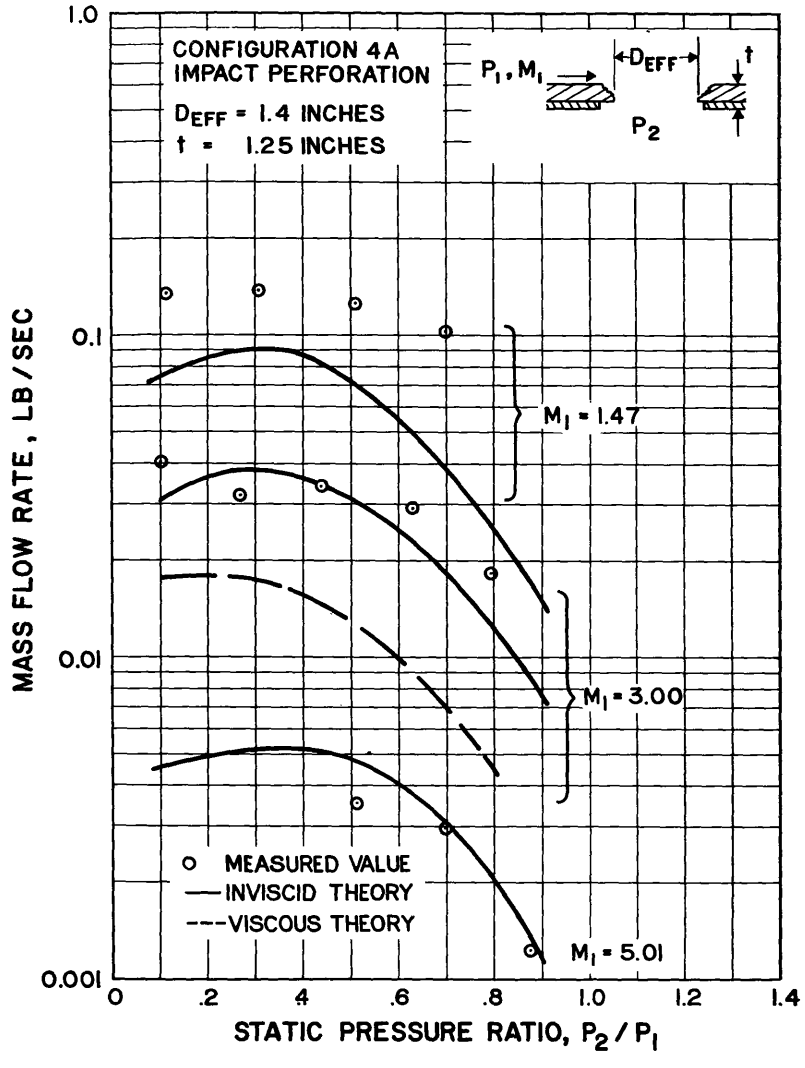

Figure 54. AEDC Orifice Flow Rates - Configuration 4A-Impact Perforation

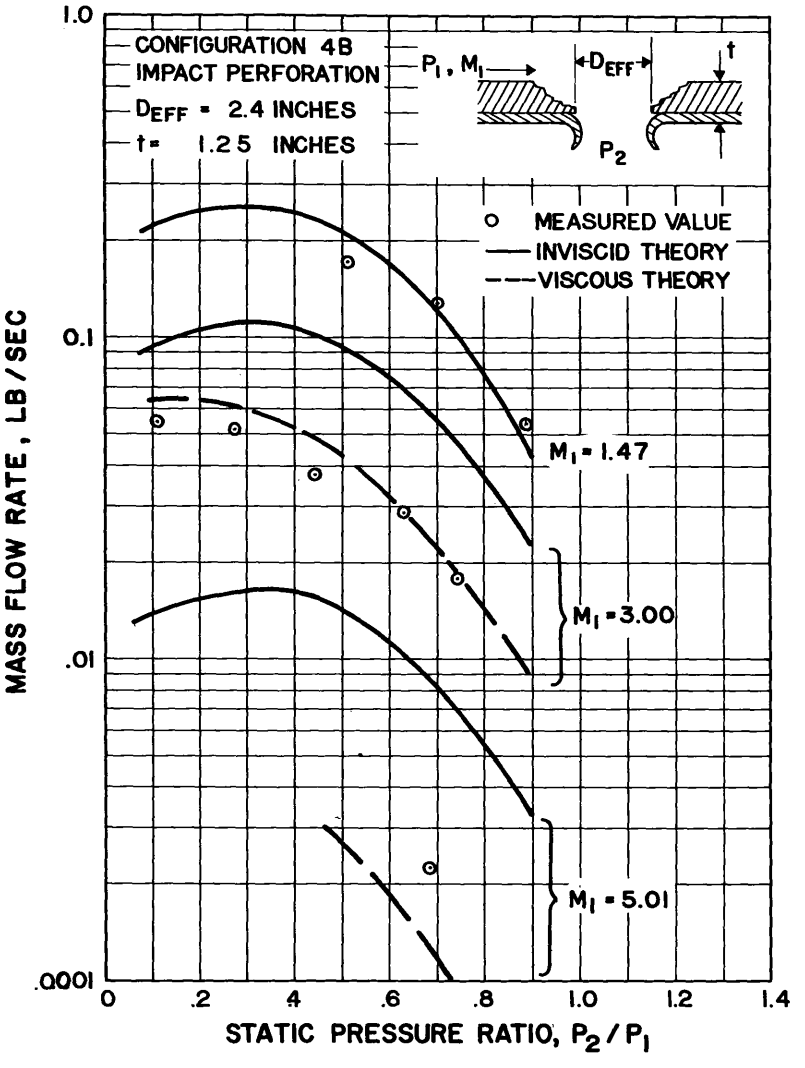

Figure 55. AEDC Orifice Flow Rates - Configuration 4B-Impact Perforation

is due to several possible causes, e.g., viscous effects due to the non-uniform velocity of the approach flow boundary layer, entropy losses due to impingement shock waves on the downstream orifice surface, and three-dimensional flow effects.

In an effort to improve the theoretical prediction of the data, an approximate method of allowing for viscous effects was devised. In this method, all the air striking the downstream edge of the orifice is assumed to enter the orifice as shown in the sketch below.

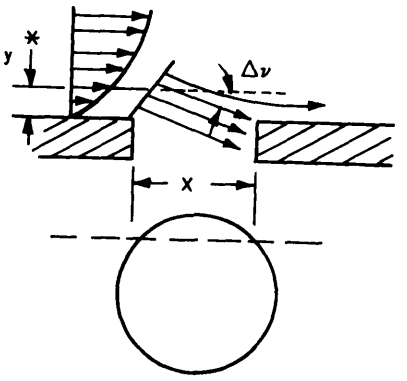

The limiting streamline which just hits the top corner of the downstream edge is assumed to have expanded through an angle $\Delta\nu$ corresponding to the local Mach number in the boundary layer at the particular height y^* of the limiting streamline. This height y^* is simply X tan $\Delta\nu$, where X is the chordwise dimension across the orifice. Since X varies across the orifice, y^* and $\Delta\nu$ must also vary. For purposes of simplification, it was assumed that an effective average value of y^* is given by:

$$y^* = 0.8\ D \tan \Delta\nu \tag{21}$$

in which 0.8 is a weighting factor to allow for the three-dimensional character of the flow. The flow rate entering the orifice per unit depth into the paper is then given by:

$$m = \int_0^{y^*} \rho U\, dy \tag{22}$$

whereas the corresponding inviscid value is:

$$m_{inv.} = \rho_e U_e y^* \tag{23}$$

Hence a viscous correction factor K_V may be defined:

$$K_V = \frac{m}{m_{inv.}} = \frac{1}{y^*/\delta} \int_0^{y^*/\delta} \frac{\rho}{\rho_e} \frac{u}{U_e}\, d\left(\frac{y}{\delta}\right) \tag{24}$$

The velocity profile was taken as the standard turbulent power law with n = 7:

$$\frac{U}{U_e} = \left(\frac{y}{\delta}\right)^{1/7} \tag{25}$$

and the density profile was determined from the Crocco distribution for a perfect gas and adiabatic wall conditions:

$$\rho/\rho_e = \left\{1 + \frac{\gamma-1}{2} M_e^2 \left[1 - \left(\frac{U}{U_e}\right)^2\right]\right\}^{-1} \tag{26}$$

Equation (24) for K_V was evaluated using $\gamma = 1.4$ and the following measured values of boundary layer thickness δ:

$M_1 = M_e = 1.47 \quad 3.00 \quad 5.01$

δ(inches) = 0.75 0.80 2.50

The corrected theoretical flow rate was then determined from the definition of K_V:

$$m = K_V \, m_{inv.} \tag{27}$$

in which m_{inv} corresponds to m of Equation (20) in the inviscid theory. The resulting values of m are plotted as dashed curves labelled "Viscous Theory" in Figures 50 through 55. Excellent agreement between measured flow rates and "Viscous Theory" predictions is seen to exist for $D \geq 2.0$ inches and $M_1 \geq 3.00$, for normal machined orifices (Figures 50, 51, and 52). No "Viscous Theory" is shown for D = 1.0 inches at $M_1 = 1.47$, as all of the flow was supplied by the subsonic portion of the boundary layer, for which the turning angle $\Delta\nu$ cannot be determined by the present method. The excellent agreement observed for normal orifices is admittedly somewhat fortuitous, as the "theory" does not predict any effect of orifice obliquity, which is obviously not the case (See Figure 53). Also, Figure 54 indicates that an actual impact perforation may give flow rates comparable to inviscid theory, being several times larger than the viscous theory prediction. This is due to increased flow rate caused by initial expansion in the outer surface spall area prior to final expansion through the orifice throat (See Figure 49). This particular conclusion applies only to an impact perforation of the Configuration 4A type, in which no petalling of the structure occurred. As seen in Figure 55, Configuration 4B (having structure petalling) gives a reduced flow rate due to increased flow resistance caused by the petalling. This effect approximately cancels the increased flow rate due to outer surface spall, resulting in reasonable agreement of viscous theory with measured flow rates.

The sensitivity of orifice flow rates to the approach boundary layer characteristics shows that no simple, accurate method exists for predicting these flow rates, even for machined orifices. An approximate theoretical method has been devised which agrees well with experiment and which also

appears to be the best way of estimating flow rates for impact perforations having petalling of the structure. This method was just developed in detail for the case of an adiabatic wall boundary layer, as existed in the AEDC tests. For the highly cooled wall boundary layers typical of re-entry conditions, Equation (26) must be replaced by the complete form of the Crocco distribution:

$$\frac{\rho}{\rho_e} = \left[\frac{T_w}{T_e} + \left(\frac{T_o - T_w}{T_e}\right)\frac{U}{U_e} - \left(\frac{T_o - T_e}{T_e}\right)\left(\frac{U}{U_e}\right)^2\right]^{-1} \qquad (28)$$

in which $T_o/T_e = 1 + \frac{\gamma-1}{2} M_e^2$. To allow for real gas effects, γ must be an effective value chosen to match the local state conditions.

D. Jet Profiles

Total pressure profiles were measured in the expanding jet entering the box for selected configurations, as indicated in Table 3. Surveys were made at several axial locations L along the jet, at 45 degree increments of the circumferential angle ϕ (See Figure 44). Typical pressure profiles are shown in Figure 56 for ϕ = 90 degrees at several values of L, for a 1 inch diameter orifice at M_1 = 1.47 and p_2/p_1 = 0.0938.* Lines of constant Mach number are superposed on Figure 56, at corresponding values of pressure ratio. A plot of constant Mach number contours is shown in Figure 57 for the same configuration and test conditions. This plot indicates that the jet is already beginning to approach an axisymmetric jet at only 0.75 inches from the exit plane of the orifice. The profiles show, however, that the axial velocity decay of the jet is much more rapid than that of an axisymmetric jet. The actual initial jet geometry as it is formed behind the shock wave at the downstream surface of the orifice is probably crescent-shaped, as shown in the following sketch.

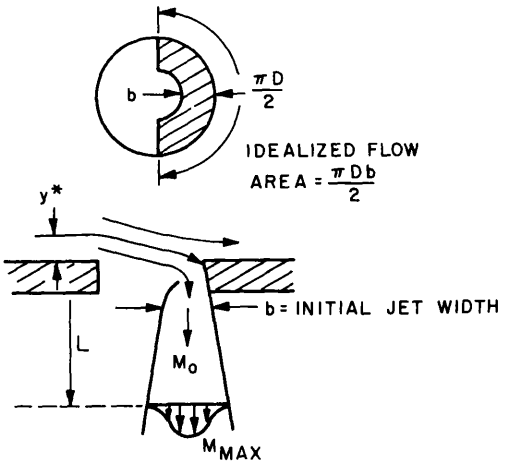

* A complete set of profiles is included in Reference 13.

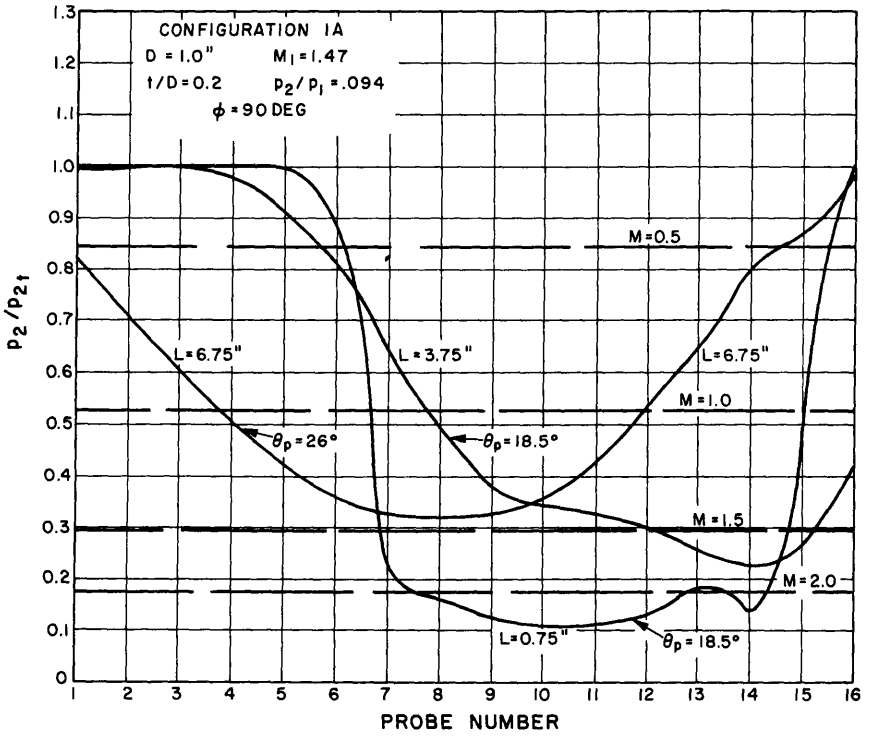

Figure 56. Typical Orifice Jet Pressure Profiles

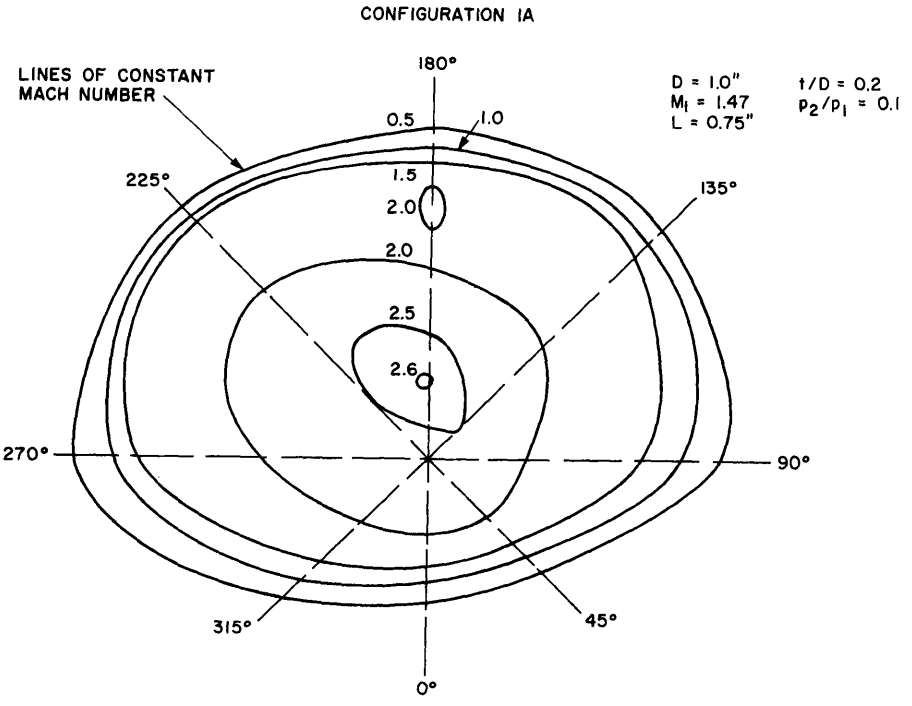

Figure 57. Typical Orifice Jet Mach Number Contours

Consequently, the jet decay should follow a two-dimensional jet decay pattern more closely than an axisymmetric jet decay. To test this hypothesis, an approximate initial jet width "b" was determined by computing the flow area $\frac{\pi Db}{2}$ from continuity requirements:

$$\frac{\pi Db}{2} = \frac{m}{\rho_2 U_2} \tag{29}$$

in which measured values of the flow rate m were used. The value of $\rho_2 U_2$ was computed by isentropic expansion to box pressure p_2 from stagnation conditions corresponding to the limiting streamline within the approach flow boundary layer at y*, as was the initial jet Mach number M_o before diffusion. The maximum Mach number M_{max} within the jet at various axial distances X was determined from the survey profiles. These values of M_{max} are plotted vs. X for the $M_1 = 3.0$ surveys in Figure 58. The jet velocity decay ratio U_{max}/U_o was computed from the Mach number ratio M_{max}/M_o with the assumption that a constant stagnation temperature existed everywhere in the jet. (True because the total temperature of the tunnel flow equalled ambient temperature within the box.) The resulting correlation of U_{max}/U_o vs L/b is shown in Figure 59. Also shown is a mean correlation line of two-dimensional jet decay data of Olsen (Reference 14) for rectangular slots of 12 to 1 aspect ratio, tested at $M_o = 0.66$ to $M_o = 2.0$. Olsen's data show that the rate of velocity decay for two-dimensional jets is independent of the initial Mach number M_o, in contrast to the axisymmetric jet. The correlation of Figure 59 appears to be weak for the thicker orifice plate (t/D = 2), perhaps because of the neglect of shock losses in total pressure which are more predominant for thicker orifices. However, the basic jet decay characteristics of jets formed by expansion of supersonic tangential approach flow through an orifice have been shown to correlate using a two-dimensional decay law. The use of axisymmetric jet diffusion data based on L/D would grossly overestimate the velocity at a given downstream station.

Further insight into the characteristics of the expanding jets was derived from a study of the oil film pictures. Typical photographs of such patterns are shown in Figures 60 through 63*. In Figure 60, two separate jets appear to intersect each other, causing a mutual deflection of their flows towards a common final direction (see sketch).

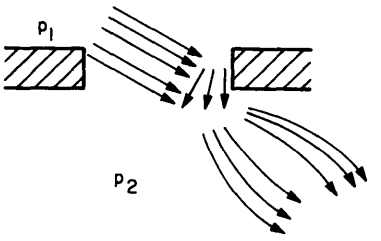

* A complete set of oil film photographs is included in Reference 13.

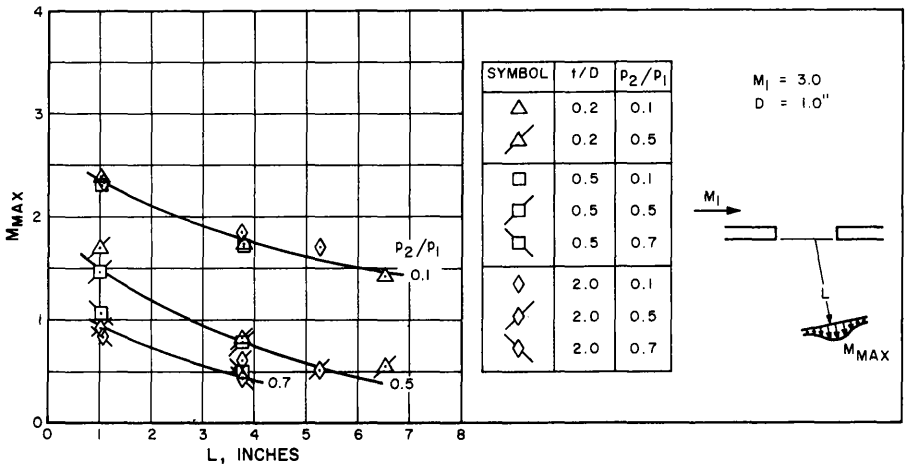

Figure 58. Maximum Orifice Jet Mach Numbers

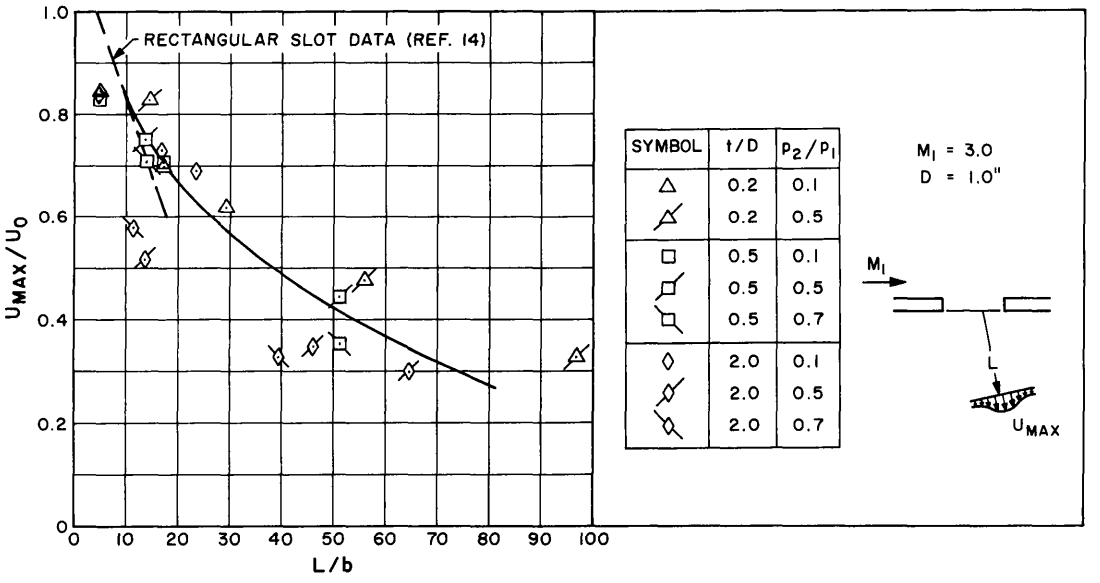

Figure 59. Orifice Jet Velocity Decay Correlation

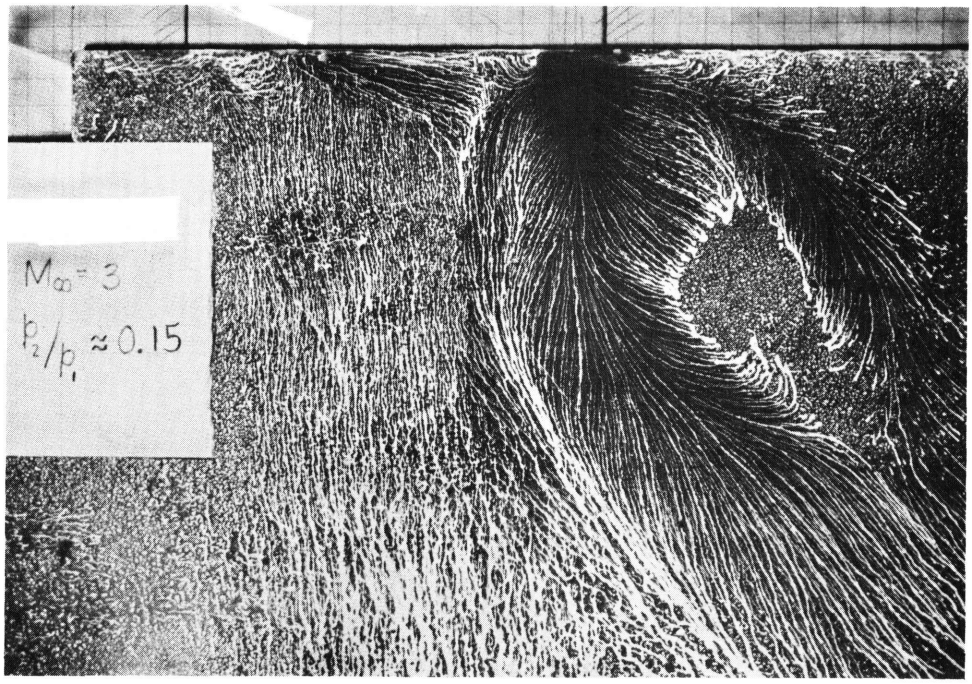

Figure 60. Oil Flow Photograph - Configuration 3A- Large Flow Deflection

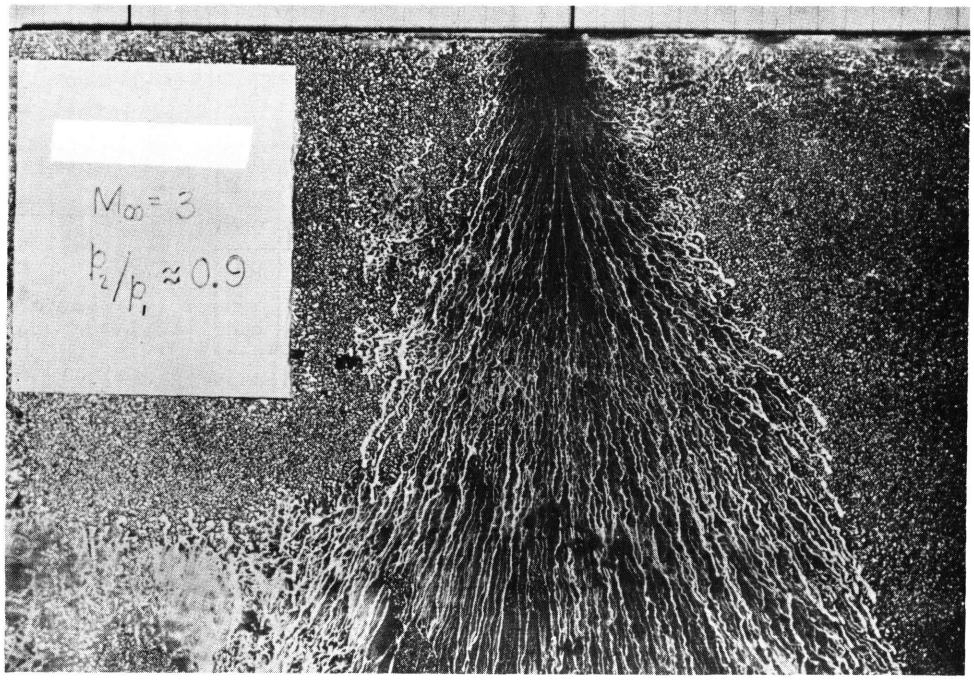

Figure 61. Oil Flow Photograph - Configuration 3A - Small Flow Deflection

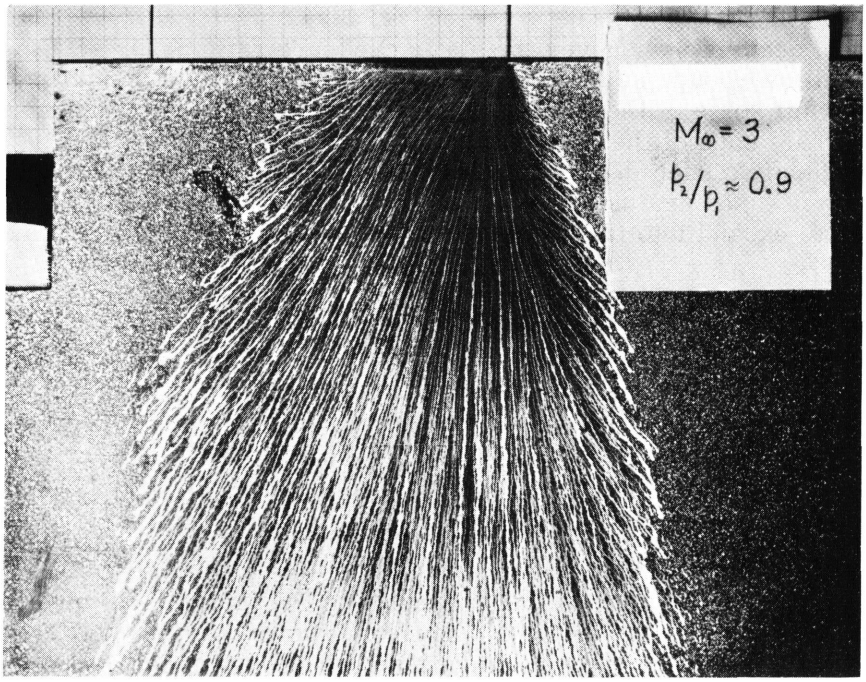

Figure 62. Oil Flow Photograph - Configuration 3B

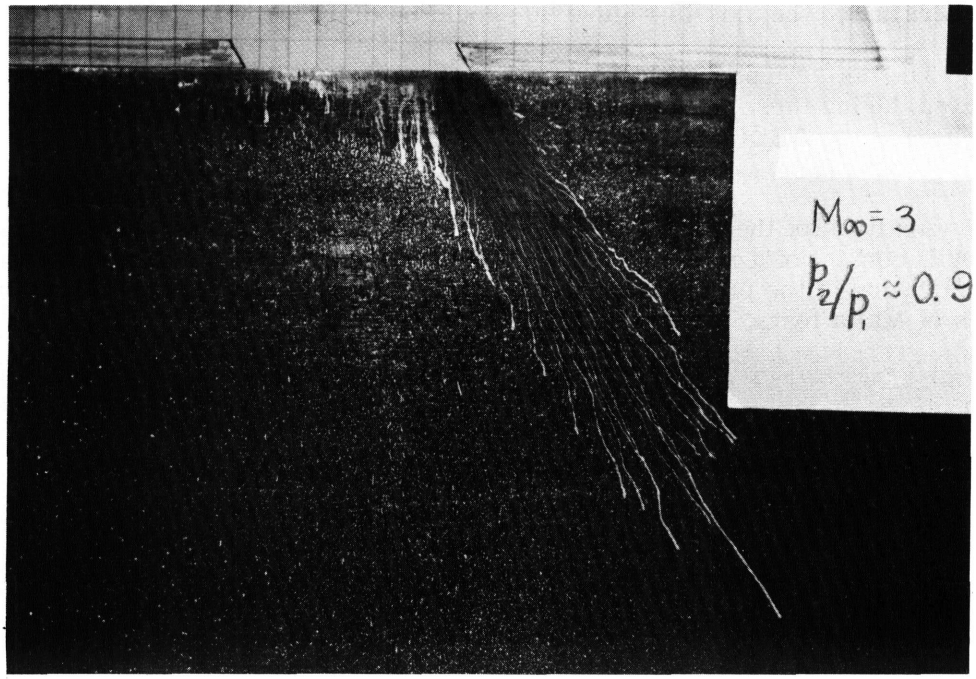

Figure 63. Oil Flow Photograph - Configuration 5A

This pattern occurred whenever the static pressure ratio p_2/p_1 across the orifice was reduced low enough such that the Prandtl-Meyer expansion angle was sufficiently large to permit some of the flow to enter the box without first compressing against the downstream edge of the orifice. In contrast, Figure 61 shows that when p_2/p_1 was close to unity, such that the Prandtl-Meyer expansion angle was small, all of the flow compresses against the down stream edge of the orifice, and then turns 90 degrees to expand into the box as illustrated in the following sketch.

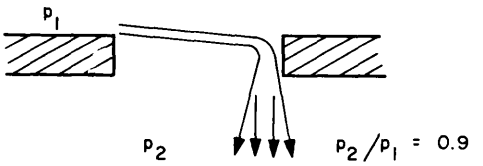

Figure 62 shows that for a thicker orifice plate (t/D = 0.5), the flow was actually turned back upstream slightly, apparently due to the asymmetric effect of the longer solid boundary during initial expansion of the jet after compression against the downstream edge of the orifice. Figure 63 shows that the jet direction follows the orifice inclination, for an oblique orifice of θ = 60 degrees.

Care must be taken in interpreting the oil flow patterns. When the tunnel flow was stopped after each run, the test pressure suddenly built up to atmospheric while the box pressure remained low. This sudden large pressure difference caused flow into the box parallel to the orifice axis, resulting in a "shut-down" oil flow superposed on the oil flows obtained during the run. Thus, the faint lines parallel to the axis in Figure 60 should be disregarded.

The deflection of the entering flow through a 90 degree angle for $p_2/p_1 \approx 1$ observed during these tests is in full agreement with the location of the maximum heat flux for the AEDC and Malta internal heating tests discussed in Sections I and II.

Analysis of the AEDC orifice tests is complete. Future study in this area will consist of a re-examination of the NOL orifice flow coefficients, and an application of the present results to the analysis of the previous and present series of Malta tests, as well as Wallops Flight Test Two.

VI. STRUCTURAL STUDIES

A. Introduction

Previous investigations into the types of structural failures associated with hypervelocity impact damage dealt with the effects of a nose puncture causing high internal pressures, and a cone puncture, in which uniform heating of the structure was assumed.

The present investigations are concerned with the effects of openings caused by impact or by local melting subsequent to impact, with no substantial pressure differential present across the wall of the re-entry vehicle. Failure under these conditions is due to loss of section and/or general instability of the structure under re-entry loads. The overall objective was to develop a semi-empirical method of predicting the residual strength of a cylindrical section subjected to a rather large, unstiffened opening. A minimal test program was conducted in support of the analytical efforts.

B. Failure Modes

While it is apparent that a particle meeting a re-entry vehicle with high velocity can produce an opening of various possible geometric description, certain ground rules were established in regard to the type of openings that should be considered in a preliminary evaluation of the structural consequences. The primary ground rule was that the structural effect of a random opening could be approximated by considering rectangular, circular, or elliptical openings, or combinations thereof. It also is very likely that any enlargement of the initial opening or creation of new openings due to thermodynamic effects will follow these same classes of geometries.

On this basis, the openings selected for investigation were rectangular or circular, or combinations thereof, with axes running axially and circumferentially. Generally speaking, in the investigative studies, one dimension of the opening would be held constant while the other was gradually increased so as to simulate the structural deterioration associated with the thermodynamic enlargement of the original puncture.

Openings that are largely axial in nature, that is, having the length of the opening several times greater than the width, can be caused by an original puncture enlarging in the axial direction due to re-entry heating. The most likely mode of failure would be through the general instability of the section under compressive re-entry loads. The increased instability effects would be magnified by any loss of section related to the circumferential size of the opening.

Openings that are large circumferentially and small axially are of less importance due to the decreased likelihood of their occurrence. Such openings could be formed by a penetration immediately forward of a heavy ring or bulkhead. If the heating effects could not burn through the ring, then the opening would enlarge circumferentially along the outer perimeter of the ring. Failure in such a case could be caused either by instability or loss of section depending primarily on the axial length of the opening.

Rectangular and circular openings which combine to form key-hole shaped openings are also considered to be important on the basis of results of thermodynamic tests (e.g., see Figures 17 and 20 of Section II). The complexities of such

combinations necessitate experimental determination of their structural consequences. While it is anticipated that a rather elaborate test program would be necessary to develop any reliable method of determining the attendant reduction in structural capacity, the minimal structural testing subsequently described provides valuable information on several types of openings in cylindrical specimens.

C. Description of Test Program

Test Specimens

Test specimens were fabricated from sheet Dupont Mylar, Type "A", by wrapping the material on a collapsible mandrel and joining the edges together in an axial lap seam of approximately 1/8 inch in width. The seam juncture was effected by using a heat curable Dupont adhesive #4684 and pressure along the seam applied by clamps. The entire assembly was subjected to oven cure of 1/2 hour at a temperature of 125°F. After cooling, the assembly was unclamped, the mandrel was collapsed, and the cylinder was removed. Openings in the cylinder wall were cut with an X-Acto knife and suitable templates.

The ease of fabricating the Mylar cylinders and the exceptional elastic properties of the material makes Mylar particularly well suited to such testing. Mylar can withstand a large amount of strain without permanent set, and will recover elastically several times from a buckling test. Thus, one cylinder would be used for a number of tests by gradually enlarging the opening after each individual test. The behavior of Mylar test specimens up to the buckling point is representative of that of metal specimens, inasmuch as Mylar has very nearly isotropic mechanical properties (according to the manufacturer), and a linear stress-strain relationship.

Certain difficulties were also encountered in the use of sheet Mylar to fabricate the test specimens. The fact that a lap seam was required in the fabrication adds an imperfection to the specimen which may alter its buckling characteristics. It was observed during the actual testing that the buckles propagated freely across the seam, and so it is concluded that the lap seam had only a minor structural effect.

Mylar is available only in sheet form up to a maximum nominal thickness of 15 mils. This limits the range of cylinder radius to thickness ratios that can be accommodated by the test fixture using the presently available cylinder mounting and manufacturing components. An R/t ratio of 360 was obtained by using for all tests a material of nominal 10 mils thickness, which was found to be actually 9 mils when checked with micrometer calipers. Dimensions of the test specimens were:

L = 10.4" Free length between mounting rings

R = 3.25" Nominal radius of cylinder and mounting rings

t = .009" Wall thickness

Equipment and Technique

The test setup is shown in Figure 64. The ends of the test specimen are held with edges fixed by an inner steel ring and an outer segmented steel ring of

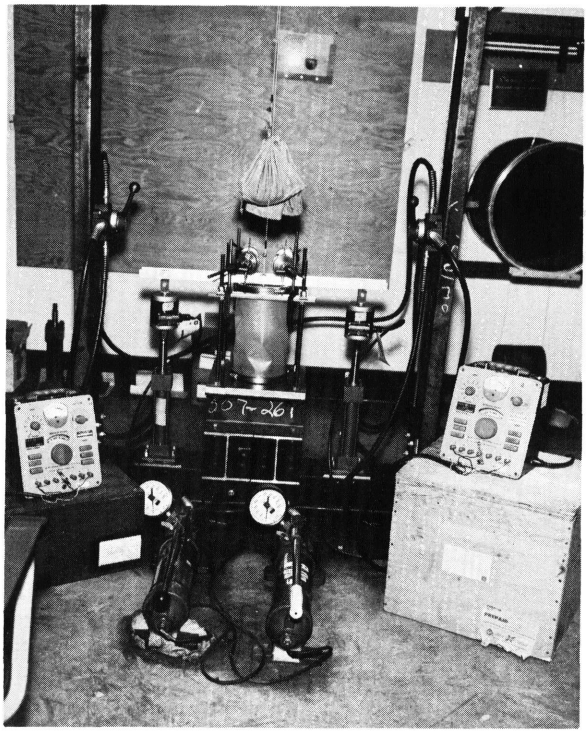

Figure 64. Cylinder Buckling Test Set-up

proper radii. The rings, with the Mylar test specimen sandwiched between them, are drawn together by a large diameter hose clamp. The bottom inner ring is rigidly bolted to the base plate while the top inner ring is bolted to a length of aluminum-alloy channel. Load is applied to the test specimen through the aluminum channel by means of two hydraulic cylinders. The load is calibrated by two Baldwin-Lima-Hamilton load cells of 50 pounds capacity mounted on the piston rods of the hydraulic cylinders and pin-connected to the aluminum channel. Four dial gages mounted 90^{o} apart and bearing on the upper clamping ring measure the vertical motion of the upper end of the test specimen. The dead weight of the fixture elements bearing on the Mylar cylinder is counter-balanced using a bag of lead shot carried on a flexible cable from the loading bar and over a pulley.

Each load cell output is monitored by a Baldwin SR-4 indicator. The hydraulic cylinders are activated by hand pumps, the load being alternately applied to opposite ends of the loading bar in increments that become increasingly smaller as the critical load is approached. Axial loading is achieved by applying equal load increments in a downward direction to each end of the loading bar. Bending load results from equal load increments being applied in opposite directions at the ends of the loading bar. Testing proceeds until failure was indicated by the sudden formation of buckles and the inability of the specimen to carry additional load. For each loading of a test cylinder, the readings of the four dial gages are recorded.

Test Procedure

The general procedure was to test each uncut specimen for both the critical axial and bending loads before subjecting the cylinder to the smallest desired cutout. The opening is enlarged upon the completion of each test until the maximum desired dimensions are reached.

The narrow axial openings were 1/8 inch wide circumferentially with rounded corners. The length of axial openings ranged from 1/2 the cylinder radius (1.625") to twice the radius (6.50"). One specimen was axially tested with diametrically opposite axial openings of 4.875" in length.

The initial circular opening was cut from a template 1.625" in diameter. This was subsequently enlarged into a key-hole shaped opening by adding a narrow axial opening of 1.625" in length, making a total axial length of opening of 3.25". The next circular opening was then cut 3.25" in diameter and so on. The final opening considered was key-hole shaped with the circular portion 4.875" in diameter and a narrow opening of 1.625" in length.

D. Test Results

The per cent of original structural capacity is tabulated in Tables 4 and 5 for the individual cylinders for all types of openings. In the case of cylinders with narrow axial openings, it was necessary to average the results of the three cylinders tested. The plotted results are shown by the solid-line curves in Figures 65 and 66. The tabulated results from the key-hole shaped openings were not graphically represented because they did not vary significantly from the cases with circular openings. Photographs of selected specimens are shown in Figures 67 through 70.

TABLE 4. STRUCTURAL TEST RESULTS FOR NARROW AXIAL OPENINGS

Cylinder Number	a/R	P_{CR}(lb)	% Original Axial Capacity	M_{CR}(in-lb)	% Original Moment Capacity
30	0	82	100	246	100
	.5	68	82.9	210	85.4
	1.0	52	63.4	123	50.0
	1.5	72.5	88.4	132	53.7
	1.5*	70.0	85.4		
10B	0	58	100	150	100
	.5	---	---	---	---
	1.0	65	112.0	120	80.0
	1.5	82	141.3	168	112.0
31	0	60.5	100	174.0	100
	.5	70.0	115.7	96.0	55.2
	1.0	55.5	91.6	96.0	55.2
	1.25	57.5	95.1	---	---
	1.50	79.0	130.7	162.0	93.1
	2.00	59.0	97.5	120.0	69.0
Average of Cylinders 30, 10B, & 31	0		100.0		100.0
	.5		96.9		72.9
	1.0		86.1		59.5
	1.25		95.1		---
	1.50		116.4		81.1
	2.00		97.5		69.0

a = axial length of opening
R = cylinder radius
*Two diametrically opposite axial openings

TABLE 5. STRUCTURAL TEST RESULTS FOR CIRCULAR AND KEY-HOLE SHAPED OPENINGS

CYLINDER NUMBER 32B

Shape of Opening	β-Angular Opening (Deg)	P_{CR} (lb)	% Original Axial Capacity	M_{CR} (in-lb)	% Original Moment Capacity
None	0	80.0	100	264	100
Circular	28.65	58.5	73.1	126	47.7
Key-Hole	28.65	58.0	72.5	114	43.2
Circular	57.30	53.0	66.3	84	31.8
Key-Hole	57.30	50.5	63.1	90	34.1
Circular	85.95	38.0	47.5	36	13.6
Key-Hole	85.95	32.0	40.0	36	13.6

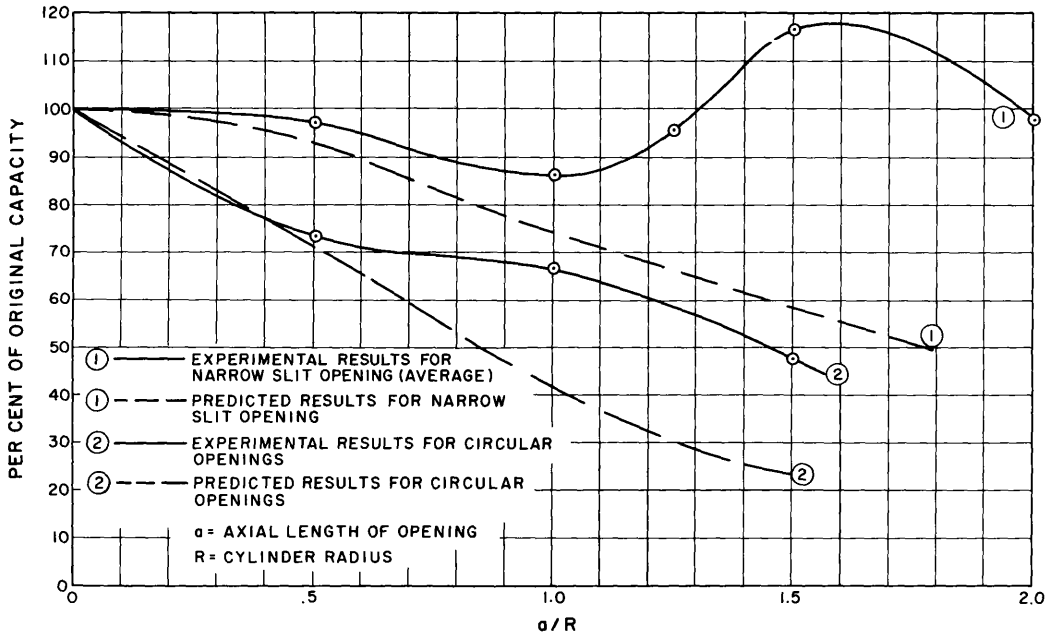

Figure 65. Comparison of Test and Predicted Results - Percent of Original Axial Capacity

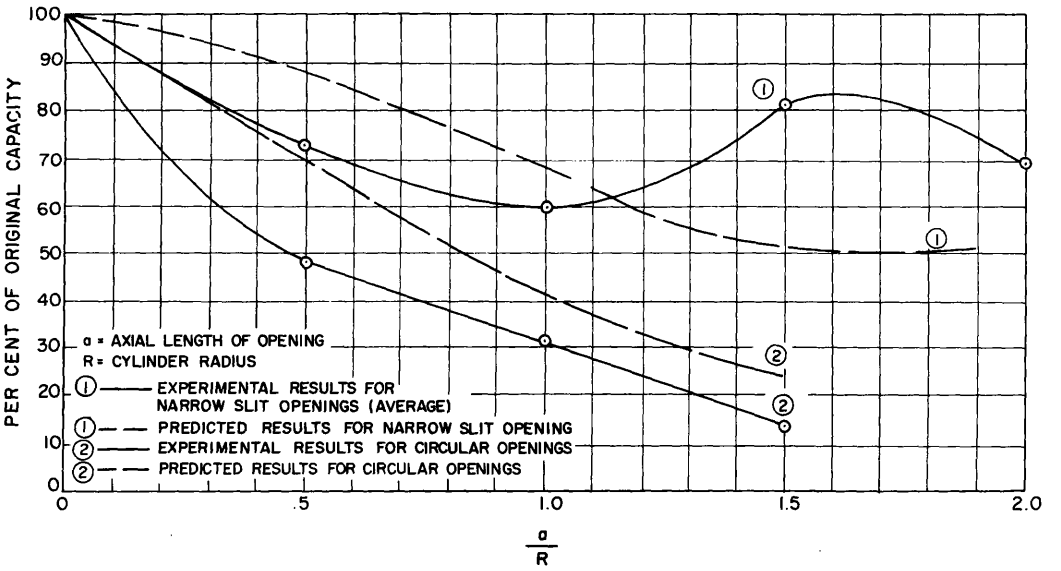

Figure 66. Comparison of Test and Predicted Results - Percent of Original Moment Capacity vs a/R

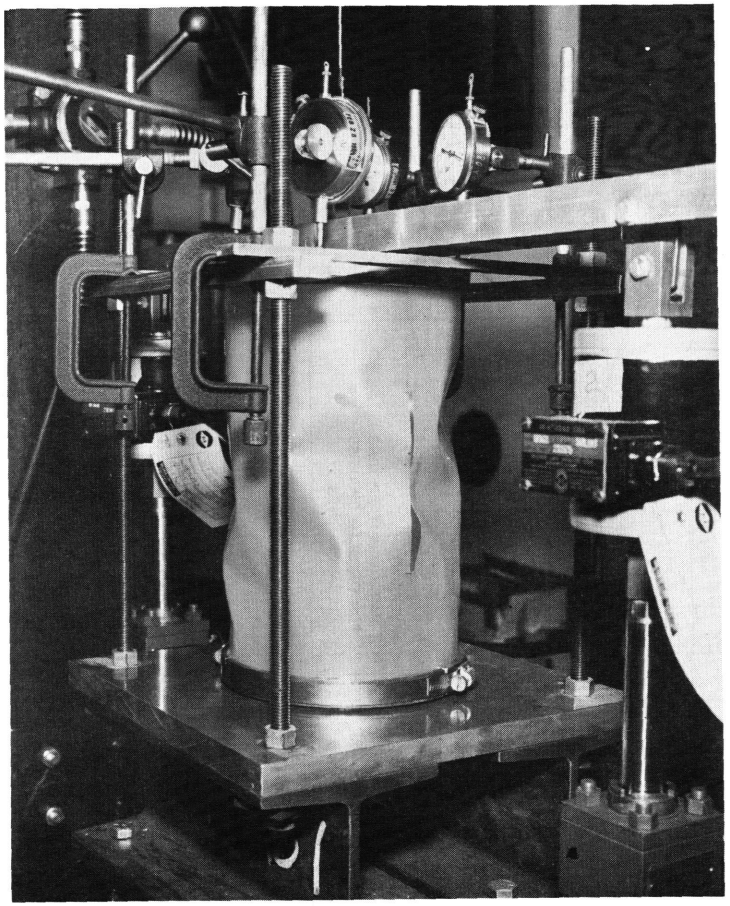

Figure 67. Cylinder at Failure Under Axial Load. Narrow Slit Opening, a/R = 1.5

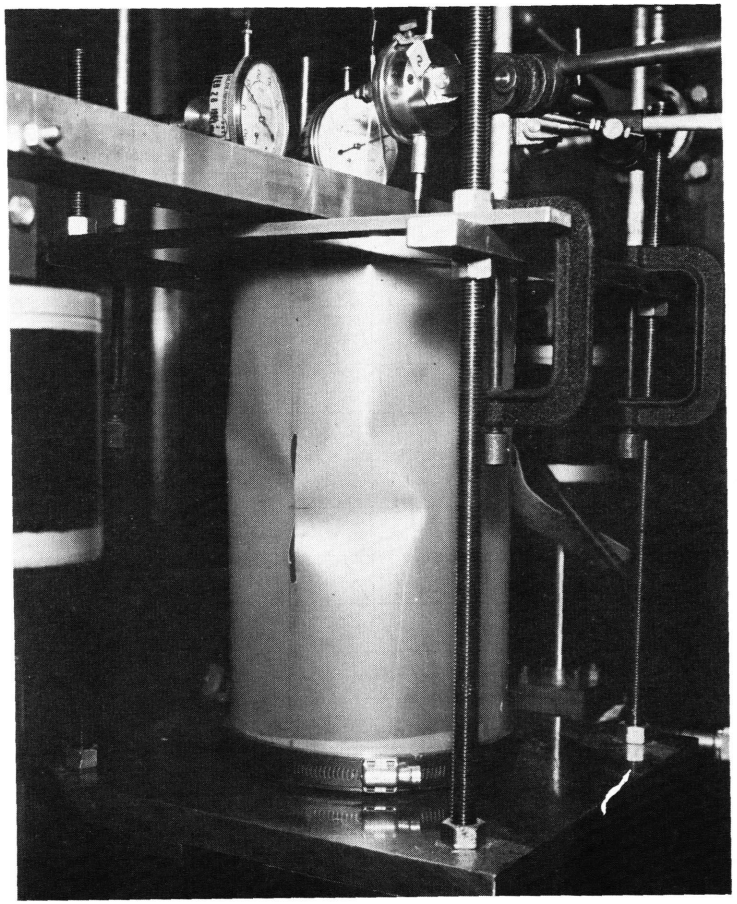

Figure 68. Cylinder at Failure Under Bending Load. Narrow Slit Opening, a/R = 1.0

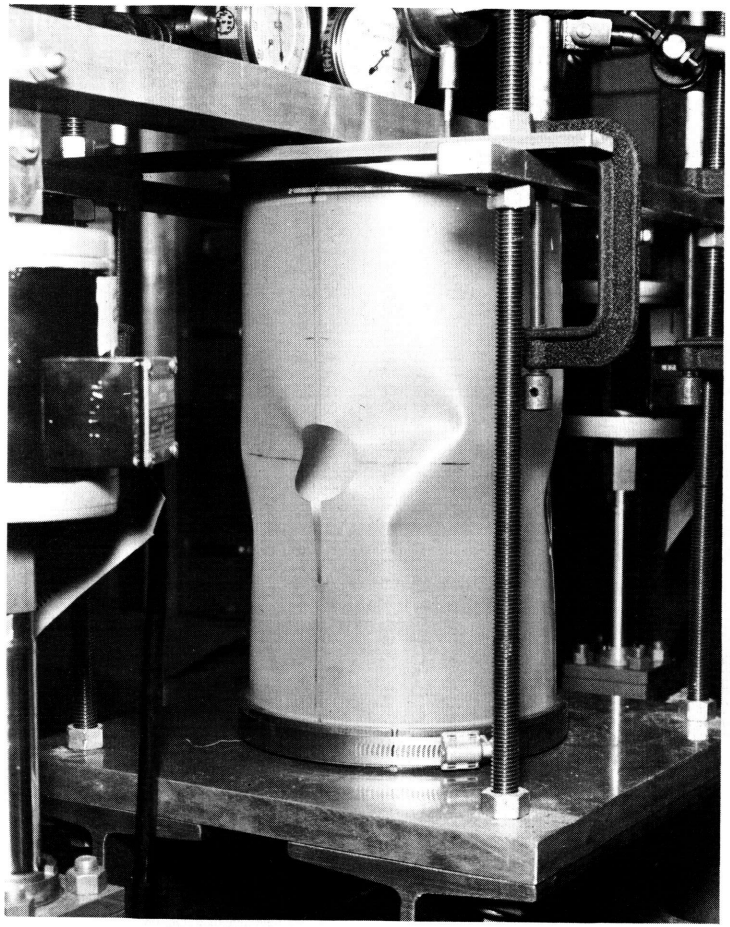

Figure 69. Cylinder at Failure under Axial Load. Keyhole Opening, Total Length = 3.25 Inches

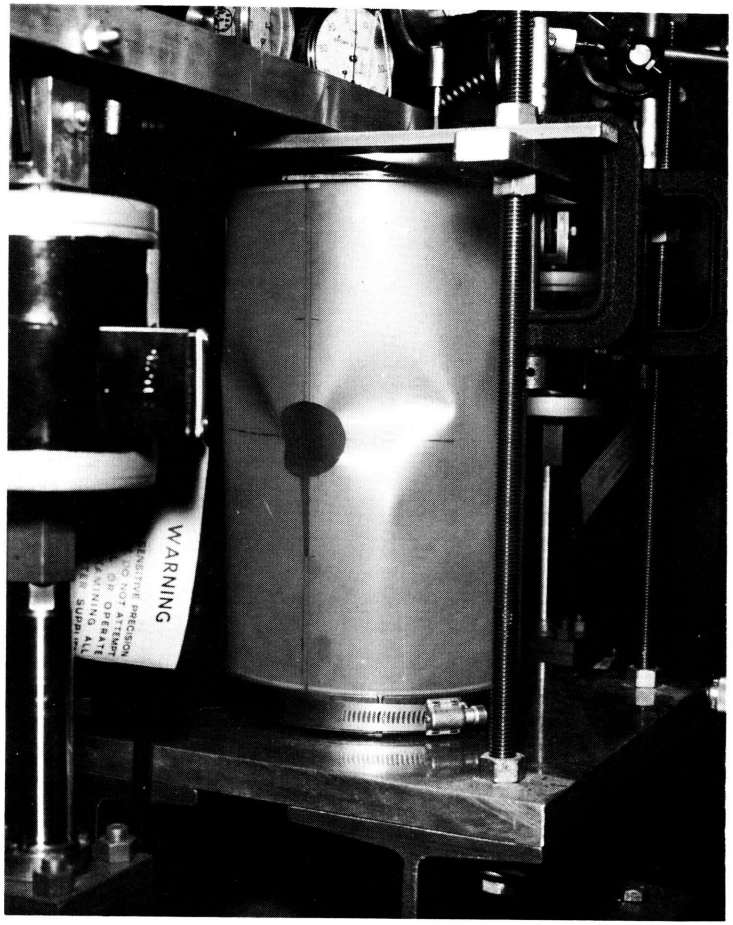

Figure 70. Cylinder at Failure under Bending Load. Keyhole Opening, Total Length = 3.25 Inches

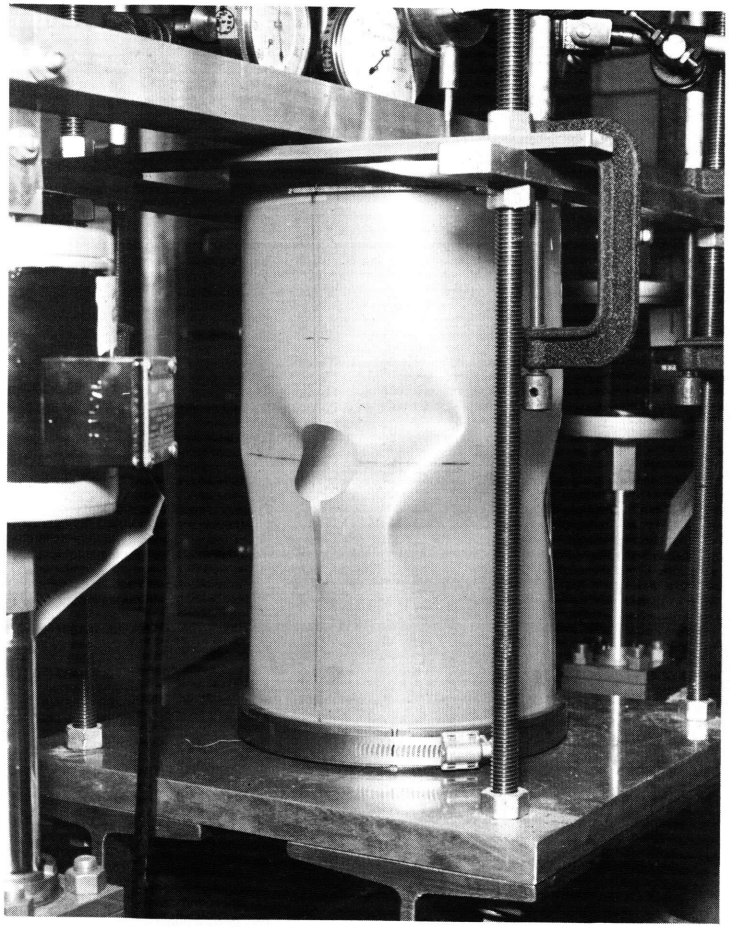

Figure 69. Cylinder at Failure under Axial Load. Keyhole Opening, Total Length = 3.25 Inches

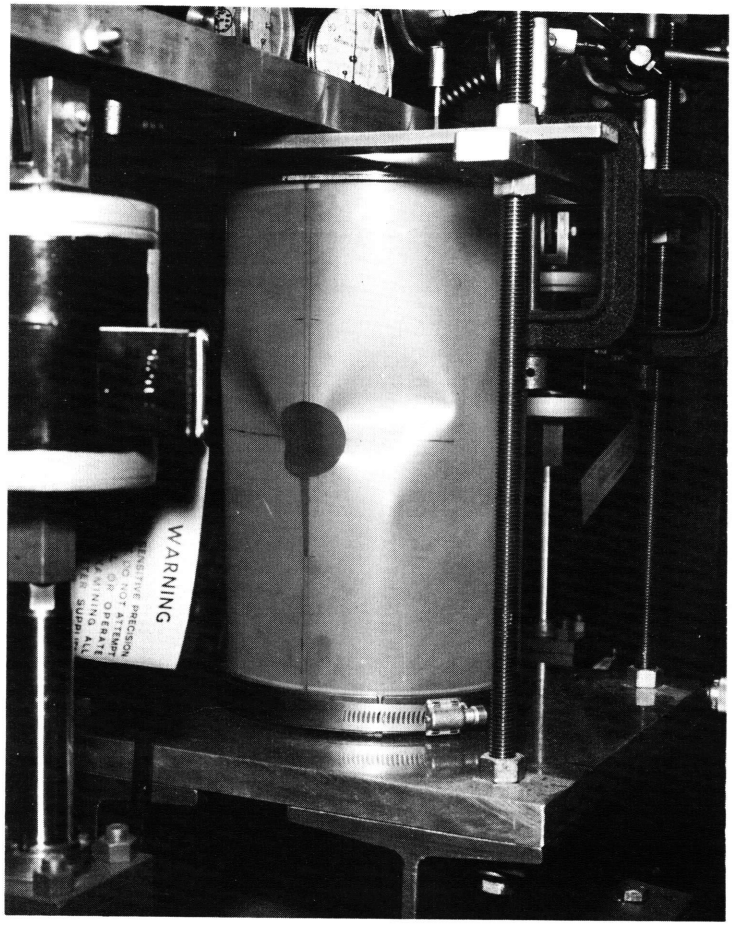

Figure 70. Cylinder at Failure under Bending Load. Keyhole Opening, Total Length = 3.25 Inches

E. Analysis

As previously mentioned, a portion of the investigative studies consisted of devising analytical methods for predicting the residual strength of cylindrical monocoque sections subjected to simple, unstiffened rectangular openings. This is considered to be the closest practical analytical approach to the structural problems associated with hypervelocity particle impact damage to present day operational re-entry vehicle designs.

The openings that have been investigated analytically are considered to be the structural equivalent of a small hole punched in a re-entry vehicle and the attendant structural deterioration for some distance aft or circumferentially due to aerothermal heating effects.

Existing techniques were not found that would enable the prediction of the residual strength of cylinders with unstiffened cutouts. The analytical approach taken was to draw an analogy between plate buckling and shell buckling in which the percent of the original buckling strength of a plate subjected to an opening was considered to be the same as for a cylinder with an equivalent opening. In such an analysis, it is assumed that the area of the shell immediately adjacent to the opening will buckle in the same manner as a plate simply supported on three sides and free on the fourth side (which is the edge of the opening). The cylinder is considered to have failed when this "plate" buckling occurs. The per cent of original buckling capacity of the cylinder corresponds to the ratio of buckling strengths of a plate simply supported on three sides and the same size plate simply supported on four sides. The same basic method is employed regardless of whether the cylinder is subjected to moment or axial load. The loss of section attendant to a circumferential cutout dimension and any resultant eccentricity of axial loading is taken into account in all calculations.

Figure 71 shows the actual structure and the analogous plate structure considered in this analysis. It will be noted that the total effective width of the analogous plate is the same for both the original and the weakened conditions. This is to insure that the reduction of buckling capacity is caused primarily by the loss of section and the loss of support at the edge of the cutout rather than being a function of the difference in effective width of the analogous plates. Even so, it is necessary to provide an estimate of the effective plate width as a function of cylinder radius that can be associated with any cutout having an angular opening β. This knowledge enables the comparison of the residual strength of the structure with the size of opening as presented in Figures 65 and 66.

A short cylinder subjected to axial load tends to behave as a wide plate column with sinusoidal buckling. Here, the effective width of an analogous plate structure can be taken as the total circumference of the cylinder. Longer cylinders such as those considered in this analysis which buckle in the characteristic diamond pattern will have much smaller effective widths. Several empirical formulas have been devised that give the buckling strength of cylinders as the sum of the plate buckling strength and that strength which is derived from the curvature of the elements. The one proposed by Kanemitsu and Nojima (Reference 15) is

$$\frac{\sigma_{CR}}{E} = 0.16\left(\frac{t}{L}\right)^{1.3} + 9\left(\frac{t}{R}\right)^{1.6} \qquad (30)$$

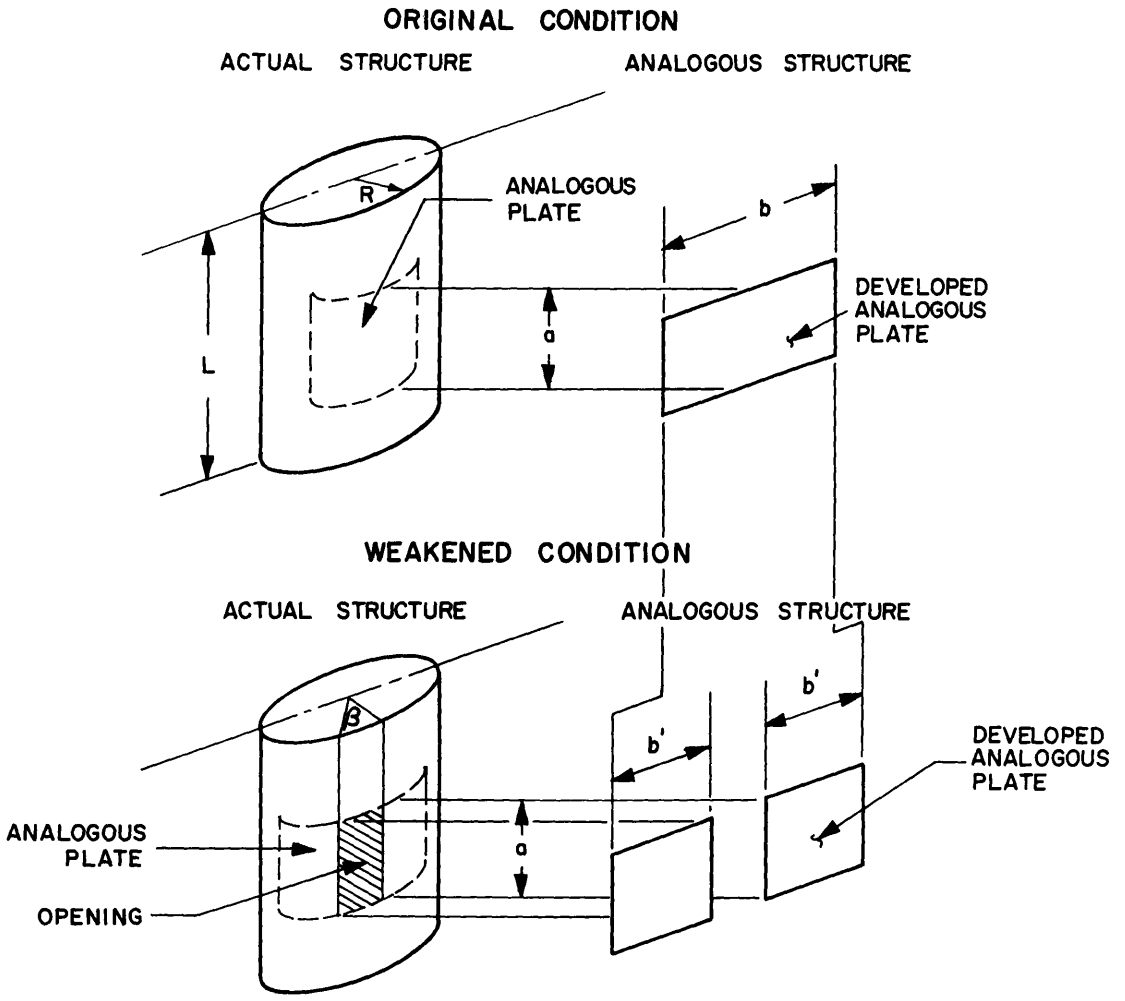

Figure 71. Analogous Structure Concept

b = the effective width of original "analogous plate" = 2b'
b'= the effective width of each of the weakened analogous plates
a = the length of "analogous plate"
β = angular opening in cylinder

where the $(\frac{t}{L})^{1.3}$ parameter is appropriate for a flat plate. The effective width for the cylinders under consideration is taken as that width which will yield a simply supported plate buckling stress equal to

$$\sigma_{CR} = 0.16\, E(\frac{t}{L})^{1.3} \tag{31}$$

Since the edges of the analogous plate parallel to the load are restrained from circumferential movement by the remainder of the shell, the normal plate buckling coefficients were reduced by a factor of $\frac{2.54}{3.62} = 0.701$ as indicated in Reference 16. The effective width of the Mylar test cylinders under axial load is calculated to be 3.7 inches. The central angle subtended by an arc length of 3.7" is 65.3°, which is a reasonable value for a cylinder with an L/R ratio of 3.2. As the L/t ratio increases, the effective width decreases to the point where Euler buckling occurs unaccompanied by local buckling.

In cylinders subjected to bending, it is known that the critical stress in bending is 30 to 40 per cent higher than the critical axial stress for the same cylinder (References 17 and 18). The effective plate width in bending, b_b, is then taken to be the width of simply supported plate associated with an axial buckling stress of

$$\sigma_{CR} = 1.3\left[0.16E\,(\frac{t}{L})^{1.3}\right] \tag{32}$$

For a cylinder of 10.4 inches in length and wall thickness of 0.009 inches, b_b is calculated to be 3.1 inches. This method of determining the effective width of analogous plate is, of course, empirical and approximate and should be used only within the limitations set for Equation (30): $(0.1 < \frac{L}{R} < 1.5;\ 500 \leq \frac{R}{t} \leq 3000)$. It will be noted that the test cylinders do not exactly meet these requirements; nevertheless, the calculated results are sufficiently close to the test results so as not to invalidate the method. Of equal importance is the fact that the original condition buckling stress predicted by Equation (30) is within the range of those encountered experimentally.

The standard equation (Reference 19)

$$\sigma_{CR} = K\,\frac{E}{1-\mu^2}\,(\frac{t}{b})^2 \tag{33}$$

is used to predict the buckling strengths of the analogous plates. Here, "K", the compressive buckling coefficient, is a function of the dimensions of the plate and the conditions of support and edge loading. "E", "t", and "μ" are, respectively, the modulus of elasticity, thickness, and Poisson's ratio of the plate material.

Depending on the condition and loading of the analogous plate under consideration, "b" can be either b_a, b_b, b'_a, or b'_b, where the subscripts "a" and "b" are applicable to cylinders loaded axially or in bending.

The graphical representation of the calculated per cent of original structural capacity is shown by the broken-line curves in Figures 65 and 66. The predicted results for circular openings were obtained by applying suitable factors for loss of section and eccentric loading to the results predicted for the narrow slit opening cases.

F. Discussion

It is apparent that the testing of Mylar specimens yields a rather wide range of results for the same test performed on different cylinders. For this reason it was necessary to average the results of the three cylinders tested for narrow axial openings to achieve a reasonably smooth curve.

Test results indicate an increased structural capacity for cylinders with narrow slit openings when the length of opening is one to two times the cylinder radius. A possible explanation for this phenomena is that the opening itself will tend to reduce the magnitude of the transverse compressive membrane stresses superimposed after initial small-deflection buckling. The complete absence of such stresses in an unweakened cylinder would permit buckling at the higher load predicted by small deflection theory rather than those achieved in actual testing. The reduction of these stresses may serve to increase the buckling capacity of the slit cylinder over what would have otherwise prevailed. No attempt has been made to account for such an effect in the development of the semi-empirical method of predicting the residual strength of weakened cylinder.

G. Conclusions and Recommendations

The buckling failure of cylinders with unstiffened openings is of such a complex nature that an empirical or semi-empirical method seems to be the only logical analytical approach. The objective of this investigation was to develop a semi-empirical analysis for one class of cylinders (R/t= 360) under limited types of loadings. The curves generated are not intended for specific design purposes, but rather to indicate the general trend of decreasing buckling capacity as a function of increasing size of opening.

It is difficult to estimate the scope of the test program that would be required to fully support the desired stability studies, but certain investigations of the type already performed are logically indicated. Of primary interest would be the similar testing of Mylar specimens within the ranges of R/t from 200 to 1000 and L/R of from 0.5 to 6. Other recommended follow-on investigations concern weakened cylinders subjected to shear, torsional, and pressure loads. More refined studies would be required to determine the interaction of several types of loadings.

VII. ICBM FLIGHT EXPERIMENT (WAC PROGRAM)

In a previous progress report (Reference 1), a description was given of an ICBM piggyback flight experiment which was being conducted on the WAC flight program. Two compartments were installed on board a sharp-nosed slender cone which was to fly an ICBM trajectory. Orifices in each compartment were to have opened at 100,000 ft altitude. Pressure and temperature histories of the compartments were to be telemetered during re-entry.

Unfortunately, the desired re-entry conditions were not achieved, due to booster malfunction. As a result, the external pressure and temperature rises were insufficient to cause the compartment orifices to open and no internal data were obtained.

APPENDIX A. INTERNAL HEATING TO A CLOSED COMPARTMENT DUE TO A SINGLE PERFORATION ("COUPLED FLOW HEATING")

In this section, an analytical model is developed for the so-called "coupled flow heating" mechanism by which a continual energy influx takes place to a closed compartment due to a single perforation. The model employs basic energy and mass balance relations, plus the equation of state for the gas, in a fashion similar to the analysis previously developed for vented compartments. The basic model concept was formulated as a result of insight into the physical phenomena gained during discussion of the Malta rocket exhaust test results with Dr. C. duP. Donaldson, to whom the writer is indebted.

Figure A-1 depicts a re-entry vehicle compartment which has undergone a single perforation. The compartment is assumed to be pressure tight, such that no venting exists to lower pressure regions.

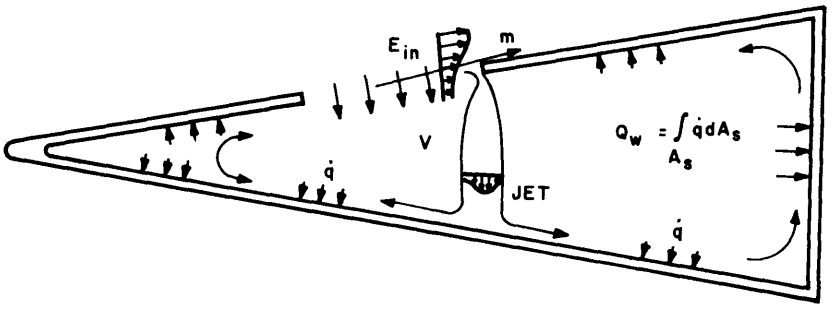

Figure A-1. Perforated Compartment Analysis Model

In Figure A-1, the following notation applies:

- V = free volume of compartment
- E_{in} = $dE/d\theta$ = rate of energy addition through the perforation
- Q_W = rate of energy absorption by compartment walls
- $\dot{q}$ = local heat flux
- A_S = internal surface area
- ρ = internal gas density
- p = internal gas static pressure
- T = internal gas static temperature
- i = internal gas specific internal energy
- h = internal gas specific enthalpy
- m = mass flow rate leaving the compartment through the perforation

The basic conservation equations for the compartment are as follows:

$$\text{Energy: } E_{in} = V\rho \frac{di}{d\theta} + Q_W + mh \tag{A-1}$$

$$\text{Mass: } O = V \frac{d\rho}{d\theta} + m \tag{A-2}$$

$$\text{State: } p = \rho RT \tag{A-3}$$

The existence of a net mass flow outward from the compartment is required by mass conservation, Equation (A-2), to compensate for the rapid initial decrease in gas density with time. Analysis of the Malta rocket exhaust internal pressure histories (Figure 36) indicates that a very rapid initial increase in internal temperature occurs, due to the low heat capacity of the mass of gas within the compartment. The pressure builds up until it is sufficient to cause a mass flow rate from the compartment which balances the rate of mass decrease within the compartment. At this point, a quasi-steady condition is achieved within the compartment, such that all internal state properties such as p, ρ, and T are almost constant ($d\rho/d\theta \approx O$, etc). When this point is reached, Equations (A-1) and (A-2) yield the following approximate relations:

$$m \approx O \tag{A-4}$$

$$Q_W \approx E_{in} \tag{A-5}$$

That is, the exit mass flow rate is small, and effectively all of the energy which enters the compartment is absorbed by the walls.

In the case of the Malta tests, the quasi-steady approximation is achieved within the first 0.5 second of the run (See Figure 36). Thereafter, the rate of internal pressure decrease is less than 2 psi/sec. Assuming a value of $T \approx 3000$ R, Equations (A-2) and (A-3) combine to yield:

$$m = -\frac{V}{RT}\frac{dp}{d\theta} = 2.3 \times 10^{-4} \text{ lb/sec}$$

Since h corresponding to 3000 R is about 2000 btu/lb for the Malta rocket exhaust mixture, it follows that:

$$mh \approx 0.5 \text{ btu/sec}$$

This rate of energy loss through mass outflow is less than one percent of the values of Q_W measured for the Malta tests, in support of the approximation of Equation (A-5).

The phenomenon of internal static pressure buildup above the external static pressure level is not unique to the current problem. Studies of cavity flow have frequently reported this condition; e.g., McDearmon (Reference 20) measured static pressures on the floors of rectangular cavities which were up to 18 percent higher than the external static pressure.

Having discussed the overall characteristics of the internal heating phenomenon, attention is now turned to the quantitative prediction of the rate of energy addition, E_{in}, which is approximately equal to the rate of energy absorption by the walls, Q_W, for quasi-steady conditions. For this purpose, the energy exchange mechanism is assumed to be that of turbulent shear layer mixing, as proposed by Donaldson in Reference 5. The analysis of Chow and Korst (Reference 7) will be utilized, as it includes compressibility effects. The model for the analysis is shown in Figure A-2. A uniform velocity field is assumed to separate from a surface at X = 0, and mix with the ambient environment below it.

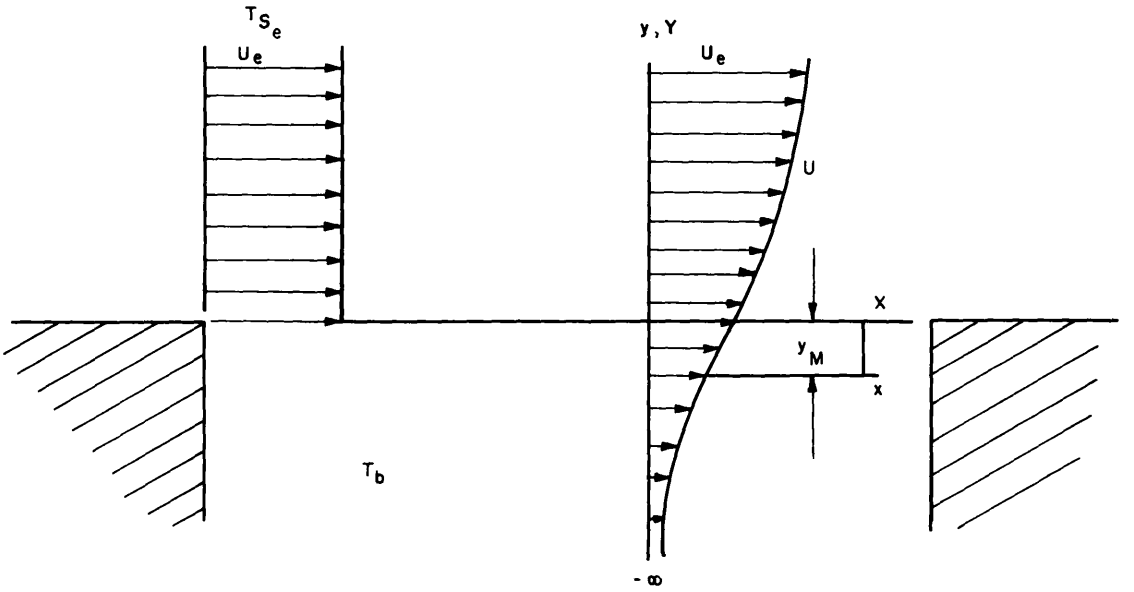

Figure A-2. Jet Mixing Region

In Figure A-2, the following notation applies:

U_e = velocity at outer edge of mixing region

T_{S_e} = stagnation temperature at outer edge of mixing region

T_b = static temperature in base region (equivalent to internal air temperature for perforated compartment).

In the footnote to Equation (13) of Reference 7, Chow and Korst show that the energy transfer across the dividing streamline of the mixing region is given by the relation:

$$St = \frac{(1 - C_e^{\,2})\, I_2\,(\eta_j)}{\sigma} \qquad \text{(A-6)}$$

in which:

$$St = \text{Stanton number} = \frac{\Omega}{C_{P_e} \rho_e U_e (T_{S_e} - T_b)} \tag{A-7}$$

Ω = energy transport rate per unit width and per unit length along the jet mixing region

C_{P_e} = gas specific heat at constant pressure, at edge of mixing region

ρ_e = gas density at edge of mixing region

C_e = Crocco number at edge of mixing region;

$$C_e = \frac{U_e}{\sqrt{2g\,J\,C_{P_e}\,T_{S_e}}} \tag{A-8}$$

$$I_2(\eta_j) = \int_{-\infty}^{\eta_j} \frac{\phi^2}{\Lambda - C_e{}^2\,\phi^2}\, d\eta \tag{A-9}$$

$$\eta = \frac{\sigma y}{x} \tag{A-10}$$

η_j = value of η for dividing streamline

$$\phi = \frac{U}{U_e} = \text{dimensionless velocity} \tag{A-11}$$

$$\Lambda = \frac{T_S}{T_{S_e}} = \text{dimensionless stagnation temperature} \tag{A-12}$$

σ = similarity parameter for co-ordinate system

The value of Λ is determined by the Crocco distribution:

$$\Lambda = \frac{T_b}{T_{S_e}} + \left(1 - \frac{T_b}{T_{S_e}}\right)\phi \tag{A-13}$$

The value of ϕ is determined by the relation:

$$\phi = \frac{1}{2}(1 + \text{erf}\,\eta) \tag{A-14}$$

The co-ordinates x and y are co-ordinates in an intrinsic co-ordinate system which is displaced from the physical co-ordinate system by a dimensionless shift η_M given by:

$$\eta_M = \eta_R - (1 - C_e^2) \int_{-\infty}^{\eta_R} \frac{\phi^2}{\Lambda - C_e^2 \phi^2} d\eta \tag{A-15}$$

where η_R is a large value of η such that $\phi \approx 1$. ($\eta_R = 1.82$ gives $\phi = 0.995$ from Equation (14)). The direction of co-ordinate shift y_M is shown in Figure A-2.

The dividing streamline (called "jet boundary streamline" in Reference 7) which separates the fluid of the external stream from the fluid entrained within the wake region is identified by η_j which satisfies:

$$I_1(\eta_j) = I_1(\eta_R) - I_2(\eta_R) = \int_{-\infty}^{\eta_R} \frac{\phi(1 - \phi)}{\Lambda - C_e^2 \phi^2} d\eta \tag{A-16}$$

in which

$$I_1(\eta_j) = \int_{-\infty}^{\eta_j} \frac{\phi}{\Lambda - C_e^2 \phi^2} d\eta \tag{A-17}$$

A study of the relations presented above will show that the value of $I_2(\eta_j)$ in Equation (A-6) is a function only of C_e and T_b/T_{S_e}. The procedure for evaluating $I_2(\eta_j)$ for given values of C_e and T_b/T_{S_e} is as follows:

- Determine η_j from Equations (A-16) and (A-17), with $\eta_R = 1.82$
- Determine $I_2(\eta_j)$ from Equation (A-9)

If velocity and temperature profiles in the physical plane are required, or if the location of the dividing streamline is required, the dimensionless co-ordinate shift η_M must be evaluated from Equation (A-15).

The expression for Stanton number (Equation A-6) can be converted to a somewhat different form by use of the equation of state:

$$p = p_e = \rho_e R T_e \tag{A-18}$$

and the definition of C_e: (Equation A-8)

$$C_e^2 = \frac{U_e^2/2gJC_{P_e}}{T_{S_e}} = \frac{T_{S_e} - T_e}{T_{S_e}} = 1 - \frac{T_e}{T_{S_e}} \tag{A-19}$$

Substituting Equations (A-18) and (A-19) into Equations (A-6) and (A-7) yields:

$$\Omega = \frac{C_{P_e}}{R} \frac{pU_e}{\sigma} \left(1 - \frac{T_b}{T_{S_e}}\right) I_2(\eta_j) \tag{A-20}$$

The rate of energy addition across a perforation of cross-section area A is simply:

$$E_{in} = \Omega A \tag{A-21}$$

Substituting Equation (A-20) into Equation (A-21) and using the identity $C_P/R = \gamma/\gamma - 1$ yields the final expression for E_{in}:

$$E_{in} = \frac{\gamma}{\gamma - 1} p U_e A \left(1 - \frac{T_b}{T_{S_e}}\right) \frac{I_2(\eta_j)}{\sigma} \tag{A-22}$$

This completes the derivation of Equation (2) of Section I.

Chow and Korst do not indicate how to determine σ, the mixing similarity parameter. In a preceding Progress Report (Reference 1, Appendix C) experimentally determined values of σ were correlated as a function of Mach number for data up to Mach 3.0. In a recent article by Channapragada (Reference 21), it was shown that the Crocco number $C = C_e$ is a preferable choice for correlating values of σ, for use when real gas effects are significant. Reference 16 also develops a theoretical relation for the ratio of σ to its incompressible value σ^*; which for Mach numbers greater than, 3.0 becomes:

$$\frac{\sigma}{\sigma^*} = \frac{4.0}{1 + \frac{T_{S_e}}{T_b}(1 - C^2)} \tag{A-23}$$

Curves of σ are given in Figure A-3, as a function of $(1-C^2)$ and $\frac{T_{S_e}}{T_b}$. The value of $1-C^2$ can be determined from a knowledge of the local edge Mach number M_e by the relation:

$$1 - C^2 = \left[1 + \frac{\gamma - 1}{2} M_e^2\right]^{-1} \tag{A-24}$$

where γ must be an effective isentropic exponent, including real gas effects.

The analysis presented above does not include the effects of a boundary layer profile upstream of the mixing region. In the actual case of interest, a turbulent velocity profile would exist upstream of the perforation. The effect of an initial turbulent boundary layer on the development of the shear layer has been treated by Nash (Reference 22) for the incompressible case. The following values were obtained for the dividing streamline velocity ratio $(U/U_e)_{DS}$:

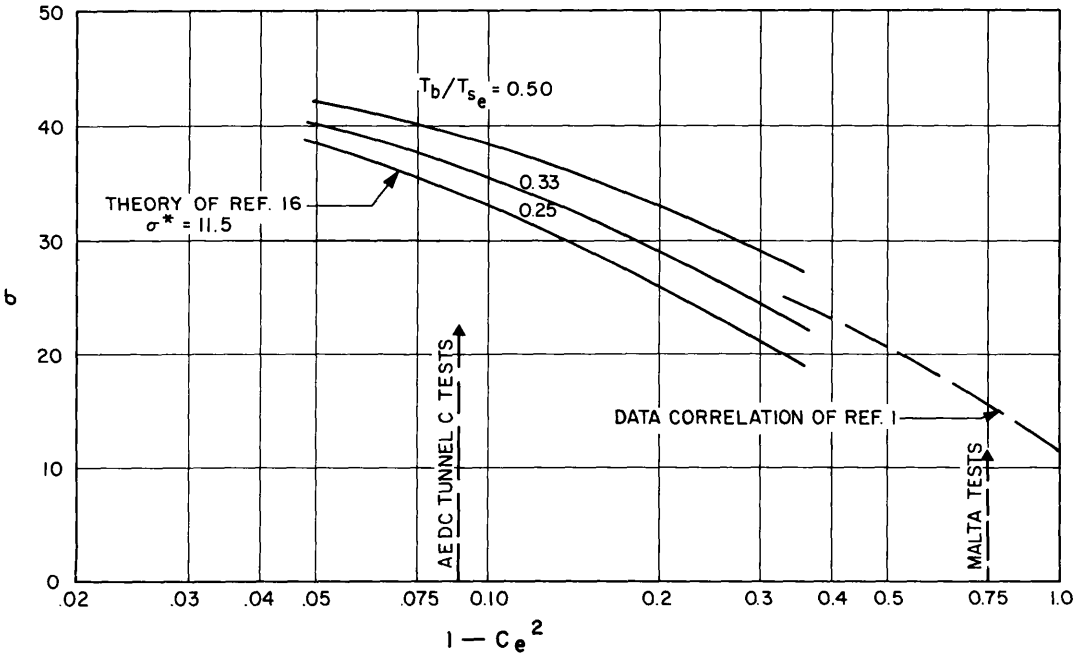

Figure A-3 Jet Mixing Parameter σ

X/θ	5	10	20	30	50	100	200
$(U/U_e)_{DS}$	0.20	0.31	0.39	0.44	0.48	0.525	0.57

where X = length of separated region

and θ = momentum thickness of upstream boundary layer.

It can be seen that $(U/U_e)_{DS}$ is asymptotically approaching the inviscid mixing value of 0.58 derived by Tollmien and x/θ increases. In most cases, the perforation diameters required for thermal kill will be sufficiently large such that X/θ is on the order of 100 or greater. It would appear that viscous approach flow effects on Equation (A-22) would be negligible. For the AEDC tests discussed in Section I, x/θ varied from 125 to 570. For the Malta tests discussed in Section II, X/θ varied from 280 to 445. Thus, little effect of initial boundary layers should have been present in these results.

REFERENCES

1. GE RSD, "Hypervelocity Kill Mechanisms Program - Aerothermal Phase, Annual Progress Report for Period Ending 30 Sept. 1963", GE RSD Document No. 63SD823, Sept. 30, 1963 (Secret).

2. Nestler, D.E., "Results of Wallops Island HKM Internal Heating Flight Tests", GE RSD Document No. 63SD885, Nov. 1963 (Secret).

3. Nestler, D.E., and Vanden Eykel, E.E., "Results of Rocket Exhaust HKM Internal Heating Tests", GE RSD Document No. 63SD564, May 1963 (Secret).

4. Mathias, R.F., and Vikestad, W.S., Personal Communication.

5. Donaldson, C. duP., "A Short Review of the Status of the Aerothermal Phase of the Hypervelocity Kill Mechanisms Program", Proc. of Sixth Hypervelocity Impact Symposium, Cleveland, Ohio, April 1963 (Secret). Also included in Reference 6, Section F.

6. Anon.,"Hypervelocity Kill Mechanisms Program", Progress Report No. 11, NRL Report 5990, June, 1963 (S-RD).

7. Chow, W.L., and Korst, H.H., "On the Flow Structure within a Constant Pressure Compressible Turbulent Jet Mixing Region", NASA TN D-1894, April 1963.

8. Charwat, A.F., Dewey, C.F. Jr., Roos, J.N., and Hitz, J.A., "An Investigation of Separated Flows - Part II: Flow in the Cavity and Heat Transfer", J. Aero. Sci. V. 28, no. 7, pp. 513-527, July, 1961.

9. Persechino, M.A., "Hypervelocity Impacts into Ablative Materials, Proceedings of the Sixth Hypervelocity Impact Symposium, Cleveland, Ohio, April 1963". Also available in reference 6.

10. Anon., "Hypervelocity Kill Mechanisms Program", Progress Report No. 2, NRL Report 1161, April 1961 (S-RD).

11. Anon., "Hypervelocity Kill Mechanisms Program", Progress Report No. 9, NRL Report 5913, Jan. 1963 (S-RD).

12. Ames Research Staff,"Equations, Tables, and Charts for Compressible Flow",NACA Report 1135 (1953).

13. Saydah, A., "Results of HKM Orifice Flow Study", GE RSD Thermodynamics Data Memo TDM-8151-017, Jan. 1964 (Secret).

14. Olson, R.E., "Fluid Amplification, No. 6 Interim Report on Aerodynamic Studies of Pure-Pneumatic Systems", United Aircraft Corp. Report A1771-16, Oct. 1962.

15. Kanemitsu, S., and Mojima, N.M., "Axial Compression Test of Thin Circular Cylinders", California Institute Tech. Thesis, 1939.

REFERENCES (Cont.)

16. The Royal Aeronautical Society: Handbook of Aeronautics, No. 1, 1952.

17. Gerard, G., and Becker, H., NACA, TN 3783, 1957.

18. Timoshenko, S., "Theory of Elastic Stability", 1936.

19. Roark, R., "Formulas for Stress and Strain", Third Ed., 1954.

20. McDearmon, R.W., "Investigation of the Flow in a Rectangular Cavity in a Flat Plate at a Mach Number of 3-55", NASA TN D-523, Sept. 1960.

21. Channapragada, R.S., "Compressible Jet Spread Parameter for Mixing Zone Analyses", AIAA J., Sept. 1963, pp. 2188-90.

22. Nash, J.F., "The Effect of an Initial Boundary Layer on the Development of a Turbulent Free Shear Layer", NPL Aero Rept. 1019, Jan. 1962.

HYPERVELOCITY KILL MECHANISMS PROGRAM (U)

Aerothermal Phase

Semiannual Technical Progress Report
for Period Ending
31 March 1964

Coleman duP. Donaldson
K. Evan Gray
Roger D. Sullivan
Richard S. Snedeker
Dale B. Ruhmel

Sponsored by
Advanced Research Projects Agency
Ballistic Missile Defense Systems Branch
ARPA Order No. 149-60

This research was supported by the Advanced Research Projects Agency, Ballistic Missile Defense Systems Branch, and was monitored by the U.S. Naval Research Laboratory (Code 6240) under Contract No. Nonr-3903(00)(X).

Aeronautical Research Ass Princeton, Inc.
50 Washington Road, New Jersey

Approved: Coleman DP. 4/30/64
Principal Investigator

SUMMARY

Management and coordination efforts undertaken by ARAP in assisting NRL in the monitoring of the Aerothermal Phase are reviewed, including a brief discussion of recent results and their implications for future program requirements. Theoretical and experimental basic research carried out by ARAP during the subject period is described and the results are discussed.

This page not used.

INTRODUCTION

Research programs conducted at ARAP during the past half-year have included theoretical and experimental studies of basic flow phenomena associated with aerothermal kill mechanisms. As a result of these and other studies by other participants in the Aerothermal Phase, particular emphasis has been placed on solving coupled flow problems, including consideration of vehicles hardened by means of foam filled interiors. In addition, ARAP has continued its efforts in assisting NRL in the management and coordination of the over-all Aerothermal Phase program.

MANAGEMENT AND COORDINATION

The effort to provide assistance to NRL in the management and coordination of the Aerothermal Phase has been maintained during the past six months. In addition to the usual liaison duties, this effort has included several meetings among personnel of the participating companies and agencies, at which time current problems and the results of test and analytical programs were discussed and evaluated. An important consequence of the test results during this period has been the increased effort directed toward understanding the mechanism of coupled flows. It has been shown both experimentally and analytically that the heat flux to the vehicle interior under such coupled conditions ($A/V^{2/3} > .05$) can be many times as great as that for uncoupled conditions ($A/V^{2/3} < .01$). A flow mechanism which can be shown to account for heat fluxes of the magnitudes observed has been developed and verified experimentally by means of heat flux mapping and flow visualization techniques. Details of this mechanism, which involves a combination of free shear layer and jet impingement effects, are discussed in a later section of this report. Plans for tests to be carried out by other groups under the Aerothermal Phase (GE and NASA) have been directed at providing data specifically pertinent to this problem. In addition, because of the important role of jet impingement in the coupled flow process as it is now defined, a program of hot jet (air arc jet) impingement experiments has been initiated (AVCO). Data resulting from these programs should provide the basis for an extension to high temperature regimes of semi-empirical methods which are being developed for predicting jet impingement, wall jet, and free shear layer heat transfer characteristics.

Of equal importance to the over-all program is the problem of possible counter-aerothermal measures in the form of light weight foam packing in a vehicle's interior. During the past six months, plans for a thorough study of the

behavior of such packing under aerothermal conditions have been formulated, and some preliminary tests under simulated environment conditions have been conducted (GE). In addition to the continued monitoring of such studies by other participants, ARAP plans to conduct basic theoretical and experimental studies of foam behavior during the future months.

JET IMPINGEMENT, WALL JET, AND FREE SHEAR LAYER STUDIES

Theoretical. At the beginning of the period, a study attempting to relate compressible jet flows to incompressible ones was under way. The approach used a general transformation similar to that of Coles but reduced it to a practical form by the use of assumptions more closely related to the physics of the problem than were the limiting value arguments of Coles. Although it proved impossible to remove a degree of arbitrariness from the transformation, the study provided increased understanding of phenomena peculiar to both laminar and turbulent compressible flows, particularly jets.

The coupled flow condition is now understood to involve energy transfer to the cavity by means of both shear layer mixing and jet impingement. Briefly, this mechanism can be described as follows. As the free stream flow leaves the forward edge of the hole, mixing with the stagnant inner gas starts. The mixing region grows in thickness as the flow approaches the aft edge of the hole, and, if that portion of the mixing region (free shear layer) velocity profile which impinges on the aft edge is supersonic, a normal shock is formed which stands off from the aft edge. In this case, the pressure behind the shock is so high relative to the cavity pressure, that a jet is formed which carries air of very high stagnation enthalpy into the interior. (The strength and direction of such a jet are, of course, dependent on the relationship of hole size and aft edge wall thickness.)

An analytical study of the characteristics of free shear flows is being conducted in order to gain some insight into the mechanism of energy transfer across the mixing region. The projected purpose of such an analysis is to provide an analytical method for the prediction of the heat flux contribution of this part of the coupled flow mechanism. Since the total heat flux into the cavity is a combination of the energy transfer across the mixing region and that due to the jet formed behind the normal shock standing off the downstream edge, an estimate of the energy transferred by this jet requires a knowledge of where the dividing streamline impinges on the downstream edge. The initial analysis, then, has been concerned with the location of the dividing streamline as a function of external flow conditions and pressure ratio. A

linear velocity profile across the mixing region was used in the first case for incompressible flow. The validity of this assumption was substantiated by the agreement obtained when compared with results for more exact profiles. The analysis was extended for the compressible case using the same assumption for velocity profile. The behavior of the dividing streamline with free stream Mach number was determined for three enthalpy ratios across the mixing regions. These cases covered both extremes of hot and cold air in the cavity and an intermediate case. The analytical expression for location of the dividing streamline will be utilized in the evaluation of experimental results as they become available.

The growth of the mixing region as a function of Mach number and enthalpy ratio has also been under study. This parameter is necessary for the estimation of that portion of the mixing region which is supersonic at the downstream edge. To date, the analysis has resulted in the development of an analytical method for estimating this growth.

Experimental. Results of an extensive study of free jets impinging normal to surfaces of several shapes have been discussed in previous status reports. In addition to such results relating to stagnation region heat transfer parameters, an unusual flow condition with several interesting features has been observed. It appears that this condition can only exist for cases in which the impinging jet is sufficiently underexpanded to require the presence of a normal shock disk in the jet core. When such a jet impinges at distances downstream of this shock, the flow near the jet axis separates, and a vortex-ring-like bubble forms on the surface. The stagnation point for maximum heat transfer now becomes a stagnation "ring" surrounding this bubble and the behavior of the radial flow near the surface becomes quite complex. A composite illustration of a typical example of this phenomenon is shown in Figure 1. The relationship between surface pressure distribution, surface streamline patterns (grease streak picture), and impinging flow density gradients (schlieren spark photograph) is quite evident. Further study of such flows will be required, however, before they are fully understood.

During the recent semiannual period, the normal impingement work was extended to include pressure distribution measurements on these same surfaces for oblique impingement angles, as well as the measurement of the azimuthal distribution of radial momentum in the wall jet as it leaves the edge of a flat plate as a function of impingement angle. Stagnation region heat transfer parameters deduced from some of the pressure distributions indicate that although the stagnation point moves slightly in an upstream direction as the impingement angle is decreased from 90° to about 60°, the heat

transfer falls off only slightly. Further conclusions for smaller impingement angles will be possible after the remaining data are analyzed. The azimuthal momentum distribution measurements which are now in progress are intended to show the manner in which the momentum of an impinging jet is distributed in the resulting wall jet. On the basis of such distributions, the peak heating areas on the inside walls of a cavity should be predictable. An example of the behavior in a typical case is shown in Figure 2. This plot shows the radial momentum flux per unit azimuth angle (ϕ) as a function of ϕ for one-half of the flat plate circumference for several impingement angles α.

A study of subsonic free shear layer phenomena was initiated during the subject period in order to aid in the development of a method for predicing energy fluxes under conditions of coupled flow as it is now understood. This work is to be continued for both subsonic and supersonic cases, and will be closely coordinated with the theoretical investigation described earlier.

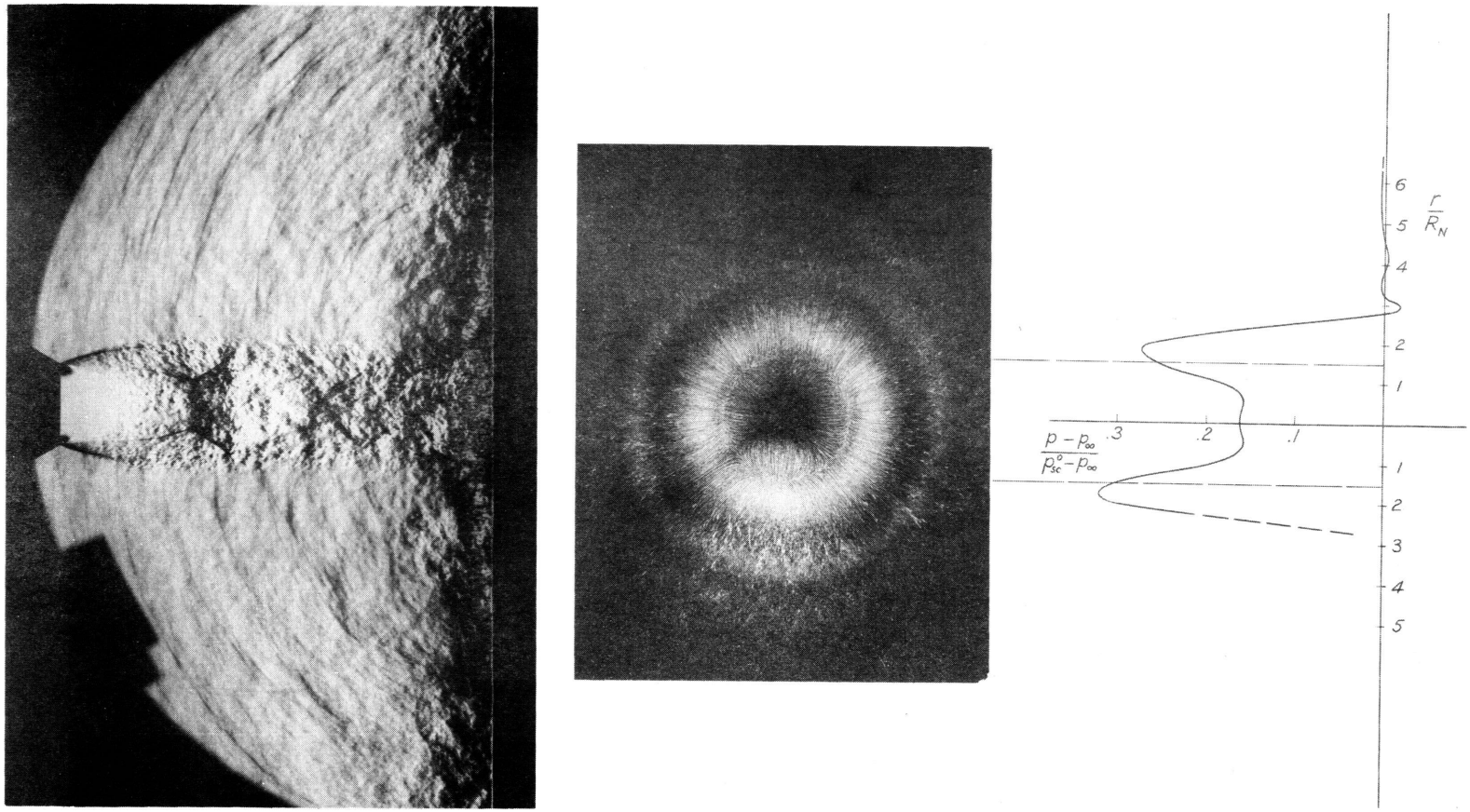

Figure 1. Typical jet impingement characteristics for a case in which a normal shock exists in the jet core. $p_j/p_\infty = 3.57$; $x/d_N = 5.32$.

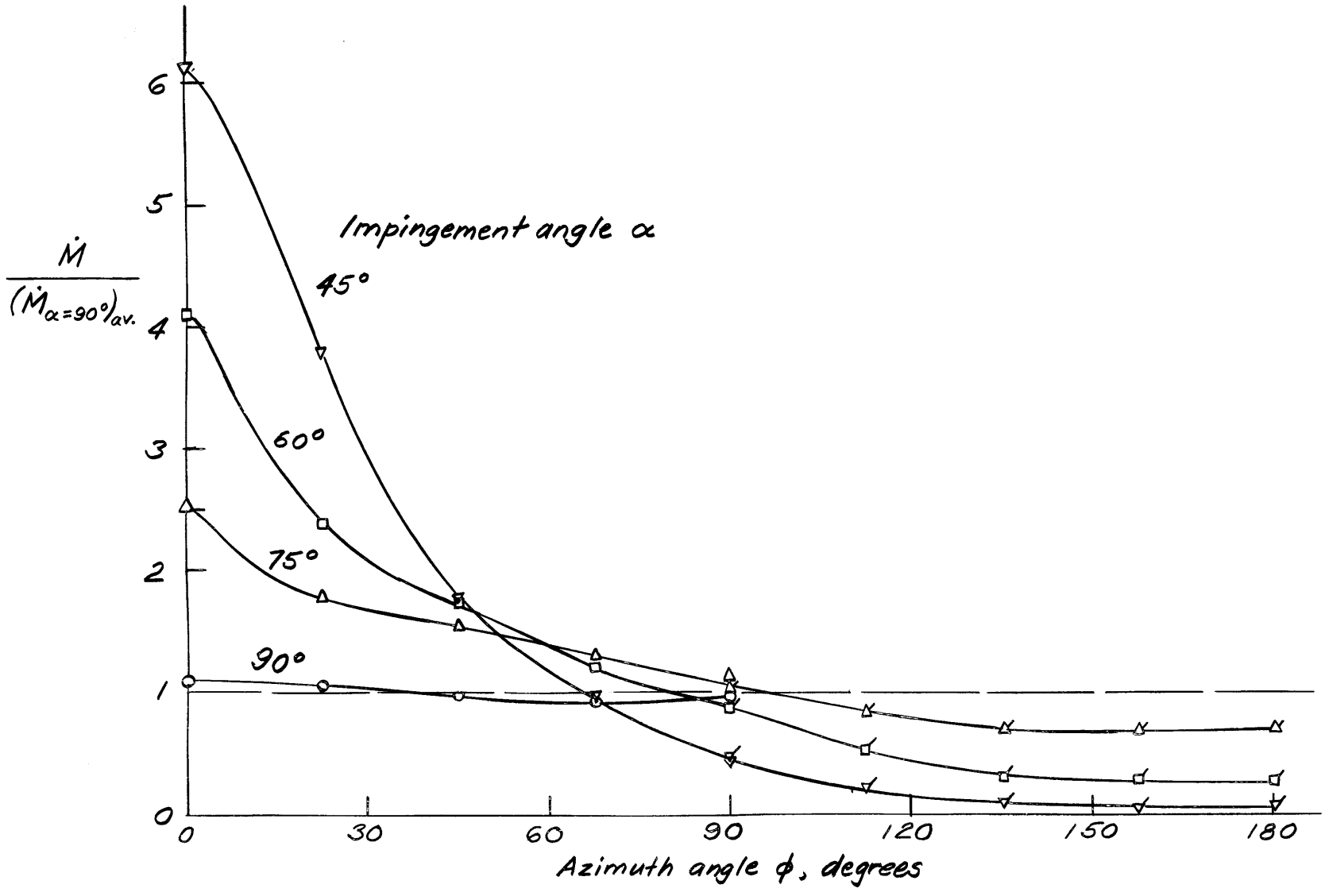

Figure 2. Momentum flux per unit azimuth angle as a function of azimuth angle for several impingement angles. $p_j/p_\infty = 1.42$; $x/d_N = 1.96$.

NOLTR 61-84

Aerodynamics Research Report 158

DAMAGE EFFECT ON RE-ENTRY BODY STATIC STABILITY AT M = 10

Prepared by:
J. D. Gates
A. P. Leonas

ABSTRACT: This report presents the results of an investigation in the U.S. Naval Ordnance Laboratory's Hypersonic Tunnel No. 4 to obtain the pitching, yawing, and rolling moments and normal and side forces of the G.E. Mark 3 XXI-H re-entry body with simulated damage. These data were obtained at Mach number 10.

U. S. NAVAL ORDNANCE LABORATORY
WHITE OAK, SILVER SPRING, MARYLAND

NOLTR 61-84 27 May 1964

DAMAGE EFFECT ON RE-ENTRY BODY
STATIC STABILITY AT M = 10

The purpose of this investigation was to obtain static stability data on the G.E. Mark 3 XXI-H re-entry body with simulated damage to the nose and flared skirt in order to find the effect of the damage upon its aerodynamic performance and augment General Electric's analytical study. The wind tunnel test was performed in the U.S. Naval Ordnance Laboratory's Hypersonic Tunnel No. 4 at the request of the General Electric Company (reference (1)) for Project Defender (ARPA Order No. 149-60) under Task Number NOL 569.

This research was supported by the Advanced Research Projects Agency, Ballistic Missile Defense Systems Branch, and was monitored by the U.S. Naval Research Laboratory (Code 6240) under Contract No. 173-6162-61.

R. E. ODENING
Captain, USN
Commander

K. R. ENKENHUS
By direction

CONTENTS

TABLES

ILLUSTRATIONS

INTRODUCTION

The Hypervelocity Kill Mechanism Research Program for Project Defender (ARPA Order No. 149-60) was established to determine the aerodynamic performance of a damaged re-entry body in comparison to the performance of an undamaged body (see reference (1)). Such performance data may indicate whether it is possible to reduce the capabilities of, or destroy, a re-entry vehicle by (1) causing a change in point of impact, (2) structural failure due to increased aerodynamic loads at induced trim angles, or (3) overheating due to a shift in the stagnation point at induced trim angles.

The G.E. Mark 3 configuration XXI-H was chosen for this investigation because it is a typical re-entry body. Damage was simulated on the re-entry body by modifications made to the nose and flare sections which caused configurational asymmetry. Static stability coefficients of pitch, yaw, and roll were obtained from wind tunnel tests performed at a Mach number of 10 on 0.04783 scale models. These data will be used to supplement the analytical program being conducted by the General Electric Company to determine the vulnerability of ICBM's to impact by relatively small hypervelocity particles.

SYMBOLS

A	reference area ($\pi d^2/4$)
c.g.	center of gravity measured from the nose (2.563 in) along the centerline of the model
C_N	normal force coefficient (F_N/qA)
C_Y	side force coefficient (F_Y/qA)
C_ℓ	rolling moment coefficient (M_X/qAd)
C_m	pitching moment coefficient (M_Y/qAd)
C_n	yawing moment coefficient (M_Z/qAd)
d	reference diameter based on the maximum flare diameter at the base of the model (2.047 in)
F_N	normal force
F_Y	side force
M_X	rolling moment

M_Y	pitching moment
M_Z	yawing moment
q	dynamic pressure
Re/ft	Reynolds number per foot based on free-stream conditions
α	angle of attack
β'	angle of sideslip in body axes
θ	angle of pitch in the vertical center plane of the tunnel
ϕ	angle of roll ($\phi = 0°$ when modification is on windward side of the model at positive angle of attack)

MODELS, TEST TECHNIQUES AND DATA REDUCTION

The models (0.04783 scale) of the G.E. Mark 3 XXI-H re-entry vehicle were designed and constructed by the Naval Ordnance Laboratory from drawings furnished by the General Electric Company (see Figures 1-18 for drawings of the models and model photographs). Eleven modifications to nose and flare sections of the configurations were made and are designated as XXI-H-1, 2, 3, 4, 5, 7, 8, 9, 10, 13 and 14.

Photographs of the NOL Hypersonic Tunnel No. 4 are shown in Figure 19. The tunnel is described in detail in reference (2).

The data were obtained using a five-component, water-cooled, internal strain gage balance (reference (3)). A thermocouple was mounted on the balance, inside the model, just forward of the forward pitch gage to monitor the balance temperature. The test was performed with less than ±2°C variance from a constant balance temperature which eliminated gage drift during testing. Immediately after each tunnel run, the wind-off tare readings were taken on all balance components.

A multiplexed single-channel, high-speed data system was used to record the force and moment data. This system amplified and digitized the strain gage analog signals and recorded them on punched paper tape which fed into a Flexoriter typewriter.

An IBM 704 computer was used to reduce the wind tunnel data to aerodynamic coefficient form. The reference diameter and area used in computing the coefficients are based on the maximum flare diameter (2.047 in.) of the model. Corrections

were made to the data for elastic deflection of the sting due to aerodynamic loading. The aerodynamic coefficients were referenced to the model axes system.

RESULTS

Table 1 gives the configuration and test conditions for each wind tunnel run. C_N (normal force coefficient), C_m (pitching moment coefficient), C_Y (side force coefficient), C_n (yawing moment coefficient), and C_ℓ (rolling moment coefficient) are listed in Table 2 as functions of α (angle of attack) and β' (sideslip angle in the body axis).

Figures 20 to 23 show the effect on static stability in the pitch plane of nose and flare modifications to one half of the model. Figures 20 and 22 show the effect of graduated modification at $\phi = 0°$, and Figures 21 and 23 show the effect of maximum modification at three roll angles ($\phi = 0°$, 45° and 90°). As might be expected, neither type of modification shows much effect when the modified area is in the lee of the wind. With modification on the windward side of the model, there is a loss of stability, and in the case of both maximum nose and flare modifications, a change in trim angle. The effect of roll angle is to diminish the effect of the modification as ϕ approaches 90°.

As an example of the effectiveness of one kind of damage, consider the H_3 configuration shown on Figure 22. The model trims at $\alpha = 8°$. The modification to the flare raises the drag coefficient by $C_n \sin\alpha$ and gives what had been a symmetrical configuration a normal force coefficient of 0.125 in trimmed flight.

REFERENCES

(1) Bonasia, J. J., Wind Tunnel Request 685, General Electric Company (1961) Confidential
(2) Danberg, J. E., Jackson, A. P., and Brown, F. W., "NOL Hypersonic Tunnel No. 4," NOLTR 62-47, to be published, Unclassified
(3) Shantz, I., Gilbert, B. D., and White, C. E., "NOL Wind Tunnel Internal Strain-Gage Balance System," NAVORD Rpt 2972 (1953) Unclassified

TABLE 1

MODEL CONFIGURATIONS AND TEST CONDITIONS

Run	Configuration	θ	φ	Mach Number	q	(Re)x10^{-6}
1	XXI-H-1	-12 to +19	0	10.15	1.13	0.025
2	"	"	+45	"	"	"
3	"	"	+90	"	"	"
4	XXI-H	"	0	"	"	"
5	XXI-H-2	"	"	"	"	"
6	"	"	+45	"	"	"
7	"	"	+90	"	"	"
8	XXI-H-3	"	"	"	"	"
9	"	"	+45	"	"	"
10	"	"	0	"	"	"
11	XXI-H-4	"	"	"	"	"
12	"	"	+45	"	"	"
13	"	"	+90	"	"	"
14	XXI-H-5	"	"	"	"	"
15	"	"	+45	"	"	"
16	"	"	0	"	"	"
17	"	"	-45	"	"	"
18	XXI-H-14	"	0	"	"	"
19	"	"	+45	"	"	"
20	"	"	+90	"	"	"
21	XXI-H-13	"	"	"	"	"
22	"	"	+45	"	"	"
23	"	"	0	"	"	"
24	XXI-H-5	"	-90	"	"	"
25	XXI-H-7	"	"	"	"	"
26	"	"	-45	"	"	"
27	"	"	0	"	"	"
28	XXI-H-8	"	"	"	"	"
29	"	"	+45	"	"	"

TABLE 1 (Continued)

MODEL CONFIGURATIONS AND TEST CONDITIONS

Run	Configuration	θ	ϕ	Mach Number	q	(Re)x10^{-6}
30	XXI-H-8	-12 to +19	+90	10.15	1.13	0.025
31	XXI-H-9	"	"	"	"	"
32	"	"	+45	"	"	"
33	"	"	0	"	"	"
34	XXI-H-10	"	"	"	"	"
35	"	"	+45	"	"	"
36	"	"	+90	"	"	"
37	XXI-H-4	"	-45	"	"	"

TABLE 2

TABULATED DATA

[NOTE:

1. The symbols used in the column headings are defined on pages 1 and 2.
2. Runs are tabulated in sequence by run numbers.
3. Column headings and decimal points are shown on run 1 of the tabulated data and are the same for all runs.]

WTR 685	RUN 01							
α	β'	C_N	C_m	C_Y	C_n	C_ℓ	ϕ
.00	.00-	.004-	.011	.011	.004-	.001-	.00
12.00-	.00-	.382-	.257	.012	.013-	.001-	.00
10.00-	.00-	.280-	.167	.012	.011-	.000-	.00
.00-	.00-	.007-	.005	.011	.010-	.001	.00
2.00	.00-	.029	.003-	.011	.011-	.001	.00
4.00	.00-	.073	.020-	.013	.011-	.001	.00
6.00	.00-	.116	.031-	.013	.008-	.000-	.00
8.00	.00-	.160	.043-	.015	.011-	.000	.00
10.00	.00-	.205	.056-	.016	.011-	.000	.00
12.00	.00-	.271	.090-	.019	.015-	.000	.00
14.00	.00-	.349	.143-	.017	.016-	.001	.00
16.01	.00-	.457	.226-	.019	.019-	.002	.00
18.01	.00	.589	.333-	.019	.022-	.004	.00
19.01	.00	.636	.361-	.020	.022-	.003	.00
10.00	.00	.200	.059-	.016	.020-	.004	.00
2.00-	.00-	.042-	.027	.011	.004-	.001-	.00
4.00-	.00-	.094-	.057	.012	.005-	.001-	.00
6.00-	.00-	.152-	.092	.011	.004-	.001-	.00
8.00-	.00-	.207-	.121	.013	.008-	.001-	.00
10.00-	.00-	.278-	.167	.012	.008-	.002-	.00
.00-	.00	.014-	.008	.010	.018-	.005	.00

WTR RUN

685	α	02	β'	C_N	C_m	C_Y	C_n	C_ℓ	ϕ
	.00		.00-	.001-	.009	.008	.007	.005-	45.00
	1.41-		1.42-	.033-	.023	.038	.010-	.006-	45.00
	2.83-		2.83-	.067-	.043	.078	.036-	.005-	45.00
	4.25-		4.25-	.106-	.065	.116	.060-	.004-	45.00
	5.68-		5.68-	.147-	.085	.154	.086-	.003-	45.00
	7.11-		7.11-	.195-	.118	.203	.117-	.003-	45.00
	8.55-		8.55-	.272-	.183	.277	.187-	.002-	45.00
	7.11-		7.11-	.197-	.116	.201	.122-	.000	45.00
	.00-		.00-	.005-	.002	.008	.006-	.001-	45.00
	1.41		1.41	.021	.004-	.024-	.012	.000-	45.00
	2.83		2.83	.049	.014-	.058-	.032	.001-	45.00
	4.25		4.25	.079	.021-	.091-	.051	.002-	45.00
	5.68		5.68	.114	.031-	.130-	.070	.003-	45.00
	7.11		7.11	.149	.044-	.179-	.101	.003-	45.00
	8.55		8.55	.198	.075-	.243-	.154	.003-	45.00
	10.00		10.00	.266	.124-	.330-	.238	.004-	45.00
	11.47		11.46	.346	.188-	.438-	.341	.005-	45.00
	12.94		12.94	.406	.215-	.522-	.402	.003-	45.00
	13.69		13.69	.431	.223-	.556-	.417	.003-	45.00
	7.11		7.11	.144	.042-	.174-	.089	.001	45.00
	.00-		.00	.008-	.006	.008	.011-	.002	45.00

WTR 685	RUN 03 α	β'	C_N	C_m	C_Y	C_n	C_l	ϕ
	.00	.00-	.005-	.009	.001-	.009	.004-	90.00
	.00	2.00-	.007-	.011	.046	.015-	.003-	90.00
	.00	4.00-	.009-	.014	.097	.048-	.003-	90.00
	.00	6.00-	.013-	.019	.152	.081-	.003-	90.00
	.00	8.00-	.019-	.022	.208	.116-	.002-	90.00
	.00-	10.00-	.024-	.025	.276	.165-	.002-	90.00
	.00-	12.00-	.028-	.026	.382	.261-	.000	90.00
	.00-	10.00-	.024-	.025	.278	.168-	.000-	90.00
	.00-	.00	.011-	.008	.001	.003-	.001-	90.00
	.00-	2.00	.011-	.011	.043-	.024	.001-	90.00
	.00	4.00	.011-	.016	.095-	.060	.003-	90.00
	.00	6.00	.012-	.022	.150-	.095	.005-	90.00
	.00	8.00	.012-	.028	.209-	.130	.005-	90.00
	.00	10.00	.013-	.029	.276-	.173	.004-	90.00
	.00	12.00	.015-	.032	.376-	.261	.003-	90.00
	.00	14.00	.020-	.034	.509-	.388	.002-	90.00
	.00	16.00	.030-	.042	.673-	.549	.002-	90.00
	.00	18.00	.038-	.053	.769-	.602	.002-	90.00
	.00	19.00	.043-	.061	.806-	.614	.003-	90.00
	.00	10.00	.020-	.028	.258-	.140	.001	90.00
	.00	.00	.001	.006	.009	.018-	.002	90.00

WTR 685	RUN 04 α	β''	C_N	C_m	C_Y	C_n	C_l	ϕ
	.00	.00-	.004	.001	.003-	.006	.003	.00
	2.00-	.00-	.039-	.026	.001-	.006	.002	.00
	4.00-	.00-	.090-	.053	.005-	.006	.001	.00
	6.00-	.00-	.147-	.085	.005-	.006	.001-	.00
	8.00-	.00-	.203-	.117	.003-	.006	.000	.00
	10.00-	.00-	.279-	.176	.002	.007	.002	.00
	12.00-	.00-	.384-	.277	.003	.009	.007	.00
	10.00-	.00-	.283-	.185	.006	.008	.007	.00
	.00	.00-	.004	.003	.002	.007	.004	.00
	2.00	.00-	.048	.024-	.001-	.006	.002	.00
	4.00	.00-	.103	.062-	.003-	.005	.000-	.00
	6.00	.00-	.158	.094-	.003-	.006	.000	.00
	8.00	.00	.218	.127-	.005-	.000	.000-	.00
	10.00	.00	.290	.175-	.005-	.005	.000	.00
	12.00	.00-	.387	.257-	.004-	.006	.000-	.00
	14.00	.00-	.523	.387-	.003	.000-	.002	.00
	.00-	.00-	.019-	.016	.001	.004	.002	.00
	.00-	.00-	.019-	.016	.001	.004	.002	.00
	10.00	.00-	.278	.153-	.008	.002-	.001	.00
	16.00	.00-	.686	.547-	.004	.000-	.002	.00
	18.00	.00-	.795	.612-	.008	.005-	.003	.00
	19.00	.00-	.637	.631-	.008	.004-	.002	.00

WTR 685	RUN 05							
	α	β'	C_N	C_m	C_Y	C_n	C_l	ϕ
	.00-	.00	.011-	.008	.016	.023-	.010	.00
	2.00-	.00	.050-	.024	.020	.025-	.009	.00
	4.00-	.00	.099-	.054	.020	.023-	.009	.00
	6.00-	.00	.158-	.089	.017	.022-	.009	.00
	8.00-	.00	.215-	.121	.013	.017-	.008	.00
	10.00-	.00	.287-	.172	.013	.016-	.005	.00
	12.00-	.00	.387-	.259	.013	.017-	.003	.00
	10.00-	.00	.284-	.169	.012	.014-	.003	.00
	.00-	.00	.009-	.010	.011	.013-	.002	.00
	2.00	.00	.023	.003	.012	.014-	.003	.00
	4.00	.00	.062	.007-	.012	.016-	.004	.00
	6.00	.00	.101	.018-	.016	.022-	.004	.00
	8.00	.00	.141	.024-	.016	.020-	.003	.00
	10.00	.00-	.185	.031-	.013	.014-	.003	.00
	12.00	.00-	.241	.054-	.012	.013-	.003	.00
	14.01	.00	.311	.090-	.011	.014-	.002	.00
	16.01	.00-	.403	.154-	.017	.017-	.003	.00
	18.01	.00	.517	.239-	.016	.019-	.004	.00
	19.01	.00	.574	.277-	.020	.022-	.004	.00
	10.00	.00	.179	.035-	.013	.021-	.007	.00
	.00-	.00	.019-	.015	.009	.018-	.005	.00

WTR RUN
685 06

α	β'	C_N	C_m	C_Y	C_n	C_l	ϕ
.00-	.00	.015-	.013	.008	.011-	.001	45.00
.00	.00-	.008-	.015	.007	.007	.007-	45.00
1.41-	1.42-	.034-	.026	.038	.010-	.007-	45.00
2.83-	2.83-	.068-	.046	.074	.032-	.007-	45.00
4.25-	4.25-	.113-	.070	.120	.066-	.006-	45.00
5.68-	5.68-	.148-	.090	.153	.079-	.007-	45.00
7.11-	7.11-	.207-	.124	.208	.131-	.002-	45.00
8.55-	8.55-	.280-	.188	.284	.198-	.001-	45.00
7.11-	7.11-	.210-	.125	.208	.131-	.001-	45.00
.00-	.00	.012-	.011	.007	.008-	.001-	45.00
1.41	1.41	.013	.008	.023-	.009	.002-	45.00
2.83	2.83	.039	.002	.055-	.029	.002-	45.00
4.25	4.25	.069	.004-	.091-	.049	.003-	45.00
5.68	5.68	.099	.009-	.134-	.073	.004-	45.00
7.11	7.11	.136	.023-	.176-	.098	.003-	45.00
8.55	8.55	.179	.047-	.236-	.143	.003-	45.00
10.00	10.00	.236	.087-	.316-	.217	.003-	45.00
11.47	11.46	.310	.141-	.421-	.315	.003-	45.00
12.94	12.94	.364	.163-	.507-	.379	.002-	45.00
13.69	13.69	.388	.168-	.539-	.396	.002-	45.00
7.11	7.11	.125	.021-	.172-	.084	.001	45.00

WTR	RUN							
685	α 07	β'	C_N	C_m	C_Y	C_n	C_l	ϕ
	.00-	.00-	.016-	.016	.007	.006-	.003-	90.00
	.00	2.00-	.015-	.017	.048	.026-	.002-	90.00
	.00	4.00-	.019-	.022	.099	.057-	.002-	90.00
	.00	6.00-	.024-	.030	.152	.086-	.002-	90.00
	.00	8.00-	.030-	.035	.207	.118-	.001-	90.00
	.00	10.00-	.032-	.039	.274	.165-	.001	90.00
	.00	12.00-	.038-	.041	.379	.259-	.002	90.00
	.00	10.00-	.032-	.036	.278	.171-	.002	90.00
	.00-	.00	.018-	.015	.003	.008-	.002	90.00
	.00-	2.00	.013-	.014	.040-	.016	.001	90.00
	.00	4.00	.016-	.022	.089-	.046	.001	90.00
	.00	6.00	.021-	.031	.142-	.078	.000-	90.00
	.00	8.00	.025-	.037	.195-	.101	.001-	90.00
	.00	10.00	.024-	.036	.267-	.151	.002-	90.00
	.00	12.00	.029-	.044	.363-	.233	.001-	90.00
	.00	14.00	.033-	.050	.500-	.366	.001-	90.00
	.00	16.00	.044-	.064	.660-	.525	.003-	90.00
	.00	18.00	.056-	.083	.762-	.586	.004-	90.00
	.00	19.00	.060-	.092	.798-	.598	.004-	90.00
	.00	10.00	.028-	.039	.262-	.139	.001	90.00
	.00-	.00	.018-	.015	.004	.015-	.003	90.00

WTR 685	RUN 08							
α	β'	C_N	C_m	C_Y	C_n	C_ℓ	ϕ
.00	8.00	.035-	.046	.188-	.094	.001-	90.00
.00	10.00	.040-	.059	.258-	.146	.003-	90.00
.00	12.00	.042-	.064	.353-	.228	.004-	90.00
.00	14.00	.051-	.078	.479-	.349	.004-	90.00
.00	16.00	.063-	.091	.634-	.499	.004-	90.00
.00	18.00	.079-	.116	.731-	.552	.004-	90.00
.00	19.00	.087-	.127	.764-	.557	.003-	90.00
.00	10.00	.039-	.055	.253-	.131	.000-	90.00
.00-	.00	.023-	.024	.005	.011-	.002	90.00
.00-	.00-	.020-	.016	.007	.005-	.001-	90.00
.00	2.00-	.020-	.027	.050	.023-	.003-	90.00
.00	4.00-	.026-	.034	.098	.053-	.003-	90.00
.00	6.00-	.030-	.041	.151	.078-	.004-	90.00
.00	8.00-	.038-	.049	.200	.104-	.002-	90.00
.00	10.00-	.039-	.052	.270	.150-	.002-	90.00
.00	12.00-	.046-	.058	.369	.237-	.000	90.00
.00	10.00-	.044-	.052	.266	.148-	.001-	90.00
.00-	.00-	.020-	.016	.005	.005-	.000	90.00
.00-	2.00	.020-	.019	.036-	.016	.000	90.00
.00	4.00	.022-	.027	.085-	.040	.000-	90.00
.00	6.00	.031-	.036	.133-	.064	.001	90.00

WTR 685	RUN 09							
α	β'	C_N	C_m	C_Y	C_n	C_ℓ	ϕ
.00	.00-	.017-	.026	.006	.005	.002-	45.00
1.41-	1.42-	.045-	.036	.034	.008-	.002-	45.00
2.83-	2.83-	.080-	.059	.067	.028-	.003-	45.00
4.25-	4.25-	.116-	.076	.109	.056-	.002-	45.00
5.68-	5.68-	.159-	.098	.150	.083-	.001-	45.00
7.11-	7.11-	.212-	.134	.200	.117-	.001-	45.00
8.55-	8.55-	.284-	.196	.275	.186-	.000	45.00
7.11-	7.11-	.209-	.131	.201	.120-	.000-	45.00
.00-	.00-	.020-	.021	.005	.002-	.001-	45.00
1.41	1.41	.003	.016	.023-	.009	.000-	45.00
2.83	2.83	.028	.015	.053-	.024	.001-	45.00
4.25	4.25	.050	.013	.085-	.040	.001-	45.00
5.68	5.68	.077	.012	.124-	.057	.001-	45.00
7.11	7.11	.106	.007	.163-	.078	.001-	45.00
8.55	8.55	.147	.011-	.218-	.117	.003-	45.00
10.00	10.00	.196	.036-	.291-	.185	.004-	45.00
11.47	11.46	.257	.073-	.389-	.275	.006-	45.00
12.94	12.94	.305	.089-	.471-	.336	.006-	45.00
13.69	13.69	.327	.094-	.498-	.352	.005-	45.00
7.11	7.11	.106	.007	.160-	.075	.001-	45.00
.00-	.00	.022-	.015	.010	.018-	.002	45.00

685 10						
.00	.00-	.003-	.009	.012	.002	.004-	.00
2.00-	.00-	.050-	.033	.015	.000	.003-	.00
4.00-	.00-	.102-	.066	.012	.003	.002-	.00
6.00-	.00-	.158-	.100	.012	.006	.002-	.00
8.00-	.00-	.212-	.125	.010	.002	.001-	.00
10.00-	.00-	.287-	.173	.012	.008-	.003	.00
12.00-	.00-	.389-	.259	.013	.014-	.004	.00
10.00-	.00-	.286-	.172	.011	.010-	.003	.00
.00	.00-	.009-	.016	.017-	.019	.001-	.00
2.00	.00	.022	.014	.024-	.019	.005-	.00
4.00	.00-	.050	.009	.022-	.027	.001-	.00
6.00	.00	.087	.005	.003-	.000	.002-	.00
8.00	.00	.126	.002-	.005-	.002	.002-	.00
10.00	.00-	.165	.007-	.024-	.027	.001-	.00
12.00	.00-	.210	.019-	.015	.013-	.002	.00
14.01	.00	.262	.040-	.015	.017-	.004	.00
16.01	.00	.335	.078-	.017	.019-	.003	.00
18.01	.00-	.432	.135-	.016	.014-	.001	.00
19.01	.00-	.478	.166-	.013	.010-	.000	.00
10.00	.00-	.184	.038-	.011	.008-	.001	.00
.00-	.00	.023-	.016	.008	.009-	.003	.00

685 11							
.00	.00-	.000	.000	.005-	.012	.001-	.00
2.00-	.00-	.037-	.022	.004-	.011	.001-	.00
4.00-	.00-	.094-	.054	.002-	.009	.001-	.00
6.00-	.00-	.150-	.089	.004-	.011	.003-	.00
8.00-	.00-	.204-	.119	.003	.006	.004-	.00
10.00-	.00	.278-	.165	.015-	.016	.001	.00
12.00-	.00	.381-	.251	.013-	.008	.004	.00
10.00-	.00	.280-	.166	.011-	.011	.003	.00
.00-	.00-	.000-	.003-	.009-	.012	.003	.00
2.00	.00-	.039	.022-	.013-	.017	.001	.00
4.00	.00-	.094	.052-	.013-	.017	.001	.00
6.00	.00-	.147	.082-	.013-	.019	.002	.00
8.00	.00-	.204	.111-	.017-	.023	.003	.00
10.00	.00-	.271	.156-	.020-	.026	.002	.00
12.00	.00-	.364	.235-	.024-	.031	.003	.00
14.00	.00-	.487	.352-	.030-	.040	.004	.00
16.00	.00-	.640	.500-	.041-	.053	.005	.00
18.00	.00-	.757	.580-	.037-	.048	.005	.00
19.00	.00-	.801	.600-	.034-	.045	.006	.00
10.00	.00	.255	.145-	.027-	.028	.006	.00
.00-	.00	.039-	.038	.021-	.018	.006	.00

685 12

.00	.00-	.001	.000-	.002-	.009	.005-	45.00
1.41-	1.41-	.031-	.017	.035	.013-	.005-	45.00
2.83-	2.83-	.068-	.039	.074	.042-	.003-	45.00
4.25-	4.25-	.109-	.064	.114	.064-	.004-	45.00
5.68-	5.68-	.148-	.086	.152	.084-	.004-	45.00
7.11-	7.11-	.196-	.117	.203	.119-	.005-	45.00
8.55-	8.55-	.273-	.183	.276	.184-	.004-	45.00
7.11-	7.11-	.197-	.117	.201	.119-	.004-	45.00
.00-	.00	.000-	.009-	.005	.006-	.000	45.00
1.41	1.41	.030	.024-	.022-	.007	.001	45.00
2.83	2.83	.067	.042-	.060-	.035	.001-	45.00
4.25	4.25	.103	.062-	.102-	.063	.001-	45.00
5.68	5.68	.148	.083-	.146-	.094	.003-	45.00
7.11	7.11	.199	.117-	.196-	.129	.003-	45.00
8.55	8.55	.270	.178-	.268-	.191	.003-	45.00
10.00	10.00	.362	.268-	.362-	.283	.003-	45.00
11.46	11.46	.481	.387-	.485-	.411	.004-	45.00
12.94	12.94	.559	.437-	.562-	.457	.003-	45.00
12.94	12.94	.551	.434-	.553-	.448	.001	45.00
14.44	14.44	.581	.444-	.586-	.466	.001-	45.00
7.11	7.11	.189	.112-	.189-	.115	.000-	45.00
.00-	.00-	.004-	.000	.005	.005-	.001	45.00

685 13

.00	.00-	.001-	.002	.002	.006	.005- 90.00
.00	2.00-	.001	.001	.047	.020-	.004- 90.00
.00	4.00-	.000	.004	.098	.053-	.005- 90.00
.00	6.00-	.006	.004	.153	.086-	.005- 90.00
.00	8.00-	.004	.006	.212	.124-	.003- 90.00
.00	10.00-	.006	.006	.283	.172-	.002- 90.00
.00	12.00-	.010	.007	.382	.257-	.003- 90.00
.00	10.00-	.007	.009	.279	.165-	.004- 90.00
.00-	.00-	.001	.002-	.000	.006	.004- 90.00
.00	2.00	.004	.003-	.046-	.031	.005- 90.00
.00-	4.00	.003	.003-	.095-	.061	.005- 90.00
.00	6.00	.003	.002-	.150-	.095	.005- 90.00
.00-	8.00	.004	.005-	.207-	.125	.005- 90.00
.00	10.00	.000	.000	.278-	.171	.004- 90.00
.00-	12.00	.001	.002-	.378-	.259	.002- 90.00
.00	14.00	.001-	.003	.517-	.395	.002- 90.00
.00	16.00	.001-	.003	.683-	.563	.002- 90.00
.00	18.00	.000	.001	.789-	.634	.002- 90.00
.00	19.00	.000	.003	.834-	.650	.002- 90.00
.00	10.00	.003	.002-	.271-	.162	.001- 90.00
.00-	.00-	.001	.003-	.005	.005-	.001- 90.00

685 14

.00-	.00-	.004-	.002	.004	.006	.006-	90.00
.00-	2.00-	.007-	.002	.047	.022-	.004-	90.00
.00-	4.00-	.011-	.008	.098	.054-	.006-	90.00
.00-	6.00-	.012-	.013	.155	.085-	.006-	90.00
.00	8.00-	.015-	.017	.208	.113-	.005-	90.00
.00	10.00-	.018-	.019	.283	.166-	.007-	90.00
.00-	12.00-	.020-	.019	.383	.258-	.003-	90.00
.00-	10.00-	.019-	.013	.282	.174-	.001-	90.00
.00-	.00	.006-	.004-	.005	.006-	.000	90.00
.00-	2.00	.006-	.003-	.036-	.016	.000-	90.00
.00-	4.00	.004-	.000	.089-	.049	.000-	90.00
.00-	6.00	.003-	.000	.146-	.087	.000	90.00
.00	8.00	.003-	.005	.207-	.124	.001-	90.00
.00	10.00	.000	.007	.277-	.181	.005-	90.00
.00	12.00	.001-	.006	.374-	.259	.004-	90.00
.00-	14.00	.005-	.005	.499-	.375	.003-	90.00
.00-	16.00	.007-	.005	.669-	.546	.001-	90.00
.00-	18.00	.008-	.006	.780-	.620	.001	90.00
.00	19.00	.007-	.008	.822-	.641	.000	90.00
.00-	10.00	.004-	.003	.266-	.154	.002	90.00
.00	.00-	.003-	.005	.001	.003	.001-	90.00

685 15

.00	.00-	.005-	.006	.004	.000-	.001-	45.00
1.41-	1.41-	.037-	.023	.039	.019-	.001-	45.00
2.83-	2.83-	.076-	.048	.075	.045-	.001-	45.00
4.25-	4.25-	.114-	.068	.114	.068-	.001-	45.00
5.68-	5.68-	.155-	.090	.157	.092-	.001-	45.00
7.11-	7.11-	.207-	.127	.205	.126-	.001-	45.00
8.55-	8.55-	.278-	.191	.273	.186-	.000-	45.00
7.11-	7.11-	.204-	.125	.199	.119-	.001-	45.00
.00-	.00-	.001-	.000	.001-	.009	.003-	45.00
1.41	1.41	.030	.015-	.028-	.020	.002-	45.00
2.83	2.83	.063	.035-	.059-	.035	.002-	45.00
4.25	4.25	.098	.054-	.099-	.060	.001	45.00
5.68	5.68	.138	.073-	.145-	.084	.001	45.00
7.11	7.11	.181	.104-	.188-	.110	.003	45.00
8.55	8.55	.252	.159-	.261-	.180	.001	45.00
10.00	10.00	.341	.244-	.353-	.271	.000-	45.00
11.46	11.46	.458	.362-	.475-	.395	.001	45.00
12.94	12.94	.533	.410-	.561-	.457	.000	45.00
13.69	13.69	.555	.411-	.589-	.474	.000	45.00
7.11	7.11	.180	.098-	.189-	.113	.003	45.00
.00-	.00	.008-	.004	.007	.009-	.003	45.00

685 16

.00	.00-	.007-	.008	.001	.004	.003-	.00
2.00-	.00-	.049-	.030	.003	.009	.004-	.00
4.00-	.00-	.099-	.060	.004	.007	.003-	.00
6.00-	.00-	.155-	.092	.009	.002-	.003-	.00
8.00-	.00-	.214-	.123	.011	.005-	.002-	.00
10.00-	.00-	.286-	.172	.012	.008-	.000	.00
12.00-	.00-	.389-	.261	.011	.010-	.000	.00
10.00-	.00-	.286-	.172	.011	.004-	.001-	.00
.00-	.00-	.004-	.003	.008	.001-	.003-	.00
2.00	.00-	.035	.014-	.006	.005	.003-	.00
4.00	.00-	.086	.041-	.006	.008	.003-	.00
6.00	.00-	.138	.071-	.006	.007	.002-	.00
8.00	.00-	.189	.096-	.003	.012	.003-	.00
10.00	.00-	.251	.131-	.000	.016	.002-	.00
12.00	.00-	.332	.197-	.006-	.014	.002	.00
14.00	.00-	.442	.292-	.016-	.029	.002	.00
16.00	.00-	.586	.425-	.026-	.044	.003	.00
18.00	.00-	.701	.501-	.030-	.055	.003	.00
19.01	.00-	.747	.524-	.030-	.058	.001	.00
10.00	.00-	.243	.123-	.004-	.015	.000-	.00
.00-	.00-	.004-	.000	.009	.007-	.001-	.00

685 17

.00-	.00-	.005-	.005	.006	.007	.005-	45.00-
1.41-	1.41	.034-	.019	.024-	.024	.005-	45.00-
2.83-	2.83	.072-	.045	.063-	.051	.006-	45.00-
4.25-	4.25	.107-	.065	.102-	.073	.006-	45.00-
5.68-	5.68	.148-	.086	.137-	.091	.006-	45.00-
7.11-	7.11	.196-	.120	.185-	.122	.006-	45.00-
8.55-	8.55	.272-	.183	.256-	.181	.005-	45.00-
7.11-	7.11	.200-	.120	.184-	.119	.005-	45.00-
.00-	.00-	.005-	.000	.011	.004-	.003-	45.00-
1.41	1.41-	.020	.015-	.045	.033-	.001	45.00-
2.83	2.83-	.052	.032-	.086	.058-	.002	45.00-
4.25	4.25-	.084	.044-	.121	.073-	.001	45.00-
5.68	5.68-	.125	.059-	.156	.085-	.000-	45.00-
7.11	7.11-	.168	.078-	.199	.105-	.003-	45.00-
8.55	8.55-	.226	.119-	.268	.162-	.004-	45.00-
10.00	10.00-	.298	.180-	.351	.238-	.004-	45.00-
11.46	11.46-	.390	.262-	.458	.346-	.004-	45.00-
12.94	12.94-	.475	.326-	.546	.406-	.005-	45.00-
13.69	13.69-	.510	.344-	.577	.419-	.005-	45.00-
7.11	7.11-	.159	.080-	.195	.114-	.000	45.00-
.00-	.00	.011-	.001-	.006	.014-	.003	45.00-

685 18

.00-	.00-	.003-	.002	.002	.009	.004-	.00
2.00-	.00-	.053-	.030	.007	.007	.006-	.00
4.00-	.00-	.112-	.065	.006	.005	.006-	.00
6.00-	.00-	.165-	.094	.006	.007	.005-	.00
8.00-	.00-	.225-	.122	.012	.007-	.002-	.00
10.00-	.00-	.298-	.173	.009	.005-	.001-	.00
12.00-	.00	.408-	.262	.013	.017-	.002	.00
10.00-	.00-	.306-	.172	.009	.009-	.002	.00
.00-	.00-	.007-	.003-	.009	.005-	.000	.00
2.00	.00-	.039	.023-	.011	.004-	.001-	.00
4.00	.00-	.093	.055-	.011	.005-	.000-	.00
6.00	.00-	.150	.087-	.009	.004-	.001-	.00
8.00	.00-	.210	.118-	.011	.004-	.001-	.00
10.00	.00-	.275	.159-	.009	.004-	.001-	.00
12.00	.00-	.374	.237-	.011	.005-	.001-	.00
14.00	.00-	.497	.351-	.011	.007-	.001	.00
16.00	.00-	.665	.512-	.013	.011-	.001	.00
18.00	.00-	.786	.596-	.015	.013-	.003	.00
19.01	.00-	.832	.616-	.013	.011-	.002	.00
10.00	.00-	.265	.151-	.009	.008-	.003	.00
.00-	.00	.012-	.002	.005	.006-	.004	.00

```
685   19
     .00-     .00-     .008-    .005     .001-    .007     .002-    45.00
    1.41-    1.41-    .042-    .024     .034     .013-    .001-    45.00
    2.83-    2.83-    .083-    .049     .077     .041-    .002-    45.00
    4.25-    4.25-    .121-    .066     .117     .064-    .001-    45.00
    5.68-    5.68-    .163-    .089     .153     .079-    .000     45.00
    7.11-    7.11-    .215-    .126     .207     .115-    .001-    45.00
    8.55-    8.55-    .295-    .189     .287     .188-    .000     45.00
    7.11-    7.11-    .208-    .116     .204     .122-    .000-    45.00
     .00      .00     .029     .014-    .031-    .008     .000-    45.00
    1.41     1.42     .030     .023-    .031-    .005     .003     45.00
    2.83     2.83     .069     .042-    .066-    .030     .002     45.00
    4.25     4.25     .114     .065-    .109-    .061     .001-    45.00
    5.68     5.68     .154     .083-    .153-    .087     .003-    45.00
    7.11     7.11     .203     .111-    .200-    .120     .005-    45.00
    8.55     8.55     .269     .166-    .269-    .175     .005-    45.00
   10.00    10.00     .356     .244-    .351-    .248     .007-    45.00
   11.46    11.46     .474     .360-    .468-    .357     .006-    45.00
   12.94    12.94     .563     .421-    .557-    .420     .005-    45.00
   13.69    13.69     .585     .428-    .582-    .425     .006-    45.00
    7.11     7.11     .154     .095-    .151-    .081     .001     45.00
     .00-     .00-    .048-    .015     .046     .027-    .003     45.00
```

685 20

.00-	.00	.008-	.002	.003	.003-	.004- 90.00
.00-	2.00-	.008-	.001	.047	.025-	.005- 90.00
.00-	4.00-	.008-	.002	.098	.057-	.004- 90.00
.00-	6.00-	.007-	.002	.157	.091-	.003- 90.00
.00-	8.00-	.011-	.002	.216	.123-	.002- 90.00
.00-	10.00-	.012-	.004	.286	.167-	.000- 90.00
.00-	12.00-	.014-	.004	.383	.249-	.002 90.00
.00-	10.00-	.014-	.004	.282	.164-	.001 90.00
.00-	.00	.008-	.001	.001-	.004-	.001- 90.00
.00-	2.00	.004-	.001-	.043-	.018	.001- 90.00
.00-	4.00	.008-	.004	.100-	.051	.003- 90.00
.00-	6.00	.007-	.003	.156-	.082	.003- 90.00
.00-	8.00	.010-	.005	.218-	.111	.003- 90.00
.00-	10.00	.007-	.005	.292-	.162	.004- 90.00
.00-	12.00	.008-	.008	.401-	.256	.005- 90.00
.00-	14.00	.015-	.014	.536-	.384	.007- 90.00
.00	16.00	.016-	.020	.701-	.541	.011- 90.00
.00	18.00	.016-	.020	.804-	.598	.011- 90.00
.00	19.01	.013-	.019	.850-	.613	.013- 90.00
.00-	10.00	.008-	.005	.282-	.153	.003- 90.00
.00-	.00	.012-	.004	.002-	.006-	.001- 90.00

685 21

.00	.00-	.000	.000	.000	.007	.004-	90.00
.00-	2.00-	.003	.003-	.042	.019-	.003-	90.00
.00-	4.00-	.000-	.001-	.099	.057-	.003-	90.00
.00-	6.00-	.003	.005-	.152	.087-	.003-	90.00
.00-	8.00-	.004	.006-	.205	.118-	.003-	90.00
.00-	10.00-	.003	.006-	.274	.165-	.003-	90.00
.00-	12.00-	.001	.006-	.375	.255-	.002-	90.00
.00-	10.00-	.001	.006-	.271	.165-	.002-	90.00
.00-	.00	.000-	.004-	.005-	.008	.003-	90.00
.00-	2.00	.001	.005-	.044-	.028	.001-	90.00
.00-	4.00	.001	.006-	.097-	.058	.001-	90.00
.00-	6.00	.000-	.001-	.153-	.095	.003-	90.00
.00	8.00	.005	.003-	.215-	.131	.003-	90.00
.00	10.00	.005	.003-	.284-	.183	.004-	90.00
.00	12.00	.005	.003-	.389-	.278	.004-	90.00
.00	14.00	.005	.003-	.524-	.412	.005-	90.00
.00	16.00	.005	.002-	.688-	.575	.005-	90.00
.00	18.00	.001	.000-	.793-	.638	.005-	90.00
.00-	19.00	.003	.003-	.828-	.647	.003-	90.00
.00-	10.00	.003	.006-	.274-	.162	.001-	90.00
.00-	.00	.001-	.006-	.005	.011-	.001-	90.00

685 22

.00	.00-	.007	.003-	.001-	.007	.002-	45.00
1.41-	1.41-	.026-	.011	.031	.013-	.001-	45.00
2.83-	2.83-	.065-	.038	.069	.037-	.002-	45.00
4.25-	4.25-	.106-	.062	.110	.061-	.002-	45.00
5.68-	5.68-	.147-	.084	.145	.079-	.003-	45.00
7.11-	7.11-	.192-	.114	.200	.120-	.002-	45.00
8.55-	8.55-	.262-	.172	.267	.179-	.002-	45.00
7.11-	7.11-	.195-	.114	.197	.118-	.001-	45.00
.00-	.00-	.005	.009-	.001	.003	.000-	45.00
1.41	1.41	.041	.026-	.029-	.021	.002-	45.00
2.83	2.83	.079	.050-	.066-	.044	.001-	45.00
4.25	4.25	.117	.073-	.102-	.065	.001-	45.00
5.68	5.68	.161	.097-	.148-	.088	.002-	45.00
7.11	7.11	.211	.128-	.196-	.123	.002-	45.00
8.55	8.55	.283	.193-	.270-	.191	.002-	45.00
10.00	10.00	.374	.284-	.366-	.286	.003-	45.00
11.46	11.46	.497	.405-	.483-	.403	.003-	45.00
12.94	12.94	.572	.450-	.554-	.448	.003-	45.00
13.69	13.69	.602	.462-	.586-	.462	.003-	45.00
7.11	7.11	.200	.119-	.193-	.115	.001-	45.00
.00-	.00	.001	.003-	.000-	.007-	.001-	45.00

685	23						
	.00	.00-	.005	.005-	.007	.000-	.000-	.00
	2.00-	.00-	.040-	.020	.008	.002-	.001-	.00
	4.00-	.00-	.094-	.057	.008	.002	.002-	.00
	6.00-	.00-	.148-	.089	.010	.004	.002-	.00
	8.00-	.00-	.203-	.117	.006	.007	.002-	.00
	10.00-	.00-	.274-	.162	.011	.001-	.002-	.00
	12.00-	.00-	.374-	.248	.012	.005-	.001-	.00
	10.00-	.00-	.274-	.161	.007	.005-	.002-	.00
	.00-	.00-	.007	.008-	.011	.004-	.002-	.00
	2.00	.00-	.052	.033-	.009	.005-	.002-	.00
	4.00	.00-	.105	.066-	.014	.004-	.002-	.00
	6.00	.00-	.162	.098-	.008	.002-	.002-	.00
	8.00	.00-	.220	.127-	.012	.007-	.001-	.00
	10.00	.00-	.288	.177-	.015	.007-	.002-	.00
	12.00	.00-	.389	.265-	.016	.009-	.002-	.00
	14.00	.00-	.526	.401-	.016	.009-	.001-	.00
	16.00	.00-	.697	.571-	.016	.009-	.001-	.00
	18.00	.00-	.801	.639-	.019	.012-	.001-	.00
	19.00	.00-	.849	.662-	.017	.016-	.000	.00
	10.00	.00-	.279	.170-	.015	.014-	.000	.00
	.00-	.00	.000-	.004-	.011	.013-	.001-	.00

```
685    24
     .00      .00-     .008-     .009      .008      .007      .003-    90.00-
     .00     2.00-     .011-     .014      .057      .023-     .004-    90.00-
     .00     4.00-     .015-     .017      .114      .063-     .002-    90.00-
     .00-    6.00-     .019-     .018      .169      .096-     .001-    90.00-
     .00-    8.00-     .019-     .019      .223      .123-     .000-    90.00-
     .00-   10.00-     .023-     .022      .303      .186-     .000-    90.00-
     .00-   12.00-     .024-     .025      .410      .286-     .000      90.00-
     .00-   14.00-     .030-     .030      .553      .427-     .001      90.00-
     .00    16.00-     .032-     .036      .703      .569-     .000      90.00-
     .00    18.00-     .044-     .052      .798      .614-     .000-     90.00-
     .00    19.00-     .049-     .057      .838      .629-     .000-     90.00-
     .00-   10.00-     .022-     .018      .293      .175-     .001-     90.00-
     .00-     .00      .008-     .001-     .013      .007-     .001-     90.00-
```

685 25

.00	.00-	.016	.003-	.014	.003	.004-	90.00-
.00	2.00	.018	.000	.033-	.035	.005-	90.00-
.00	4.00	.018	.000	.087-	.071	.005-	90.00-
.00	6.00	.012	.002	.141-	.094	.003-	90.00-
.00	8.00	.011	.005	.198-	.135	.006-	90.00-
.00	10.00	.015	.004	.265-	.178	.006-	90.00-
.00	12.00	.007	.007	.362-	.249	.002-	90.00-
.00	10.00	.008	.004	.263-	.158	.002-	90.00-
.00	.00-	.010	.001-	.019	.013-	.002-	90.00-
.00	2.00-	.010	.001-	.070	.043-	.003-	90.00-
.00	4.00-	.012	.002-	.122	.075-	.003-	90.00-
.00	6.00-	.011	.001-	.178	.108-	.003-	90.00-
.00	8.00-	.010	.001-	.237	.145-	.002-	90.00-
.00	10.00-	.008	.001-	.326	.216-	.003-	90.00-
.00	12.00-	.008	.002-	.437	.324-	.001-	90.00-
.00	14.00-	.008	.004-	.586	.475-	.001-	90.00-
.00	16.00-	.005	.003-	.728	.607-	.000-	90.00-
.00	18.00-	.005	.005-	.825	.658-	.000-	90.00-
.00	19.00-	.005	.005-	.864	.670-	.000	90.00-
.00	10.00-	.007	.002-	.311	.204-	.000-	90.00-
.00	.00-	.011	.004-	.015	.013-	.001-	90.00-

685 26

.00	.00	.011	.002-	.012	.014-	.000	45.00-
1.41-	1.41	.018-	.019	.020-	.018	.002-	45.00-
2.83-	2.83	.061-	.044	.058-	.041	.002-	45.00-
4.25-	4.25	.102-	.068	.096-	.064	.001-	45.00-
5.68-	5.68	.141-	.090	.133-	.084	.002-	45.00-
7.11-	7.11	.192-	.121	.181-	.114	.001-	45.00-
8.55-	8.55	.261-	.181	.252-	.177	.002-	45.00-
7.11-	7.11	.192-	.123	.182-	.117	.002-	45.00-
.00	.00-	.018	.007-	.013	.008-	.000-	45.00-
1.42	1.41-	.054	.029-	.051	.032-	.001	45.00-
2.83	2.83-	.089	.044-	.094	.063-	.001	45.00-
4.25	4.25-	.120	.054-	.133	.084-	.001	45.00-
5.68	5.68-	.157	.068-	.174	.107-	.000-	45.00-
7.11	7.11-	.204	.100-	.227	.141-	.001-	45.00-
8.55	8.55-	.279	.162-	.301	.208-	.000-	45.00-
10.00	10.00-	.369	.255-	.397	.308-	.001	45.00-
11.46	11.46-	.492	.378-	.516	.428-	.001	45.00-
12.94	12.94-	.570	.433-	.589	.475-	.001	45.00-
13.69	13.69-	.604	.450-	.622	.490-	.002	45.00-
7.11	7.11-	.194	.091-	.221	.142-	.000-	45.00-
.00	.00-	.016	.004-	.016	.007-	.001-	45.00-

685 27

.00	.00-	.019	.007-	.016	.013-	.001-	.00
2.00-	.00-	.033-	.024	.015	.011-	.003-	.00
4.00-	.00-	.087-	.059	.016	.011-	.005-	.00
6.00-	.00-	.150-	.096	.015	.013-	.004-	.00
8.00-	.00-	.205-	.122	.013	.011-	.004-	.00
10.00-	.00-	.275-	.171	.015	.011-	.004-	.00
12.00-	.00-	.378-	.257	.015	.016-	.004-	.00
10.00-	.00-	.275-	.168	.015	.016-	.002-	.00
.00	.00-	.020	.007-	.013	.014-	.002-	.00
2.00	.00	.065	.031-	.013	.016-	.002-	.00
4.00	.00-	.111	.044-	.017	.017-	.003-	.00
6.00	.00-	.150	.053-	.017	.016-	.003-	.00
8.00	.00-	.201	.074-	.016	.016-	.003-	.00
10.00	.00-	.265	.117-	.015	.014-	.002-	.00
12.00	.00	.365	.205-	.013	.016-	.000	.00
14.00	.00	.495	.339-	.015	.017-	.000	.00
16.00	.00	.677	.531-	.016	.019-	.001	.00
18.00	.00	.810	.640-	.016	.019-	.001	.00
19.00	.00	.853	.660-	.016	.019-	.002	.00
10.00	.00	.259	.112-	.012	.016-	.001	.00
.00	.00	.016	.006-	.011	.014-	.001-	.00

685 28

.00	.00-	.055	.000-	.016	.010-	.001	.00
2.00-	.00-	.006-	.038	.011	.005-	.001	.00
4.00-	.00-	.074-	.079	.011	.005-	.000-	.00
6.00-	.00-	.133-	.110	.012	.002-	.003-	.00
8.00-	.00-	.189-	.136	.011	.002-	.004-	.00
10.00-	.00-	.270-	.187	.011	.001-	.003-	.00
12.00-	.00-	.372-	.268	.013	.010-	.001-	.00
10.00-	.00-	.269-	.183	.012	.011-	.001-	.00
.00	.00-	.054	.000-	.013	.011-	.001-	.00
2.00	.00-	.099	.014-	.012	.008-	.002-	.00
4.00	.00-	.136	.012-	.013	.008-	.002-	.00
6.00	.00-	.170	.008-	.013	.008-	.001-	.00
8.01	.00-	.209	.010-	.015	.007-	.002-	.00
10.01	.00-	.251	.020-	.012	.005-	.001-	.00
12.01	.00-	.312	.057-	.013	.007-	.000-	.00
14.01	.00-	.392	.128-	.016	.013-	.001	.00
16.01	.00-	.526	.266-	.016	.016-	.001	.00
18.01	.00-	.724	.489-	.013	.013-	.000	.00
19.01	.00-	.805	.572-	.017	.017-	.001	.00
10.01	.00-	.244	.023-	.011	.011-	.001	.00
.00	.00	.047	.003	.008	.011-	.002	.00

```
685    29
     .00      .00-     .055     .000-     .003     .004     .002-   45.00
    1.41-    1.41-     .012     .031      .036     .016-    .001-   45.00
    2.83-    2.83-     .035-    .059      .082     .051-    .001-   45.00
    4.25-    4.25-     .082-    .081      .121     .075-    .000-   45.00
    5.68-    5.68-     .127-    .104      .158     .094-    .000     45.00
    7.11-    7.11-     .179-    .138      .205     .129-    .000-   45.00
    8.55-    8.55-     .259-    .200      .282     .202-    .000     45.00
    7.11-    7.11-     .179-    .135      .205     .129-    .000-   45.00
     .00      .00-     .058     .004-     .003     .004     .000-   45.00
    1.42     1.41      .093     .016-     .035-    .029     .002-   45.00
    2.83     2.83      .119     .016-     .071-    .054     .002-   45.00
    4.25     4.25      .147     .017-     .109-    .071     .002-   45.00
    5.68     5.68      .181     .026-     .146-    .091     .003-   45.00
    7.11     7.11      .225     .047-     .193-    .121     .003-   45.00
    8.55     8.55      .287     .096-     .256-    .173     .002-   45.00
   10.00    10.00      .367     .170-     .344-    .257     .002-   45.00
   11.47    11.46      .476     .280-     .458-    .374     .003-   45.00
   12.94    12.94      .586     .384-     .563-    .463     .001-   45.00
   13.69    13.69      .625     .408-     .594-    .479     .001-   45.00
    7.11     7.11      .212     .040-     .184-    .103     .001-   45.00
     .00      .00      .047     .005      .007     .011-    .001-   45.00
```

685 30

.00	.00-	.048	.004	.007-	.011	.002	90.00
.00	2.00-	.047	.009	.046	.022-	.002	90.00
.00	4.00-	.044	.014	.102	.062-	.001	90.00
.00	6.00-	.039	.017	.160	.098-	.002	90.00
.00	8.00-	.037	.019	.219	.133-	.003	90.00
.00	10.00-	.033	.020	.296	.198-	.004	90.00
.00	12.00-	.032	.019	.405	.299-	.002	90.00
.00	10.00-	.031	.022	.293	.193-	.003	90.00
.00	.00-	.048	.003	.003-	.003	.001	90.00
.00	2.00	.047	.006	.051-	.032	.000	90.00
.00	4.00	.044	.012	.107-	.072	.000-	90.00
.00	6.00	.046	.015	.162-	.106	.001-	90.00
.00	8.00	.040	.021	.221-	.142	.002-	90.00
.00	10.00	.039	.021	.299-	.201	.002-	90.00
.00	12.00	.040	.020	.409-	.305	.002-	90.00
.00	14.00	.037	.020	.550-	.449	.003-	90.00
.00	16.00	.037	.019	.693-	.589	.004-	90.00
.00	18.00	.031	.023	.784-	.635	.003-	90.00
.00	19.00	.031	.022	.824-	.648	.003-	90.00
.00	10.00	.036	.020	.282-	.174	.000	90.00
.00	.00	.044	.003	.011	.014-	.000-	90.00

685 31

.00	.00-	.007	.005-	.003-	.008	.000-	90.00
.00	2.00-	.005	.003-	.047	.022-	.001-	90.00
.00	4.00-	.004	.002-	.101	.057-	.001-	90.00
.00	6.00-	.005	.002-	.157	.091-	.001-	90.00
.00	8.00-	.007	.003-	.212	.117-	.003-	90.00
.00	10.00-	.004	.003-	.285	.169-	.002-	90.00
.00-	12.00-	.004	.005-	.386	.258-	.001-	90.00
.00-	10.00-	.004	.005-	.282	.167-	.001-	90.00
.00	.00-	.008	.006-	.004-	.011	.001-	90.00
.00	2.00	.008	.006-	.046-	.030	.001-	90.00
.00	4.00	.011	.008-	.099-	.063	.001-	90.00
.00	6.00	.010	.004-	.154-	.095	.002-	90.00
.00	8.00	.007	.001	.215-	.129	.003-	90.00
.00	10.00	.008	.002	.288-	.182	.003-	90.00
.00	12.00	.010	.002	.397-	.281	.003-	90.00
.00	14.00	.010	.004	.533-	.417	.004-	90.00
.00	16.00	.008	.005	.694-	.575	.004-	90.00
.00	18.00	.007	.006	.793-	.631	.005-	90.00
.00	19.00	.008	.005	.836-	.647	.004-	90.00
.00	10.00	.006	.003	.276-	.165	.003-	90.00
.00	.00	.005	.005-	.004	.006-	.002-	90.00

685 32

.00	.00-	.014	.004-	.001-	.015	.003-	45.00
1.41-	1.42-	.023-	.015	.031	.005-	.002-	45.00
2.83-	2.83-	.068-	.042	.077	.045-	.002-	45.00
4.25-	4.25-	.109-	.067	.118	.066-	.002-	45.00
5.68-	5.68-	.147-	.085	.157	.089-	.002-	45.00
7.11-	7.11-	.197-	.119	.208	.127-	.002-	45.00
8.55-	8.55-	.273-	.182	.279	.189-	.001-	45.00
7.11-	7.11-	.197-	.117	.204	.123-	.001-	45.00
.00	.00-	.012	.007-	.003	.003	.002-	45.00
1.42	1.41	.046	.025-	.027-	.020	.002-	45.00
2.83	2.83	.082	.043-	.064-	.043	.003-	45.00
4.25	4.25	.110	.055-	.101-	.059	.001-	45.00
5.68	5.68	.149	.071-	.141-	.081	.002-	45.00
7.11	7.11	.193	.103-	.184-	.103	.001-	45.00
8.55	8.55	.267	.166-	.253-	.159	.002-	45.00
10.00	10.00	.354	.254-	.337-	.242	.001-	45.00
11.46	11.46	.475	.378-	.457-	.365	.002-	45.00
12.94	12.94	.564	.445-	.544-	.431	.003-	45.00
13.69	13.69	.598	.458-	.577-	.448	.004-	45.00
7.11	7.11	.192	.097-	.183-	.100	.002-	45.00
.00-	.00	.003	.003-	.009	.015-	.001	45.00

685	33						
.00	.00-	.010	.004-	.007	.003-	.002	.00
2.00-	.00-	.039-	.025	.008	.004-	.002	.00
4.00-	.00-	.094-	.058	.009	.008-	.002	.00
6.00-	.00-	.152-	.092	.012	.008-	.001	.00
8.00-	.00-	.208-	.124	.010	.001-	.001-	.00
10.00-	.00-	.277-	.171	.007	.004	.002-	.00
12.00-	.00-	.372-	.254	.007	.005	.004-	.00
10.00-	.00-	.278-	.167	.011	.004-	.001-	.00
.00	.00-	.012	.008-	.007	.005-	.001	.00
2.00	.00-	.057	.032-	.009	.005-	.000-	.00
4.00	.00-	.109	.058-	.016	.011-	.000	.00
6.00	.00-	.157	.080-	.019	.015-	.001-	.00
8.00	.00-	.215	.112-	.016	.011-	.001-	.00
10.00	.00-	.286	.161-	.017	.010-	.002-	.00
12.00	.00-	.387	.253-	.013	.005-	.002-	.00
14.00	.00-	.521	.385-	.011	.002-	.001-	.00
16.00	.00-	.698	.568-	.012	.007-	.000	.00
18.00	.00-	.811	.647-	.012	.008-	.000	.00
19.00	.00-	.655	.665-	.015	.011-	.000	.00
10.00	.00-	.276	.156-	.015	.014-	.000-	.00
.00	.00-	.008	.005-	.008	.008-	.001-	.00

685 34

.00	.00-	.030	.006-	.001	.003	.000-	.00
2.00-	.00-	.022-	.022	.001	.000-	.000	.00
4.00-	.00-	.080-	.059	.005	.002-	.000	.00
6.00-	.00-	.141-	.096	.008	.005-	.000-	.00
8.00-	.00-	.199-	.125	.009	.007-	.001	.00
10.00-	.00-	.272-	.173	.008	.005-	.000	.00
12.00-	.00-	.369-	.255	.008	.008-	.001	.00
10.00-	.00-	.269-	.168	.009	.007-	.000-	.00
.00	.00	.029	.011-	.004	.006-	.001	.00
2.00	.00	.071	.025-	.007	.009-	.001	.00
4.00	.00	.118	.042-	.011	.015-	.000	.00
6.00	.00	.159	.052-	.016	.022-	.000-	.00
8.00	.00	.209	.068-	.018	.025-	.001-	.00
10.00	.00	.258	.094-	.017	.023-	.001-	.00
12.00	.00	.342	.159-	.016	.022-	.000	.00
14.00	.00	.460	.271-	.018	.025-	.001	.00
16.00	.00	.631	.455-	.016	.023-	.001	.00
18.00	.00	.802	.618-	.015	.019-	.001	.00
19.00	.00	.853	.650-	.015	.019-	.001	.00
10.00	.00	.254	.092-	.018	.028-	.001	.00
.00	.00	.022	.007-	.005	.011-	.001	.00

```
685    35
      .00      .00-     .031     .009-     .009-     .014     .001-   45.00
     1.41-    1.41-     .008-     .012      .028      .006-    .001-   45.00
     2.83-    2.83-     .052-     .042      .070      .036-    .000-   45.00
     4.25-    4.25-     .096-     .067      .112      .058-    .000-   45.00
     5.68-    5.68-     .137-     .088      .153      .084-    .001-   45.00
     7.11-    7.11-     .188-     .121      .204      .120-    .002-   45.00
     8.55-    8.55-     .264-     .182      .275      .184-    .001-   45.00
     7.11-    7.11-     .188-     .119      .201      .119-    .001-   45.00
      .00      .00-     .029      .011-     .004-     .008     .002-   45.00
     1.42     1.41      .059      .020-     .032-     .020     .001-   45.00
     2.83     2.83      .088      .023-     .067-     .036     .002-   45.00
     4.25     4.25      .115      .027-     .102-     .051     .001-   45.00
     5.68     5.68      .151      .038-     .143-     .072     .003-   45.00
     7.11     7.11      .193      .063-     .190-     .099     .002-   45.00
     8.55     8.55      .255      .116-     .252-     .149     .003-   45.00
    10.00    10.00      .346      .204-     .340-     .233     .004-   45.00
    11.47    11.46      .464      .328-     .457-     .353     .004-   45.00
    12.94    12.94      .573      .428-     .560-     .441     .003-   45.00
    13.69    13.69      .605      .448-     .593-     .457     .001-   45.00
     7.11     7.11      .185      .058-     .182-     .081     .000-   45.00
      .00      .00      .023      .007-     .001      .007-    .001-   45.00
```

685 36

.00	.00-	.022	.000	.011-	.015	.002-	90.00
.00	2.00-	.018	.003	.034	.005-	.002-	90.00
.00	4.00-	.013	.011	.092	.040-	.002-	90.00
.00	6.00-	.011	.011	.153	.079-	.003-	90.00
.00	8.00-	.010	.013	.212	.114-	.003-	90.00
.00	10.00-	.010	.010	.282	.164-	.003-	90.00
.00	12.00-	.010	.007	.382	.254-	.003-	90.00
.00	10.00-	.008	.010	.281	.163-	.003-	90.00
.00	.00-	.025	.003-	.008-	.015	.004-	90.00
.00	2.00	.023	.001-	.051-	.030	.002-	90.00
.00	4.00	.021	.006	.110-	.067	.002-	90.00
.00	6.00	.018	.014	.166-	.099	.003-	90.00
.00	8.00	.018	.018	.226-	.132	.004-	90.00
.00	10.00	.014	.023	.303-	.185	.003-	90.00
.00	12.00	.016	.023	.414-	.285	.004-	90.00
.00	14.00	.013	.025	.557-	.426	.003-	90.00
.00	16.00	.016	.024	.710-	.571	.005-	90.00
.00	18.00	.018	.024	.815-	.630	.005-	90.00
.00	19.00	.021	.024	.851-	.643	.006-	90.00
.00	10.00	.015	.020	.290-	.166	.004-	90.00
.00	.00	.021	.004-	.003	.003-	.004-	90.00

685 37

.00-	.00-	.003	.003-	.014	.001-	.001-	45.00-
1.41-	1.41	.027-	.015	.017-	.016	.001-	45.00-
2.83-	2.83	.067-	.037	.055-	.039	.001-	45.00-
4.25-	4.25	.107-	.064	.094-	.061	.001-	45.00-
5.68-	5.68	.147-	.084	.133-	.082	.001-	45.00-
7.11-	7.11	.195-	.115	.178-	.110	.000-	45.00-
8.55-	8.55	.262-	.173	.244-	.166	.001-	45.00-
7.11-	7.11	.193-	.112	.178-	.110	.002-	45.00-
.00-	.00-	.003	.006-	.015	.007-	.001-	45.00-
1.41	1.42-	.034	.022-	.048	.024-	.002-	45.00-
2.83	2.83-	.069	.042-	.086	.046-	.002-	45.00-
4.25	4.25-	.106	.062-	.124	.068-	.002-	45.00-
5.68	5.68-	.143	.079-	.164	.090-	.002-	45.00-
7.11	7.11-	.193	.112-	.215	.129-	.002-	45.00-
8.55	8.55-	.257	.166-	.289	.194-	.002-	45.00-
10.00	10.00-	.348	.250-	.386	.289-	.002-	45.00-
11.46	11.46-	.453	.347-	.498	.396-	.002-	45.00-
12.94	12.94-	.535	.403-	.576	.445-	.003-	45.00-
13.69	13.69-	.562	.413-	.602	.453-	.003-	45.00-
7.11	7.11-	.184	.104-	.211	.122-	.002-	45.00-
.00-	.00-	.001-	.003-	.015	.011-	.001-	45.00-
.00-	.00-	.001-	.003-	.015	.011-	.001-	45.00-

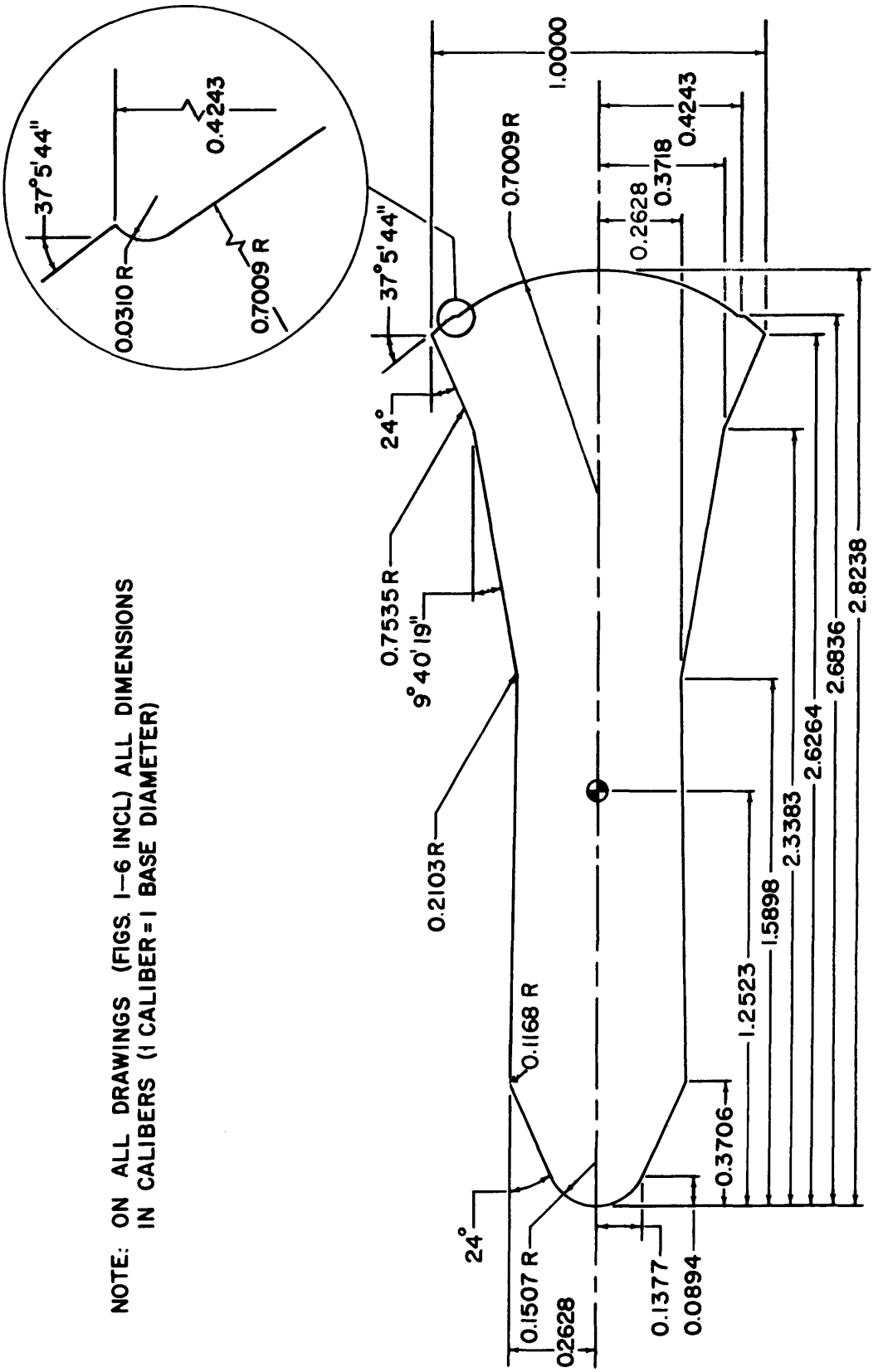

NOTE: ON ALL DRAWINGS (FIGS. I–6 INCL) ALL DIMENSIONS IN CALIBERS (1 CALIBER = 1 BASE DIAMETER)

FIG. 1 G.E. MARK 3 CONFIGURATION XXI–H

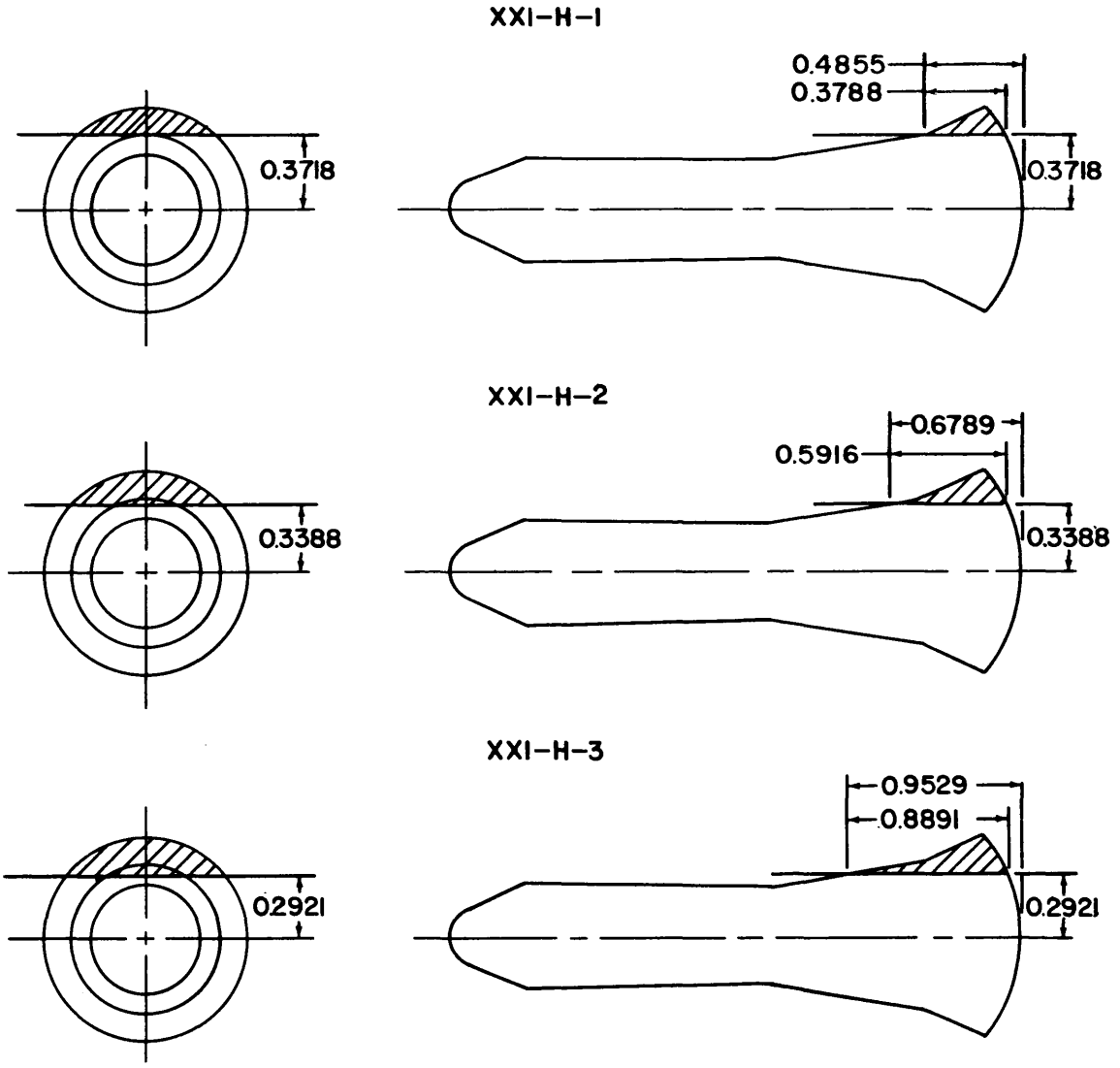

NOTE: ALL MATERIAL IN CROSS-HATCHED AREA HAS BEEN REMOVED

FIG. 2 MARK 3 CONFIGURATIONS WITH FLARE MODIFICATIONS, XXI-H-1, 2, AND 3

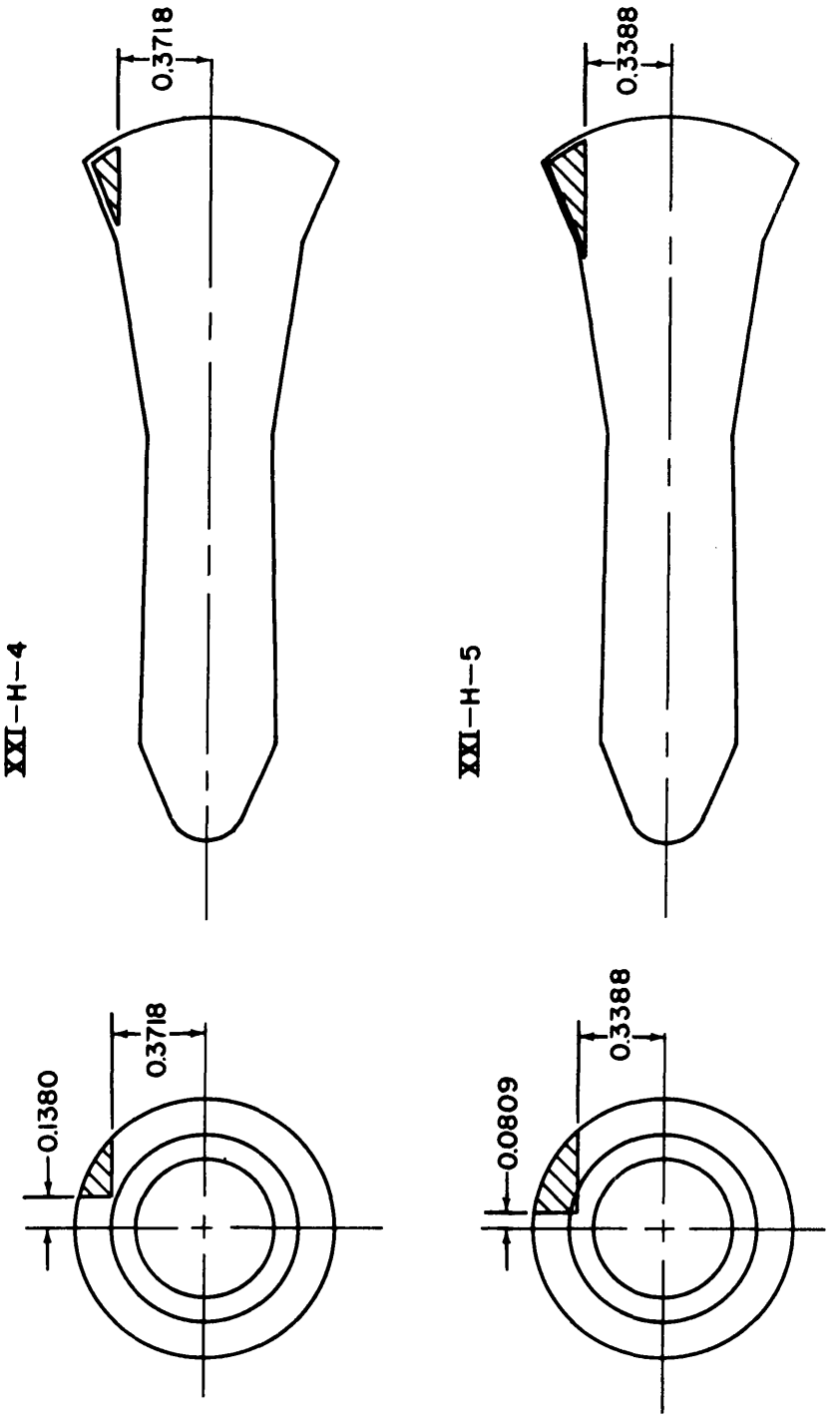

FIG. 3 MARK 3 CONFIGURATIONS WITH FLARE MODIFICATIONS, XXI-H-4 AND 5

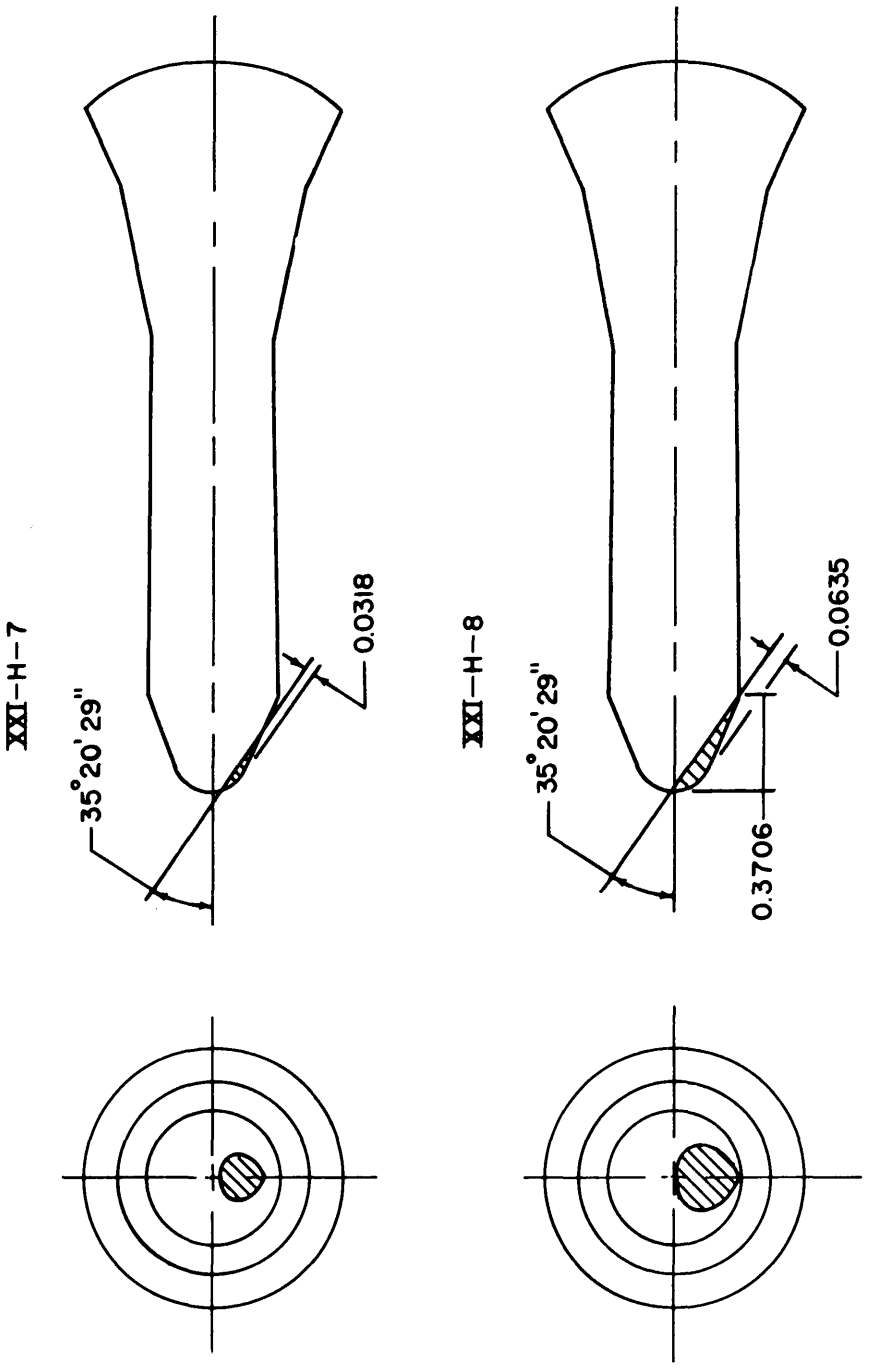

FIG. 4 MARK 3 CONFIGURATIONS WITH NOSE MODIFICATIONS, XXI-H-7 AND 8

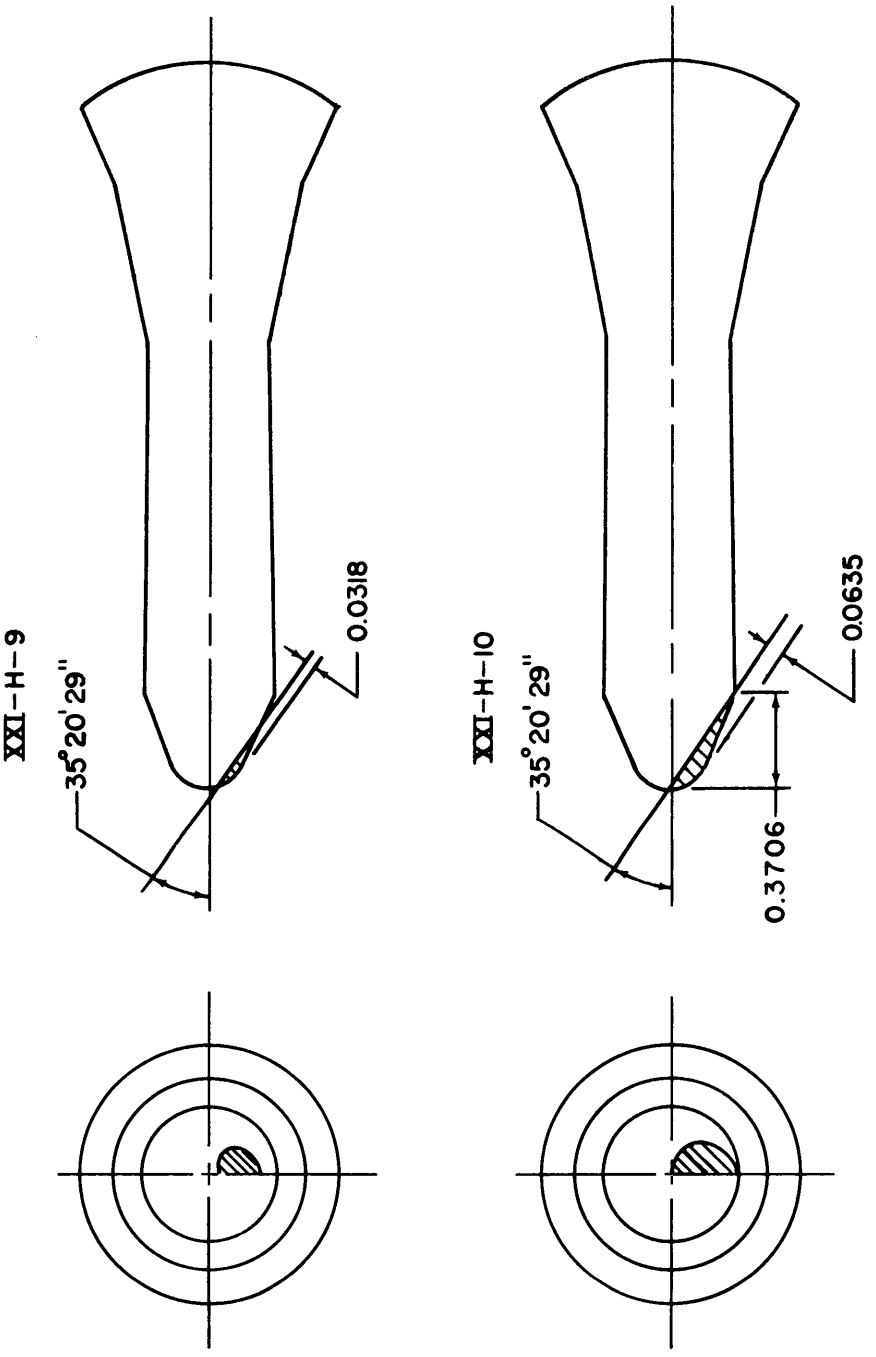

FIG. 5 MARK 3 CONFIGURATIONS WITH NOSE MODIFICATIONS, XXI-H-9 AND 10

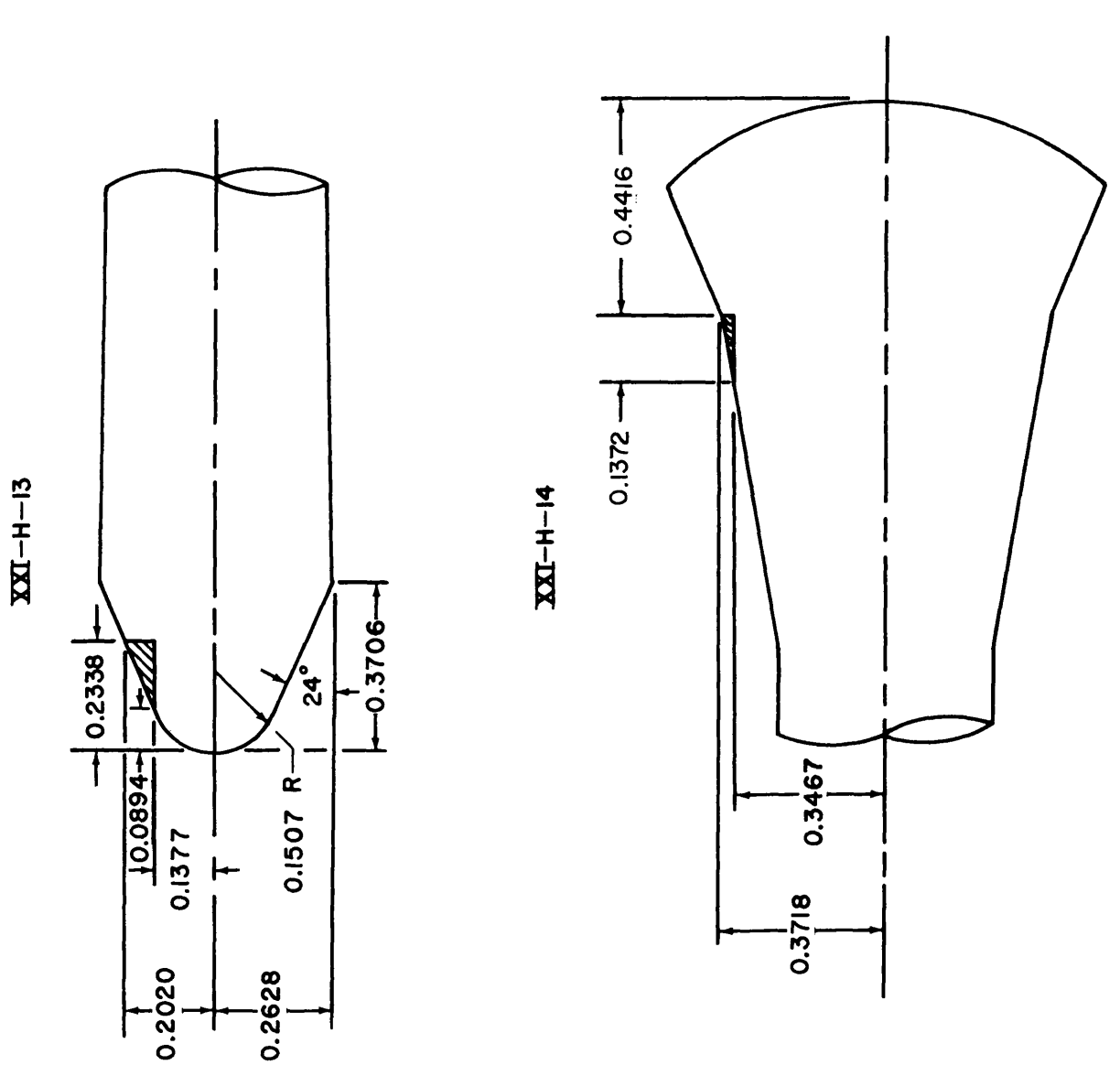

FIG. 6 MARK 3 CONFIGURATIONS WITH NOSE AND FLARE MODIFICATIONS, XXI-H-13 AND 14

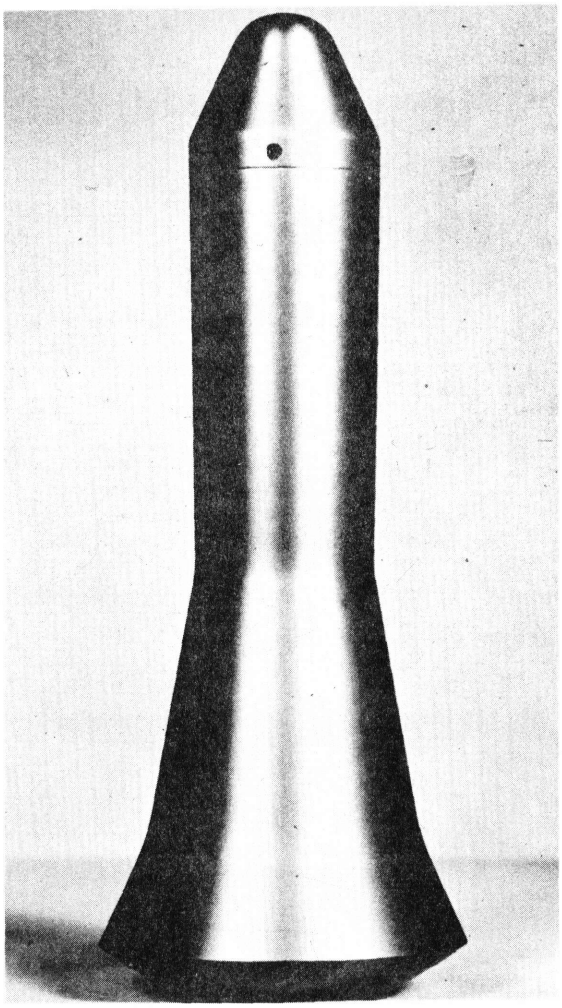

FIG. 7 G. E. MARK 3 XXI - H MODEL

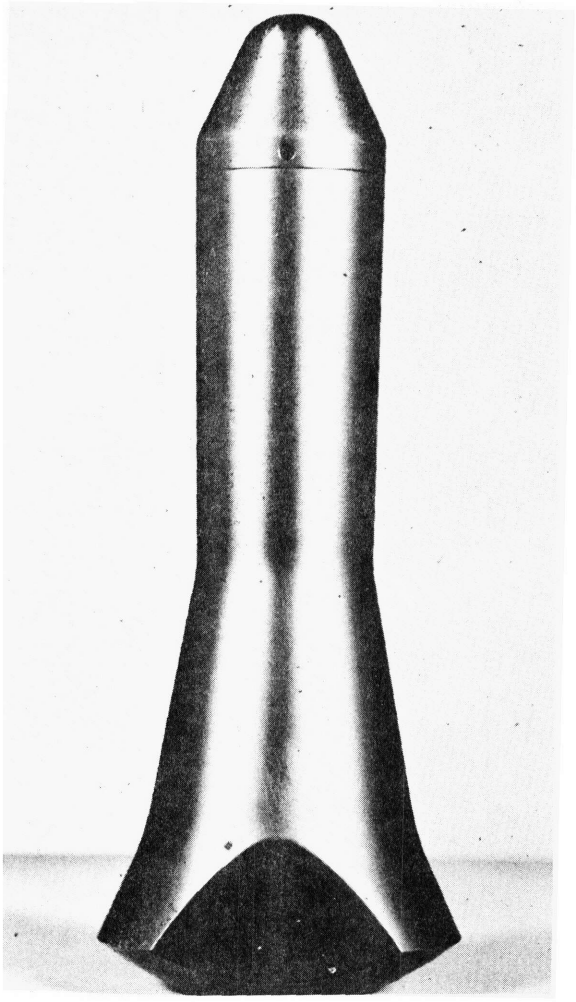

FIG. 8 XXI - H-1 MODEL

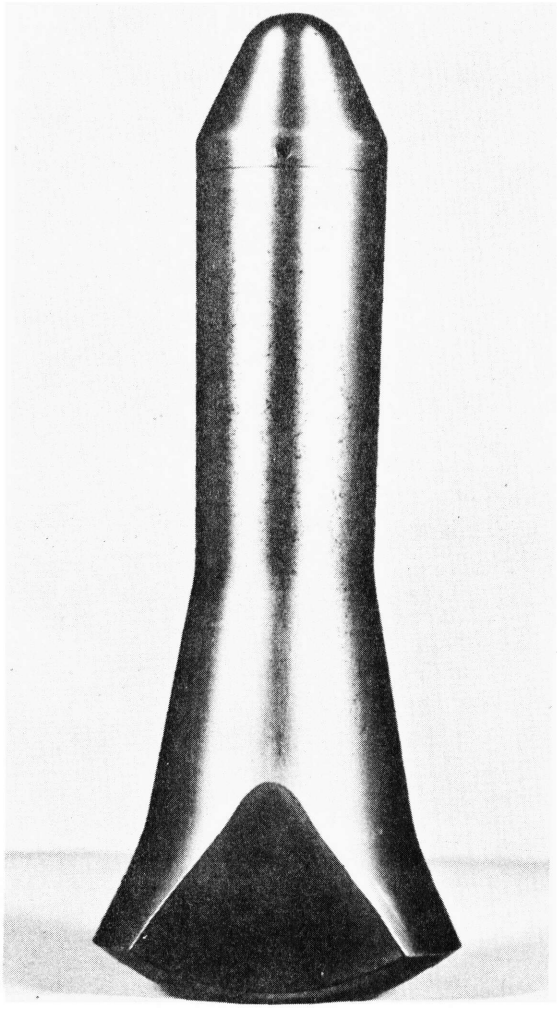

FIG. 9 XXI - H - 2 MODEL

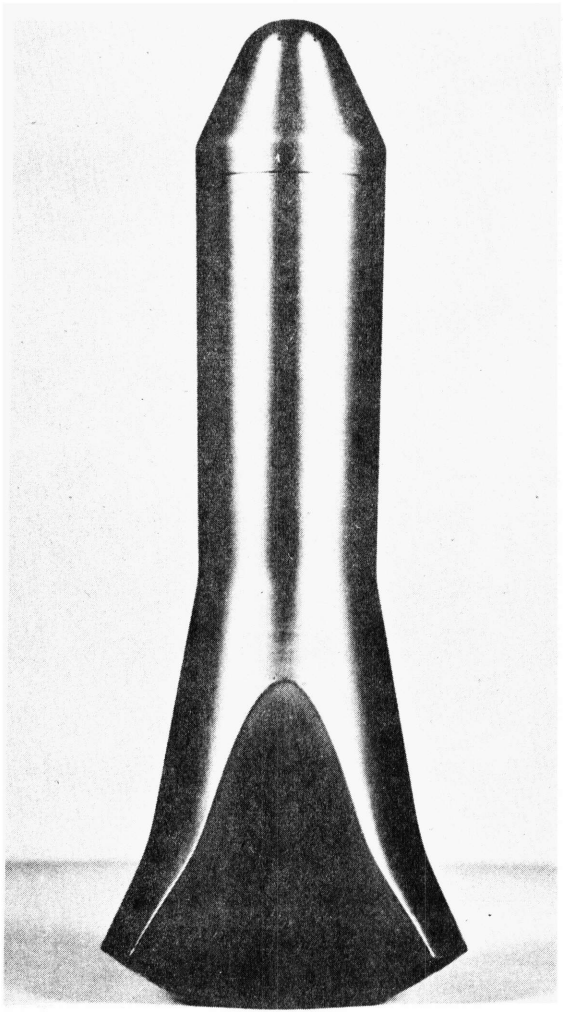

FIG. 10 XXI - H - 3 MODEL

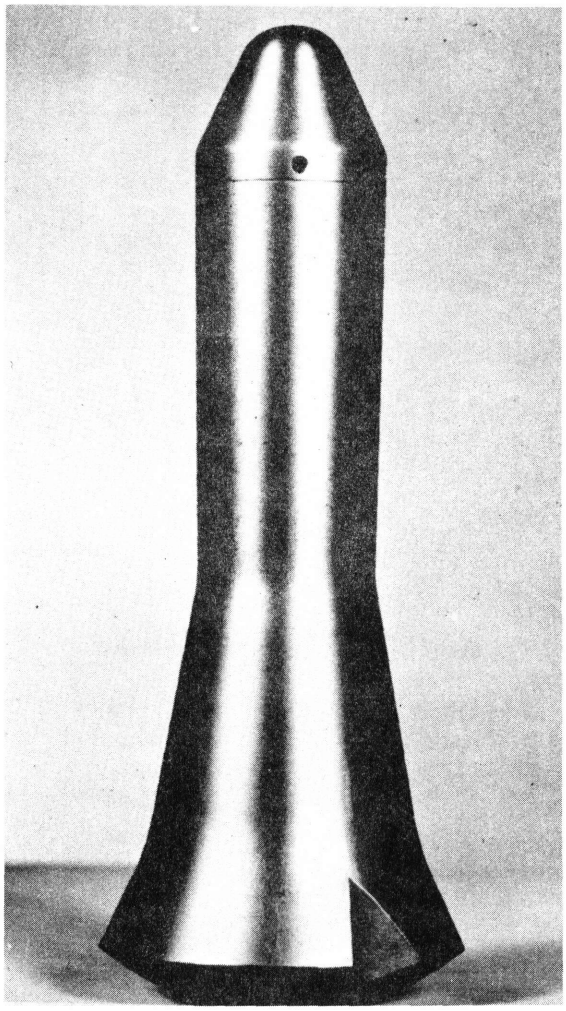

FIG. 11 XXI - H - 4 MODEL

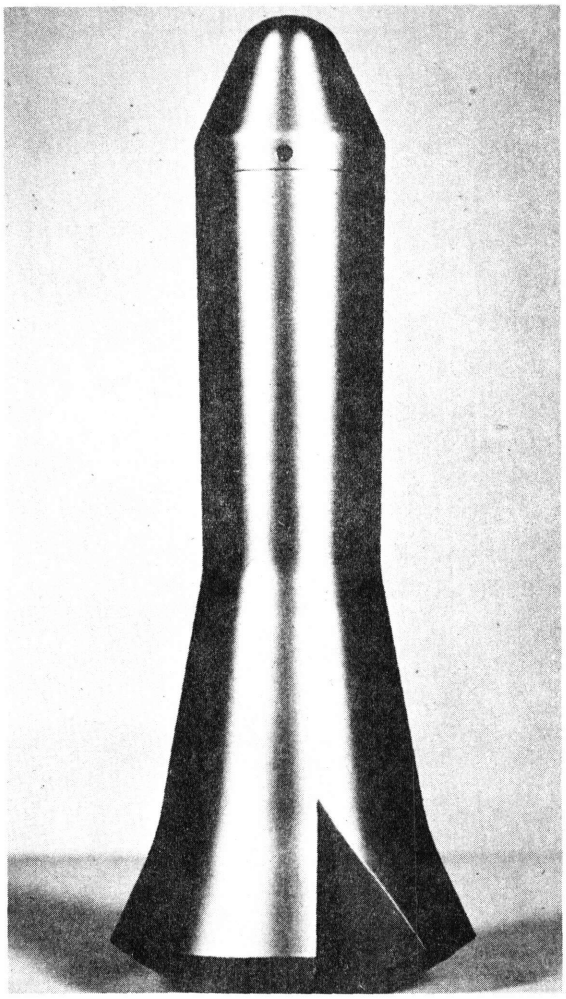

FIG. 12 XXI - H - 5 MODEL

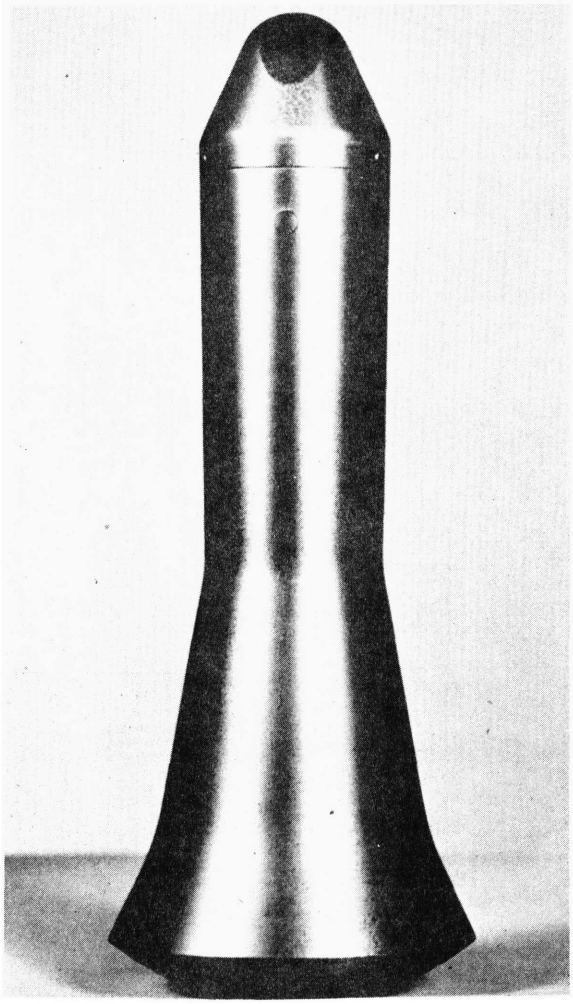

FIG. 13 XXI - H - 7 MODEL

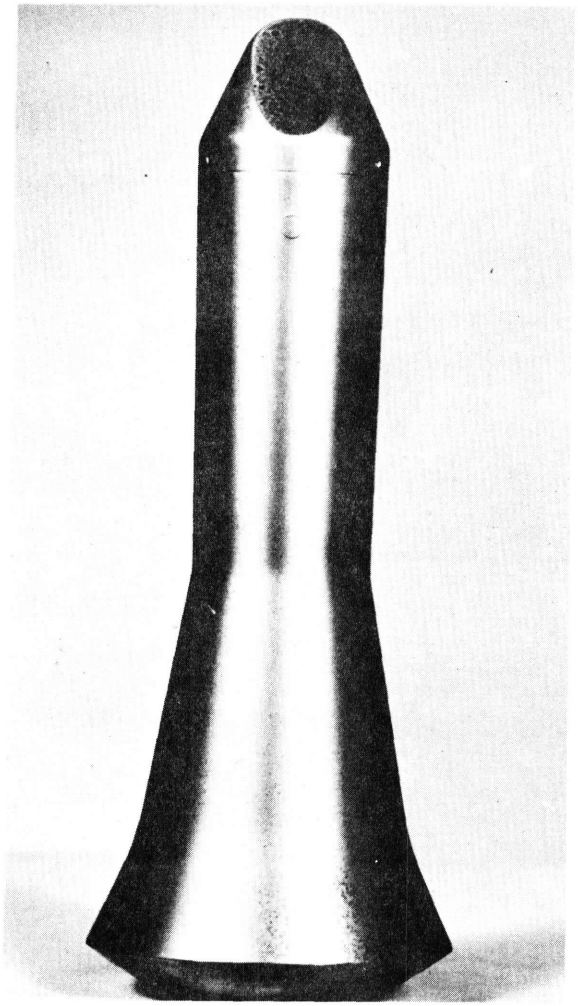

FIG. 14 XXI - H - 8 MODEL

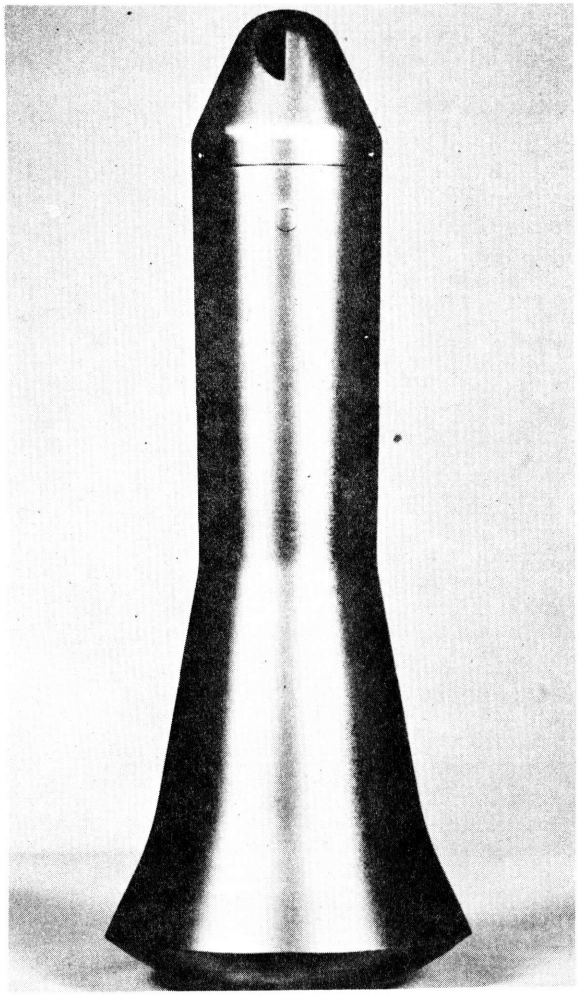

FIG. 15 XXI-H-9 MODEL

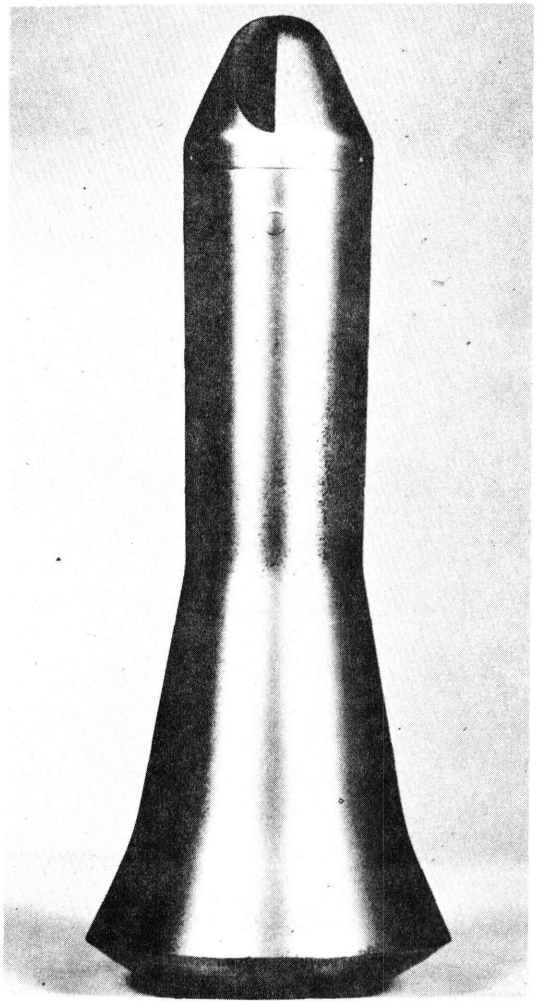

FIG. 16 XXI-H-10 MODEL

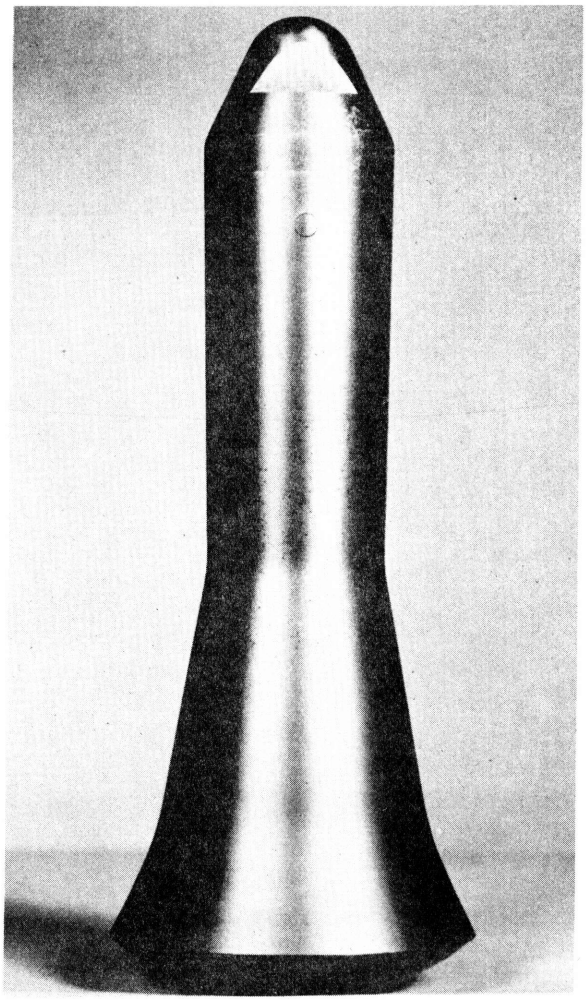

FIG. 17 XXI-H-13 MODEL

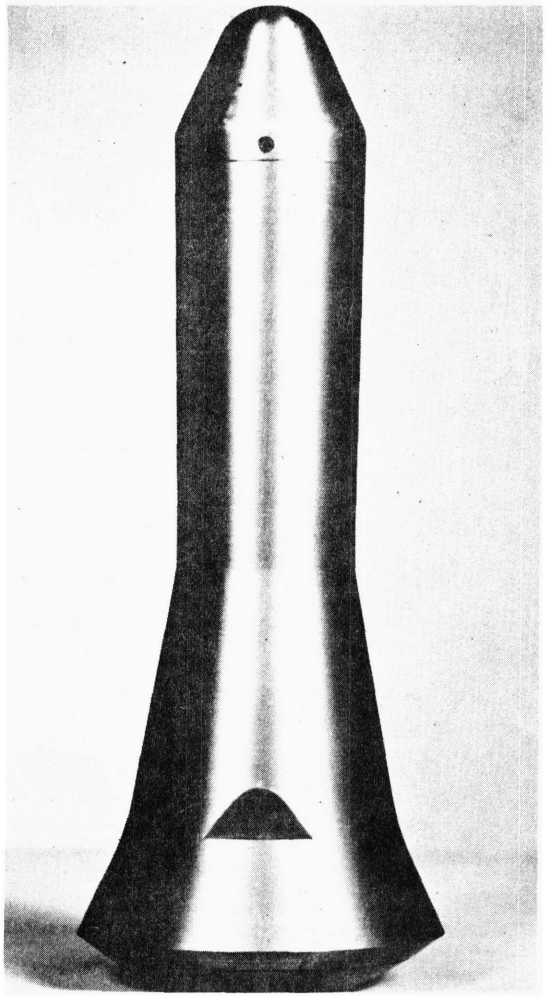

FIG. 18 XXI - H - 14 MODEL

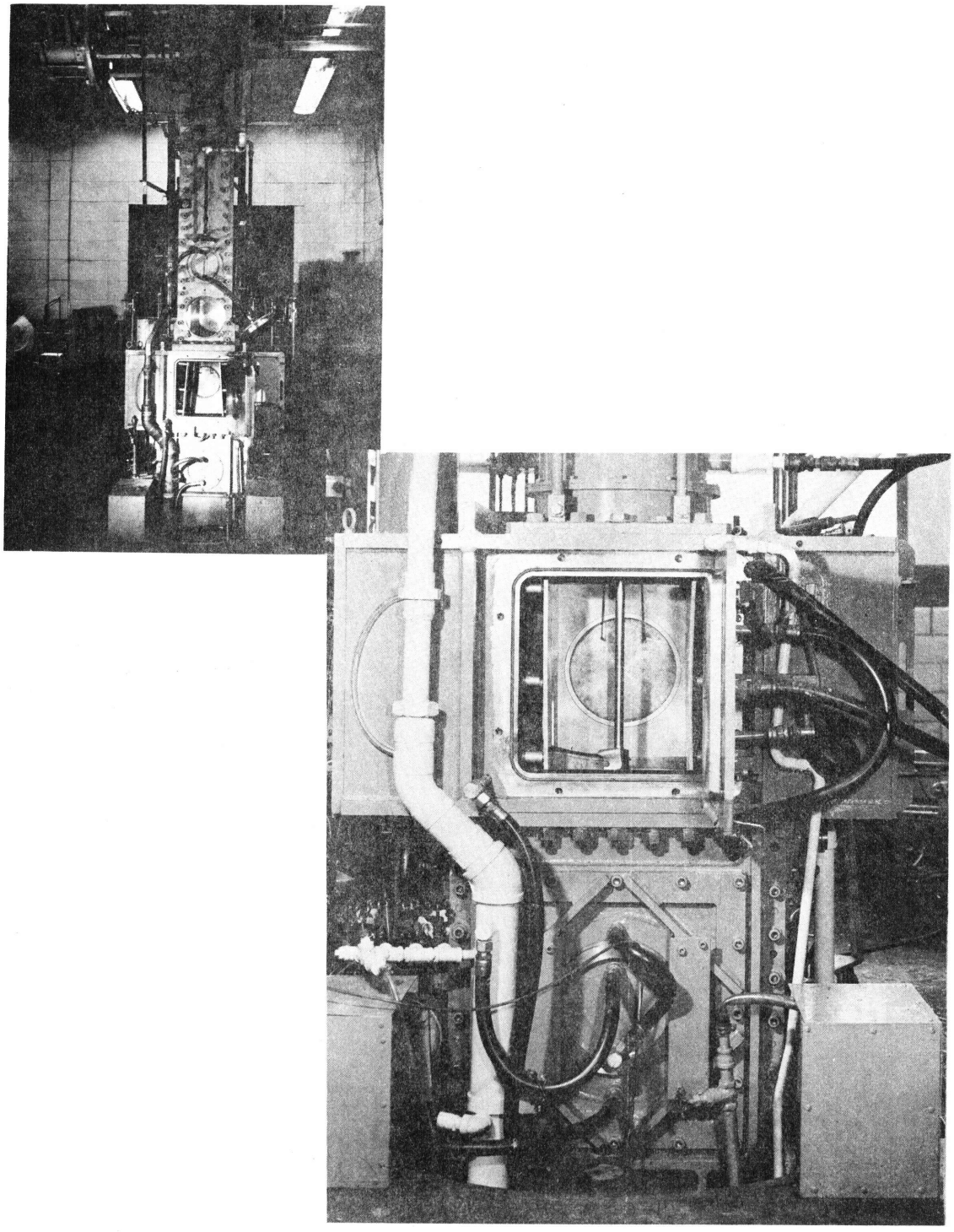

FIG. 19 NOL HYPERSONIC TUNNEL No. 4

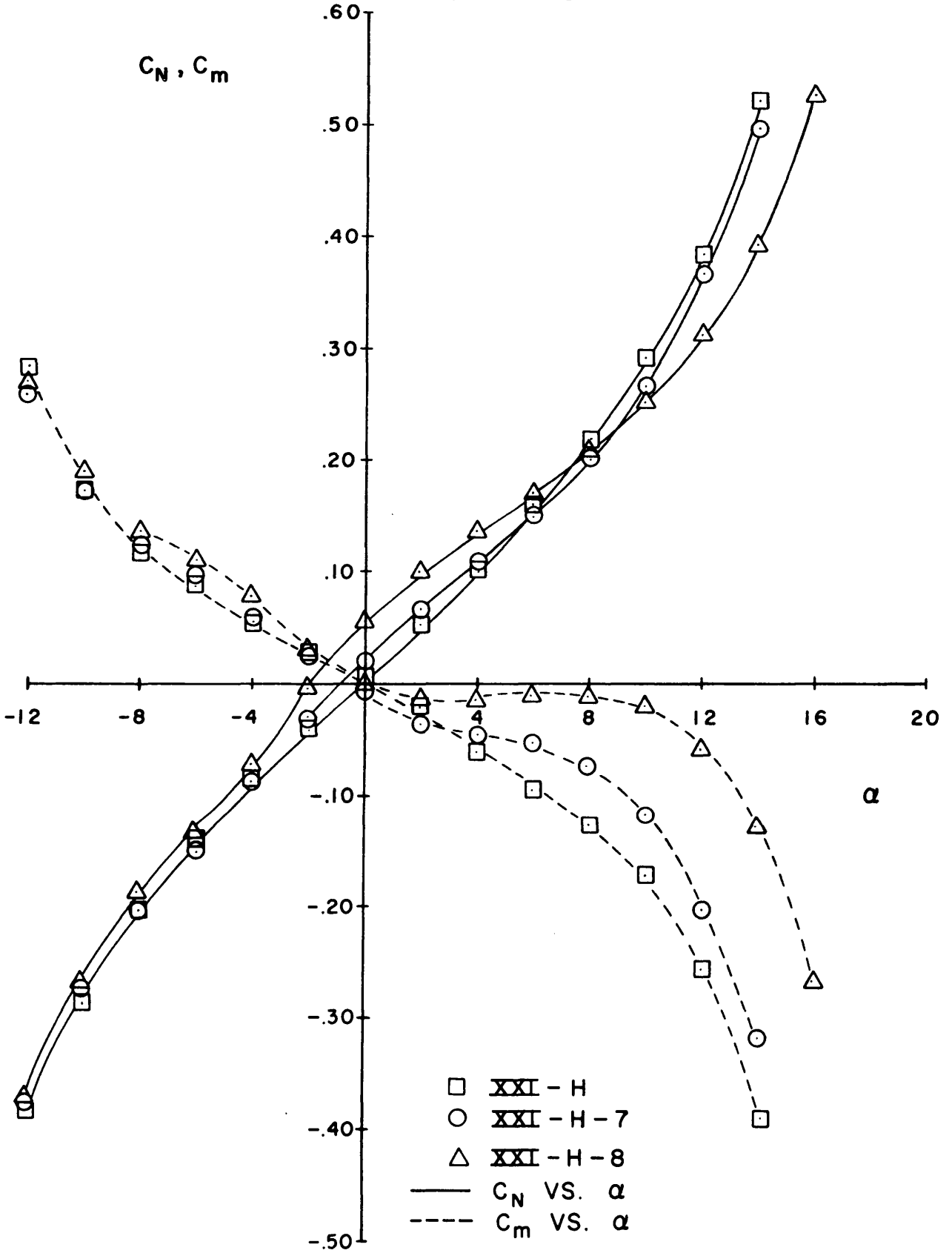

FIG. 20 EFFECT OF GRADUATED NOSE MODIFICATION ON NORMAL FORCE AND PITCHING MOMENT AT $\phi = 0°$

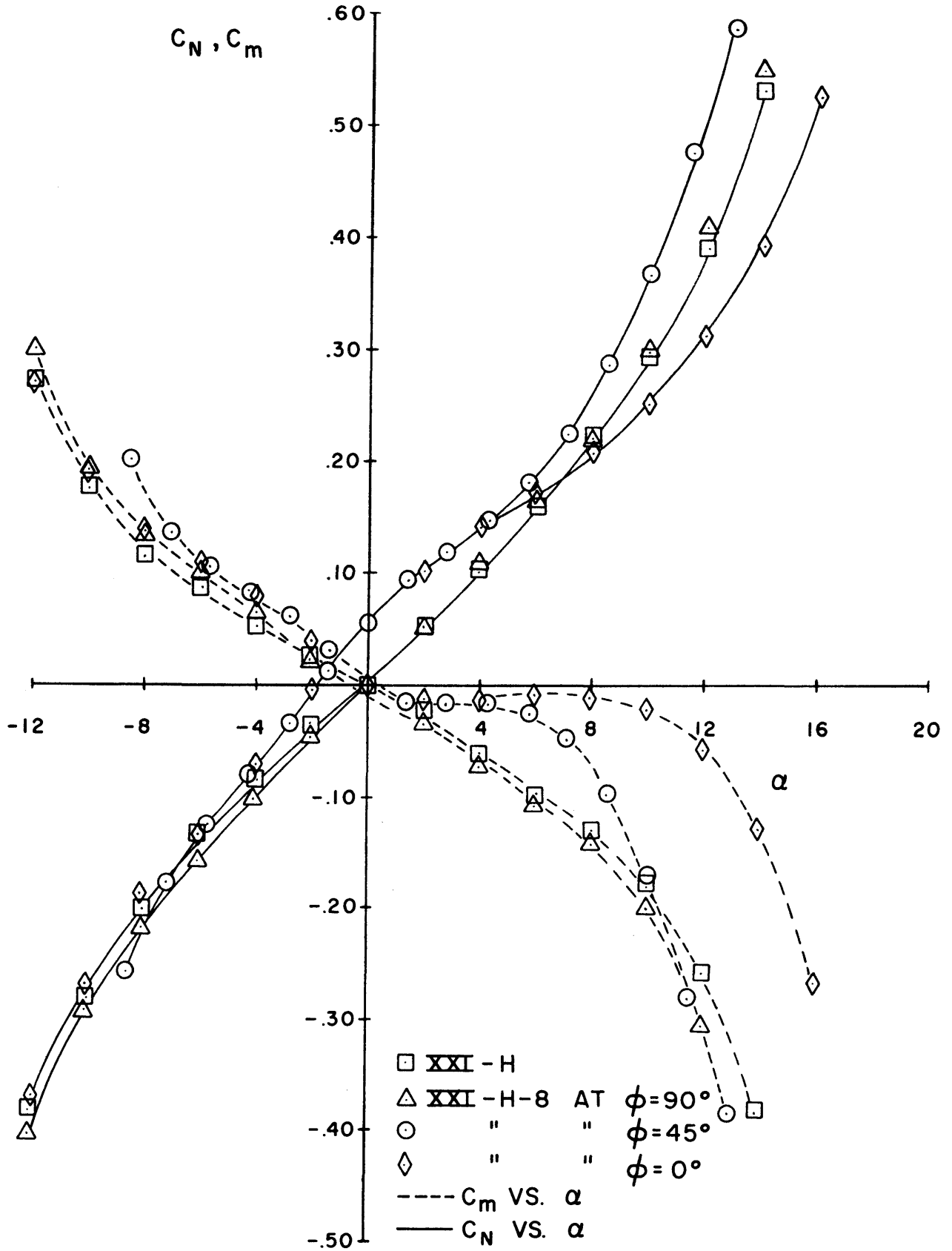

FIG. 21 EFFECT OF ROLL ANGLE ON THE NORMAL FORCE AND PITCHING MOMENT OF NOSE MODIFICATION XXI-H-8

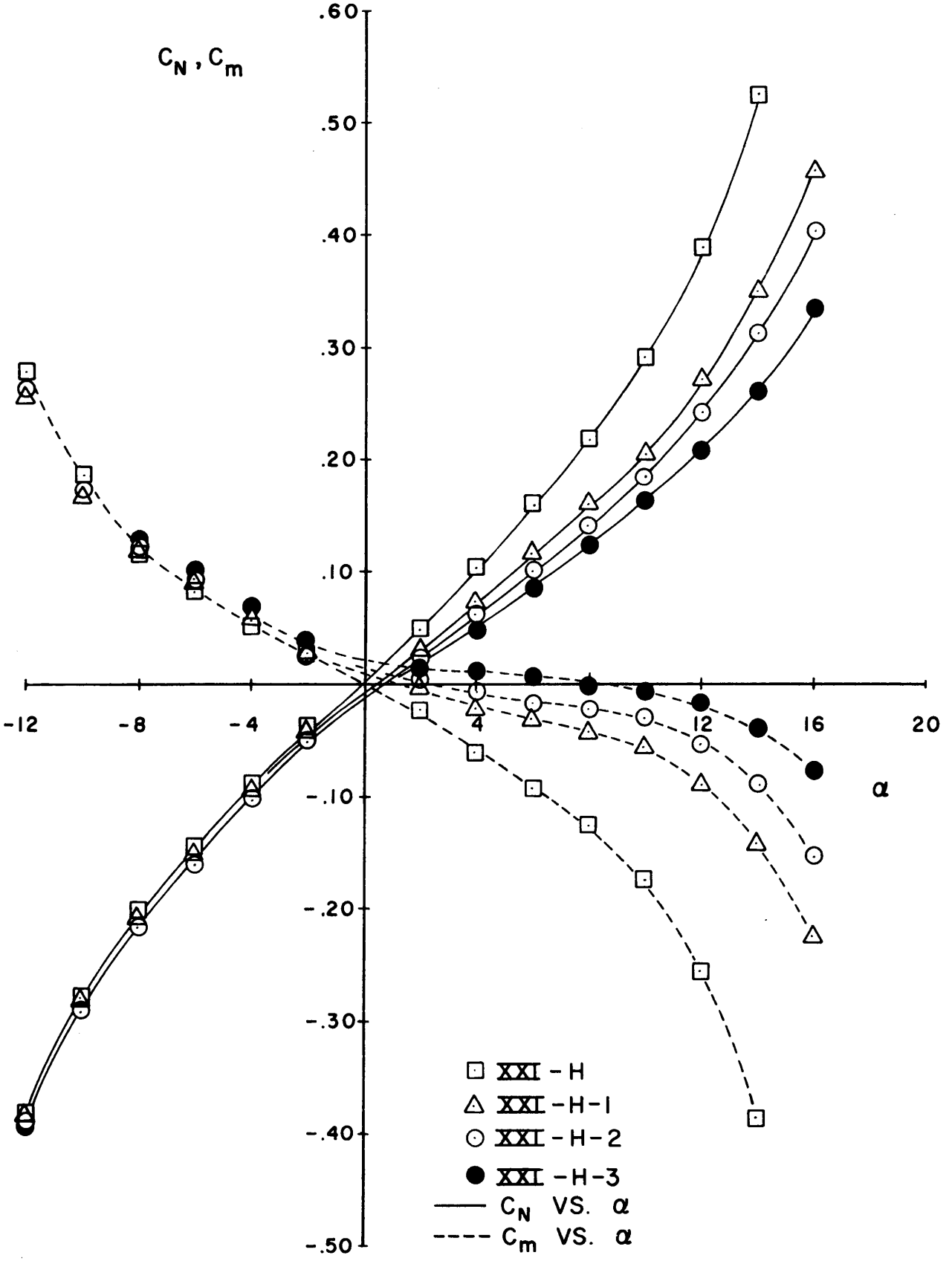

FIG. 22 EFFECT OF GRADUATED FLARE MODIFICATION ON NORMAL FORCE AND PITCHING MOMENT AT $\phi = 0°$

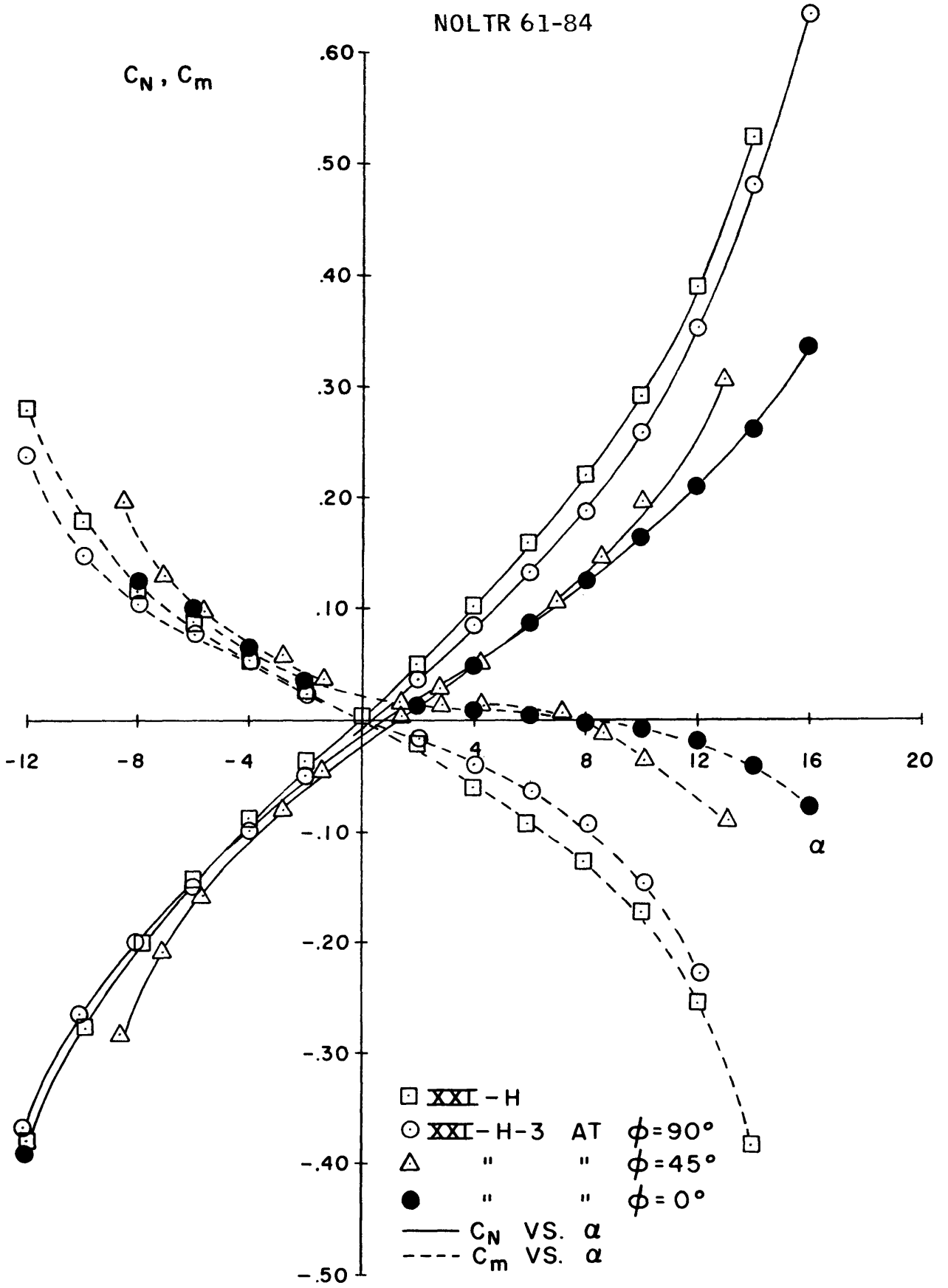

FIG. 23 EFFECT OF ROLL ANGLE ON THE NORMAL FORCE AND PITCHING MOMENT DATA OF FLARE MODIFICATION XXI-H-3

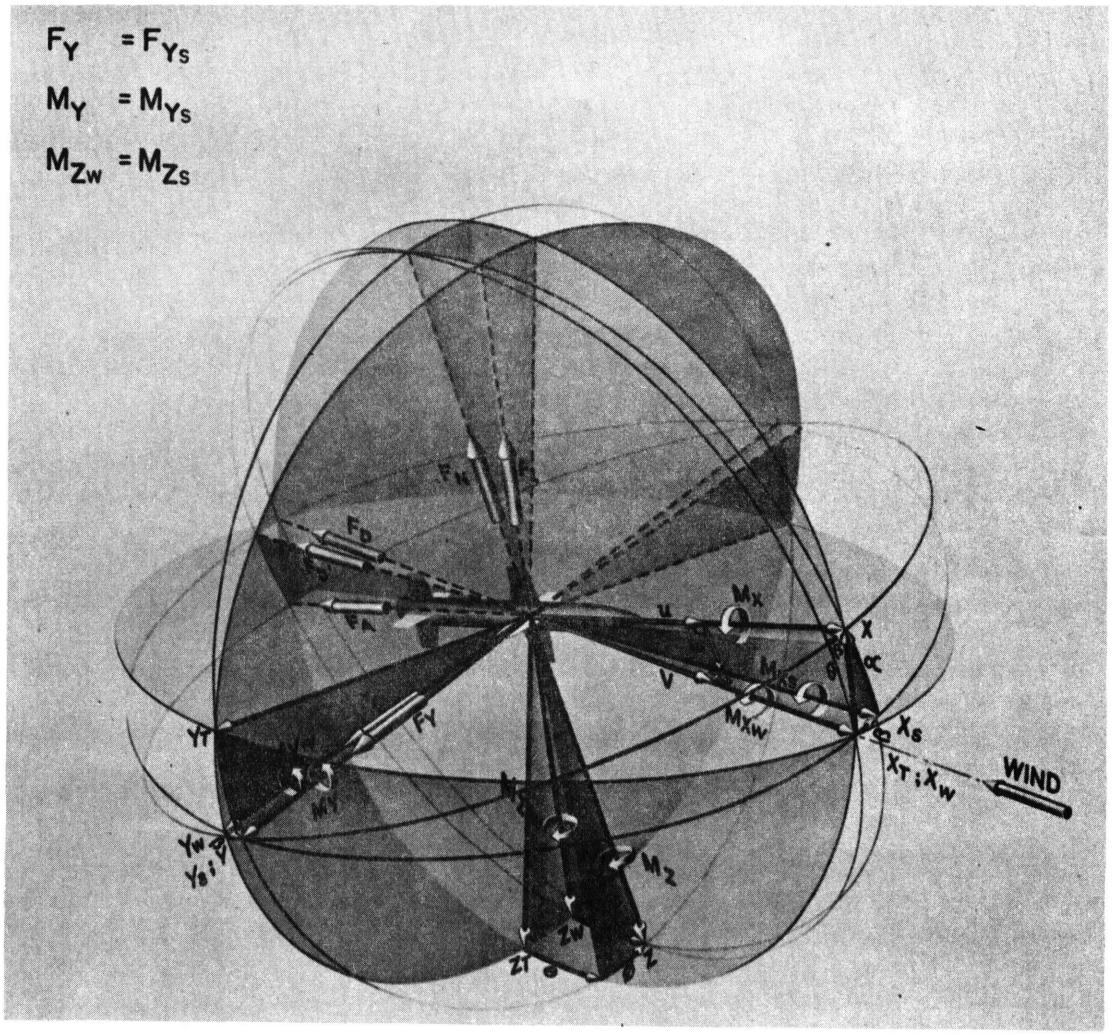

FIG. 24 SIGN CONVENTION

EXTERNAL DISTRIBUTION

	No. of Copies
Director, U.S. Naval Research Laboratory Attn: W. W. Atkins, Code 6240	150
NASA Goddard Space Flight Center Greenbelt, Maryland Attn: J. D. Gates	
Chief, Bureau of Naval Weapons Washington 25, D. C. Attn: Library, DIS 3	2

CATALOGING INFORMATION FOR LIBRARY USE

BIBLIOGRAPHIC INFORMATION

	DESCRIPTORS	CODES		DESCRIPTORS	CODES
SOURCE	NOL technical report	NOLTR	SECURITY CLASSIFICATION AND CODE COUNT	Secret - 21	SØ21
REPORT NUMBER	61-84	61ØØ84	CIRCULATION LIMITATION	Proprietary Information	PPIN
REPORT DATE	27 May 1964	Ø564	CIRCULATION LIMITATION OR BIBLIOGRAPHIC		
			BIBLIOGRAPHIC (SUPPL., VOL., ETC.)		

SUBJECT ANALYSIS OF REPORT

DESCRIPTORS	CODES	DESCRIPTORS	CODES	DESCRIPTORS	CODES
Damage	DAMA	Rolling	ROLL		
Re-entry	REEN	Motion	MOTI		
Body	BODY	Configuration	COFI		
Stability	STBI	Coefficients	COEF		
Static	STAC	Mark	MARK		
Mach	MACH	3 mod 0 (Minor)	3MØN		
10	1ØXØØ	General Electric	GENL		
Hypersonic	HYPR	Aerodynamics	AERD		
Wind Tunnels	WINU	Shapes	SHAP		
Tests	TEST				
Pitching	PITC				
Yaw	YAWE				

ARPA 149 TECHNICAL REPORTS

1. Raytheon Company, "Soviet ICBM Re-Entry Body Study," BR-1065, 21 November 1960 (S-RD)

2. Progress Report No. 1, "Hypervelocity Kill Mechanisms Program," NRL Memorandum Report 1136, January 1961 (S-RD)

3. AVCO Corporation, "Feasibility Study of a Flight Test Aggravation Program, Hypervelocity Kill Mechanism Program-Aerothermal Phase," TAD-TR-29-61-4. 13 February 1961 (S)

4. Progress Report No. 2, "Hypervelocity Kill Mechanisms Program," NRL Memorandum Report 1161, April 1961 (S-RD)

5. Progress Report No. 3, "Hypervelocity Kill Mechanisms Program," NRL Memorandum Report 1209, July 1961 (S-RD)

6. Summary Report, "Fifth Hypervelocity Kill Mechanisms Progress Meeting," of 29-30 June 1961, NRL Memorandum Report 1220, August 1961 (S-RD)

7. Progress Report No. 4, "Hypervelocity Kill Mechanisms Program," NRL Memorandum Report 1240, Quarterly Progress for Period Ending 20 September 1961 (S-RD)

8. "Force Tests on Modified General Electric Mark III Nose Cone Models at Mach Number 18," AEDC-TN-61-151, von Karman Gas Dynamics Facility, ARO, Inc., November 1961 (S)

9. Progress Report No. 5, "Hypervelocity Kill Mechanisms Program," NRL Memorandum Report 1261, Volume I and Volume II, Annual Technical Progress Report December 1961 (S-RD)

10. Progress Report No. 6, "Hypervelocity Kill Mechanisms Program," NRL Memorandum Report 1269, Quarterly Progress for the Period Ending 20 December 1961 (S-RD)

11. NRL Memorandum Report 1314, "Investigation of ICBM Vulnerability to ARPAT Dart," 30 April 1961 (S-RD)

12. General Electric Company, "Hypervelocity Kill Mechanisms Feasibility Study-Internal Heating," Document No. 62SD560 28 May 1962 (S)

13. Progress Report No. 7 "Hypervelocity Kill Mechanisms Program," NRL Report 5813, Semiannual Technical Progress Report for period ending 20 March 1962 - June 1962 (S-RD)

14. Progress Report No. 8, "Hypervelocity Kill Mechanisms Program," NRL Report 5840, Quarterly Progress Report for Period ending 20 June 1962 (S-RD)

15. Progress Report No. 9, "Hypervelocity Kill Mechanisms Program," NRL Report 5913, Annual Technical Progress Report for period ending 30 September 1962 (S-RD) Vols. I and II

16. Progress Report No. 10, "Hypervelocity Kill Mechanisms Program," NRL Report 5931, Quarterly Progress Report for period ending 20 December 1962 (S-RD)

17. General Electric Company,"Results of Rocket Exhaust HKM Internal Heating Tests," Document No. 63SD564 of 20 May 1963 (S)

18. Progress Report No. 11, "Hypervelocity Kill Mechanisms Program", NRL Report 5990, Semiannual Technical Progress Report for Period Ending 20 March 1963.(S-RD)

19. Progress Report No. 12, "Hypervelocity Kill Mechanisms Program," NRL Quarterly Progress Report 6011, August 1963(S)

20 NRL Report No. 6032 "Hypervelocity Impact Damage to Spaced Structures by Massive Projectiles," October 1963 (S)

21. General Electric Company, "Results of Wallops Island HKM Internal Heating Flight Tests," Document No. 63SD885, 4 November 1963 (S)

22. Picatinny Arsenal T.R. No. 3118, "Vulnerability of Nuclear Warheads to Aerothermal Effects," December 1963 (S-RD)

23. Progress Report No. 13 "Hypervelocity Kill Mechanisms Program", NRL Report 6077, February 1964 (S)

24. "Propulsion System Damage Study", Volume I, Summary, Conclusions, and Recommendations; ASD-TDR-64-2, January 1964 (S)

25. "Propulsion System Damage Study", Volume II, Vulnerability Analyses; ASD-TDR-64-2, January 1964 (S)

26. "Propulsion System Damage Study", Volume III, Impact-Damage Studies; ASD-TDR-64-2, January 1964 (S)

27. "A Damage Effects Investigation on a 10-Degree Half-Angle Cone at Mach 10" TDR No. AEDC-TDR-64-80, von Karman Gas Dynamics Facility, ARO Inc. May 1964 (S)

DISTRIBUTION LIST

	No. of Copies
Director Advanced Research Projects Agency Washington, D.C. 20301	6
Director of Defense Research and Engineering Washington, D.C. 20301	1
Director Weapons Systems Evaluation Group Room 1E 875, Pentagon Washington, D.C. 20301	1
Central Intelligence Agency Washington, D.C. 20505	1
Defense Documentation Center Building #5, Cameron Station Alexandria, Virginia 22314	20
Commander Ballistic Systems Division, AFSC, USAF Norton Air Force Base, Calif.	2
Commander Space Systems Division AFSC, USAF, AF Unit Post Office Los Angeles, California 90045	2
Commander Hq. AFCCDD (ESRB) LG Hanscom Field Bedford, Mass. 07131 Attn: MAJOR Hippler	1
Commander Detachment 4, ASD, AFSC U.S. Air Force Eglin Air Force Base, Florida 32542 Attn: Mr. Dale Davis Technical Library (PGTRI)	2
Commander Air Force Special Weapons Center Kirtland Air Force Base, New Mexico 87117 Attn: MAJOR M.R. Nedler,(SWRA) CAPT. Gillespie (S WRA-3175)	2
Commander Field Command Defense Atomic Support Agency (DASA) Sandia Base, P.O. Box 5800 Albuquerque, New Mexico 87115	2

No. of Copies

Air University Library 1
U.S. Air Force
Maxwell Air Force Base
Alabama 36112

Commander 3
Aeronautical Systems Division, AFSC, USAF
Wright-Patterson Air Force Base, Ohio 45433
Attn: ASRCEA/LT D.L. Wells
ASRNGW-1 Leo Krautmann
AF Technical Information Center

Headquarters 1
United States Air Force
Air Force Technical Applications Center/TD, Wash, D.C.

Director 2
Ballistic Research Laboratories
Aberdeen Proving Ground, Aberdeen, Maryland, 21005
Attn: Dr. R. J. Eichelberger
Dr. C. Glass

Officer in Charge 1
U.S. Continental Army Command
Office of Special Weapons Developments
Fort Bliss, Texas 79916
Attn: CAPT. T.W. Love

Commanding Officer 1
U.S. Army Air Defense Combat Development Agency
Fort Bliss, Texas 79916
Attn: CAPT. J. Monza

Commanding Officer 1
Army Material Command RD
Washington, D.C. 20315
Attn: Mr. G. Stetson

Commanding Officer 2
Picatinny Arsenal
Dover, New Jersey 07801
Attn: Mr. Fred Saxe
Dr. A. Nordio

Commander 5
U.S. Army Missile Command
Redstone Arsenal
Huntsville, Alabama 35809

	No. of Copies
Chief of Naval Operations (OP-761) Department of the Navy Washington, D. C. 20350	1
Chief of Naval Operations (OP9221D) Department of the Navy Washington, D. C. Attn: Mr. E. Cecil 20350	1
Chief Bureau of Naval Weapons (RTAD) Attn: D.J. Brockway Washington, D. C. 20360	1
Commanding Officer U.S. Naval Air Development Center Johnsville, Pennsylvania	1
Commanding Officer U.S. Naval Weapons Evaluation Facility Kirtland Air Force Base New Mexico Attn: Code 3432 Mr. C.B. Massengill	1
Director U.S. Naval Research Laboratory Washington, D. C. 20390 Attn: Mr. W. W. Atkins	3
Director, National Aeronautics & Space Administration Langley Research Center, Langley Field, Virginia 23365 Attn: Mr. R. Hopko	1
University of California Lawrence Radiation Laboratory Technical Information Division P.O. Box 808, Livermore, California 94557 Attn: Clovis G. Craig	1
Aeronautical Research Associates of Princeton, Inc. 50 Washington Road Princeton, N. J. 08540 Attn: Dr. C. duP. Donaldson	2
Aerospace Corporation P. O. Box 95085 Los Angeles 45, California Attn: Library Technical Documents Group Dr. D. Singer Dr. J. Brown	3

No. of Copies

AVCO Corporation 2
Research and Advanced Development Division
201 Lowell Street
Wilmington, Massachusetts 01887
Attn: Mr. R.S. Timmins

Battelle Memorial Institute 2
505 King Avenue
Columbus 1, Ohio 43201
Attn: Battelle - Defender

Bell Telephone Laboratories, Inc. 1
Whippany, New Jersey
Attn: Mr. D. Pope

Douglas Aircraft Company, Inc. 1
Missiles and Space Systems
3000 Ocean Park Boulevard
Santa Monica, California
Attn: Mr. T.J. Wolinski

General Atomic 1
P.O. Box 608
San Diego 12, California
Attn: Mr. A. J. Navoy

General Electric Company 2
Missile and Space Vehicle Department
3198 Chestnut Street
Philadelphia, Penna. 19104
Attn: Mr. D. Nestler

Hughes Aircraft Company 2
Culver City, California
Attn: Mr. G. Henry

Institute of Defense Analysis 1
1666 Connecticut Avenue, N.W.
Washington, D. C. 20009

Rand Corporation 1
1700 Main Street
Santa Monica, California 90406 Attn: Library 79

Shock Hydrodynamics, Inc.
15010 Ventura Boulevard 1
Sherman Oaks, Calif. 91403
Attn: Mr. K.N. Kreyenhagen